Doctoral Dissertation
Doctoral Program in Aerospace Engineering (30^{th}cycle)

Space Exploration Robotic Systems

Orbital Manipulation Mechanisms

By

Marco Dolci

******

Supervisor(s):
Prof. Giancarlo Genta, Politecnico di Torino
Mrs. Simona Ferraris, Thales Alenia Space Italy
Mr. Joseph Parrish, NASA JPL - Caltech

Doctoral Examination Committee:
Mr. Robert Lock, Referee, NASA JPL - Caltech
Prof. Zdzislaw Gosiewski, Referee, Bialystok Technical University
Prof. Massimo Sorli, Politecnico di Torino
Prof. Giorgio Figliolini, Università di Cassino
Prof. Vincenzo Parenti Castelli, Università di di Bologna

Politecnico di Torino
2018

Declaration

I hereby declare that, the contents and organization of this dissertation constitute my own original work and does not compromise in any way the rights of third parties, including those relating to the security of personal data.

Marco Dolci
2018

* This dissertation is presented in partial fulfillment of the requirements for **Ph.D. degree** in the Graduate School of Politecnico di Torino (ScuDo).

I would like to dedicate this thesis to my daughter Agnese and to my wife Marta

Acknowledgements

I would like to acknowledge Prof. Giancarlo Genta for his extraordinary support in mentoring me through these years under his guide. His mentorship was really appreciated during my months in Italy, working on the SAPERE project in Thales Alenia Space in Turin and also during my research period at NASA JPL - Caltech. I will never stop being grateful for what he taught me and how he supported me and my desire to go daring might things!

I would like to acknowledge Mrs. Simona Ferraris (and Ms. Genny Scalise) for their support and availability such as their professionalism in working together.

I would like to acknowledge Mr. Joseph Parrish for his support and his really valuable availability and mentorship. It has been a great pleasure being exposed to ROCS under guide.

Abstract

In the future, orbital space robots will assist humans in space by constructing and maintaining space modules and structures. Robotic manipulators will play essential roles in orbital operations. This work is devoted to the implemented designs of two different orbital manipulation mechanical grippers developed in collaboration with Thales Alenia Space Italy and NASA Jet Propulsion Laboratory – California Institute of Technology.

The consensus to a study phase for an IXV (Intermediate eXperimental Vehicle) successor, a preoperational vehicle called SPACE RIDER (Space Rider Reusable Integrated Demonstrator for European Return), has been recently enlarged, as approved during last EU Ministerial Council. One of the main project task consists in developing SPACE RIDER to conduct on orbit servicing activity with no docking. SPACE RIDER would be provided with a robotic manipulator system (arm and gripper) able to transfer cargos, such as scientific payloads, from low Earth orbiting platforms to SPACE RIDER cargo bay. The platform is a part of a space tug designed to move small satellites and other payloads from Low Earth Orbit (LEO) to Geosynchronous Equatorial Orbit (GEO) and viceversa. The assumed housing cargo bay requirements in terms of volume (<100l) and mass (<50kg) combined with the required overall arm dimensions (4m length), and mass of the cargo (5-30kg) force to developing an innovative robotic manipulator with the task-oriented end effector. It results in a seven degree-of-freedom arm to ensure a high degree of dexterity and a dedicate end-effector designed to grasp the cargo interface. The gripper concept developed consists in a multi-finger hand able to lock both translational and rotational cargo degrees of freedom through an innovative underactuation strategy to limit its mass and volume. A configuration study on the cargo handle interface was performed together with some computer aided design models and multibody analysis of the whole system to prove its

feasibility. Finally, the concept of system control architecture, the test report and the gripper structural analysis were defined.

In order to be able to accurately analyze a sample of Martian soil and to determine if life was present on the red planet, a lot of mission concepts have been formulating to reach Mars and to bring back a terrain sample. NASA JPL has been studying such mission concepts for many years. This concept is made up of three intermediate mission accomplishments. Mars 2020 is the first mission envisioned to collect the terrain sample and to seal it in sample tubes. These sealed sample tubes could be inserted in a spherical envelope named Orbiting Sample (OS). A Mars Ascent Vehicle (MAV) is the notional rocket designed to bring this sample off Mars, and a Rendezvous Orbiting Capture System (ROCS) is the mission conceived to bring this sample back to Earth through the Earth Entry Vehicle (EEV). MOSTT is the technical work study to create new concepts able to capture and reorient an OS. This maneuver is particularly important because we do not know an OS incoming orientation and we need to be able to capture, to reorient it (2 rotational degrees of freedom), and to retain an OS (3 translational degrees of freedom and 2 rotational ones). Planetary protection requirements generate a need to enclose an OS in two shells and to seal it through a process called Break-The-Chain (BTC). Considering the EEV would return back to Earth, the tubes orientation and position have to be known in detail to prevent any possible damage during the Earth hard landing (acceleration of $\sim$1300g). Tests and analysis report that in order for the hermetic seals of the sample tubes to survive the impact, they should be located above an OS equator. Due to other system uncertainties an OS presents the potential requirement to be properly reoriented before being inserted inside the EEV. Planetary protection issues and landing safety are critical mission points and provide potential strict requirements to MOSTT system configuration. This task deals with the concept, design, and testbed realization of an innovative electro-mechanical system to reorient an OS consistent with all the necessary potential requirements. One of these electro-mechanical systems consists of a controlled-motorized wiper that explores all an OS surface until it engages with a pin on an OS surface and brings it to the final home location reorienting an OS. This mechanism is expected to be robust to the incoming OS orientation and to reorient it to the desired position using only one degree of freedom rotational actuator.

Contents

List of Figures **xiv**

List of Tables **xxxiv**

Nomenclature **xxxvi**

Introduction **1**

Space Robotics: Goals and Technologies 1

Overview of the Historical Development of Space Robots 1

Future of Space Robotics 3

Thesis Internal Structure 3

Thales Alenia Space Italy Project 5

Goal of this Thesis - 1 5

SAPERE-STRONG Projects 6

Thesis Structure - 1 8

NASA Jet Propulsion Laboratory Project 9

Goal of the Thesis - 2 9

Mars In-Orbit Sample Transfer Technologies 9

Mars Sample Return Introduction: Past, Present, and Future Mars Exploration 10

Mars Sample Return Mission Architecture 13

Thesis Structure - 2 14

1 Space Robotic Grasping Manipulator Design Process 16

1.1 Introduction 17

1.1.1 SAPERE - STRONG projects 17

1.1.2 Past, Present and Future Scenarios 18

1.1.3 Robotic Grippers in an Unstructured Environment . . . 19

1.1.4 Work Goal 20

1.2 Robotic System Constraints and Mission Profile 20

1.2.1 Mission Scenario 20

1.2.2 System Requirements and Constraints 21

1.2.3 System Control Architecture 22

1.2.4 System Configuration Trade-Off 24

1.3 Robotic Arm Preliminary Design 25

1.3.1 Design assumptions 25

1.3.2 Design description 26

1.4 Robotic Manipulator Design 26

1.4.1 Gripper requirements identification 26

1.4.2 Handle Requirements 31

1.4.3 Gripper Possible Configuration Identification and Trade-offs Executions 32

1.5 Robotic Manipulator Baseline Configuration 35

1.5.1 Geometrical models 35

1.5.2 Materials 42

1.6 Single Finger Kinematic Analysis 44

1.7 Gripper Dynamic Analysis 47

1.8 Gripper Functional Model 50

1.8.1 Motor and Gearbox Model 50
1.8.2 Functional Model General Architecture 53
1.8.3 BLDC Motor System-Level Model 54
1.8.4 Control Architecture 56
1.8.5 Control Strategy: Impedance Control 57
1.9 Test Report 59
1.9.1 Physical model 59
1.9.2 Software Model 70
1.10 Structural Analysis Considerations 72
1.10.1 Single Finger FEA Analysis 73
1.10.2 Blocking Bar FEA Analysis 77
1.10.3 Handle FEA Analysis 82
1.11 Acknowledgments 86

2 A Potential Mars Sample Return: Science and Technology 87
2.1 Current Knowledge of Mars 87
2.2 Exploration of Mars 88
2.3 Determine if life ever arose on Mars 95
2.4 Importance of Mars Sample Return 95
2.4.1 Sample Return is the Next Step 96
2.5 A Potential Mars Sample Return Mission Architecture 100
2.5.1 Overview 100
2.5.2 Technology Maturity 102
2.5.3 Key Trades 103
2.6 A Potential Mars Sample Return Campaign Technical Overview 103
2.6.1 Mars 2020 105
2.6.2 The Lander Mission 108

2.6.3 Flight System 110
2.6.4 Mars Returned Sample Handling Concept 114
2.6.5 Planetary Protection 116

3 SE Approach to the OS CRR Problem 117

3.1 NASA Mission Concept Approach 118
3.2 System Engineering Approach 119
3.3 Problem Statement 119
3.3.1 Symmetry Conservation 122
3.4 State of the Art - Previous Study 123
3.4.1 NASA OS Capture Previous Study and Test 123
3.4.2 ESA OS Capture Previous Study and Test 125
3.5 Current Study 128
3.6 Conceptual Design Solutions 129
3.6.1 Manipulation Object Scenarios 129
3.6.2 Potential System Requirements 131
3.6.3 N^2 Diagram 133
3.6.4 Potential System Criteria 135
3.6.5 Conceptual Designs 136
3.7 Assessment Process - Trade-off Study 146
3.7.1 TOPSIS Approach 147
3.7.2 Reorientation Mechanism Concept Study 149
3.8 Conceptual Wiper Design Integrated in the MSR Spacecraft . . 153

4 Wiper Design and Analysis 157

4.1 Testbed Design 158
4.1.1 Mechanism Sizing 159
4.1.2 Mechanism Modeling 161

4.2 Wiper Analysis 165
4.2.1 Potential Wiper Requirements 165
4.2.2 Wiper 2D Analysis 166
4.3 Wiper 3D Analysis - Evolutionary Process 169
4.3.1 Case 1: Arc-Arc Scenario 170
4.3.2 Wiper 3D Analytical Profile 171
4.3.3 Case 2: Arc-Wiper Scenario 178
4.3.4 Case 3: Wiper-Wiper Scenario 179
4.3.5 Case 4: Optimized Wiper-Wiper Scenario 183
4.4 3D-Printed Wiper 205

5 Testbed Design and Analysis 209

5.1 Testbed N.1: Three-Roller Wiper Testbed Description 210
5.1.1 Wiper - Positive Feature Shape and Profile 212
5.1.2 Pin Dimensions 213
5.1.3 Actuator Housing Support 214
5.1.4 Motor Shaft-Wiper Connection 215
5.1.5 Electronic System 219
5.1.6 Testbed Assembling 228
5.1.7 Testbed Alignment 230
5.2 Testbed Apparatus 230
5.2.1 Testbed Apparatus Actuation 231
5.2.2 Results 236
5.3 Testbed N.2: Water Wiper Testbed Description 237
5.3.1 Electronic System 240
5.3.2 Results 246
5.3.3 Water Testbed Considerations 247

5.4 Final MOSTT Wiper Testbed 247
5.5 OS Retention Mechanism 248

6 Experimental Setup 252

6.1 Apparatus Description 252
6.1.1 Electronics 254
6.1.2 Inertial Mass Unit (IMU) 255
6.1.3 DFRobot Bluetooth Bee 257
6.2 Extended Kalman Filter - Sensor Fusion 258
6.2.1 Tait-Bryan Angles 258
6.2.2 Quaternions 262
6.2.3 Sampling Rate 263
6.2.4 Data Low-Pass Filter: Moving Average 264
6.3 Tests and Data Acquisition 265
6.3.1 Procedure 265
6.3.2 Data Handling 265
6.3.3 Test Considerations 271
6.3.4 Motor No.1 Approach 273
6.3.5 Motor No.2 Approach 274
6.4 Representative Results 275
6.4.1 Design Of Experiment 275
6.4.2 Results 276
6.4.3 Results 294
6.5 Conclusion 295
6.5.1 Future Perspectives 296
6.6 Acknowledgements 296

Conclusions 298

Conclusion 298
Thales Alenia Space Torino 298
NASA JPL - Caltech 299

Bibliography **301**

List of Figures

1 Close loop to support the creation and verification of innovative gripper concepts. 4

2 Thesis Organization Map. 5

3 SPACE RIDER Operational Phases. The spacecraft will be launched from Europe's Spaceport in Kourou, French Guiana, stay in orbit as required by its payloads, and then perform a ground landing Courtesy of ESA. 7

4 Thesis Strategic Map. 8

5 Potential Mars Sample Return Architecture. Courtesy of NASA. 9

6 Thesis Strategic Map. 15

1.1 Mission scenario elements. Left: a general platform architecture is attached to the Space Tug. On the platform there is the payload to be brought on the ground. Right: reentry vehicle attached to the VEGA upper stage (AVUM). In the cargo bay of the reentry vehicle a robotic manipulator is located. This work is devoted to define its requirements determination and its preliminary design [41]. 21

1.2 Space RIDER-Space Tug rendez-vous maneuver. 22

1.3 Camera-marker scheme to infer position and attitude possible errors. This is fundamental in order to obtain a first evaluation of the camera design [41]. 30

1.4 Palmoptical system (geometric optical approach) developed to guarantee a higher redundancy degree. 31

1.5 Finger mechanism actuation phases. The finger stays open, to guarantee the handle capturing requirement with ±30mm and ±6° uncertainties. After that, the distal phalanx was closed. The proximal phalanx does not move thanks to a torsional spring that holds it in place. This happens until the mechanism hits a stop located on the proximal phalanx. In doing that, the whole finger rotates around a hine located on the point that connects the proximal phalanx to the gripper palm and the whole finger rotates capturing the handle side [41]. 34

1.6 Phalanx kinematics plot. Phalanx angular velocity as a function of time for the proximal phalanx and the distal phalanx. It is worth noting that while the mechanism is working, the first phalanx holds, while the second moves. When the second phalanx is open the whole finger will rotate at the same angular velocity. As expected, after 1 s, the absolute angular displacement of the phalanxes is the same. The noise affecting the phalanxes in the angular displacement plot is due to the handle interaction disturbances [41]. 35

1.7 CAD of the reentry vehicle grasping handle. This tool is attached to the payload external surface. The dimensions were reported in mm [41]. 36

1.8 Reentry vehicle payload and preliminary handle positioning. This tool is attached to the payload external surface. The dimensions were reported in mm [41]. 37

1.9 Re-entry vehicle payload and preliminary handle positioning simulation. This tool will be attached to the payload external surface. Nine snapshots of the gripper closure on the handle rear are shown. 38

1.10 Finger grasping closure operating at a distance of 40mm. Blue line: finger phalanxes; red line: handle sides; black line: payload profile. 38

1.11 Finger grasping closure operating at a distance of 40mm. It takes into consideration camera-marker tracker uniformly distributed positioning errors (±2.5 mm). 39

1.12 Single finger grasping basic kinematics. Right: second phalanx open; Left: second phalanx closed [41]. 40

1.13 Single finger grasping tool main design CAD using Autodesk Inventor [41]. 41

1.14 Reentry vehicle LEO payload grasping tool: front view [41]. The dimensions were expressed in mm. 42

1.15 Reentry vehicle LEO payload grasping tool: lateral view [41]. The dimensions were expressed in mm. 42

1.16 Single finger Matlab scheme [41]. 44

1.17 First phase finger forward kinematics [41]. 45

1.18 Second phase finger forward kinematics [41]. 45

1.19 Point A (upper left), B (upper right), C (loIr left), D (loIr right) workspace as variation of l_0. For each point the red line refers to the first phase working operation, while the blue line to the second phase [41]. 46

1.20 Point E (upper left), G (upper right), I (lower left), L (lower right) workspace as variation of l_0. For each point the red line refers to the first phase working operation, while the blue line to the second phase [41]. 47

1.21 Mechanical components constituting the gripper. From left to right: grasping mechanism, ball screw mechanism, motor+gear box [41]. 48

1.22 MSC Adams multibody system simulation. The payload inertial properties were reported (30kg mass, inertia moments) such as the ones of the gripper and the kinematic connections between its different parts [41]. 49

1.23 Detail of the closure phase of the grasping mechanism-handle system. The arrows represent the forces exchanged between the second phalanxes of each finger and the handle side, such as the handle palm and the handle surface. The gripper cover is here transparent to better show how the rigid tendons work [41]. . . 50

1.24 Motor velocity diagram speed as a function of time. It is a steep diagram because a system that can start very fast and have a quick response was needed. 52

1.25 Reentry vehicle gripper grasping robotic control system. There are three main blocks: the Control Overall System Block, the Control Arm Block and the Control Robotic Hand Block [41]. . 54

1.26 From top to bottom: rotor speed (rpm), mechanical power (W) and efficiency (%) as a function of time. All these plots follow the same expected trend due to the voltage system [41]. 56

1.27 End-effector position velocity and acceleration closed-loop control system using Simulink. 58

1.28 Reference frame (left) and a gripper-payload system picture (right). X-y plane defines the grasping maneuver plane, while the z-axis identifies the direction normal to this plane. 59

1.29 Workspace relative to the possible grasping configurations within the assigned error recovering. 60

1.30 Linear displacements (x, y, z, absolute distance) of the handle as a function of time during the grasping maneuver. 61

1.31 Linear and angular velocity of the handle-payload system as a function of time during the grasping maneuver. 61

1.32 Linear displacements (x, y, z, absolute distance) of the handle as a function of time during the grasping maneuver. 62

1.33 Linear and angular velocity of the handle-payload system as a function of time during the grasping maneuver. 62

1.34 Linear displacements (x, y, z, absolute distance) of the handle as a function of time during the grasping maneuver. 63

1.35 Linear and angular velocity of the handle-payload system as a function of time during the grasping maneuver. 63

1.36 Linear displacements (x, y, z, absolute distance) of the handle as a function of time during the grasping maneuver. 64

1.37 Linear and angular velocity of the handle-payload system as a function of time during the grasping maneuver. 64

1.38 Linear displacements (x, y, z, absolute distance) of the handle as a function of time during the grasping maneuver. 65

1.39 Linear and angular velocity of the handle-payload system as a function of time during the grasping maneuver. 65

1.40 Linear displacements (x, y, z, absolute distance) of the handle as a function of time during the grasping maneuver. 66

1.41 Linear and angular velocity of the handle-payload system as a function of time during the grasping maneuver. 66

1.42 The maneuver starts [41]. 67

1.43 The distal phalanx contacts the handle side [41]. 67

1.44 The fingers bring the handle to the correct position [41]. 67

1.45 The fingers close on the handle side using also the nearest phalanx [41]. 68

1.46 The grasping is performed successfully [41]. 68

1.47 The grasping retains the handle surface against the gripper palm [41]. 68

1.48 Simulation analysis data regarding the position variation of the handle center of mass with respect to the gripper palm. The handle was positioned at an absolute distance of 37.5mm (22.4mm, -14.2mm, 26.4mm) with respect to the gripper palm. Even if the distance was greater than 30mm, the whole mechanism proves to be robust working successfully [41]. 69

1.49 Linear and angular velocity of the handle-payload system as a function of time during the grasping maneuver. The initial velocity for the payload + handle ensemble was set to be 3mm/s (y-axis) and 5°/s (around x-axis) [41]. 69

1.50 Matlab and Simulink gripper control block. 71

1.51 Absolute distance in mm (red line) and grasping activity actuation signal (black line) as a function of time. The whole maneuver takes about 10s. 72

1.52 Linear actuator force as a function of time for the entire grasping maneuver. 100N force was considered as the worst case scenario with a short duration (<1s). 73

1.53 Single finger FEA analysis. Some constraints were defined: the distal and nearest phalanx were considered fixed, the joints were properly described, a force of 100N was applied on the back of top l-structure (pink arrows), and a temperature load was considered on the top surfaces of the l-structures. 74

1.54 Von Mises stress considering only the force acting on the finger. 75

1.55 Von Mises stress considering the force acting on the finger together with a temperature load of -150C. 75

1.56 Von Mises stress considering the force acting on the finger together with a temperature load of +150C. 76

1.57 Blocking bar compression load as a function of time for the entire grasping maneuver. 300-MPa load was considered as the worst case scenario with a short duration (<1 s). 77

1.58 Gripper finger detail, from bottom to top: nearest phalanxes, blocking bar and medium beam. 78

1.59 Blocking bar FEA analysis. Some constraints were defined: both the nearest phalanx were considered fixed, a uniform pressure of 300MPa was applied on the cylindrical surface of the blocking bar (pink arrows). 78

1.60 Von Mises stress considering only the pressure acting on the blocking bar. 79

1.61 Only blocking bar FEA analysis. Some constraints were defined: both the cylindrical faces were considered fixed, a uniform pressure of 300MPa was applied on the cylindrical surface of the blocking bar (orange arrows), and a temperature load was considered (blue arrows). 79

1.62 Von Mises stress considering only the pressure acting on the blocking bar. 80

1.63 Von Mises stress considering the pressure acting on the blocking bar together with a temperature load of -150C. 80

1.64 Von Mises stress considering the force acting on the finger together with a temperature load of +150C. 81

1.65 Gripper palm-handle contact force as a function of time for the entire grasping maneuver. 100-N force was considered as the worst case scenario with a short duration (<1s). Blue line represents the contact force between the handle and the distal phalanx, orange line represents the contact force between the handle and the nearest phalanx, gray line represents the contact force between the handle and the gripper palm. After the grasping phase the contact force sets to ∼8.5N. 82

1.66 Handle FEA analysis. Some constraints were defined: the surface attached to the payload was considered fixed (green arrows), a force of 100N was applied on the external surfaces and on the internal surface (pink arrows), and a temperature load was considered on the whole handle body. 83

1.67 Von Mises stress considering only the force acting on the external and internal surfaces. 83

1.68 Von Mises stress considering the force acting on the external and internal surfaces. together with a temperature load of -150C. 84

1.69 Factor of safety (FOS) considering the force acting on the external and internal surfaces together with a temperature load of -150C. 84

1.70 Von Mises stress considering the force acting on the external and internal surfaces. together with a temperature load of +150C. 85

1.71 Factor of safety (FOS) considering the force acting on the external and internal surfaces. together with a temperature load of +150C. 86

2.1 Examples of globally data sets highlight major accomplishments from multiple recent missions [14]. 89

2.2 Examples of the diversity of environments and their mineralogy and morphology [66]. 92

2.3 Notional MSR architecture, see [89] and [90]. 100

2.4 Potential MSR Mission: Key Technologies, see [89] and [90]. . . 102

2.5 Proposed MSR Campaign, see [89] and [90]. 104

2.6 Potential MSR Elements, Functions, and Sample States, see [89] and [90]. 105

2.7 NASA's 2020 Mars rover mission would go to a region of Mars thought to have offered favorable conditions long ago for microbial life, and the rover would search for signs of past life there. It would also collect and cache samples for potential return to Earth, for many types of laboratory analysis [96]. 106

2.8 OS concept baseline design: exploded view [97]. 107

2.9 OS concept design with a detail of the sample tube [89]. 108

2.10 OS concept FEM with close up image of flexure claw structure [97]. 108

2.11 Lander System Concepts, see [89] and [90]. 110

2.12 Two-Stage Solid Rocket MAV Concept in Proposed Launch Configuration, see [70] and [98]. 110

2.13 Preliminary Orbiter Configuration, see [89] and [90]. 111

2.14 Rendez-vous and Capture System Concept [88]. 112

2.15 Rendezvous with a potential Solar Electric Propulsion (SEP) Orbiter, see [89] and [90]. 113

2.16 Earth Entry Vehicle Design concept [91]. 114

2.17 Mars Returned Sample Handling Concept [100]. 115

3.1 System engineering approach diagram. 119

3.2 CADs of notional OS configurations. During this thesis work, when the author refers to *the OS*, the author refers only to one of the two potential OS configurations reported in this figure. . 122

3.3 NASA rendezvous and sample capture design concept, see [92]. . 124

3.4 NASA test setup overview, see [88]. 124

3.5 Test hardware. Left: frame, capture cone, and launcher. Top right: OS simulator with shell. Bottom right: OS simulator without shell, see [88]. 125

3.6 ESA Sample canister Capture Mechanism flight model concept, see [113]. 126

3.7 ESA complete test schematics, [113]. 127

3.8 ESA experiment ready for parabolic flight test campaign, [113]. 127

3.9 N^2 diagram for CRR orbital system. 134

3.10 Ring plus gear thin pattern working concept. 138

3.11 Ring plus gear thick pattern working concept. 139

3.12 Clump with two side OS container [117]. 140

3.13 Power spectrum density (PSD) as a function of spatial frequencies. 141

3.14 Components that characterize this case. Left: complete system with OS. Top right: chamfered cylinder. Bottom right: flat cylinder. 141

3.15 Chamfered wall tunnel OS interaction complete system [117]. . . 142

3.16 Story board of the Chamfered wall tunnel OS interaction complete system using MSC Adams [117]. 143

3.17 Space cup with the OS that presents a positive annular ring, see [117]. 144

3.18 CAD of the Wiper mechanism with the OS that presents a positive feature (pin). 145

3.19 Orientation design tree. 151

3.20 Preliminary Wiper system assembly attached to a concept of the SRO spacecraft. 153

3.21 Preliminary Wiper system assembly attached to a concept of the SRO spacecraft (zoom-in). 154

3.22 Conceptual Wiper Design integrated in the SRO spacecraft (to be continued). 155

3.23 Conceptual Wiper Design integrated in the SRO spacecraft. . . 156

4.1 Wiper mechanism system. The Wiper sweeps a spherical profile around the OS engaging the pin in a converging fashion such that the pin terminates in a predetermined location [124]. 158

4.2 Ideal Wiper mechanism system component sizing. 159

4.3 CAD of one-way flexure fingers in shell to keep the OS centered [124]. 161

4.4 Free-body diagram of the OS in space in a zero-g environment. The forces and torques acting on the OS are reported. 161

4.5 Free-body diagram of the OS in space in a zero-g environment. . 163

4.6 Free-body diagram detail of the Wiper-positive feature interaction with the pin. 163

4.7 Wiper-positive feature interaction with the OS pin has to guarantee a larger scissor angle (3D angle Wiper-positive feature profile angle) for least friction [124]. In this case the rotation angle is 0°. It increases counterclockwise. 164

4.8 Wiper 2D analysis. 167

4.9 Wiper 2D analysis results. 167

4.10 Modified Wiper 2D analysis results. 168

4.11 Modified Wiper 2D analysis results. 168

4.12 Wiper 3D evolutionary process analysis. The four candidates that are discussed in the next Sections. Top line: CAD drawings. Bottom line: Z-Ultra 3D-printed models to have a practical understanding of the problem and for tests [124]. 169

4.13 Arc-Arc scenario 3D Matlab simulation. 170

4.14 Arc-Arc scenario 3D Matlab simulation results as functions of the rotation angles from 0-180°. Top left: scissor angle. Top right: MA. Bottom: static rolling friction coefficient. 171

4.15 From the intersection of the cylinder of radius $\frac{R}{2}$ and center $(\frac{R}{2},0)$ and a sphere with center $(0,0,0)$ and radius R Viviani curve is born. 172

4.16 Graphical representation of the Viviani curve on a sphere [132]. 173

4.17 Search algorithm simulation details. 177

4.18 Arc-Wiper scenario 3D Matlab simulation. 178

4.19 Arc-Wiper scenario 3D Matlab simulation results as functions of the rotation angles from 0-180°. Top left: scissor angle. Top right: MA. Bottom: static rolling friction coefficient. 179

4.20 Wiper-Wiper scenario 3D Matlab simulation. 180

4.21 Wiper-Wiper scenario 3D Matlab simulation. The blue line represents the Wiper, the green line the positive feature, the red lines represent the normal curves to both the Wiper and the positive feature. Their intersection determines the pin position and the scissor angle evaluation (black crosses). 181

4.22 Frames of a video simulation produced using Matlab and ImageJ about the Wiper (blue)-positive feature (green)-pin (red) interaction. 182

4.23 Wiper-Wiper scenario 3D Matlab simulation results as functions of the rotation angles and parametrized with respect to the pin radius (blue 5mm, green 10mm, red 15mm). Top left: scissor angle. Top right: MA. Bottom left: static rolling friction coefficient. Bottom right: CAD model. 183

4.24 The parameters associated to three different parts of the original Wiper (side view). 185

4.25 The parameters associated to three different parts of the optimized Wiper (3D view) [124]. 185

4.26 When the OS will be inserted in this mechanism, the Wiper will start in the rest position (rotation angle of 180°). The red arrow shows the increasing of the value of this parameter. Having a large parameter 1 value brings to have a hole in between the modified Wiper and the positive feature where the pin could remain stuck. 186

4.27 The system at a rotation angle of 100°. The red arrow shows the increasing of the value of parameter 2. A curve too flat (lower parameter 2) or too steep (higher parameter 2) could bring to a possible pin jamming condition. 187

4.28 System at a rotation angle of 0°. The red arrow shows the increasing of the value of parameter 3. Different curves could present a local minimum (lower parameter 3) or a local maximum (higher parameter 3) and each of them could bring to a possible pin jamming condition. 187

4.29 Global parameters variation as a function of the MA for a rotation angle of 40°. The red dot indicates the parameter combination that produces the highest MA. 188

4.30 Wiper profile obtained using the parameters that maximize the MA for a rotation angle of 40°. The same color code use for Case 3 was adopted here. 189

4.31 Scissor angle and MA as functions of the rotation angle parametrized on different values for parameter 1. 190

4.32 Scissor angle and MA as functions of the rotation angle parametrized on different values for parameter 2. 191

4.33 Scissor angle and MA as functions of the rotation angle parametrized on different values for parameter 3. 192

4.34 Final optimization of the modified Wiper profile. 192

4.35 Different planes of the final optimization of the modified Wiper profile. 193

4.36 Upper limit static rolling friction coefficient curve for the version 4 optimized Wiper (blue line). The dashed line refers to the lower limit friction coefficient of 0.2. The blue line is always above the dashed black line. 194

4.37 Wiper radius as function of the Wiper angle among two lines that represent the Wiper radius ± pin height. This shows that the spherical constraint is respected, i.e., the modified Wiper lays on a spherical surface without exceeding the imaginary curves described by the pin added to the Wiper. 195

4.38 Scissor angle and MA as functions of the rotation angle parametrized on different values for parameter 1 for operational angle of 70°. . 196

4.39 Scissor angle and MA as functions of the rotation angle parametrized on different values for parameter 2 for operational angle of 70°. . 197

4.40 Scissor angle and MA as functions of the rotation angle parametrized on different values for parameter 3 for operational angle of 70°. . 198

4.41 Final optimization of the modified Wiper profile for operational angle of 70°. 199

4.42 Different planes of the final optimization of the modified Wiper profile for operational angle of 70°. 200

4.43 Different planes of the final optimization of the modified Wiper profile for operational angle of 70°. 201

4.44 Upper limit static rolling friction coefficient curve for the version 4 optimized Wiper (blue line). The dashed line refers to the lower limit friction coefficient of 0.2. Note that the blue line is always above the dashed black line [124]. 202

4.45 Wiper radius as function of the Wiper angle among two lines that represent the Wiper radius ± pin height. Only half of the Wiper is considered for symmetry reason. This shows that the spherical constraint is respected, i.e., the modified Wiper lays on a spherical surface without exceeding the imaginary curves described by the pin added to the Wiper. 203

4.46 Final scissor angle and the MA as a function of the rotation angle for Case 4 optimized Wiper with respect to Case 3 [124]. . 204

4.47 Final Wiper optimized CAD drawings (Case 4). 206

4.48 Optimized Wiper model [124]. 207

4.49 Optimized Wiper model (side view) [124]. 207

4.50 Optimized Wiper model (top view) [124]. 208

4.51 Optimized Wiper model (front view) [124]. 208

5.1 Testbed N.1: Three-roller Wiper testbed [124]. 211

5.2 The Solidworks CAD of the testbed is illustrated. Three different views are shown: (a) front view, (b) side view and (c) top view. The author personal contributions discussed in the next sections are related to the green highlighted components. 212

5.3 SolidWorks CAD drawing of a possible pin configuration. Left: pin isometric view. Right: pin top view, lateral and bottom view. 213

5.4 SolidWorks CAD drawing of the actuator housing support connected to the 80 / 20 structural frame. Left: support isometric view. Right: support front, top, back, and lateral view. 214

5.5 SolidWorks CAD drawing of the actuator housing support motor holder. Left: support holder isometric view. Right: support holder front, top, back, and lateral view. 214

5.6 SolidWorks CAD assemble drawing of the actuator housing support motor and the holder. 215

5.7 SolidWorks CAD drawing of the motor shaft-Wiper connection. Left: isometric view. Right: connection front, top, back, and lateral view. 216

5.8 McMaster SolidWorks CAD drawing of shaft coupler between the motor shaft and the Wiper connection [137]. 217

5.9 McMaster SolidWorks CAD drawing of shaft coupler between the motor shaft and the Wiper connection [137]. 218

5.10 SolidWorks CAD assembly detail. It is possible to notice (from right to left) the actuator, its housing, the shaft coupler, the motor shaft-Wiper connection and the two retaining rings on the both sides of the connection support to the 80 / 20 frames. . 219

5.11 Mechanical hardware assembly detail. 219

5.12 Electronic system. From the top left to the bottom right, it is possible to notice a E-switch connected to a breadboard, a Arduino Micro processor, a Motor Driver Carrier. This elements were connected to a Polulu Actuator. 220

5.13 Electronic system schematic using Eagle PCB design software [138]. Five elements were present: the Arduino Micro processor, the power supply, the motor driver, the breadboard, the E-switch, the DC motor. 221

5.14 Arduino Micro (USA only) and Genuino Micro (outside USA) [139]. 222

5.15 Arduino Micro schematic [139]. 222

5.16 Polulu VNH5019 motor driver carrier [140]. 224

5.17 Polulu VNH5019 motor driver carrier schematic, labeled top view [140]. 224

5.18 Left: Polulu 75:1 Metal Gearmotor 25Dx54L mm LP 6V with 48 CPR Encoder. Right: close-up view of encoder [140]. 226

5.19 MATLAB plot motor performance curves for Pololu brushed DC gear motors. 227

5.20 Screen shot of the Arduino control (left) and the user window to insert the desired rotation in degrees (right) are displayed. . . 228

5.21 Proportional motor control diagram implemented in Arduino. . 228

5.22 Main 80 / 20 structural assembly components. From left to right: T-slot profile, bolt, slide-in T-nut centered thread, angle bracket. 229

5.23 Testbed apparatus [124]. 231

5.24 Testbed architectural flow and connections. The double-headed arrows indicate connections in both ways, both forward and backward. 231

5.25 Testbed apparatus actuation with the OS initial orientation with the pin located opposite to the retention mechanism. 233

5.26 Testbed apparatus actuation with a random OS initial orientation. 234

5.27 Detail of the most critical configuration where the pin locates between the Wiper and the positive feature and where a jamming condition could happen caused by a small scissor angle. 234

5.28 Testbed apparatus actuation related to the most critical configuration where the pin locates between the Wiper and the positive feature and where a jamming condition could happen caused by a small scissor angle. 235

5.29 Testbed apparatus actuation controlled in reverse. 236

5.30 Water Wiper testbed [124]. 237

5.31 Water Testbed front view. 238

5.32 Water Testbed side view. 239

5.33 Water Testbed top view. 239

5.34 Testbed architectural flow and connections. The double-headed arrows indicate connections in both ways, both forward and backward. Two other blocks are present (in orange): IMU and the electronic system, both inside the OS to collect data regarding OS motion in real time. 240

5.35 Electronic system schematic using Eagle PCB design software [138]. Four elements are present: the Arduino Uno processor, the power supply, the motor driver, the breadboard, the DC motor. 241

5.36 Electronic physical hardware, from left to right: Power Supply, Arduino Uno and Motor Driver and DC motor. 242

5.37 Arduino Uno R3 USB Microcontroller [139]. 242

5.38 3267E actuator with encoders [142]. 245

5.39 MATLAB plot motor performance curves for 3267E actuator. . 246

5.40 PID motor control diagram implemented in Arduino. 246

5.41 Final MOSTT Wiper testbed [124]. 248

5.42 The Wiper reorients the OS and retains it through a retention mechanism (red circle). 248

5.43 OS retention mechanism concept design: Spring Loaded Trap. . 250

5.44 SolidWorks drop-off dynamic simulations to verify if the presented concept could survive the worst condition scenario that is a hard landing with accelerations around 1300g drop test at 44m/s of impact speed. The stress reported are below the Al 6061-T6 yield stress. 251

6.1 OS designed for the DOE. 253

6.2 OS inserting water proof electronic box [124]. 253

6.3 Water proof electronic box (close). 254

6.4 Water proof electronic box (open) [124]. 254

6.5 Inertial Mass Unit [143]. 255

6.6 DFRobot Bluetooth Bee wireless module [143]. 257

6.7 OS orientation velocity was considered constant, but during the pin trap (multi-body MSC Adams simulation software). 260

6.8 Experimental setup system communication protocols. 264

6.9 Body frame sensors with respect to testbed reference frame (inertia reference frame) [124]. 266

6.10 Testbed angular reference frame considered during tests. 266

6.11 Water testbed initial OS positioning performances. The absolute angular error (root sum square of the azimuth and elevation errors) as function of the azimuth and elevation angles. 267

6.12 Example test to illustrate the testbed operations. In this case the pin is located at a position of (θ=90°, ϕ=0°) [124]. 268

6.13 Coordinate x data [124]. 268

6.14 Coordinate y data [124]. 269

6.15 Coordinate z data. 269

6.16 Quaternions as a function of time obtained through the EKF. . 270

6.17 Tait-Bryan angles as a function of time obtained through the EKF. 271

6.18 Pin OS hand holding. 272

6.19 Pin OS magnetic pick up stick holding. 272

6.20 Kapton-wrapped pin. 272

6.21 Electronic box and the location of the two weights (red circles) adopted to create an intentionally inertial asymmetry. 273

6.22 Water Wiper testbed with the Motor No.1 location (red circle). 273

6.23 Case that shows the OS dynamic condition caused by the Wiper high speed. 274

6.24 Case that shows the OS quasi-static condition caused by the Wiper slower speed. 275

6.25 Example test to illustrate the testbed operations. In this case the pin was located at a position of (θ=0°, ϕ=30°). 277

6.26 Tait-Bryan angles as a function of time obtained through the EKF. 278

6.27 Example test to illustrate the testbed operations. In this case the pin was located at a position of (θ=0°, ϕ=180°). 279

6.28 Tait-Bryan angles as a function of time obtained through the EKF. 280

6.29 Example test to illustrate the testbed operations. In this case the pin was located at a position of (θ=60°, ϕ=120°). 281

6.30 Tait-Bryan angles as a function of time obtained through the EKF. 282

6.31 Torque measuring data. 284

6.32 Critical pin location test. In this case the pin diameter was 5mm and it was located at (θ=90°, ϕ=90°). 286

6.33 Torque end efficiency results for 5mm pin. 287

6.34 Critical pin location test. In this case the pin diameter was 10mm and it was located at (θ=90°, ϕ=90°). 288

6.35 Torque end efficiency results for 10mm pin. 289

6.36 Critical pin location test. In this case the pin diameter was 15mm and it was located at (θ=90°, ϕ=90°). 290

6.37 Torque end efficiency results for 15mm pin. 291

6.38 Non-spherical OS, the inner radius was 10mm smaller than outer radius [124]. 291

6.39 Critical pin location test for a non-spherical OS. In this case the pin diameter was 10mm and it was located at (θ=90°, ϕ=0°). . 292

6.40 Critical pin location test for the non-spherical OS. In this case the pin diameter was 10mm and it was located at (θ=90°, ϕ=90°).293

6.41 Critical pin location test for the non-spherical OS. In this case the pin diameter was 10mm and it was located at (θ=180°, ϕ=0°).294

6.42 Testbed tests performed at different initial OS pin direction. . . 295

List of Tables

1.1 Trade-off study to select the prehension scenario. In the upper right part of the table the possible scenarios are reported, while in the left part of the table the trade-off parameters are present. The impactive-ingressive scenario is selected due to its higher total score. 28

1.2 Trade-off results to select the material for the robotic gripper handle system. 43

1.3 Servomotor driver (mask): implements an abstracted model of a servomotor and driver configured for closed-loop speed control. . 55

1.4 Scenarios to validate this grasping technology workspace. If these scenarios were satisfied, then the whole grasping workspace was actually covered. 60

2.1 Major Accomplishments of Studies of Mars in the Past Decade [15]. 91

3.1 Manipulation scenarios compared to the key features required in a space environment for the present case study. Green represents suitability, orange intermediate level, and red unsuitability. . . . 131

3.2 Permutations among all the CRR operations after the capture and possible working concepts. 137

3.3 Trade-off study. 146

3.4 TOPSIS method candidate results. 149

4.1 Design dimensions in mm for the testbed system. 160

4.2 Variable explanation table. 162

4.3 Optimized parameters values at different rotation angles together with their scissor angles and mechanical advantage. 204

5.1 Clamp-on Helical Flexible Shaft Coupling features and values from McMaster [137]. 217

5.2 Clamp-on Helical Flexible Shaft Coupling features and values from McMaster [137]. 218

5.3 Arduino micro specifications from Arduino [139]. 223

5.4 VNH5019 motor driver carrier specifications [140]. 225

5.5 Polulu 75:1 Metal Gearmotor 25Dx54L LP 6V with 48 CPR Encoder specifications [140]. 226

5.6 3267E actuator specifications [142]. 245

6.1 Possible sources of error to characterize the accelerometer within the EKF. 256

6.2 Possible sources of error to characterize the gyro within the EKF. 256

6.3 Wiper design of experiment test matrix. Critical Pin Locations (CPL) is (90°, 90°) where the pin was located between the Wiper and the positive feature at rotation angle ∼0°. 276

Nomenclature

Greek Symbols

α Scissor angle

β Rotation angle

μ'' OS-shell friction coefficient

μ' Pin-shell friction coefficient

θ Wiper angle

k Wiper spring stiffness

Acronyms / Abbreviations

AO Announcement of Opportunity

$BLDC$ BrushLess Direct Current

BSL Bio-Safety Level

BTC Break-The-Chain

CAD Computer-Aided Design

CCD Charge-Coupled Device

CML Concept Maturity Level

CRR Capture, Reorientation, and Retain

$DARPA$ Defense Advanced Research Projects Agency

DOE Design Of Experiment

dof degree of freedom

EDl Entry, Descent, and Landing

EEV Earth Entry Vehicle

EKF Extended Kalman Filter

ESA European Space Agency

EVA ExtraVehicular Activity

F Inner radius of the positive feature

F_μ Friction force between the OS and the shell

F_a Friction force between pin and shell

F_{cl} Clearance between the positive feature and the Wiper

F_l Reaction force between the OS and the shell generated by the sprung Wiper

F_s Sprung Wiper force on the OS

FEA Finite Elements Analysis

FEM Finite Element Model

FOS Factor Of Safety

Ft Radial width of the positive feature

GER Global Exploration Roadmap

IMU Inertial Measurement Unit

$ISECG$ International Space Exploration Coordination Group

IXV Intermediate eXperimental Vehicle

JPL Jet Propulsion Laboratory

l Wiper spring displacement vector

LEO Low Earth Orbit

M_f Torque exerted on the OS by the Wiper to reorient it

MA Mechanical Advantage

MAV Mars Ascent Vehicle

$MEPAG$ Mars Exploration Program Analysis Group

MER Mars Exploration Rovers

MOI Mars Orbit Insertion

$MOSTT$ Mars In-Orbit Sample Transfer Technologies

$MREP$ Mars Robotic Exploration Preparation

MRO Mars Reconnaissance Orbiter

$MRSH$ Mars Returned Sample Handling

MS Modifiable Surface

MSL Mars Science Laboratory

MSR MArse Sample Return

$NASA$ National Aeronautics and Space Administration

NRC National research Council

O_{max} Offset with maximum pin length

OS Orbiting Sample

P Pin length off OS surface

PDR Preliminary Design Review

PPO Planetary Protection Office

R Radius of the OS

$ROCS$ Rendezvous Orbiting Capture System

RSM Remote Sensing Mast

RTD Research and Technical Development

RTG Radioisotope Thermoelectric Generator

S Minimum radius of shell

S_{cl} Clearance between the shell and the positive feature

$SAPERE$ Space Advanced Project for Excellence in Research and Enterprise

$SCCM$ Sample Canister Capture Mechanism

SE System Engineering

SFA Small Fine Arm

$SPACERIDER$ Space Reusable Integrated Demonstrator for European Return

SRF Sample Receiving Facility

SRO Sample Return Orbiter

$STRONG$ Systems Technology and Research National Global Operations

TEI Trans-Earth Injection

$TOPSIS$ Technique for Order Preference by Similarity to Ideal Solution

TPS Thermal Protection System

TRL Technology Readiness Level

UHF Ultra High Frequency

$UTTR$ Utah Test and Training Range

W Outer radius of the Wiper

W_{cl} Clearance between the Wiper and the OS

Wt Radial width of the Wiper

Introduction

Space Robotics: Goals and Technologies

Overview of the Historical Development of Space Robots

The term *robot* comes from the word *robota*, which means serf labor or hard work in the Slavic languages (Czech, Slovak and Polish). It was largely introduced to the public by the Czech writer Karel Capek (1890-1938) in his play R.U.R. (Rossum's Universal Robots), which was premiered in 1920. In this play, the robots are described as artificial creatures, or androids, which can be mistaken for humans. Today, the word robot is used for an intelligent machine or artificial agent that can exhibit interactive behavior with its environment or a human in a coordinated manner. Although humanoids, or human-looking robots, have attracted public attention, the typical robots used in industry are automated or programmable handling devices that do not necessarily look like humans. Actually, many such industrial robots are successfully working in the mass-production lines of industrial factories, conducting repetitive tasks such as assembling motor vehicles. However, the majority of research efforts now involve robots that can work outside the factory, such as in offices, homes and hospitals, or in outdoor fields or outer space, or even in inner space (medical robots, which can work inside the human body). Robotics is a discipline involving system integration, which forms the basis for most of our knowledge of many different subject areas including mechanics, electronics, computer technology, and bioengineering, along with various topics in human sciences, such as anthropology and sociology. Autonomy is a key issue in robotics, and at a primitive level, any non-crewed spacecraft that is under automated sequence control may be referred to as a robotic satellite. However, when the term space

robot is used it implies a more capable mechanical system that can facilitate manipulation, assembly, or service tasks in orbit as an assistant to astronauts, or can extend the areas and abilities of exploration on remote planets as a surrogate for human explorers. The main research tracks with the related open problems in space robotics are characterized as follows [1]:

- Manipulation: Although manipulation is a basic technology in robotics, the microgravity of the orbital environment requires special attention to the motion dynamics of the manipulator arms and the objects being handled. The reaction dynamics that affect the base body, impact dynamics when the robotic hand contacts an object to be handled, and vibration dynamics due to structural flexibility are included in this issue. Orbital manipulation open problems are related to [2]:
  - Motion dynamics in a space environment;
  - Low weight and high reliability (simplicity vs capability trade-off);
  - System engineering approach to the design of innovative concepts.
- Mobility: Locomotion is particularly important in exploration robots (rovers) that travel on the surface of a moon or planet. These surfaces are natural and rough, and thus challenging to traverse. Sensing and perception, traction mechanics, and vehicle dynamics, control and navigation are all mobile robotics technologies that must be demonstrated in a natural unstructured environment.
- Teleoperation and Autonomy: There is non-negligible time delay between a robotic system in space and a human operator in an operation room on Earth. In early orbital robotics demonstrations, this latency was typically a few seconds, but can be several tens of minutes, or even hours for planetary missions. Telerobotics technology is therefore indispensable in space exploration, and the introduction of autonomy is a reasonable consequence.
- Extreme Environments: In addition to the microgravity environment, which affects the motion dynamics of a robot, there are many other issues related to extreme space environments that are challenging and must be solved to enable practical engineering applications. Such issues

include extremely high or low temperatures, high vacuum or high pressure, corrosive atmospheres, ionizing radiation, and very fine dust.

- Versatility: This is the ultimate goal when designing and developing a robot, and is especially highlighted in space applications. Due to the nature of space missions, once launched into space, a robot must perform all of its tasks by itself using its own resources. A space robot, therefore, should be adaptable to the extreme space environments mentioned above and possess the versatility to handle many different situations and scenarios, including contingent ones that arise unexpectedly.

Future of Space Robotics

Orbital space robots will be able to assist humans in space by constructing and maintaining space modules and structures. Robotic manipulators will play essential roles in orbital operations. Moreover, satellite servicing missions are crucial to prevent the increase of space debris. The concept of servicing robots, or free-flying robots, has been discussed for many years, but there has been a limited number of validation flights in orbit, so far. More technological developments are expected to realize free-flying robots for servicing, rescuing or capture-and-removal missions of existing spacecraft in orbit.

Thesis Internal Structure

The first main result of this work was identified in the conception of a close loop that reflects a common adopted path to support the creation and verification of innovative gripper concepts, see Fig.1:

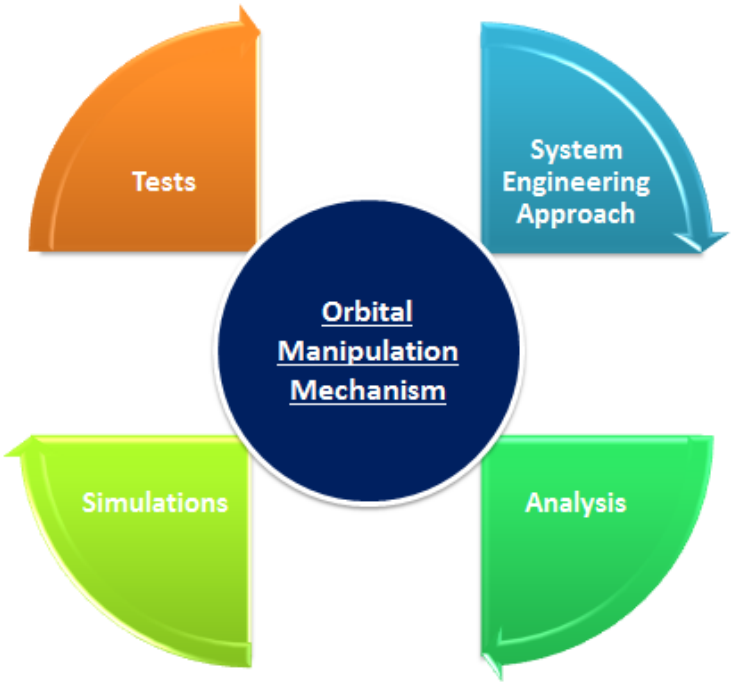

Figure 1 Close loop to support the creation and verification of innovative gripper concepts.

- System Engineering Approach - A system engineering study was performed to collect all the information, to evaluate the existing scenarios, with the intent to create new concepts more suitable to the existing mission scenario. Requirements were delivered to identify what the mechanism has to accomplish.
- Analysis - Analysis were performed to identify the main parameters needed for the mechanism to satisfy its requirements.
- Simulations - Simulations were run to verify that under the known conditions the mechanism was able to accomplish the tasks for which it was created and to fulfill its requirements.
- Tests - Tests were executed to validate the mechanism meeting the needs for which it was created.

This itinerary brought to the creation of two different innovative orbital manipulation mechanisms.

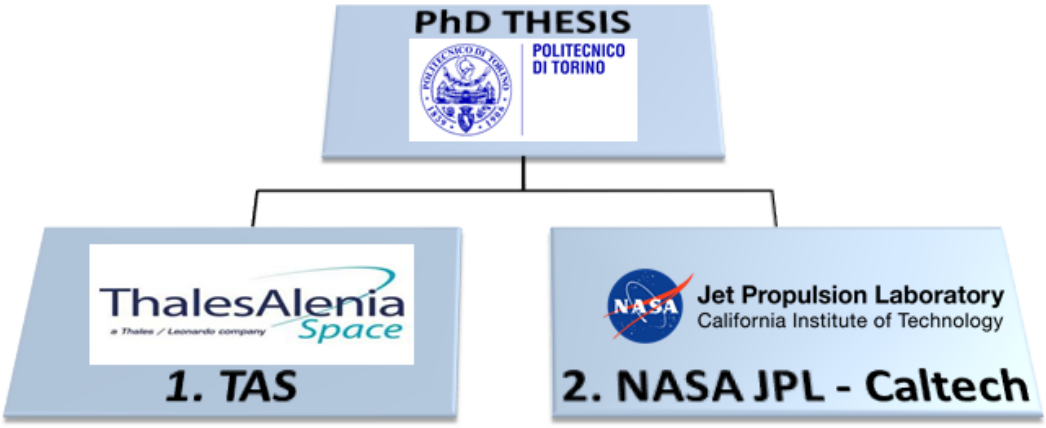

Figure 2 Thesis Organization Map.

As Fig.2 reports, this thesis work was composed by two main segments. The first part of the PhD period was dedicated to the design of an on orbit robotic gripper mechanical system in collaboration with Thales Alenia Space in Turin. The second part of PhD period took place at NASA Jet Propulsion Laboratory - California Institute of Technology (USA) supporting the design of an electro-mechanical system to reorient a spherical orbital sample for a potential Mars Sample Return mission concept.

Both these two topics are related to Space Exploration Robotic Systems - Orbital Manipulation Mechanisms.

Thales Alenia Space Italy Project

Goal of this Thesis - 1

This work describes an innovative on orbit robotic gripper mechanical system in terms of concepts of operation, elements and baseline process. Considering the different masses, forces, sizes and lengths as starting points for the concept of the robotic arm the Small Fine Arm (SFA) baseline configuration [3], a baseline configuration for the system was produced. A literature research was performed for what concerns the grasping tool [4], [5] and trade-offs were conducted. An underactuation strategy was finally selected [1], [6], [7], [8]. It minimizes the

number of actuators (single-actuator gripper) consequently the grasping tool mass at the cost of a certain mechanical and software complexity. This work is devoted to the description of the grasping manipulator design and mechanics of this robotic system architecture, able to correctly perform and successfully obtain the expected result.

SAPERE-STRONG Projects

Under the Space Advanced Project for Excellence in Research and Enterprise (SAPERE) project, there is the Systems Technology and Research National Global Operations (STRONG) project, related to the theme of space exploration, servicing in orbit and access to space. STRONG is related to the theme of space exploration and access to space having the objective of increasing the operability national space in this area by expanding the capacity industry in the creation of a Space Tug, an essential element in any space exploration scenario and enable, starting from intermediate orbits as those of the space station, launching tools and platforms with considerable savings in weight and a strong optimization of the ratio between payload and platform itself. The IXV evolution system called Space Reusable Integrated Demonstrator for European Return (SPACE RIDER), developed by ESA [9], is a reusable demonstration of a return vehicle intended to the development of European technologies as equipment for aerodynamic and aerothermodynamics, heat-protection and navigation control system.

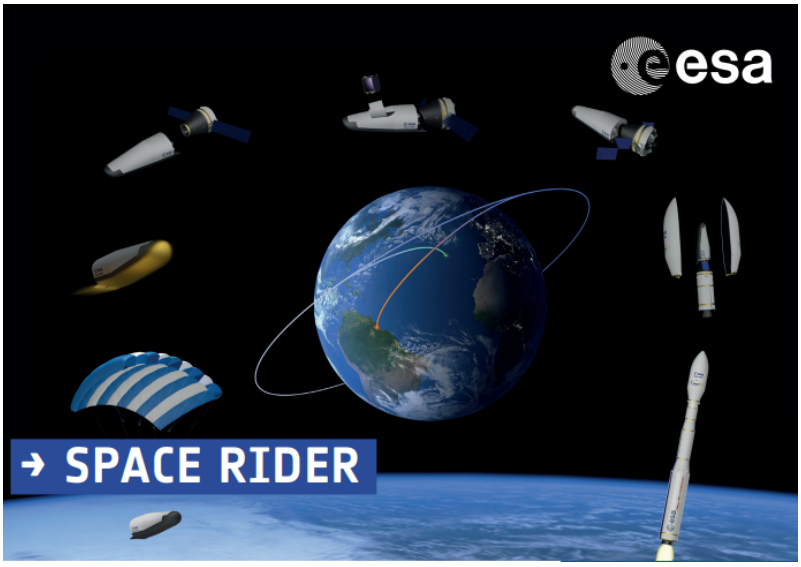

Figure 3 SPACE RIDER Operational Phases. The spacecraft will be launched from Europe's Spaceport in Kourou, French Guiana, stay in orbit as required by its payloads, and then perform a ground landing Courtesy of ESA.

This vehicle is designated by ESA to be the intermediate element in the European roadmap for the technological development with a view to future operative vehicles. The first step was the demonstrator IXV launched by ESA on 11 February 2015 [10]. Differently from its precursor, this demonstrator executes a landing on the runway and not a splash down as last step of the reentry phase. However, in this case SPACE RIDER is in charge of bringing back to the ground a payload from the platform attached to the Space Tug. To achieve this goal is essential to develop a specific robotic system that allows the approach and the grasping of the selected payload and his placement in the cargo bay of the vehicle. The payload object of this service could be experiments related to the material science, advanced propulsion or radiation protection. This work is devoted to the description of the grasping manipulator design and mechanical aspect of this robotic system architecture. To reach this goal some assumptions and trade-offs, described in Ch.1 of this work, were considered to identify the best arrangement of the system.

Thesis Structure - 1

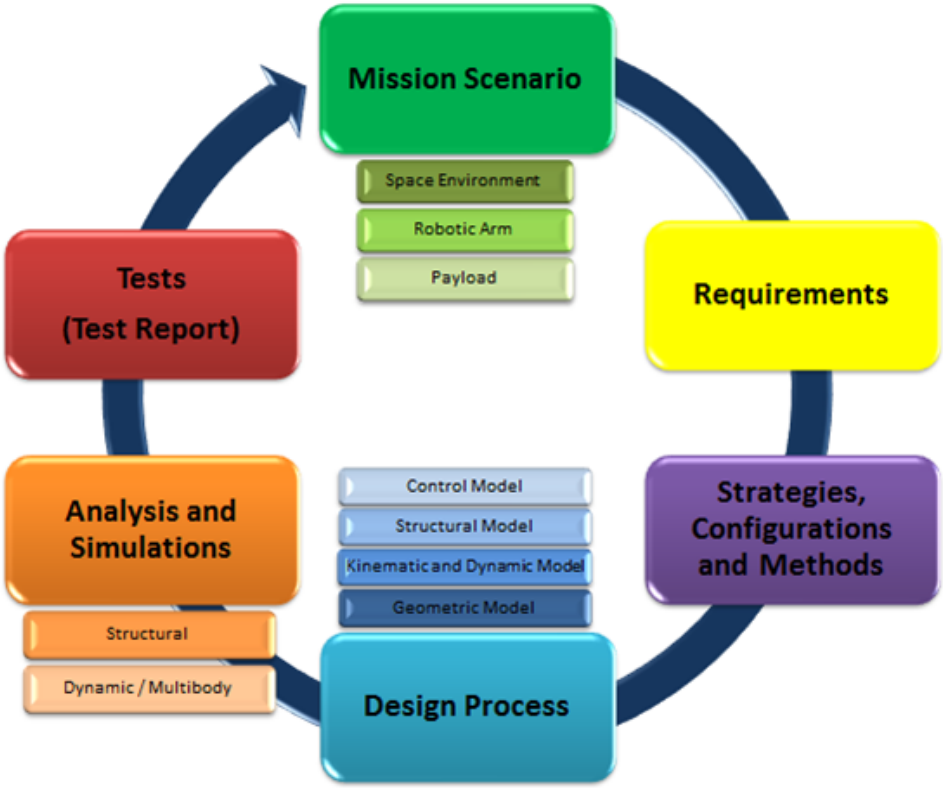

Figure 4 Thesis Strategic Map.

In Fig.4 the approach to deliver the requested product is presented. First of all, there is the Mission Scenario, in which starting from the mission profile, robotic system and payload features and requirements the requirements related to the gripper subsystem were defined. Then, there is a phase called Strategies, Configurations and Methods where the possible system candidates were presented and info about the requirement satisfaction were given. Then the Design Process phase starts in which the geometric model, the kinematic and dynamic models, the structural model and the control model were illustrated. These models were analyzed and tests were run to validate these analysis. Unfortunately, only computational tests have been performed and not tests in the real physical world. Finally, iterations were required to optimized the product and to fully satisfy the Mission Scenario and Requirements phases.

NASA Jet Propulsion Laboratory Project

Goal of this Thesis - 2

The work developed took place at NASA Jet Propulsion Laboratory - California Institute of Technology supporting the design of an electro-mechanical system to reorient a spherical orbital sample for a potential Mars Sample Return mission concept.

The research reported in this document was carried on at NASA Jet Propulsion Laboratory - California Institute of Technology (JPL) from April 2016 to August 2017.

Mars In-Orbit Sample Transfer Technologies

Mars In-Orbit Sample Transfer Technologies (MOSTT) is an internal JPL Research and Technical Development Task (RTD) to study and design concepts to manipulate an Orbiting Sample (OS) in orbit around Mars. During his staying at NASA JPL the author supported MOSTT task as a PhD visiting researcher.

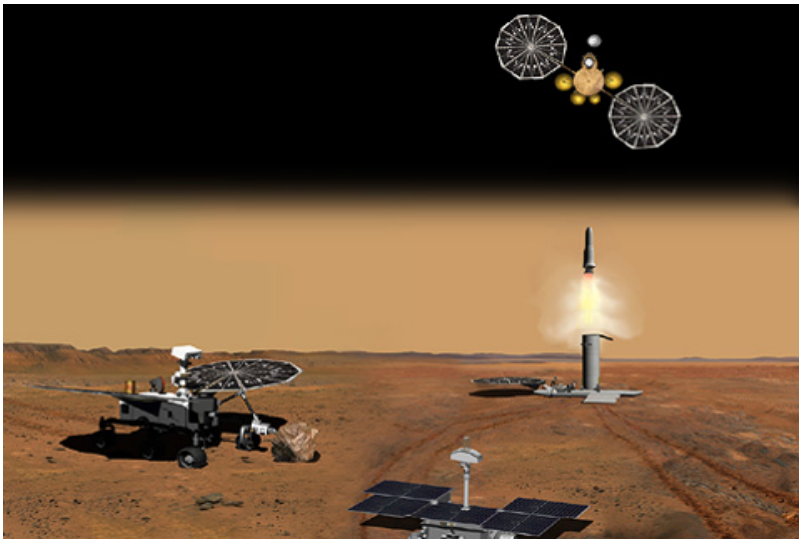

Figure 5 Potential Mars Sample Return Architecture. Courtesy of NASA.

This task is part of a notional Mars Sample Return (MSR) architecture, see Fig.5, that deals with a robotic mission to bring back to Earth a sample of the Martian soil, to determine if live has ever arisen on Mars, as prioritized by the National Academy of Sciences' Planetary Science Decadal Survey. For the MSR architecture to be considered viable, NASA JPL must demonstrate an end-to-end sample transfer chain that is compatible with the evolving MSR architecture.

Mars Sample Return Introduction: Past, Present, and Future Mars Exploration

As described in [11] and [12] Mars presents a unique place in solar system exploration: it holds keys to many compelling planetary science questions and it is accessible enough to allow rapid, systematic exploration to address and answer these questions. The scientific objectives for Mars center on understanding the evolution of the planet as a system, focusing on the interplay between the tectonic and climatic cycles and moreover on the implications for habitability and life. Mars presents a great opportunity to investigate the major question of habitability and life in the whole solar system. Conditions on Mars, particularly early in its history, are thought to have been conducive to formation of prebiotic compounds and potentially to the origin and continued evolution of life. Mars has also experienced major changes in surface conditions, driven by its thermal evolution, orbital evolution, and by changes in solar input and greenhouse gases, that have produced a wide range of environments. Of critical significance is the excellent preservation of the geologic record of early Mars, and thus the potential for evidence of prebiotic and biotic processes and how they relate to the evolution of the planet as a system. This crucial early period is when life began on Earth, an epoch largely lost on our own planet. Thus, Mars provides the opportunity to address questions about how and whether life arose elsewhere in the solar system, about planetary evolution processes, and about the potential coupling between biological and geological history. Progress on these questions, important to both the science community and the public, could be made more readily at Mars than anywhere else in the solar system. This concept is strongly support by the 2011 Decadal Survey and 2015 NASA Planetary Science. The idea that humans could reach Mars is quite old and was advocated by many

pioneers of spaceflight. Apart from fictional descriptions, sometimes bypassing completely the problem of getting there, and of pioneristic work dealing with the general aspect of the problem, the first detailed study of a human Mars mission was done by Wernher von Braun who published in 1949 Das Mars Projekt, a technically sound project, demonstrating that it was possible to reach Mars with a technology predictable for a not too far future. This project, although technologically consistent, did not take in due account the relevant costs and, as perhaps unavoidably with a first attempt to put the problem in a rational way, was not sustainable. Since then many concepts were published by space agencies, individual researchers and companies from many different countries, but after 65 years human Mars exploration seems to be still a goal far in the future [13]. The International Space Exploration Coordination Group (ISECG) produced a Global Exploration Roadmap (GER) in which three destinations for exploration missions are contemplated: the Moon, the cislunar space and the asteroids, and Mars. While in the roadmap the goal of human Mars exploration is left as a goal to be achieved in a more distant future, several stepping stones are stated, among which there is a strong program of Mars robotic exploration. The spacecraft exploration of Mars began in 1965 with an exploration strategy of flybys, followed by orbiters, landers, and rovers with kilometers of mobility. This systematic investigation has produced a detailed knowledge of the planet's character, including global measurements of topography, geologic structure and processes, surface mineralogy and elemental composition, the near-surface distribution of water, the intrinsic and remnant magnetic field, gravity field and crustal structure, and the atmospheric composition and time-varying state. The orbital surveys framed the initial hypotheses and questions and identified the locations where in situ exploration could test them. The surface missions such as the Viking landers, Pathfinder, Phoenix, and the Mars Exploration Rovers have acquired detailed information on surface morphology, stratigraphy, mineralogy, composition, and atmosphere-surface dynamics and confirmed what was strongly suspected from orbital data: Mars has a long-lasting and varied history during which water has played a major role [14]. A new phase of exploration began with the Mars Express and Mars Reconnaissance (MRO) orbiters, which carry improved instrumentation to pursue the questions raised in the earlier cycles of exploration. Among the discoveries is the realization that Mars is a remarkably diverse planet with a wide range of aqueous environments.

The role of water and the habitability of the ancient environment have been further investigated by the Mars Science Laboratory (MSL), launched in 2011, which carried the most advanced suite of instrumentation ever landed on the surface of a planetary object. The program of Mars exploration over the past 20 years has provided a framework for systematic exploration, allowing hypotheses to be formulated and tested and new discoveries to be rapidly and effectively pursued with follow-up observations. In addition, the program has produced missions that support each other both scientifically and through infrastructure, with orbital reconnaissance and site selection, data relay, and critical event coverage significantly enhancing the quality of the in situ missions [15]. Finally, this program has allowed the Mars science community to construct a logical series of missions that are each modest in scope and systematically advance our scientific understanding of Mars. Over the past decade the Mars science community, as represented by the Mars Exploration Program Analysis Group (MEPAG) [16], has formulated four major science themes that pertain to understanding Mars as a planetary system with the related overarching science questions that drive future Mars exploration:

- Life - Understand the potential for life elsewhere in the universe.
- Climate - Characterize the present and past climate and climate processes.
- Geology - Understand the geological processes affecting Mars's interior, crust, and surface.
- Prepare for human exploration - Obtain knowledge of Mars sufficient to design and implement a human mission with acceptable cost, risk and performance.

The next decade holds great promise for Mars exploration to address in detail the questions of habitability and the potential origin and evolution of life on Mars. The major focus of the next decade could be a Mars Sample Return campaign, beginning with a rover mission to collect and cache samples, followed potentially by missions to retrieve these samples and return them to Earth. It is widely accepted within the Mars science community that analysis of carefully selected samples from sites that have the highest scientific potential that are returned to Earth for intense study using advanced analytical techniques would

provide the highest scientific return on investment for understanding Mars as a planetary system. These samples could be collected and returned to Earth in a sequence of three missions that collect the samples, place them into Mars orbit, and return them to Earth. This modular approach is scientifically, technically, and programmatically robust, with each mission possessing a small number of discrete engineering challenges, and multiple sample caches providing resiliency against failure of subsequent elements. This modular approach also allows a sample return campaign to proceed at a pace determined by prioritization within the solar system objectives and by available funding.

Mars Sample Return Mission Architecture

The current MSR architecture being studied by NASA is essentially a campaign, rather than a single mission or flight project. NASA is considering a notional four-element campaign architecture [17]:

1. A collecting rover.
2. An MSR Lander to fetch the sample tubes and launch the samples into Mars orbit.
3. An MSR Orbiter for return of samples to Earth.
4. Mars Returned Sample Handling (MRSH) facility and related components.

The Orbiter Mission would be one of three missions concepts comprising the proposed MSR campaign [17]. The Mars 2020 rover, due for launch in July/August 2020, will collect and cache at least 20 samples, with the sample tubes left on the surface for possible future return to Earth. The orbiter would be launched nominally on a medium-class vehicle reaching Mars in ∼9 months. The orbiter would insert into a highly elliptical orbit and aerobrake down to a 500km circular orbit over 6-9 months. The orbiter would provide critical event coverage of the lander entry/descent/landing, and provide telecom relay for the proposed lander and its fetch rover dispatched to retrieve the sample cache. Approximately 6 months after lander arrival, an OS container would be launched by a Mars Ascent Vehicle (MAV) and an OS would be released in a 500km orbit comparable with the orbiter. This is all part of the Lander

Mission concept. The orbiter would provide critical event coverage of the MAV ascent and OS release and capture. Using an optical camera, the orbiter would detect and track an OS, while maneuvering to rendezvous. The OS would be captured via a basket, sealed into an outer container, and placed in an Earth Entry Vehicle (EEV). Nominally, within ∼3 months, the orbiter would leave Mars on a non-impact trajectory to Earth, and shortly before arrival, would target Earth, release the EEV, and then divert away from Earth. The EEV would enter and hard land at a recovery site to be determined. This return trajectory and entry/descent/landing sequence is similar to the Genesis and Stardust missions, except it would not have a parachute. The MRSH element would then be responsible for safe transport of the EEV to a Sample Receiving Facility (SRF), where the hardware and samples would remain in quarantine until they are determined to be safe (either by analysis or by sterilization). A testing protocol would be applied to the samples to determine if they are safe for release. This might take approximately one year and is considered part of the MRSH element. If the samples are determined to be non-hazardous to Earth's biosphere, the samples would be released to a curation facility for safe keeping and distribution to the international science community. A nominal cost is included for such a facility, potentially part of the current MRSH would be implemented by NASA with potential help from other agencies for safe transport of the EEV. A new SRF is the baseline plan, but augmentation to an existing bio-safety level-4 (BSL-4) lab is also being considered.

Thesis Structure - 2

Fig.6 reports the thesis strategic map. Each chapter generates output data adopted in the next chapter as inputs.

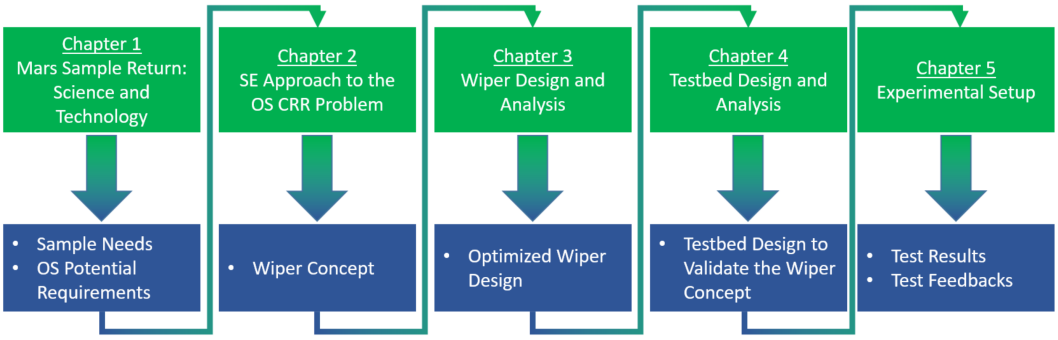

Figure 6 Thesis Strategic Map.

This work is related to the Mars environment and the MSR previous studies existing in the literature (Chapter 1) followed by the systems engineering study conducted to identify a mechanism to satisfy OS potential requirements and its features (Chapter 2). Analysis were shown to obtain an analytical Wiper profile to demonstrate the deterministic behavior of this mechanism (Chapter 3). A creation of the testbed has been supported under MOSTT and the author contribution to the testbeds (both hardware and electronics) are reported (Chapter 4). The experimental setup to collect data to characterize it was depicted (Chapter 5). Conclusions summarize the overall obtained results.

Chapter 1

Space Robotic Grasping Manipulator Design Process

In this chapter the work executed to develop an Orbital Manipulation Mechanism in collaboration with Thales Alenia Space in Turin is described. This mechanism consists in a robotic gripper with an underactuated finger strategy motion.

Parts of this chapter were published in:

- Robotic gripper for payload capture in low Earth orbit. Genta G., **Dolci M.**; accepted to the second edition of Journal of Chinese Society of Astronautics, July 2017.
- Robotic gripper for payload capture in low Earth orbit. Genta G., **Dolci M.**; ASME 2016 International Mechanical Engineering Congress & Exposition, IMECE 2016-65429, Phoenix (AZ USA), 11-17 November 2016.
- Robotic gripper technology for cargo transfer in low Earth orbit. **Dolci M.**, Genta G., Ferraris S.; 67th International Astronautical Congress, IAC-16,D2,3,3,x32043, Guadalajara, Mexico 26-30 September 2016.
- Gripper for capturing a payload in Low Earth Orbit. Genta G., **Dolci M.**; Memorie Accademia delle Scienze di Torino, serie V - Classe di Scienze Fisiche ISSN 1120-1630, presented on January, 13th 2016.

- Robotic system study for a LEO orbiting vehicle payload capturing. **Dolci M.**, Ferraris S., Genta G., Pellegrino P., Richiardi D., Scalise G.; 23rd Conference of the Italian Association of Aeronautics and Astronautics", Politecnico di Torino (Italy), 17-19 November 2015.

1.1 Introduction

1.1.1 SAPERE - STRONG projects

Under the SAPERE project, there is the STRONG project, related to the theme of space exploration, servicing in orbit and access to space. STRONG is related to the theme of space exploration and access to space having the objective of increasing the operability national space in this area by expanding the capacity industry in the creation of a Space Tug, an essential element in any space exploration scenario and enable, starting from intermediate orbits as those of the space station, launching tools and platforms with considerable savings in weight and a strong optimization of the ratio between payload and platform itself. The IXV evolution system called Space Reusable Integrated Demonstrator for European Return (SPACE RIDER), developed by ESA [9], is a reusable demonstration of a return vehicle intended to the development of European technologies as equipment for aerodynamic and aerothermodynamics, heat-protection and navigation control system. This vehicle is designated by ESA to be the intermediate element in the European roadmap for the technological development with a view to future operative vehicles. The first step was the demonstrator IXV launched by ESA on 11 February 2015 [10]. Differently from its precursor, this demonstrator executes a landing on the runway and not a splash down as last step of the reentry phase. However, in this case SPACE RIDER is in charge of bringing back to the ground a payload from the platform attached to the Space Tug. To achieve this goal is essential to develop a specific robotic system that allows the approach and the grasping of the selected payload and his placement in the cargo bay of the vehicle. The payload object of this service could be experiments related to the material science, advanced propulsion or radiation protection. This work is devoted to the description of the grasping manipulator design and mechanical aspect

of this robotic system architecture. To reach this goal some assumptions and trade-offs, described in the successive sections, have been considered to identify the best arrangement of the system.

1.1.2 Past, Present and Future Scenarios

This work focuses on the design study of a gripper for capturing payload in Low Earth Orbit (LEO). Grasping devices have evolved to help humans in manipulation for handling objects of different sizes, materials, and conditions. Grasping has been always considered as an essential part of manipulation and only recently a specific attention has been addressed to grasping devices as independent mechanical/mechatronic designs with theory, practice, and application. Grasping can be brought also into space activities and being customized for specific applications. The first robotic manipulator arm used in the orbital environment was the Space Shuttle Remote Manipulator System (SRMS) [18]. This success opened a new era of orbital robotics and inspired numerous mission concepts. A long-term goal that has been discussed extensively since the early 1980s is the application of a robotic freeflyer or free-flying space robot to the rescue and servicing of malfunctioning spacecrafts. As other orbital space robots there are SRMS, International Space Station Mounted Robot Manipulator Systems, Rotex [19] and Rokviss [20], [21] and Orbital Express [22] and ETS-VII [3]. At present, the existing grippers developed for space applications are the already cited Space Station Remote Manipulator System developed by Canadian Space Agency (CSA) [23], [24], [25], the end-effector of European Robotic Arm developed by ESA [26], [27], [28], [29], and a Canadian under-actuated end-effector named by SARAH [30]. Particular attention has been given to the Robonaut [31], [32]. Robonaut is a dexterous humanoid robot designed and built at NASA's Johnson Space Center in the United States. Robonaut's future upgrade could enable it to move outside to help astronauts with ExtraVehicular Activity (EVA) tasks or perform repairs on the exterior of the station. Combined with a surface mobility system like legs or wheels, Robonaut could perform as a human-like manipulation system for future exploration missions on the Moon or Mars. Orbital space robots will be able to assist humans in space by constructing and maintaining space modules and structures. Robotic manipulators have played essential roles in

orbital operations. Moreover, satellite servicing missions are crucial to prevent the increase of space debris. More technological developments are expected to realize free-flying robots for servicing, rescuing or capture-and-removal missions of existing spacecraft in orbit.

1.1.3 Robotic Grippers in an Unstructured Environment

Capable robot hands are important for a wide range of applications, such as industrial warehouse operation, household chores, military, handling of hazardous materials and/or for space. Robotic manipulators for space applications are now a well-established technology in space applications, as they are routinely used for handling and assembling large space modules and for reducing human EVAs at the international space station. These applications all involve grasping objects in unstructured environments, where the properties of the target object and its surroundings are uncertain a priori with sensing disposable to error. Grasping objects in unstructured environments represents is one of the important issues in robotics, see [33] and [34]. Indeed, grasping tasks in unstructured environments performs without a precise knowledge of the relevant properties of the object and environment (object size, shape, mass, surface properties, position and orientation, and properties of the surroundings). The uncertainties about the grasped object and gripper leads to use of robot hands with complex mechanisms and elaborate transmission and sensing systems, resulting in hands that are heavy, expensive, and fragile. Furthermore, in such hands to control contact forces to establish successful grasps results to be very difficult. To face these problems, a project started at the University of Bologna in the framework of a research program supported by Italian Space Agency, to design and experimentally test a robotic gripper for space applications (see [35], [36], [37], [38], [39]). A finer approach in dealing with the uncertainty inherent in unstructured grasping task is through passive mechanical compliance and adaptability/underactuation in fingers and hand structure. The compliant fingers adaptation allows the gripper to passively conform to object geometry during grasping without need to the complex control. Moreover, an adaptive underactuated hand has fewer actuators than degrees of freedom that are simple, light, cheap, and capable of grasping a large variety of objects.

In this work a new gripper concept for on orbit servicing is presented in terms of:

- Numbers of actuators;
- Underactuated working strategy;
- Mass and size minimization.

1.1.4 Work Goal

This work describes an innovative orbital robotic gripper mechanical system in terms of concepts of operation, elements and baseline process. Considering the different masses, forces, sizes and lengths as starting points for this concept the SFA baseline configuration [3], a baseline configuration for this particular system was produced. A literature research was performed for what concerns the grasping tool [4], [5] and trade-offs were conducted. An underactuation strategy was finally selected [1], [6], [7], [8], [40]. It minimizes the number of actuators, the grasping tool mass at the cost of a certain mechanical and software complexity. Some assumptions and trade-offs, described in the successive sections, were considered to identify the best arrangement of the system to reach this goal.

1.2 Robotic System Constraints and Mission Profile

1.2.1 Mission Scenario

This mission scenario depicts a standard satellite platform carrying a payload of interest (i.e. scientific or military). This satellite is docked to a Space Tug, capable of bringing it in low orbit and then releasing it in a known destination [41]. To complete the processing of the payload, it has to be brought back to the ground at the end of its operating cycle using a reentry vehicle with a small cargo bay, housing the robotic system. This robotic system has to operate in

synergy with the Space Tug to capture the payload from the standard platform. A schematic view of this scenario is shown in Fig.1.1.

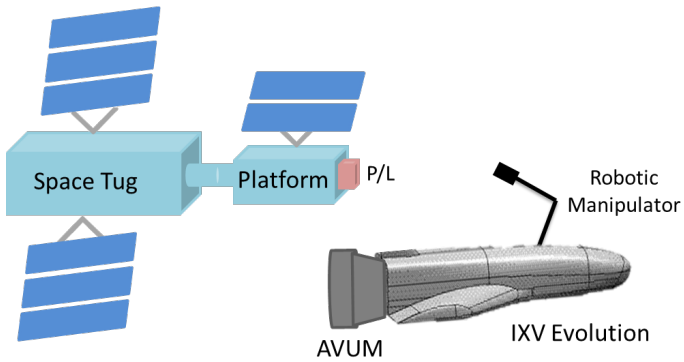

Figure 1.1 Mission scenario elements. Left: a general platform architecture is attached to the Space Tug. On the platform there is the payload to be brought on the ground. Right: reentry vehicle attached to the VEGA upper stage (AVUM). In the cargo bay of the reentry vehicle a robotic manipulator is located. This work is devoted to define its requirements determination and its preliminary design [41].

1.2.2 System Requirements and Constraints

The requirements and constraints imposed by considering a realistic VEGA (European launcher [42]) payload are difficult to satisfy in terms of dimensions and weight:

- Cargo Bay Main dimensions about 550 mm x 240mm x 1250 mm;
- Maximum storable mass: 50kg;
- Maximum available volume: 100l.

It is clear that the robotic system design is very challenging, moreover considering that the robotic arm should be stowed in the bay long at least 4m (to ensure the required safety during its operations, having a margin distance to exploit in an emergency case or in any case that required a moving away of robotic arm from the target) equipped with appropriate grasping tool and cameras, a battery for its elements power supply, a computer with its dedicate control system, all interfaces with the bay and payload, once the capture is performed. In addition, the robotic manipulator shall be able to withstand all

the mechanical, thermal and electromagnetic environments which occur during the launch, orbital and reentry phase.

1.2.3 System Control Architecture

The robotic manipulator operations start in the final phase of rendezvous between the Target and the Chaser, when the relative motion between them is limited by the Space Tug attitude control and AVUM. It was supposed that in this phase the Target and the Chaser were in the Launch Orbit, circular LEO with 5° inclination and 350km altitude at about 4m distance, as depicted in Fig.1.2.

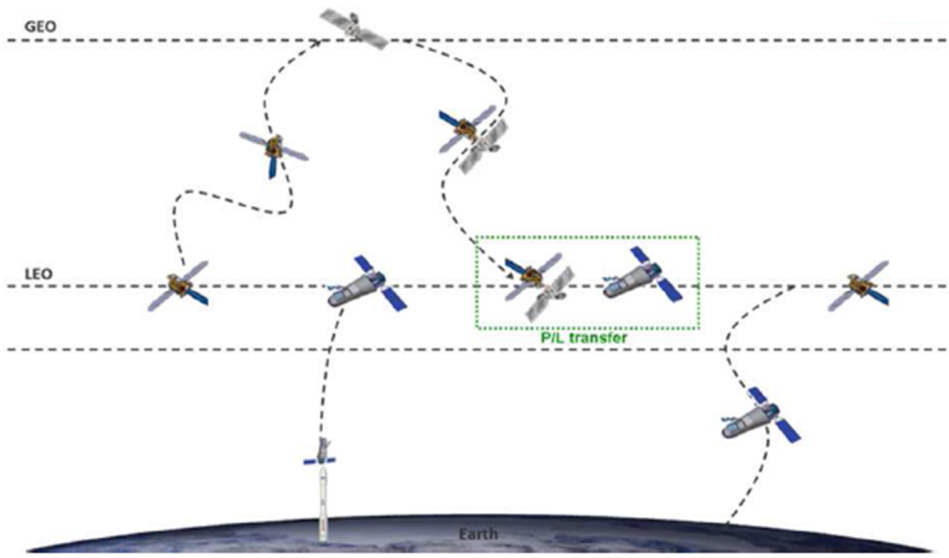

Figure 1.2 Space RIDER-Space Tug rendez-vous maneuver.

The capturing strategy is described [43]:

1. Manipulator Deployment - From 4m to 0.5m the Manipulator is deployed in a safe position, carefully selected such as to not obscure the sensor field of view on the elbow and to maintain it to a safe distance with respect to the Target. Direct kinematics algorithms are adopted to reach the selected final position. Half-orbit period was considered to accomplish this phase. Possible in-camera directed/reflected Sun rays were considered

and consequently sensor saturation. If this happens, tracking algorithm software stops the deployment until the camera sensor is not saturated anymore, then it continues. Obviously, half-orbit period (∼45') is a time overestimation, but especially at this design level was preferred to be conservative. Half-orbit period to operate the arm closure was also considered.

2. Marker on Target Search - Thanks to a sensor on the elbow, through a tracking algorithms, the Target pose with respect to the Chaser one is computed.

3. Target Approach - The manipulator is commanded to move towards the Target using inverse kinematics algorithms and to stop at 0.5m of distance from it.

4. Marker on payload Search - The sensor on the elbow infers, through a tracking algorithm, the Target object pose (i.e. the handle, payload component to be grasped) with respect to the Chaser. From 0.5m to 0.05m control system will switch to the gripper-palm camera following the marker on the handle. This phase is camera-performance dependent. The possibility of introducing another camera on the wrist to increase the system redundancy will be evaluated in the future phases of this project.

5. Approach to payload - The manipulator is commanded to move towards the payload using inverse kinematics algorithms and to stop at a certain distance from it to position the grasping tool in proximity of the handle installed on the payload. It stops at 0.05m of distance from it.

6. Payload Grasping - The manipulator is commanded to capture the handle driven by a force control able to manage the occurred contact forces. Necessary information from sensor about successful or unsuccessful grasping have to be provided as a recovery procedure to follow in case of not successful capture occurs. Errors on position assume values less than ±5mm, using wrist actuators (roll, pitch, yaw) to correct the hand position and attitude. Particular attention should be considered for payload release mechanisms. They should enable the release once recorded the exceeding of a force threshold level. One-orbit period was considered to accomplish the grasping phase. Possible in-camera directed/reflected Sun rays were

considered and consequently sensor saturation. If this happens, tracking algorithm software interrupts the grasping until the camera sensor is not saturated anymore, then it continues. Obviously, one-orbit period (∼90') is a time overestimation, but especially at this design level was preferred to be conservative.

7. Stowing in Cargo Bay - Once performed the successful capture, the manipulator is commanded to return in a safe position avoiding any obstacles through inverse kinematics control and to place itself with the payload in the cargo bay adopting a direct kinematics control.

1.2.4 System Configuration Trade-Off

As shown in Fig.1.2 the elements taken into account are the Target, composed by the Space Tug and a standard platform carrying the payload, and the Chaser, composed by the orbiting vehicle and the VEGA upper stage, AVUM. Space Tug and AVUM are the unique elements equipped with an attitude control to perform the cooperative rendez-vous and docking. Although most of the studies in the literature focus on active-passive (non-cooperative) rendez-vous, there are also works considering active-active (cooperative) rendez-vous [44]. The system under study does not belong to any of these two classes. In this case, for cooperative rendez-vous, is meant that a spacecraft (reentry vehicle) is performing active rendez-vous through a reaction control system, while the other one presents a stable control and attitude behavior without actively cooperating during the rendez-vous phase. This was stated as a semi-cooperative rendez-vous. The robotic system shall ensure both a robust contact, allowing a firm hooking of the payload, and a soft contact to guarantee a certain degree of compliance. No mechanisms to make stable the grasping operations were considered. The two vehicles will maintain themselves placed side by side without a physical docking. An arm-grasping mechanism was realized to carry out the payload. This results to be the most suitable system configuration despite its higher software complexity. Mass and volume minimizations were considered more relevant with respect to the system complexity due to the stricter cargo bay requirements [45].

1.3 Robotic Arm Preliminary Design

1.3.1 Design assumptions

To proceed with the preliminary design of the robotic arm some assumptions were made, in particular:

- The payload that has to be moved inside the cargo bay has a mass of 30kg;
- The limbs assumed to be aluminum cylindrical tubes with an external diameter 50mm and 2mm thick;
- The actuator sizing process has been based on the calculation of the worst case payload acceleration α_{max} [46].

This latter one has been calculated considering the main available data from the Japanese SFA [3] of the JEMRMS completely extended with the maximum tip force applied to the payload orthogonally with respect to the arm (starting still and reaching the maximum velocity). This results to be 0.05rad/s^2. From this value of acceleration the inertial resistance torques required to each actuators were calculated, considering:

- The actuators are activated one by one (while the others are still);
- The i-th actuator has to be able to rotate the subsequent chain of actuators + links + payload of 30kg with the angular acceleration previously calculated;
- This subsequent chain is seen as whole rigid body. Its mass is the sum of all actuators, links, end effector and payload that follow the i-th actuator/joint. The chain has also a geometric configuration that maximize its inertia matrix with respect to rotation axis of the i-th actuator.

1.3.2 Design description

The robotic arm has 7 degrees of freedom/joints to have more dexterity during its operations: 3 degrees of freedom in the shoulder, 1 degree of freedom in the elbow and 3 degrees of freedom in the wrist, linked by two 2m-limbs. The manipulator has to be stowed inside a cargo bay whose length is about 1.25m; this constraint forces to fold each limb in half (for a total of 4 cylindrical tube) with the aid of two dedicated actuators, adding 2 degrees of freedom during the deployment of the arm itself (once deployed the two limbs will remain completely extended). The following factors were considered for the motor choice: application, environment, thermal, efficiency, weight, volume, life, complexity, torque, speed, torque ripple, power source, envelope, duty cycle, and controllability. The choice has fallen on BLDC motors because of their long life, high torque, high efficiency, and low heat dissipation, while, concerning the gears, planetary gears seems to be the preferable choice in terms of mass savings. Summarizing, the chosen concept is an actuator composed by a BLDC motor (with electronic drive + encoder + brake) and a planetary gearbox.

1.4 Robotic Manipulator Design

1.4.1 Gripper requirements identification

To perform a first choice of the gripper configuration parameters, it is important to describe the existing prehension methods and their advantages and disadvantages both from the gripper side and from the grasped object points of view [47]. Following [1], there are four possible configurations for prehension scenarios:

- Impactive: the retention force provided by these tools is based on the physical effects of newtonian mechanics, mainly associated with mass points and forces, and requiring more or less extensive mechanisms;
- Ingressive: gripping methods which permeate a material surface to some given depth;

- Astrictive: providing a continuous holding force without the application of compressive stress;
- Contigutive: prehension techniques which rely on direct contact contiguity between gripper and object surfaces.

The adopted trade-off criteria are:

- Supplied power to grasp and hold the payload;
- Technology Readiness Level (TRL). This represents a method of estimating technology maturity of important technology elements of a program during the acquisition process, see [48];
- No rigid impact damping systems in the gripper;
- Error tolerance, i.e. how gripper helps to recover positioning ($\pm$30mm) and attitude ($\pm 6°$) errors;
- Volume occupied by the integrated system interface and end-effector (design driven);
- Gripper force to grasp and to hold the payload;
- Payload degrees of freedom blocked by the gripper.

After a trade-off study an impactive-ingressive gripper scenario was chosen. This trade-off study is reported in Tab.1.1. The selected scenario was constituted by a multi-finger hand and a handle. In the second column the weights are present, they go from 1 (inappropriate) to 5 (optimum). Once the prehension scenario was selected, it was fundamental to focus on a preliminary multi-finger hand-handle configuration study. Without having any knowledge about the nature of the payload, the payload was characterized considering the following features:

- Payload mass range [5-30]kg;
- Payload volume 16l (200mm x 200mm x 600mm);
- Single-element payload considered.

One fundamental aspect to design a robotic grasping system was to determine the position and attitude errors present in the whole system.

Prehension scenarios **Trade-off parameters**	**Weight (1-5)**	Scenario 1 Impactive-ingressive **Multi finger-Hand & Handle**	Scenario 2a Ingressive **Fitter & Conical Fitting**	Scenario 2b Ingressive **Conical Fitting & Fitter**
Supplied power: dissipated power to grasp and hold the P/L	**5**	4	4	4
Heritage: Technology Readness Level	**5**	3	3	1
No rigid Impact possibility: damping systems in the gripper	**4**	4	3	3
Error tolerance: how gripper helps to recover positioning (±3 cm) and attitude (±6°) errors	**4**	4	3	3
Occupied volume: occupied volume by the integrated system interface+end-effector (design dependent)	**3**	4	4	4
Prehended force: force developped by the gripper to grasp and hold the P/L	**2**	5	5	5
Impeded P/L dofs: how many P/L dofs the gripper can block	**4**	5	5	5
Total		**109**	**97**	**91**

Table 1.1 Trade-off study to select the prehension scenario. In the upper right part of the table the possible scenarios are reported, while in the left part of the table the trade-off parameters are present. The impactive-ingressive scenario was selected due to its higher total score [41].

The overall systems error are ±30mm for the relative position misalignment and ±6° for 3-axis relative attitude. summation of the former errors, rounded to the higher value. The functional requirements for the whole robotic system can be evaluated for this scenario. Together with the trade-off criteria they become necessary for a first design evaluation:

- Due to the mission profile the system shall operate in an environment with temperature range [-150°C, 150°C] [44].
- Volume (<16l) and mass (<3kg) occupied by the gripper-handle system shall respect the imposed limits.
- System degrees of freedom and consequently system control complexity shall be minimized.
- The grasping activity shall accommodate possible errors in positions (±30mm) and attitude (±6°). This limits were imposed by the Attitude

Determination and Control System of a realistic orbiting vehicle-platform and by the grasping strategy.

- The applied force per finger shall be minimized.
- The payload degrees of freedom shall be blocked. Three different modes were identified: Grasping. Holding and Releasing. Only a prehension activity was needed. Neither anthropomorphism nor high-level dexterity were required.

The desired capabilities have to be translated into technical requirements that result in a trade-off between system complexity, capabilities, reliability, volume, weight and possibly also cost.

Moreover, a camera sensor is located on the gripper palm to drive N.4-5-6 phases of the capturing strategy. The proposed camera sensor shall be:

- No rolling shutter camera;
- No constant focal length;
- In-camera shade condition: 4 white-light led lights are present symmetrically around the camera to illuminate the marker in shadow conditions;
- In-camera Sun rays condition: tracking algorithm software stops grasping action if saturation is present due to direct or reflected Sun light.

In this work a 1MP Radiation Hard CMOS Image Sensor (square size, 30mm side length) was considered. A preliminary characterization of the camera was presented. To size it the worst possible cases were taken into consideration. Camera position has an uncertainty of ±30mm with respect to the marker tracker, see Fig.1.3. $\pm 6°$ errors were considered in attitude for ϕ_x and ϕ_y (angles respectively related to the x and y axis). These are in plane rotation errors (θ_{ir}). Then, due to ϕ_z, an apparent enlargement of the marker tracker was present. The worst case was where the nominal side has to be multiplied by a factor of $\sqrt{2}$ (square diagonal factor). This effect produces an out of plane rotation error (θ_{or}). At the end, the new modified camera nominal field of view ($\theta_n^{'}$) is 98.5°.

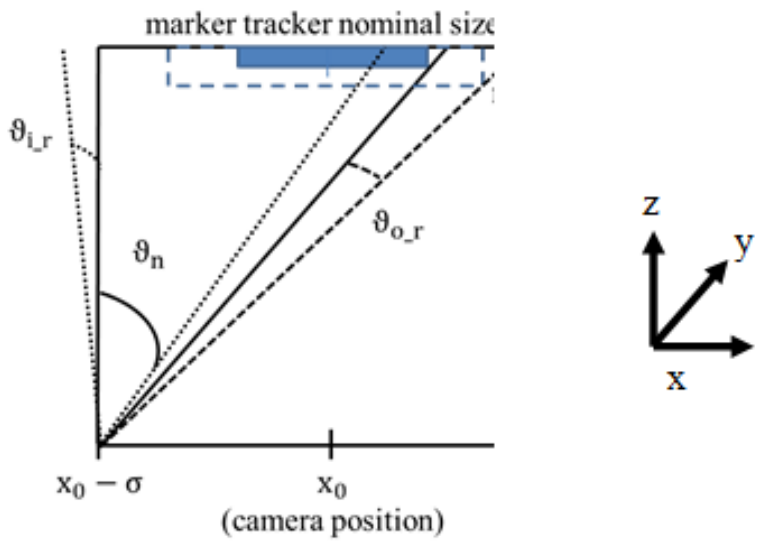

Figure 1.3 Camera-marker scheme to infer position and attitude possible errors. This is fundamental in order to obtain a first evaluation of the camera design [41].

For what concerns the error in z direction, at a certain distance from the marker tracker (50mm) the control system works using the instantaneous marker tracker angular diameter. Once it is 56° (at 40mm distance), the gripper will start the grasping phase. At that point the only errors present will be those related to the marker tracker-camera system (±2.5mm and ±2.8°). These errors were included in the sizing of the new modified camera field of view (61.8°). The camera system has to work with a lens-marker tracker working distance varying from 50mm (start working distance of the camera) to 15mm (stop working distance of the camera) and with a camera lens-CCD distance of 15mm (palm depth). A requirement about the focal length interval is needed. The focal length has to vary according to the different working distances with a focus/zoom mechanism. Obviously, the camera needs to have a very high sampling frequency (higher than the control system one). As aforementioned, due to structural constraints a maximum thickness of 15mm was adopted. In this space the whole system has to be accommodated. It consists of the optical system (lens) and the CCD sensor that will transmit signals to the central electronic board. Moreover, to ensure a higher redundancy level it is possible doubling the CCD sensors. Another CCD sensor was added using the same optical system illustrated before. About that, the use of beam splitter

structures (prismatic or planar) was taken into consideration. A scheme of the optical system is depicted in Fig.1.4.

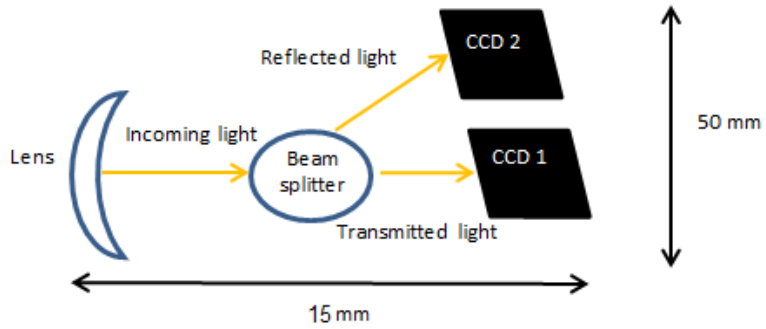

Figure 1.4 Palmoptical system (geometric optical approach) developed to guarantee a higher redundancy degree.

More technical details about the camera model selection and the tracking algorithms (machine vision) are not object of this current work and they will be dealt with in a future more detailed approach, during the realization of this project. More information can be found in the Open Source Computer Vision library [49].

1.4.2 Handle Requirements

Before starting to determine gripper requirements, it was essential to indicate and to preliminary describe what the gripper is going to grasp [50]. As handle requirements, the following ones were considered:

- Blocked degrees of freedom (translational and rotational ones);
- Wedge-in handle profile;
- Maximum grasping in all possible handle positions;
- Possibility to host a 30mm-side marker on the palm of the gripper;
- Perimeter-area ratio as figure of merit of profile configurations;
- Volume minimization.

As possible handle profile configurations circular, triangular and rectangular profiles were selected. Taking into account all above requirements, a triangular configuration profile was the first choice. This allows to block all the degrees of freedom and to host in the middle of the palm a 30mm-side marker (90 mm-handle side length). Moreover, this profile maximizes the figure of merit perimeter/area, having in this way a larger perimeter to allow the grasping and a smaller area to reduce the occupied volume. This handle presents a triangle basis of 80mm side (to host the marker and to allow the complete closure of the fingers), 30mm depth (to minimize the occupied payload volume) and 25° extrusion angle (to minimize the payload attached area and to maximize the grasped area). The handle marker shall be: 30mm side square, asymmetric pattern, low reflectivity material (no metallic) to avoid in-camera reflections, black and white pattern to increase contrast [51]. Obviously, the size of the sensor will affect the size of the handle. More technical details about the maker selection and the tracking algorithms (machine vision) are not an object of this current work and they will be dealt with in a future more detailed approach, during the realization of this project.

1.4.3 Gripper Possible Configuration Identification and Trade-offs Executions

Before executing the grasping features trade-offs, the gripper configuration parameters to design the tool [1], [7] are reported:

- Actuation architectures and actuation placement;
- Number of dependent/independent fingers;
- Number of actuators;
- Number of phalanxes per finger;
- Thumb presence.

Gripper Configuration Results

After this configuration study the robotic hand system was characterized by:

- Three-contact-independent-finger under actuated (2 degrees of freedom per finger, single actuator) hand:
  - Finger and phalanxes adjustment to compensate for misalignment;
  - The distal phalanx closes before the proximal one, allowing to grasp the handle side and limiting the handle length and volume.
- Two-phalanx fingers;
- No thumb, a high-dexterity level was not needed;
- Remote (palm located) actuator, with possibilities to implement also redundancies;
- Double acting actuator.

Underactuation Strategy

Underactuation is a widely used and a relatively old concept in robotics. Basically, it expresses the property of a system to have an input vector of smaller dimension than the output vector [41]. Practically, in robotics, it means having fewer actuators than degrees of freedom. Applying this concept to robotic grasping arises from a simple fact: it is better to be able to grasp objects using a simple control rather than having to command and coordinate several actions. The idea behind underactuation in grasping is to use an ingenious mechanical system that can adapt to the shape of the object automatically. This mechanical intelligence, embedded in the hand, is based on the principle of differential systems. The latter devices automatically distribute one input to several outputs, the ratio between the different outputs being determined by the design parameters and the output states themselves [52]. While in the literature in usual actuation architectures [1], [6], [7], [53], [54], underactuated systems have been realized where the first (proximal) phalanx closure led afterwards to the closure of the second (distal) one using the loading of a torsional springs and mechanical linkages, in this application a new underactuation strategy was developed, allowing to grasp the handle side and limiting the handle length and volume. This concept will allow the distal phalanx to move independently from the proximal one. A rigid tendon architecture is adopted to move the

distal phalanx and a torsional spring (4Nmm/°) to hold the movement of the proximal one. This concept is innovative with respect to the usual ones, because the kinematics works in the opposite way. As first proof of concept, a very simple model dynamic simulation was run. The three plots in Fig.1.5 depict the three phases of the finger actuation mechanism. The finger stays open, allowing to capture the handle with ±30mm and ±6° uncertainties. After that, the distal phalanx was closed. The proximal phalanx does not move thanks to a torsional spring that holds it in place. This happens until the mechanism hits a stop located on the proximal phalanx. In doing that, the whole finger rotates around a hinge located on the point that connects the proximal phalanx to the gripper palm and the whole finger rotates capturing the handle side.

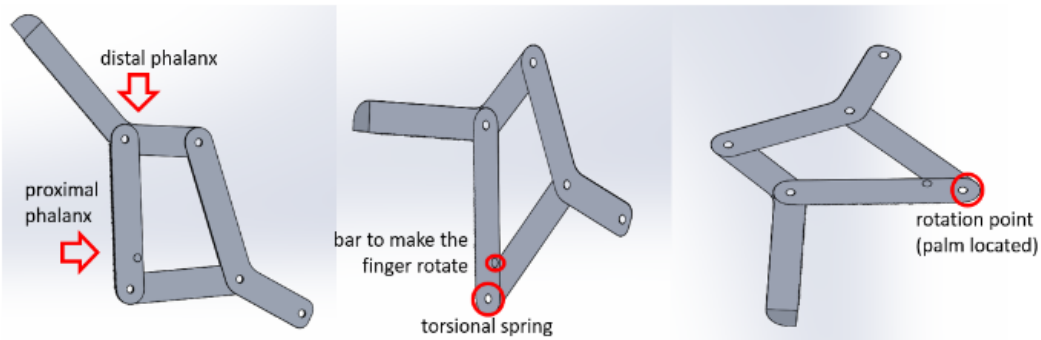

Figure 1.5 Finger mechanism actuation phases. The finger stays open, to guarantee the handle capturing requirement with ±30mm and ±6° uncertainties. After that, the distal phalanx was closed. The proximal phalanx does not move thanks to a torsional spring that holds it in place. This happens until the mechanism hits a stop located on the proximal phalanx. In doing that, the whole finger rotates around a hine located on the point that connects the proximal phalanx to the gripper palm and the whole finger rotates capturing the handle side [41].

Fig.1.6 shows that the movement of the proximal phalanx (phalanx 1 solid line) holds while the distal one moves (phalanx 2 dotted line). When the second phalanx is open the whole finger will rotate at the same angular velocity (after 1s).

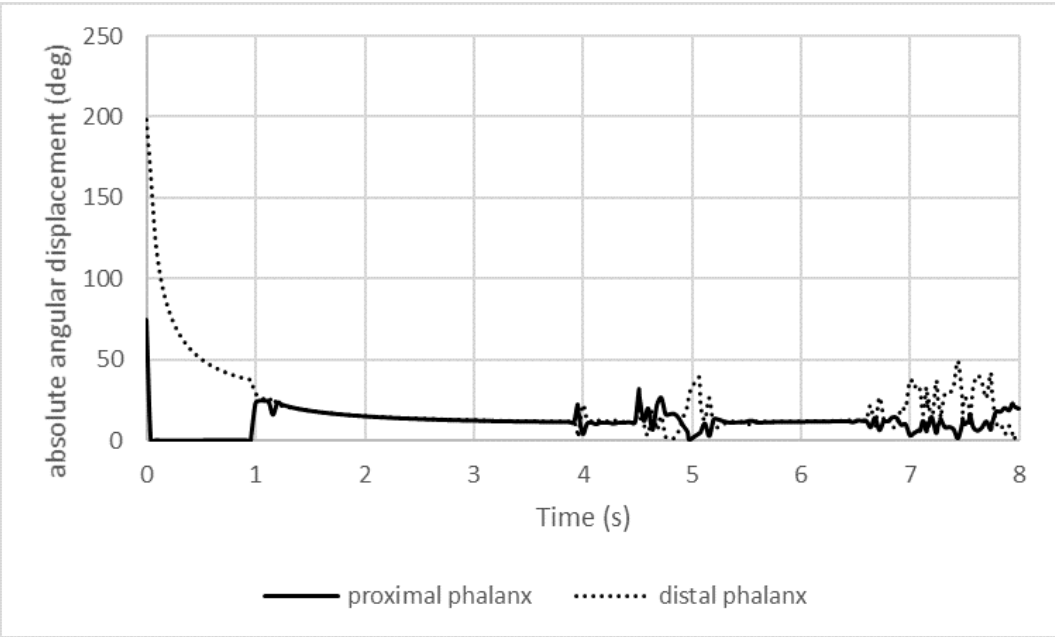

Figure 1.6 Phalanx kinematics plot. Phalanx angular velocity as a function of time for the proximal phalanx and the distal phalanx. It is worth noting that while the mechanism is working, the first phalanx holds, while the second moves. When the second phalanx is open the whole finger will rotate at the same angular velocity. As expected, after 1 s, the absolute angular displacement of the phalanxes is the same. The noise affecting the phalanxes in the angular displacement plot is due to the handle interaction disturbances [41].

1.5 Robotic Manipulator Baseline Configuration

1.5.1 Geometrical models

The geometric models of the handle, the single finger and the gripper were described and discussed.

Handle

Starting from the handle requirements in SubSec.1.4.2, in Fig.1.7 the CAD of the reentry vehicle grasping handle is reported. This tool is attached to the payload external surface. Fig.1.8 shows the CAD of the payload with the

attached handle. Although, the exact place of this attachment is not specified in this work, obviously it will be placed on a surface that can be reached from the robotic arm. More details on this specific point will be the object of a future more detailed study performed, during the realization phase of this project.

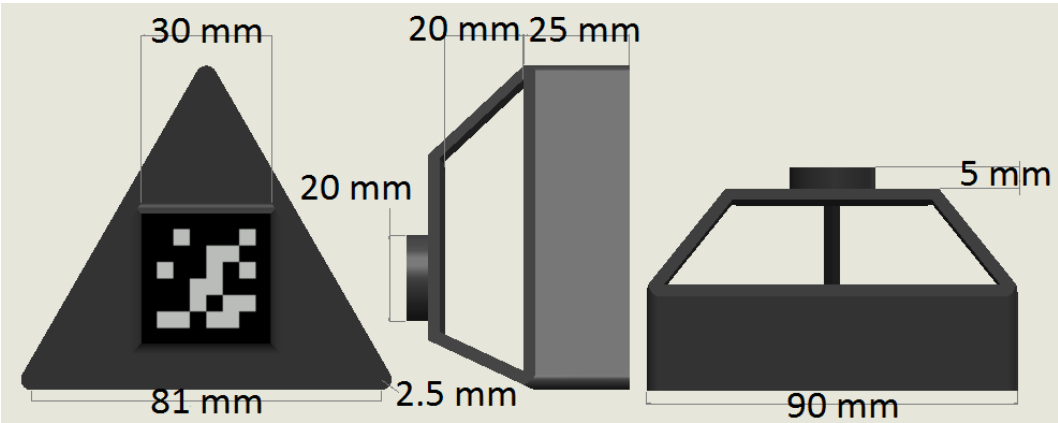

Figure 1.7 CAD of the reentry vehicle grasping handle. This tool is attached to the payload external surface. The dimensions were reported in mm [41].

The handle dimensions are determined to comply with all the requirements stated previously. The handle hole width (20mm) (place where the phalanxes realize an ingressive grasping) favors a better grasping control, taking into account that the error on the gripper positioning will be ±2.5mm in the final grasping phase. The full handle width (45mm) guarantees a better grasping control and minimizes the payload volume occupied. The handle side length (90mm) allows the position of the 30mm-square marker tracker and the perfect closing of the fingers to stabilize the grasping.

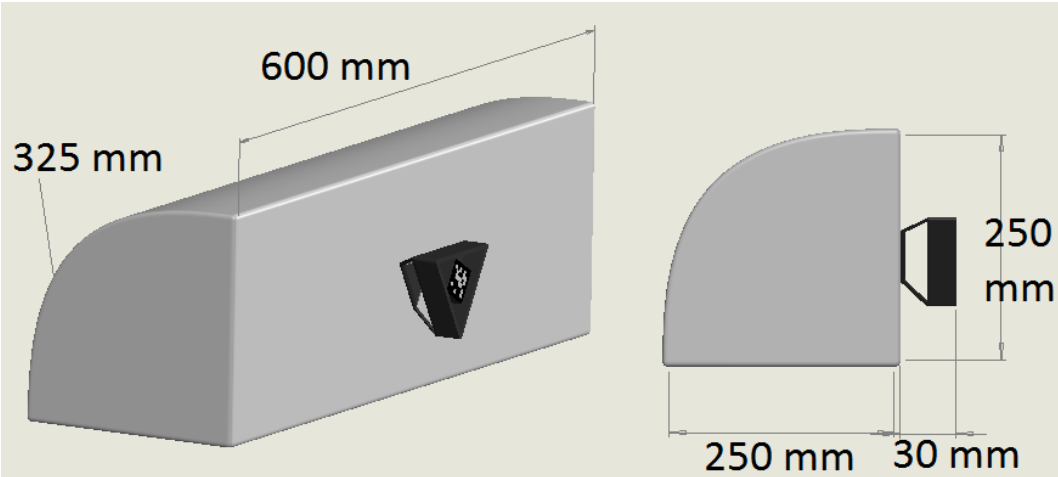

Figure 1.8 Reentry vehicle payload and preliminary handle positioning. This tool is attached to the payload external surface. The dimensions were reported in mm [41].

Single Finger Grasping Tool

In Fig.1.9 the three finger grasping closure activity viewed from the back of the handle was reported. They are so thick, because this simulations were run 10 times, with a uniform distributed positioning errors due to the camera-marker tracker system. The three fingers are not attached in the middle point of the palm side, but they are 10mm apart. In this way, they close without touching each other. We use also this study to determine the handle side length.

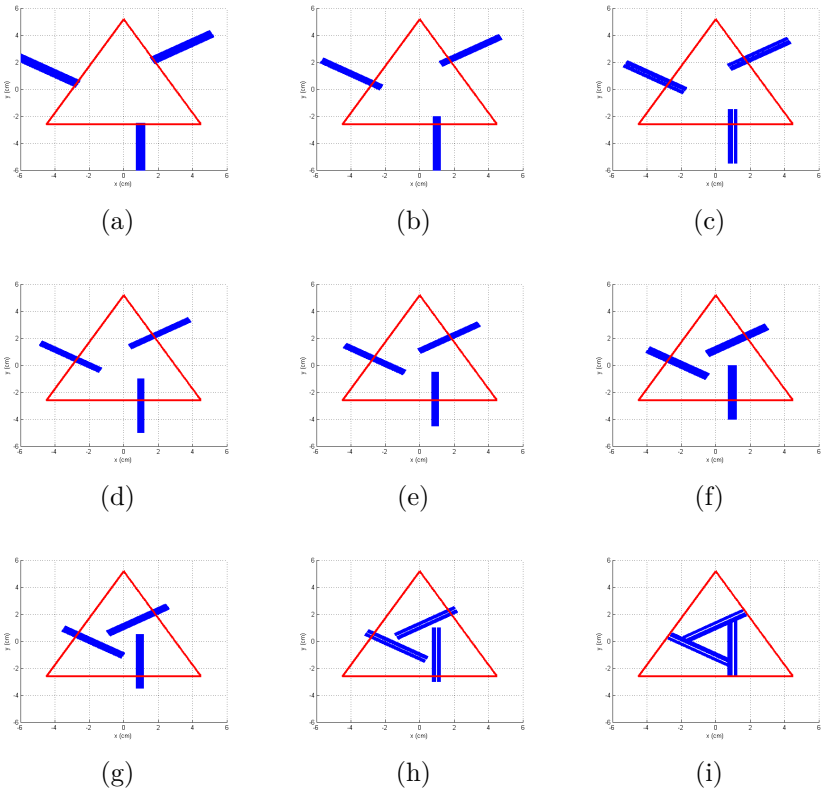

Figure 1.9 Re-entry vehicle payload and preliminary handle positioning simulation. This tool will be attached to the payload external surface. Nine snapshots of the gripper closure on the handle rear are shown.

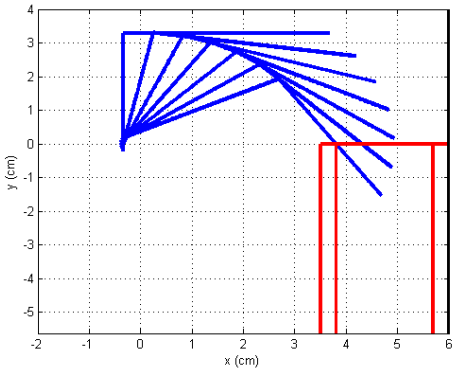

Figure 1.10 Finger grasping closure operating at a distance of 40mm. Blue line: finger phalanxes; red line: handle sides; black line: payload profile.

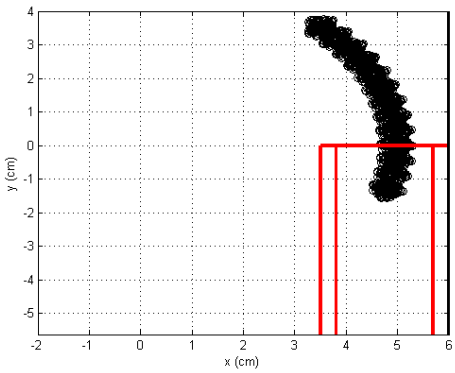

Figure 1.11 Finger grasping closure operating at a distance of 40mm. It takes into consideration camera-marker tracker uniformly distributed positioning errors (±2.5 mm).

Fig.1.10 reports a Matlab analysis about the finger grasping closure operating at a distance of 40mm. The blue line represents the finger phalanxes, the red line the handle sides and the black line the payload wall. Fig.1.11 reports a Matlab analysis about the finger grasping closure operating at a distance of 40mm. It takes into consideration camera-marker tracker uniformly distributed positioning errors (±2.5mm). The above analysis allow us to define the two phalanx finger lengths: the first one (proximal) is 35mm, while the second one (distal) 40mm. The next step is to size the vertical beam lengths.

For what concerns the grasping tool, once the geometric model of a single finger was defined, then three fingers were assembled together to a palm to realize the gripper. The main constraint in designing the finger was the proximity constraint. It dealt with not touching the handle and the payload before the final grasping closure phase happens. For this reason, the second phalanx should be longer than the first one. Moreover, at the same time to assure an adequate length of the first phalanx was needed to respect the requirements in terms of error recovery. This grasping closure interval takes into consideration the camera-marker tracker system errors. A numerical analysis (using a specific Matlab program) is run about the finger grasping closure operation to study the possible lengths. In Fig.1.12 the basic finger kinematics is depicted to size the two vertical beams constituting the chain. When the

chain moves (Eq.1.1), the two arcs cover the same path lengths (Eq.1.2)

$$s_1 = 2\pi l_1 \frac{\theta_1}{360°} \quad s_2 = 2\pi l_2 \frac{\theta_2}{360°}. \tag{1.1}$$

Considering that

$$s_1 = s_2, \tag{1.2}$$

The equality expressed in Eq.1.3 was obtained

$$\frac{l_1}{l_2} = \frac{\theta_2}{\theta_1}. \tag{1.3}$$

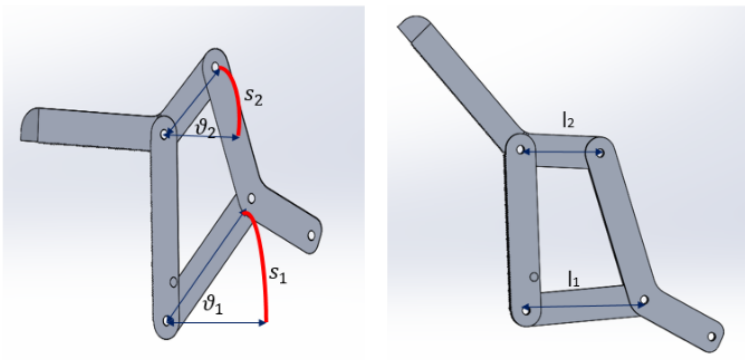

Figure 1.12 Single finger grasping basic kinematics. Right: second phalanx open; Left: second phalanx closed [41].

Assuming θ_2=45°, θ_1=30° and l_1=30mm, l_2 =20mm was found. The results of these preliminary analysis were later confirmed by the correct behavior of the multibody simulation results using MSC Adams software. The single finger grasping tool CAD is shown in Fig.1.13. The thickness of all these components is 7.5mm. This value was later confirmed through structural analysis.

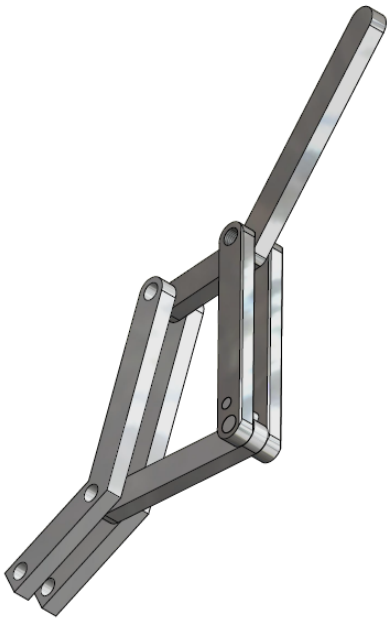

Figure 1.13 Single finger grasping tool main design CAD using Autodesk Inventor [41].

Assembled Grasping Tool

The three fingers together were assembled to the palm. In Figg.1.14 and 1.15 the whole structure is shown. A triangular-base palm is present where the three fingers are attached. This palm has the same shape of the handle. In this way an optimal superposition between the gripper and the hand was executed and a higher holding stability was reached. Furthermore, the three finger mechanism was connected to a cylindrical tube. It contains the actuator interface to transfer the linear actuator motion to the mechanical system.

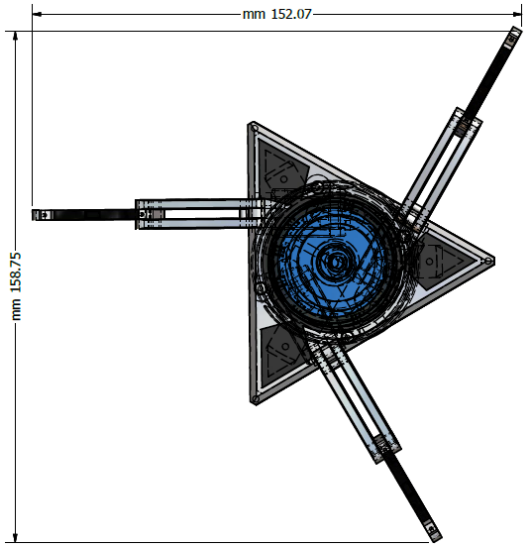

Figure 1.14 Reentry vehicle LEO payload grasping tool: front view [41]. The dimensions were expressed in mm.

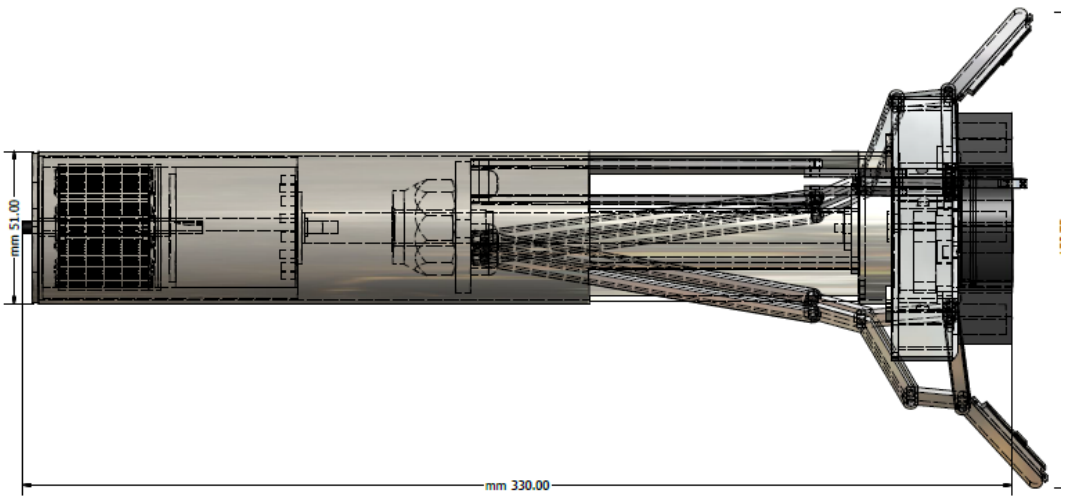

Figure 1.15 Reentry vehicle LEO payload grasping tool: lateral view [41]. The dimensions were expressed in mm.

1.5.2 Materials

For what concerns material choice, a trade-off among steel, stainless steel, aluminum 6061, and titanium was executed. These are the most used materials

in space applications [2]. For convenience, the same material both for the handle and the gripper was selected. As choice criteria the static friction coefficient, the Young modulus, the density, and the yield stress were adopted. The static friction coefficient takes into account the contact coupling between the handle and the grasping tool phalanxes. The Young modulus reflects the material elasticity and the density the material mass. The yield stress gives a preliminary result about the structural analysis. The trade-off results were reported in Tab.1.2. The maximum upper limit expected force in this system was ∼1000N and that the system dimensions were ∼10mm^2, an average pressure of 100MPa was obtained. After this preliminary trade-off study, aluminum 6061 was considered the best choice. This because with respect to the compared materials:

- Al presents a very high static friction coefficient value (Al on Al);
- Al presents a very low density and a very high E/ρ ratio;
- Al presents a pretty low yield stress, but enough to guarantee operability for this current application.
- Al presents a higher thermal expansion coefficient. For this design study level it works well in the environmental temperature gradient.

Material	μ [-]	E [GPa]	ρ [g/cm^3]	E/ρ [GPa cm$^3/g$]	σ_Y [MPa]	Thermal expansion [$10^{-6}\,K^{-1}$]
Steel	0.74	200	7.75÷8.05	24.8÷25.8	448	11.0÷13.0
Stainless steel	0.80	196	7.85÷8.06	24.3÷24.9	520	10.1÷17.3
Aluminum 6061-T6	1.1÷1.7	69	2.7	25.5	276	23.1
Titanium	0.36	110.3	4.54	24.3	130	8.6

Table 1.2 Trade-off results to select the material for the robotic gripper handle system [41].

However, to have a higher yield stress value and a lower thermal expansion coefficient other aluminum alloys or composites could be introduced, which however show other disadvantages such as a higher density or a higher conductivity. For now μ, ρ and E/ρ are the most important design constraints

for this design phase. Moreover, the palm and the second phalanx of each finger presents a layer (3mm thick) of Torlon [55]. It is a Polyamide-Imide that absorbs and dissipates impact energy. It is used in space applications. It offers low friction and wear, high pressure and velocity limits, excellent mechanical properties and heat resistance. This was used to damp the impact between the handle and the gripper.

1.6 Single Finger Kinematic Analysis

A detailed kinematic functional model of a single finger was depicted [41].

Forward Kinematics

The forward kinematics of a robot refers to the calculation of the position and orientation of its end-effector frame from its joint values. In this case the finger tip was considered as the end-effector.

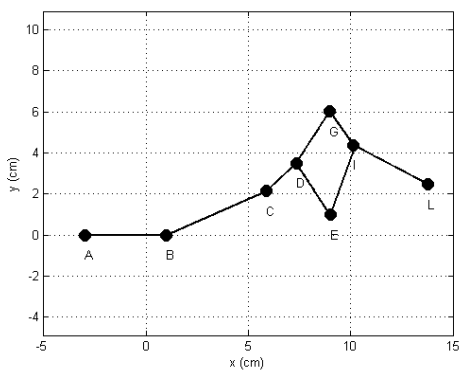

Figure 1.16 Single finger Matlab scheme [41].

To model the forward kinematics, Matlab software was adopted. The finger scheme is shown in Fig.1.16. A systematic method of deriving the 2D-forward kinematics would be to first attach reference frames to each of the joints; the eight link reference frames are respectively labeled with capital letters. The forward kinematics can then be written as a product of eight SE(2) matrices (special Euclidean group with two dimensions). To pass from a reference frame attached to a point to the next one some rototraslation matrices were defined.

During the working operation of this mechanism two phases were noticeable. First of all, there was a phase that goes from the position at rest up to the closure of the distal phalanx. After that, the second phase was characterized by the closure of the first phalanx, and by the subsequent rotation of the finger structure.

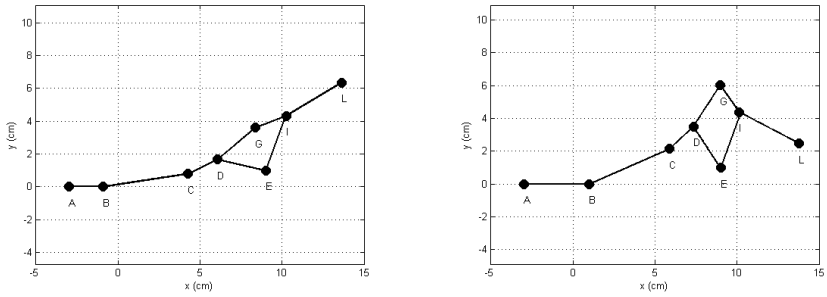

(a) (b)

Figure 1.17 First phase finger forward kinematics [41].

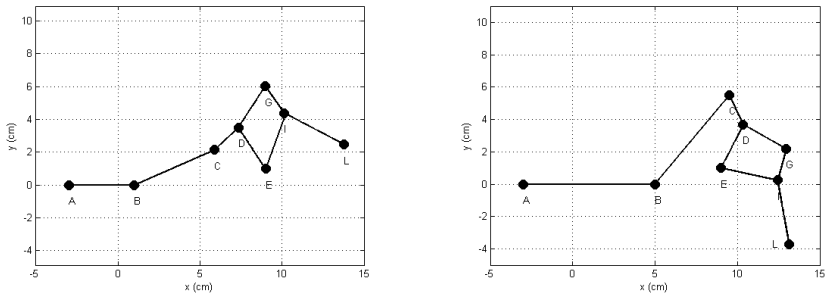

(a) (b)

Figure 1.18 Second phase finger forward kinematics [41].

Fig.1.17 shows the first phase finger forward kinematics and Fig.1.18 shows the second phase finger forward kinematics.

Inverse Kinematics

2D-inverse kinematics refers to the use of the kinematics equations of a robot to determine the joint parameters that provide a desired position of the end

effector. In this case, the only responsible for the main motion of the finger was the linear actuator attached to point A. Its intrinsic variable was l_0. So, as inverse kinematics analysis was shown the workspace (x,y) variations of the points constituting the finger mechanism as consequences of the variation of l_0 due to the linear actuator operation. In Fig.1.19 the workspaces of points A, B, C and D are reported. For each point the red line refers to the first phase working operation, while the blue line to the second phase. In Fig.1.20 the workspaces of points E, G, I and L are reported. For each point the red line refers to the first phase working operation, while the blue line to the second phase. All the workspace show trends that reflect the expected evolutions.

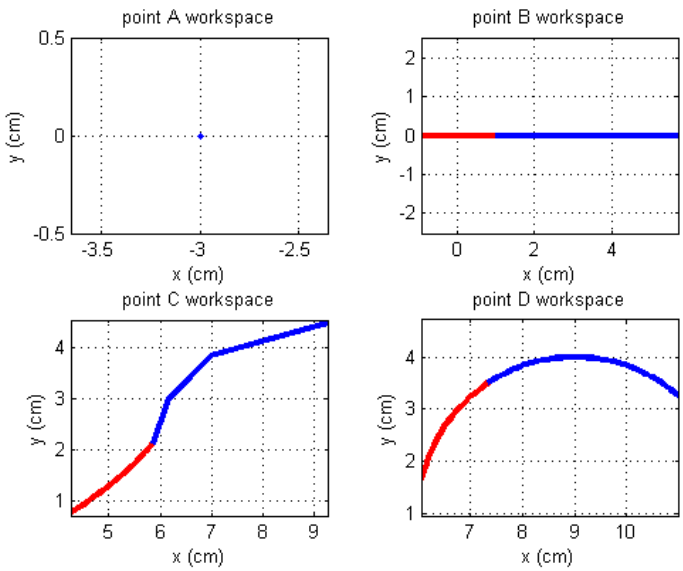

Figure 1.19 Point A (upper left), B (upper right), C (loIr left), D (loIr right) workspace as variation of l_0. For each point the red line refers to the first phase working operation, while the blue line to the second phase [41].

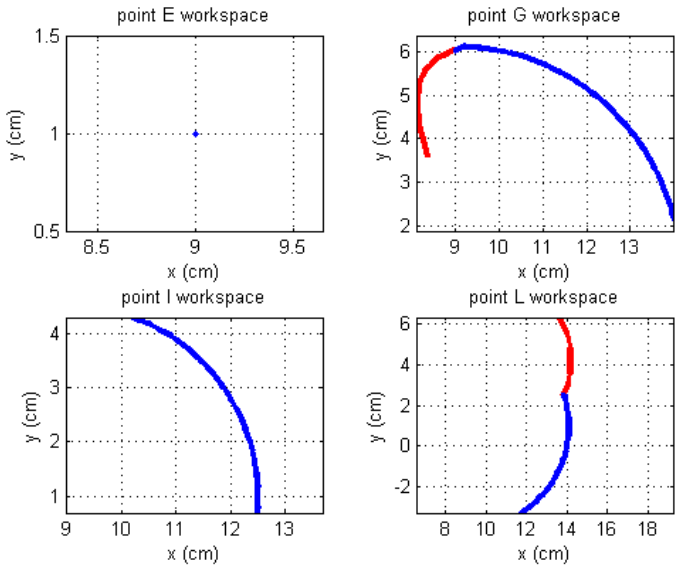

Figure 1.20 Point E (upper left), G (upper right), I (lower left), L (lower right) workspace as variation of l_0. For each point the red line refers to the first phase working operation, while the blue line to the second phase [41].

In particular, all these plots are constituted by points that are discrete steps due to l_0 variation. Therefore, for every desired point (x,y) of point L workspace it is possible to know the variations of the other joints of the system at the respective l_0.

1.7 Gripper Dynamic Analysis

The mechanical system is made up of three main components:

1. The motor and the gear box;
2. The torque transmission mechanism (ball screw);
3. The grasping mechanism (three-finger underactuated mechanism).

These components are shown in three red rectangles in Fig.1.21.

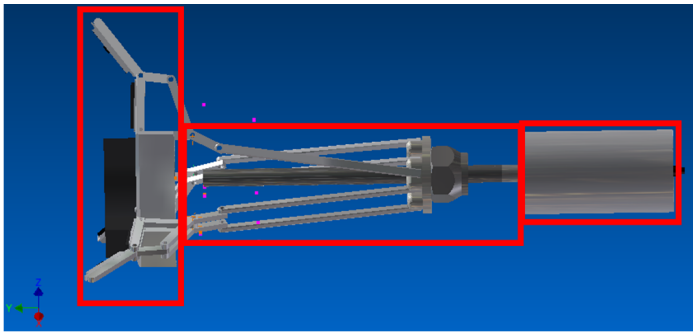

Figure 1.21 Mechanical components constituting the gripper. From left to right: grasping mechanism, ball screw mechanism, motor+gear box [41].

For this design study characterize each component was characterized [56], [57]:

1. Motor: Maxon BLDC 353399 EC 32, 15W, 24V with integrated electronics, with cover. Gear box: Maxon spur gearbox 110453 GS 38 A, 18:1, efficiency 73% with holding brake.

2. Ball screw (preload): screw diameter 10mm, screw length 130mm, lead 5mm, efficiency 95%.

3. Grasping mechanism: retention force 31.7N (30kg payload), assumed efficiency 90%.

For what concerns the dynamic analysis MSC Adams software was adopted. The Autodesk Inventor assembly .iam model was imported to MSC Adams. After that all the connections between the parts were created. In Fig.1.22 the gripper-payload configuration is presented using MSC Adams.

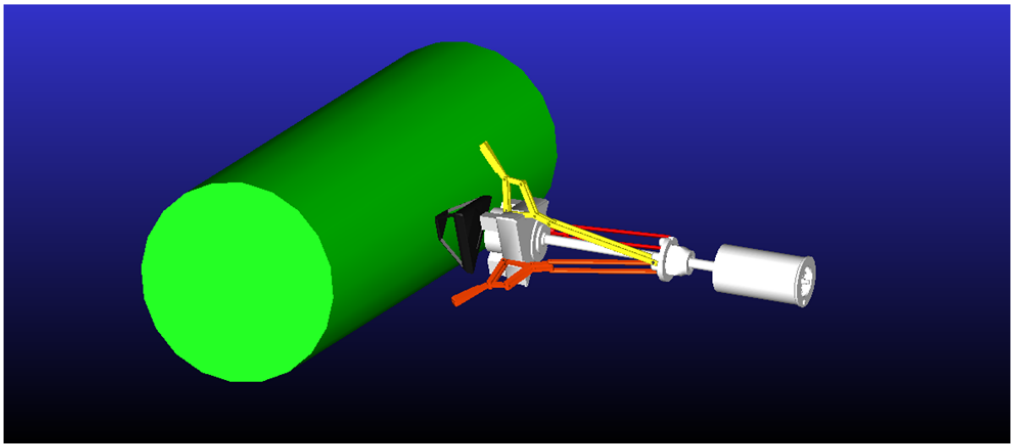

Figure 1.22 MSC Adams multibody system simulation. The payload inertial properties were reported (30kg mass, inertia moments) such as the ones of the gripper and the kinematic connections between its different parts [41].

The grasping of the handle and consequently of the payload is shown in Fig.1.23. The red arrows represent the forces exchanged between the second phalanxes of each finger and the handle side, such as the handle palm and the handle surface. The contact forces between the handle (Al 6061) and the fingers (Al 6061) and between the handle (Al 6061) and the palm (Torlon) have been modeled in the proper way (Coulomb contact).

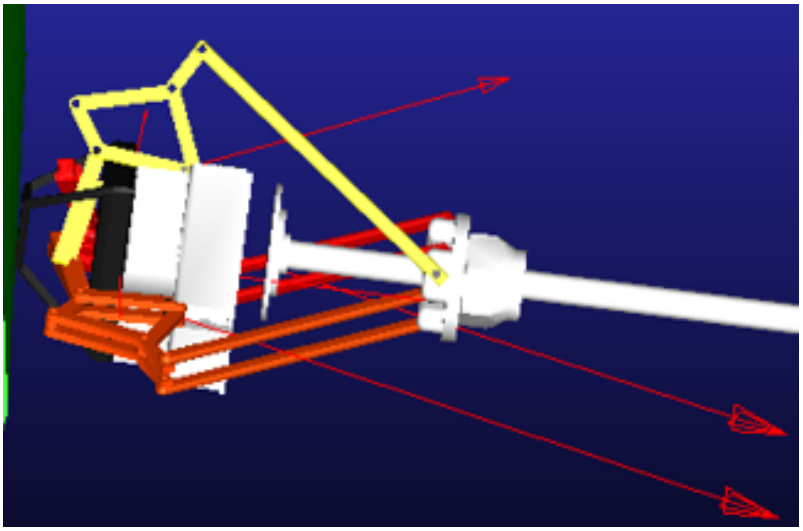

Figure 1.23 Detail of the closure phase of the grasping mechanism-handle system. The arrows represent the forces exchanged between the second phalanxes of each finger and the handle side, such as the handle palm and the handle surface. The gripper cover is here transparent to better show how the rigid tendons work [41].

The retention contact force between the palm and the handle was measured after the grasping transition period. It results to be 8.5N. It is larger than the estimated force necessary for a 30kg-payload holding (>5.5N).

1.8 Gripper Functional Model

1.8.1 Motor and Gearbox Model

A BLDC motor was preferred with respect to a brushed motor mainly due to less required maintenance due to absence of brushes, it enables operation at all speeds with rated load, it presents a higher efficiency (no voltage drop across brushes), a reduced size due to superior thermal characteristics and a lower electric noise generation at the cost of a higher cost and more complex control. For the load torque calculation for the ball screw Eq.1.4 [57] was adopted

$$M_L = \left(\frac{F_g P_B}{2\pi \eta_{mech} \eta_{bs}} + \frac{\mu_0 F_0 P_B}{2\pi} \right) \times \frac{1}{i}, \tag{1.4}$$

where F_g is the grasping force in newtons, to hold the payload attached to the end effector during arm motion, Al-Al contact with static friction of 1.1, P_B is the ball screw lead in mm, η_{mech} is the mechanism efficiency in %, η_{bs} is the ball screw efficiency in %, μ_0 is the friction coefficient, F_0 is the preload (usually 1/3 of F_g), and i is the ball screw gear thread (here i =1, worst case scenario). According to the design of the mechanism so far, F_g =28.5N was assumed, P_B =5mm, η_{mech} =90%, η_{bs} =95%, and μ_0 =0.2. The leads to the following resulting load torque: M_L =28.3mNm.

The calculation of the inertia is dependent on the mechanics of the system [57]. For the ball screw the inertia can be calculated by

$$J_{bs} = k_1 D_{bs}^4 L_{bs}, \tag{1.5}$$

where J_{bs} is the screw inertia in g cm^2; k_1 is a dimensional scaling constant, 7.57×10^{-12}; D_{bs} is the screw diameter in mm; L_{bs} is the screw length in mm. In this case D_{bs} =10mm and L_{bs} = 130mm. The inertia of the load using a ball screw mechanism was calculated using

$$J_{load} = k_2 \frac{m_{load}}{P^2}, \tag{1.6}$$

where J_{load} is the payload inertia in g cm^2; k_2 is a dimensional scaling constant, 2.55×10^{-8}, m_{load} is the payload mass in kg, and P is the screw pitch in rev/mm.

From the results above, the inertia at the motor shaft is

$$J_L = J_{bs} + J_{load} = 19.5 gcm^2. \tag{1.7}$$

Let us suppose that the friction torque is 100mNm. The inertia of the motor and of the gear box were neglected. In Fig.1.24 the motor velocity diagram is shown. It is a steep diagram because a system that can start very fast and have a quick response was needed. The step time was 0.1s, the whole grasping phase lasts 5s, and that the ball screw advancing speed is V_{bs} = 20mm/s. So the regime speed is $(P \times V_{bs}) \times 60$=240rpm. Obviously, this speed will be adjusted to the orbital maneuver time duration.

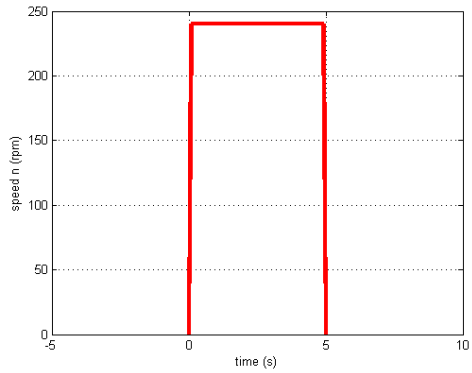

Figure 1.24 Motor velocity diagram speed as a function of time. It is a steep diagram because a system that can start very fast and have a quick response was needed.

Following [57], the necessary torque for the acceleration and for the braking were calculated

$$M_\alpha = J_L \frac{\pi \Delta n}{30 \Delta n} = 0.5 mNm. \tag{1.8}$$

For the different phases of the speed diagram:

- Acceleration (0.1s) 100.5mNm;
- Constant speed (4.8s) 100.0mNm;
- Braking (0.1s) 99.5mNm.

The peak torque is during the acceleration phase, The RMS torque of the working cycle is

$$M_{RMS} = \sqrt{\frac{t_1(M_1+M_L)^2 + t_2(M_2+M_L)^2 + t_3(M_3-M_L)^2}{t_{tot}}} = 127.4 mNm. \tag{1.9}$$

For the gear box choice, a gear box that permits the maximum torque was selected. Its maximum speed is 5000rpm. This allows a gear box ratio of

$$i_{max} = \frac{n_{max_g b}}{n_L} = 21:1. \tag{1.10}$$

A gear box with 3 stages with a gear box ratio of i = 18. Its efficiency is 73% was selected. Speed and torque were recalculated at the motor shaft

$$n_{mot} = i \times n_L = 4320 rpm, \tag{1.11}$$

$$M_{mot_{RMS}} = \frac{M_{RMS}}{i\eta} = 9.69mNm, \tag{1.12}$$

$$M_{mot_{max}} = \frac{M_{max}}{i\eta} = 9.80mNm. \tag{1.13}$$

A 25% margin was considered for the calculation of the maximum torque that this motor has to provide. The final result is

$$M_{mot_{RMS}} = 12.12mNm, \tag{1.14}$$

$$M_{mot_{max}} = 12.25mNm. \tag{1.15}$$

The ratio between the ball screw combined with the mechanism inertia and the rotor combined with the gear box inertia (load-to-motor inertia) is 0.5. In general, in a rotary motor system, the best load-to-motor inertia match is 1:1 because it minimizes power consumption and increases system stability. In this case, 0.5 was reached for the load-to-motor ratio. This means that the load inertia is half of the load inertia of the motor. This ensures stability to the whole gripper configuration system [41].

1.8.2 Functional Model General Architecture

In Fig.1.25 the general control architecture of reentry vehicle grasping robotic control system is shown [41]. There are three main blocks: the Control Overall System Block, the Control Arm Block and the Control Robotic Hand Block.

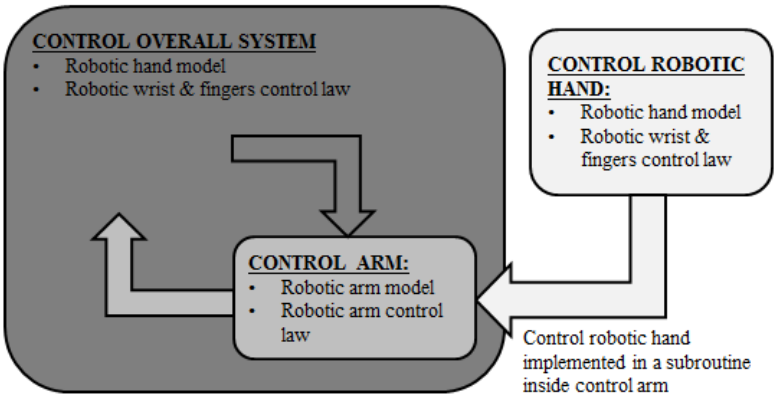

Figure 1.25 Reentry vehicle gripper grasping robotic control system. There are three main blocks: the Control Overall System Block, the Control Arm Block and the Control Robotic Hand Block [41].

The control block of the robotic hand consists of a subroutine that was implemented inside control arm. As inputs (actuator commands) were considered:

- Wrist actuator commands;
- Finger actuator commands.

As outputs (sensor data) were considered:

- Marker alignment data;
- Wrist actuator encoders;
- Finger actuator encoder;
- Finger actuator force-torque sensor;
- Phalanx tactile sensors: tactile sensors [58], [59], considered together with finger momentum and position in back action.

1.8.3 BLDC Motor System-Level Model

To implement the BLDC motor actuator, an existing Matlab-Simulink library was adjusted to this case [60]. The motor and driver were modelled as a single

masked subsystem. In this model of a BLDC motor, the standard configuration was modeled whereby an inner feedback loop controls current and an outer feedback loop controls motor speed. Simulation results characterizing the motor are shown in Fig.1.26. The first plot is the motor speed (rpm) as a function of time, the second plot is the mechanical power (W) as a function of time and the third plot is the motor efficiency (%) as a function of time. All these plots follow the same expected trend due to the voltage system. For what concerns the efficiency it reaches about 60%. This was due also to the fact that an oversized servomotor was adopted (a more powerful motor to have a lower torque) to guarantee a higher robustness to the system, instead of having a higher efficiency correlated to higher risks. In Tab.1.3 the data sheet values adopted together with the BLDC Simulink system level model are reported.

Electrical		**Efficiency**	
Nominal voltage (V)	24	Efficiency (%)	66
No-load DC current to drive (A)	$84.6\ 10^{-3}$	Speed at which efficiency is measured (rpm)	6000
Current loop time constants (s)	$20.1\ 10^{-3}$	Torque at which efficiency is measured (Nm)	$18.6\ 10^{-3}$
Mechanical		**Controller**	
Stall torque (Nm)	$35.8\ 10^{-3}$	Proportional gain	$5\ 10^{-3}$
Rotor inertia (kg m²)	$35.7\ 10^{-7}$	Integral gain	$5\ 10^{-3}$
Rotor initial speed (rpm)	0	Maximum reference voltage (V)	10
Load used when quoting efficiency (Nm)	$18.6\ 10^{-3}$	Speed at maximum reference voltage (rpm)	6000

Table 1.3 Servomotor driver (mask): implements an abstracted model of a servomotor and driver configured for closed-loop speed control.

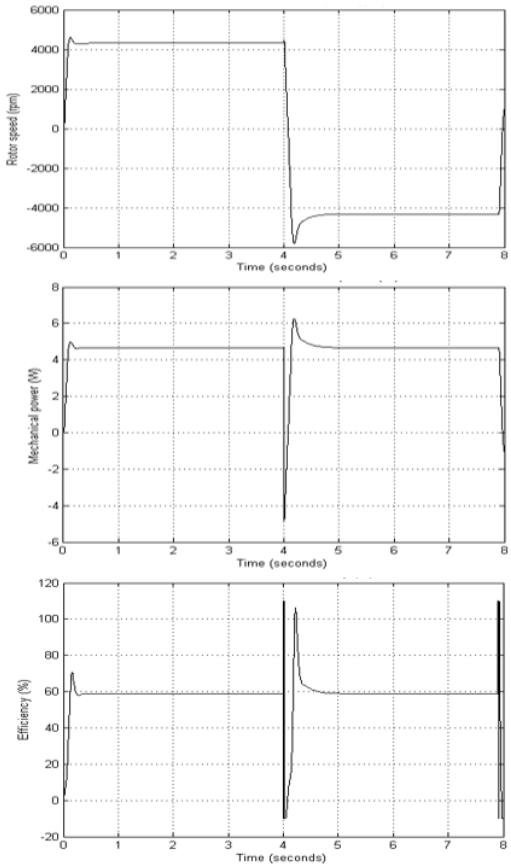

Figure 1.26 From top to bottom: rotor speed (rpm), mechanical power (W) and efficiency (%) as a function of time. All these plots follow the same expected trend due to the voltage system [41].

A proportional and an integral gain were chosen to assure a reasonable small time constant (0.2s) for the current controller.

1.8.4 Control Architecture

It was essential to model space robot systems in terms of dynamic facing problems inevitably unique to this field [61]. In this regard, it was necessary to distinguish between the systems currently used, the free flying and the free floating. In the first, the spacecraft's position and attitude were controlled by means jet thrusters or reaction wheels during the manipulator activity, clearly such systems provide highly redundancy and versatility making their workspace almost unlimited. However, the big drawback was the consumption of excessive

amounts of reaction jet attitude control fuel, expensive and non-renewable resource in the space, which could greatly limit the useful on-orbit life of the system. To avoid this problem it was possible to adopt the free floating systems, in which the spacecraft moves freely in response to the dynamical disturbances caused by the manipulator's motion, not being actively controlled in the position and in attitude. In this case the latter type of system was considered, moreover, more advantageous in the case of capture of a fragile payload [62]. Considering such system composed by a manipulator arm mounted on a base spacecraft floating in the inertial space without any external forces or moments applied, it was evident that the movements of the manipulator have effects on the base and vice versa. To better understand this dynamic coupling was necessary to refer to the motion equation of a generic space robot, that, assuming in the operational space the linear and angular velocities of the base $\dot{\mathbf{x}}_b = [\dot{\mathbf{p}}_b, \dot{\boldsymbol{\omega}}_b]^T \in R^{6\times 1}$ (respectively end effector linear and angular velocities) with respect to the inertial frame and the motion rate of the joints $\dot{\mathbf{q}} \in R^{n\times 1}$ (n are the manipulator degree of freedom) as the generalized coordinates, is expressed in Eq.1.16 [63]

$$\begin{bmatrix} \mathbf{H}_b & \mathbf{H}_{bm} \\ \mathbf{H}_{bm}^T & \mathbf{H}_m \end{bmatrix} \begin{bmatrix} \ddot{\mathbf{x}}_b \\ \ddot{\mathbf{q}} \end{bmatrix} + \begin{bmatrix} \mathbf{c}_b \\ \mathbf{c}_m \end{bmatrix} = \begin{bmatrix} \mathbf{F}_b \\ \boldsymbol{\tau} \end{bmatrix} + \begin{bmatrix} \mathbf{J}_b^T \\ \mathbf{J}_m^T \end{bmatrix} \mathbf{F}_h, \tag{1.16}$$

where $\mathbf{H}_b$ is the inertia matrix of the base body, $\mathbf{H}_m$ is the inertia matrix of the manipulator arm, $\mathbf{H}_{bm}$ is the inertia matrix that takes in account the coupling between base and arm, $\mathbf{c}_b$ is the non-linear velocity dependent term of the base body, $\mathbf{c}_m$ is the non-linear velocity dependent term of the arm, $\mathbf{F}_b$ is the external forces/moments acting on the base, τ is the joint torque vector on the arm, $\mathbf{J}_b$ is the Jacobian matrix dependent of the base body motion, $\mathbf{J}_m$ is the Jacobian matrix dependent of the arm motion, and $\mathbf{F}_h$ is the external forces/moments acting on the end effector of the arm.

1.8.5 Control Strategy: Impedance Control

The strategy to track a target used during the simulation for the robot Chaser was based on an Impedance Control [64]. This choice was driven by the need to have a control that could be adapted to the main phases of a servicing mission: rendezvous and docking and stabilization. Indeed the impedance control, being

a dynamic model-based compensation control, guarantees accurate tracking of the desired end effector trajectory, essential to perform the approach maneuvers, and in the same time provides a control of the contact forces that were carried out during the capture phase of the Target, including their measurements in the control loop. Fig.1.27 depicts the end-effector position velocity and acceleration closed-loop control system using Simulink..

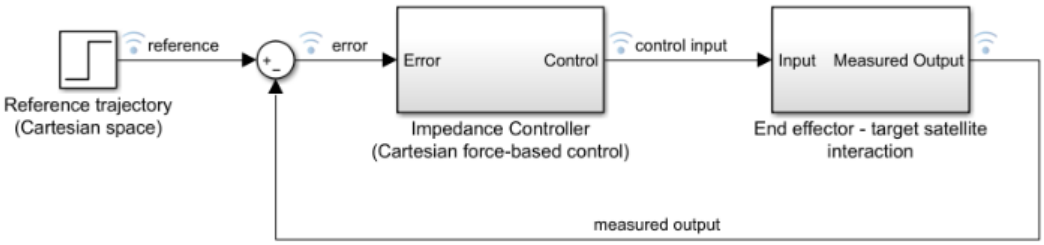

Figure 1.27 End-effector position velocity and acceleration closed-loop control system using Simulink.

The particular feature of this type of control was to ensure that the end effector of the manipulator manifests the behavior of an impedance, equivalent to a mass-damper-spring system. It was thanks to the possibility to regulate such mechanical impedance to make this control more suitable than other for our application. Furthermore, the control was defined in the operational space for two main reasons. First of all the motion specification, i.e., the trajectories to follow, were assigned in the Cartesian space. If the control was referred to the joint space an inverse kinematics algorithm was needed to convert the variables in those corresponding in the joint space. This process has an increasing computational load when the inversion of first- and second-order differential kinematics is required to convert the desired time history of the end effector position, velocity and acceleration in the corresponding quantities in joint space. Instead, referring to the operational space the trajectory inversion was replaced with a coordinate transformation, using the direct kinematics relations to transform the measured joint space variables in the corresponding operational space, that will be compared with the desired values. Notice that in this case the kinematics equations are inside the loop, thus having to perform many computations for each loop the system could run at a lower sampling frequency compared to joint-based systems, that may lead to degrading the stability and

the disturbance rejection capabilities of the overall control system. Despite this limitation, the operational-based control is essential when the manipulator has to interact with the environment (in our case with the target satellite), indeed in this case is necessary to control both position and contact forces, a joint space control can provide only the first one with the risk of incurring in errors due to a not complete knowledge of the environment. The impedance control utilized during the experiments was a Cartesian force-based control, i.e., the command signal that it generates is a generalized force, including forces and moments. It was designed in two fundamental steps: decoupling and linearization in the operational space and imposition of the desired Impedance Model to correctly react to the external forces/moments acting on the end effector of the arm ($\mathbf{F}_h$). Further results regarding the application of this control law to the whole system and, in particular, to the gripper are not part of this work.

1.9 Test Report

1.9.1 Physical model

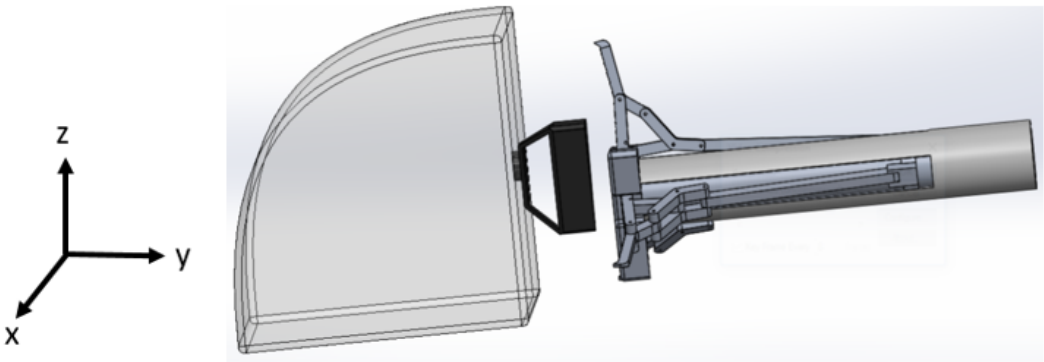

Figure 1.28 Reference frame (left) and a gripper-payload system picture (right). X-y plane defines the grasping maneuver plane, while the z-axis identifies the direction normal to this plane.

The reference frame illustrated in Fig.1.28 is considered attached to the intersection point of the triangular gripper palm bisectors. The workspace relative to the possible grasping configurations with error recovering is illustrated in

Fig.1.29. In the Tab.1.4 the possible scenarios are reported to validate this model in terms of error recovering.

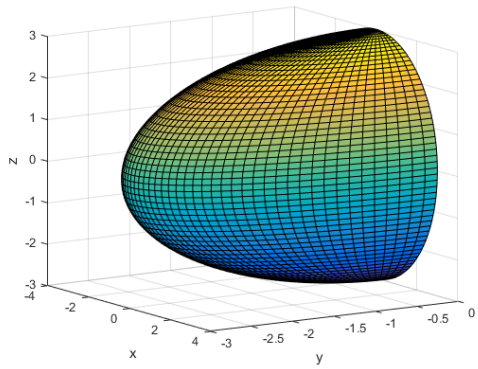

Figure 1.29 Workspace relative to the possible grasping configurations within the assigned error recovering.

To validate the requirements related to recovering from errors in position and attitude (±30mm offset and ±6° around axis) different scenarios were evaluated [41].

	Scenario 1	Scenario 2	Scenario 3	Scenario 4	Scenario 5	Scenario 6
x-axis	30mm	0	0	6°	0	0
y-axis	0	30mm	0	0	6°	0
z-axis	0	0	30mm	0	0	6°

Table 1.4 Scenarios to validate this grasping technology workspace. If these scenarios were satisfied, then the whole grasping workspace was actually covered.

All of these scenarios were simulated properly with successful results. For each of these scenarios two plots are reported below: the first ones identify the linear displacements (x, y, z, absolute distance) of the handle as a function of time during the grasping maneuver. The second ones depict the linear velocity and the angular velocity of the handle-payload system as a function of time during the grasping maneuver. The handle-payload system was modeled taking into account the mass and the inertia properties of the payload itself. It is possible to notice displacement and velocity fluctuations caused by the uneven

interaction of the gripper fingers with the handle. All the fluctuations stabilize once the grasping is complete.

Scenario 1

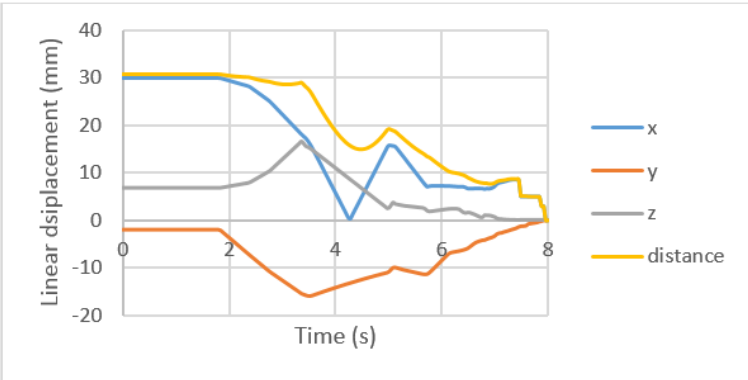

Figure 1.30 Linear displacements (x, y, z, absolute distance) of the handle as a function of time during the grasping maneuver.

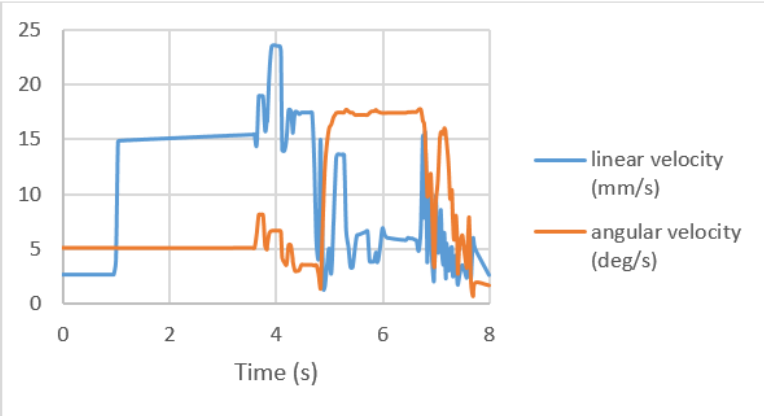

Figure 1.31 Linear and angular velocity of the handle-payload system as a function of time during the grasping maneuver.

Scenario 2

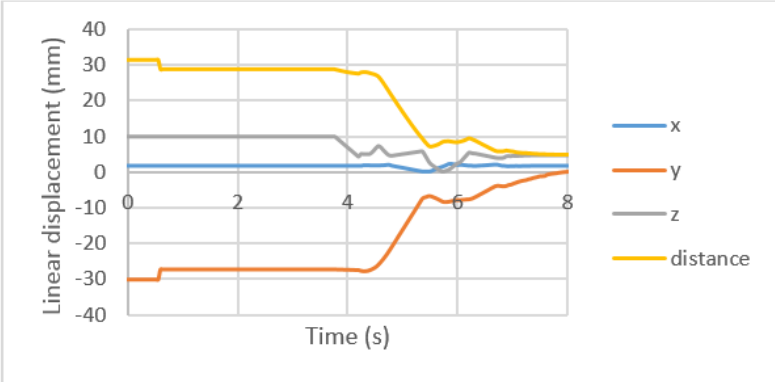

Figure 1.32 Linear displacements (x, y, z, absolute distance) of the handle as a function of time during the grasping maneuver.

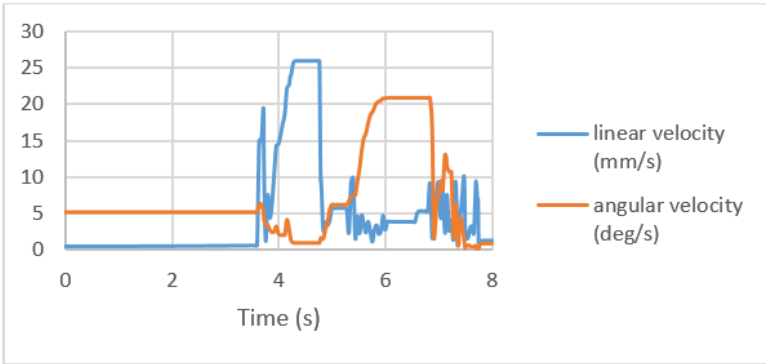

Figure 1.33 Linear and angular velocity of the handle-payload system as a function of time during the grasping maneuver.

Scenario 3

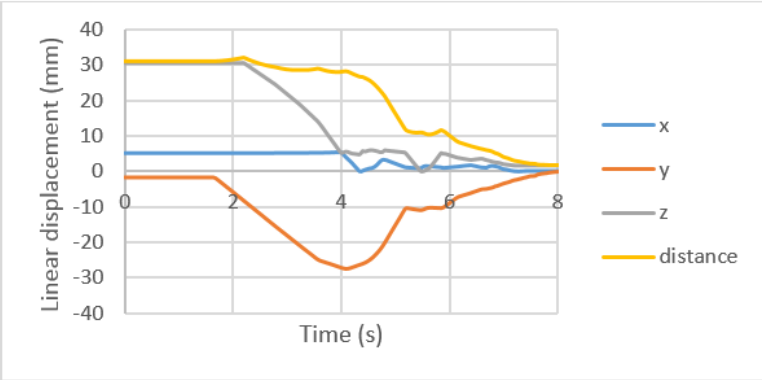

Figure 1.34 Linear displacements (x, y, z, absolute distance) of the handle as a function of time during the grasping maneuver.

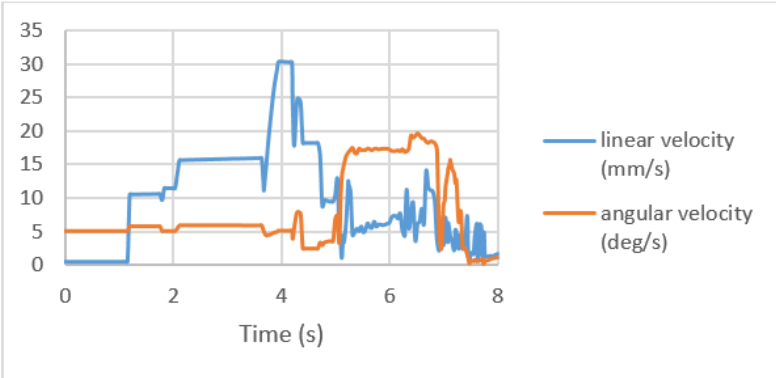

Figure 1.35 Linear and angular velocity of the handle-payload system as a function of time during the grasping maneuver.

Scenario 4

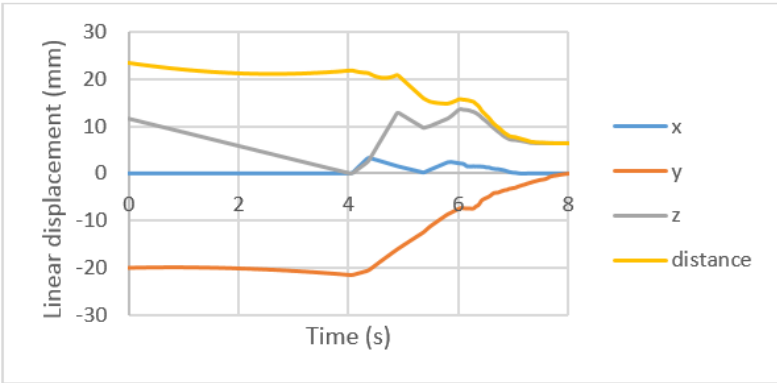

Figure 1.36 Linear displacements (x, y, z, absolute distance) of the handle as a function of time during the grasping maneuver.

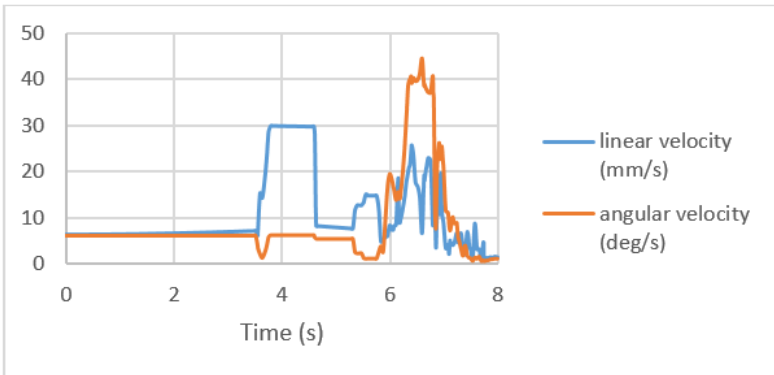

Figure 1.37 Linear and angular velocity of the handle-payload system as a function of time during the grasping maneuver.

Scenario 5

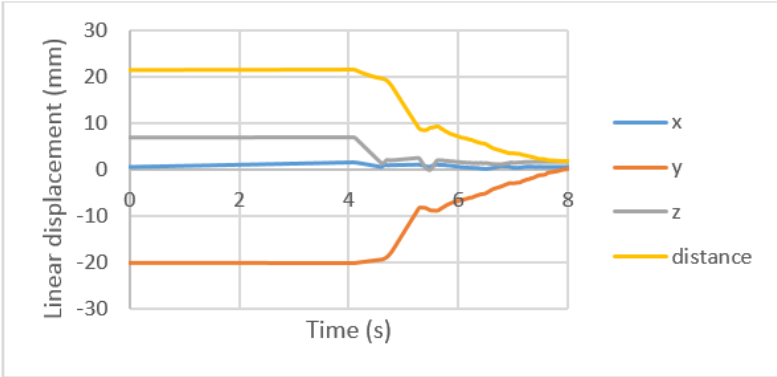

Figure 1.38 Linear displacements (x, y, z, absolute distance) of the handle as a function of time during the grasping maneuver.

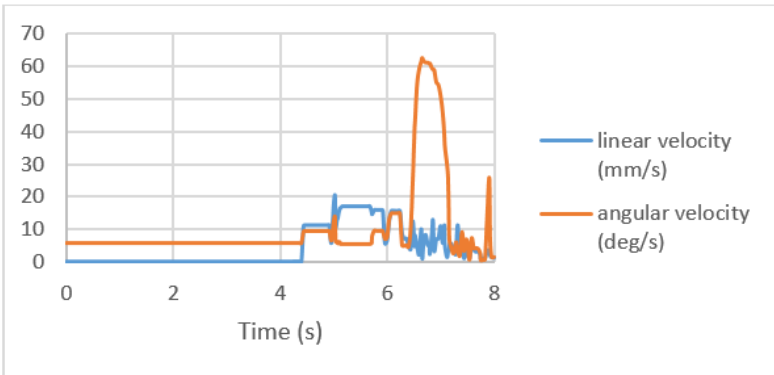

Figure 1.39 Linear and angular velocity of the handle-payload system as a function of time during the grasping maneuver.

Scenario 6

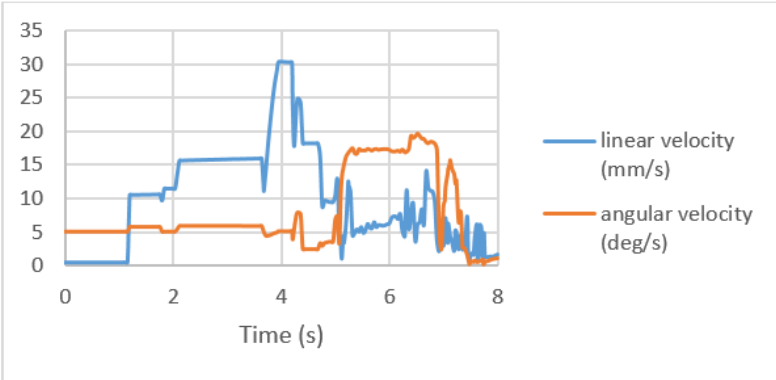

Figure 1.40 Linear displacements (x, y, z, absolute distance) of the handle as a function of time during the grasping maneuver.

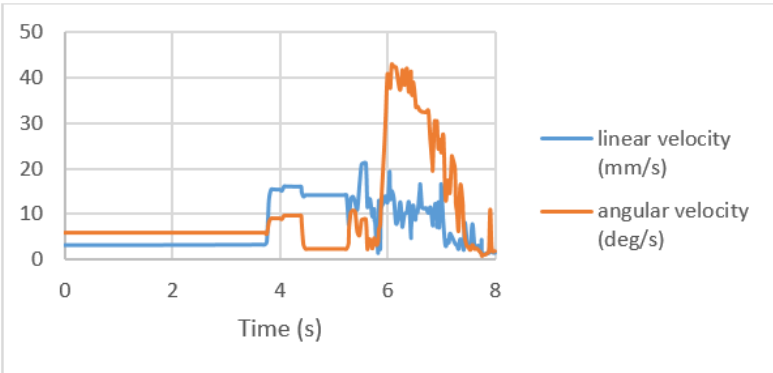

Figure 1.41 Linear and angular velocity of the handle-payload system as a function of time during the grasping maneuver.

A Complete Example

A more complete example is shown below regarding a particular case. Here the handle starts at a distance of 37.5mm (22.4mm, -14.2mm, 26.4mm) with respect to the gripper palm. Even in this case the grasping activity results to be successful. Some snapshots describing what happen during the maneuver are reported.

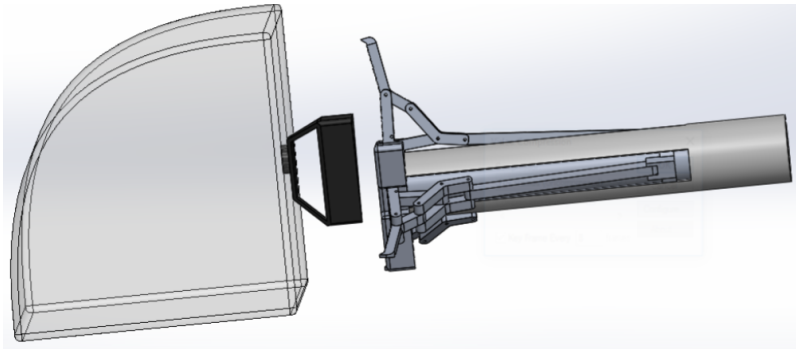

Figure 1.42 The maneuver starts [41].

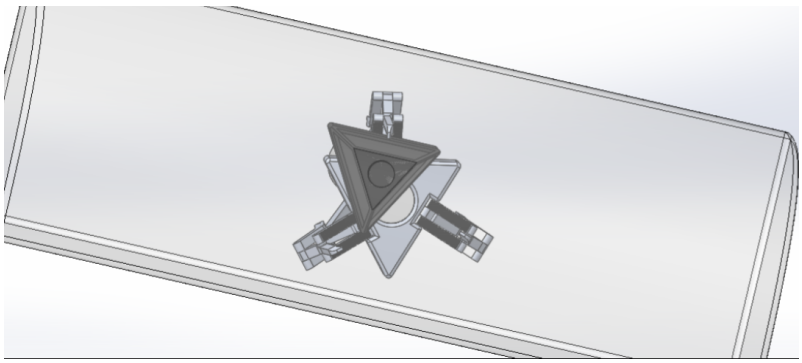

Figure 1.43 The distal phalanx contacts the handle side [41].

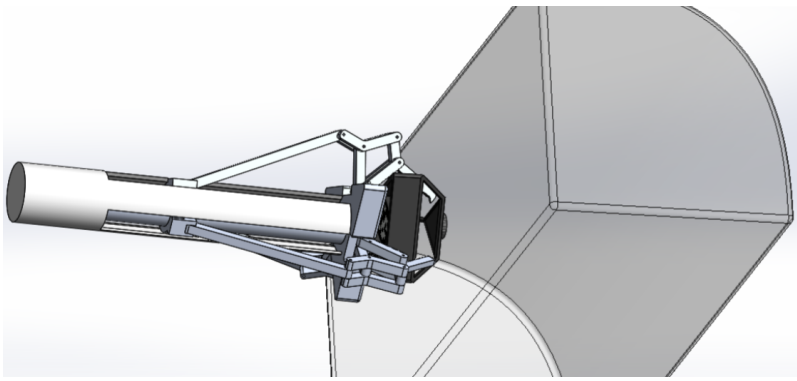

Figure 1.44 The fingers bring the handle to the correct position [41].

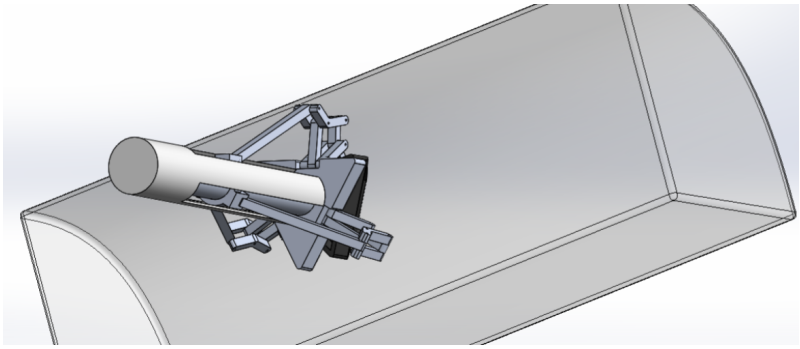

Figure 1.45 The fingers close on the handle side using also the nearest phalanx [41].

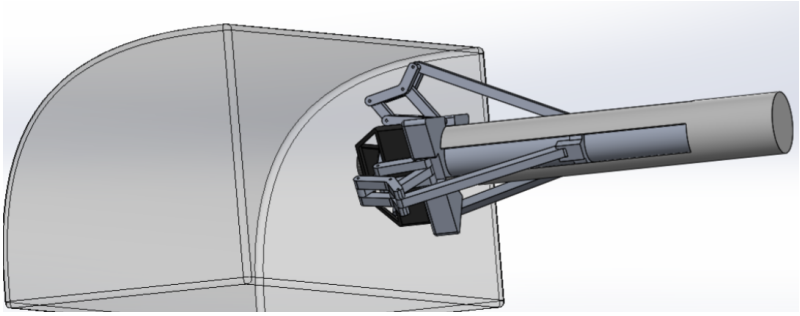

Figure 1.46 The grasping is performed successfully [41].

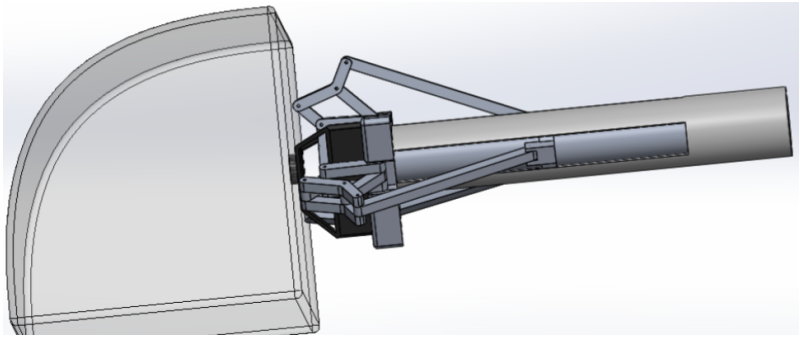

Figure 1.47 The grasping retains the handle surface against the gripper palm [41].

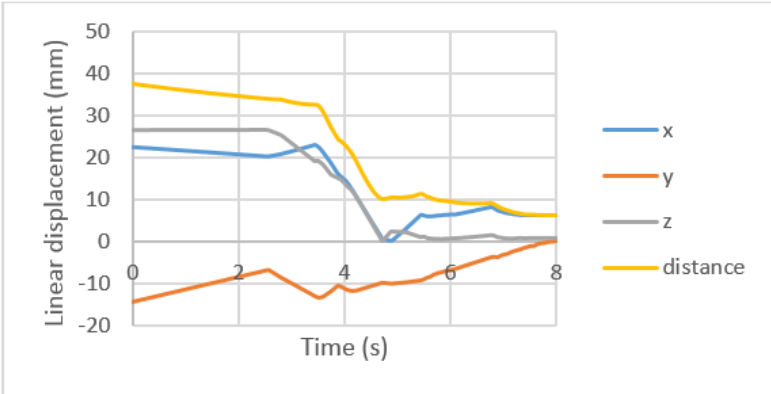

Figure 1.48 Simulation analysis data regarding the position variation of the handle center of mass with respect to the gripper palm. The handle was positioned at an absolute distance of 37.5mm (22.4mm, -14.2mm, 26.4mm) with respect to the gripper palm. Even if the distance was greater than 30mm, the whole mechanism proves to be robust working successfully [41].

Simulation analysis data regarding the position variation of the handle center of mass with respect to the gripper are reported in Fig.1.48.

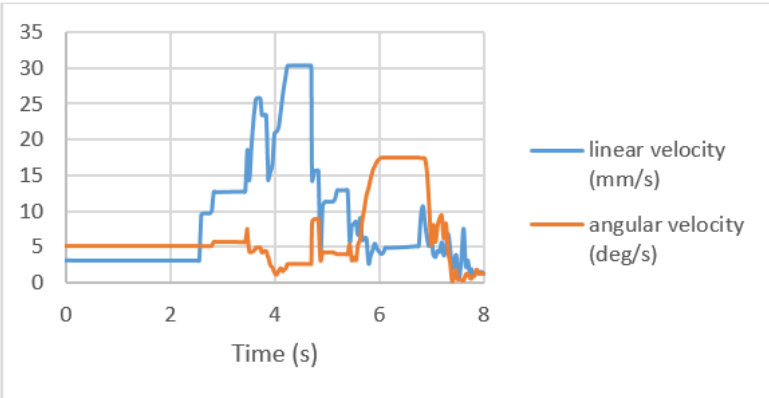

Figure 1.49 Linear and angular velocity of the handle-payload system as a function of time during the grasping maneuver. The initial velocity for the payload + handle ensemble was set to be 3mm/s (y-axis) and 5°/s (around x-axis) [41].

The linear velocity (solid line) and the angular velocity (dotted line) of the handle during the capture are reported in Fig.1.49. To show the robustness of this mechanical design the initial velocity for the payload and handle ensemble was set to be 3mm/s (y-axis) and 5°/s (around x-axis). Both these curves

show to converge towards zero after the capture was performed. Also here the displacement and velocity fluctuations stabilize once the grasping is complete.

1.9.2 Software Model

In the Matlab and Simulink developed model the requested inputs from the reentry vehicle-arm system consist of:

- Gripper position (x-y-z coordinates) and errors;
- Gripper attitude (Tait-Bryan angles 3-2-1 Yaw-Pitch-Roll) and errors;
- Actuator features: only a boolean command is considered (0 off / 10 on);
- Force sensor resolution.

The outputs were:

- The measured distance between the camera (gripper palm) and the handle (marker tracker);
- The actuation of the grasping mechanism;
- The measured coordinates related to the position (x-y-z coordinates) and to the attitudes (Yaw-Pitch-Roll angles).

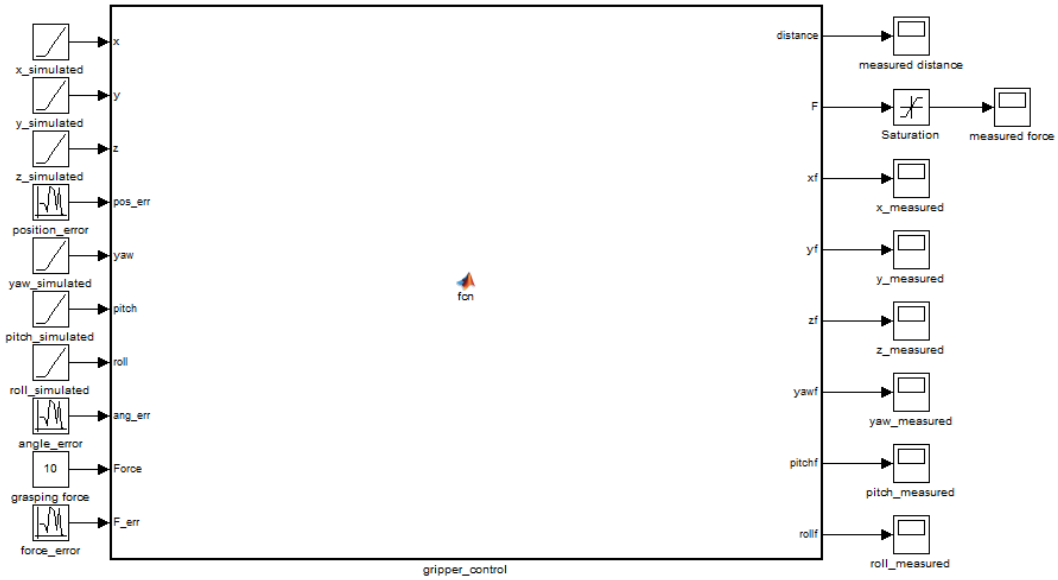

Figure 1.50 Matlab and Simulink gripper control block.

Fig.1.50 shows the Matlab and Simulink gripper control block. The grasping control consists of:

1. Identifying the distance between the camera (gripper palm) and the handle (marker tracker);
2. Ensuring to be satisfying the given requirements (±30mm in position, ±6° in attitude);
3. Actuating the grasping mechanism.

Fig.1.51 depicts the absolute distance in mm (red line) and grasping activity actuation signal (black line) as a function of time. The whole maneuver takes about 10s.

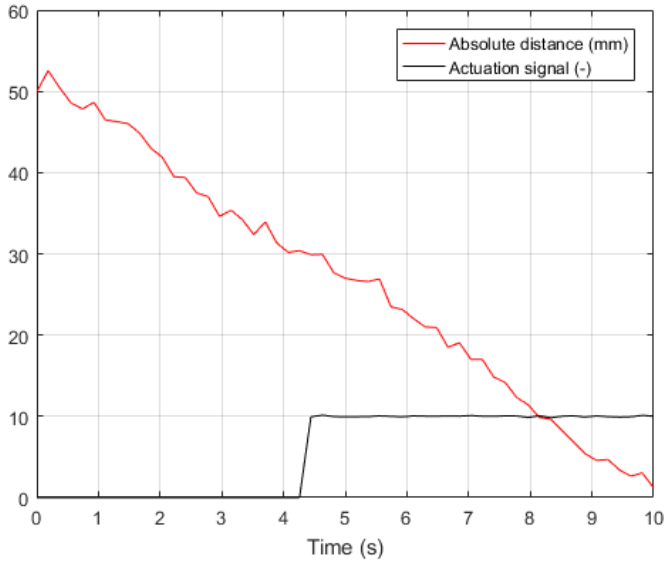

Figure 1.51 Absolute distance in mm (red line) and grasping activity actuation signal (black line) as a function of time. The whole maneuver takes about 10s.

As it is possible to notice from Fig.1.51, when the absolute distance is below 30mm, the actuation signal starts and the grasping activity was executed to bring the distance between the gripper and the handle to a distance of 0mm.

1.10 Structural Analysis Considerations

Structural analysis considerations are reported to show completeness related to this work [41]. The single finger and the handle Finite Elements Analysis (FEA) were carried out to demonstrate that this system can withstand the applied loads.

1.10.1 Single Finger FEA Analysis

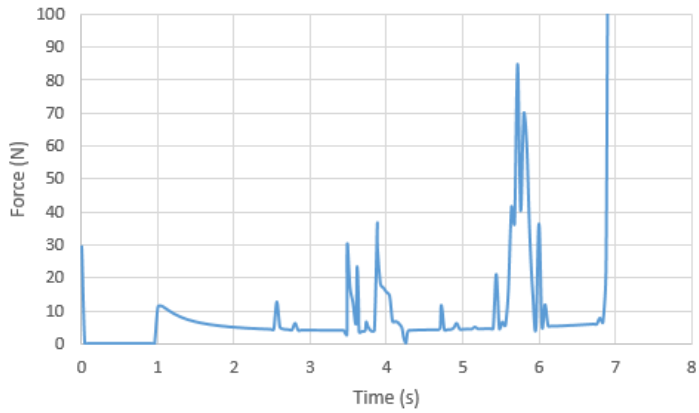

Figure 1.52 Linear actuator force as a function of time for the entire grasping maneuver. 100N force was considered as the worst case scenario with a short duration (<1s).

A single finger FEA analysis was taken into account. Some constraints were defined: the distal and nearest phalanx are considered fixed, the joints were properly described, a force of 100N (see Fig1.52) was applied on the back of top l-structure (see Fig.1.53 pink arrows), and a temperature load was considered on the top surfaces of the l-structures. 100-N force was considered as the worst case scenario with a short duration (<1s).

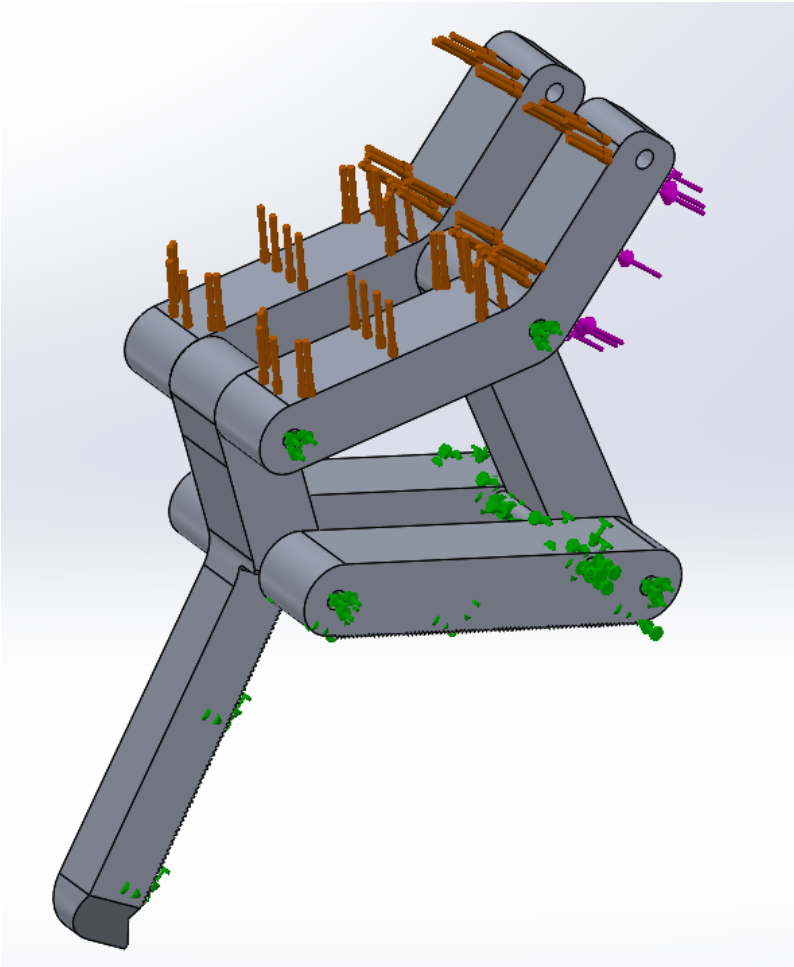

Figure 1.53 Single finger FEA analysis. Some constraints were defined: the distal and nearest phalanx were considered fixed, the joints were properly described, a force of 100N was applied on the back of top l-structure (pink arrows), and a temperature load was considered on the top surfaces of the l-structures.

As results Von Mises stress are reported. Von Mises stress considering only the force acting on the finger are reported in Fig.1.54

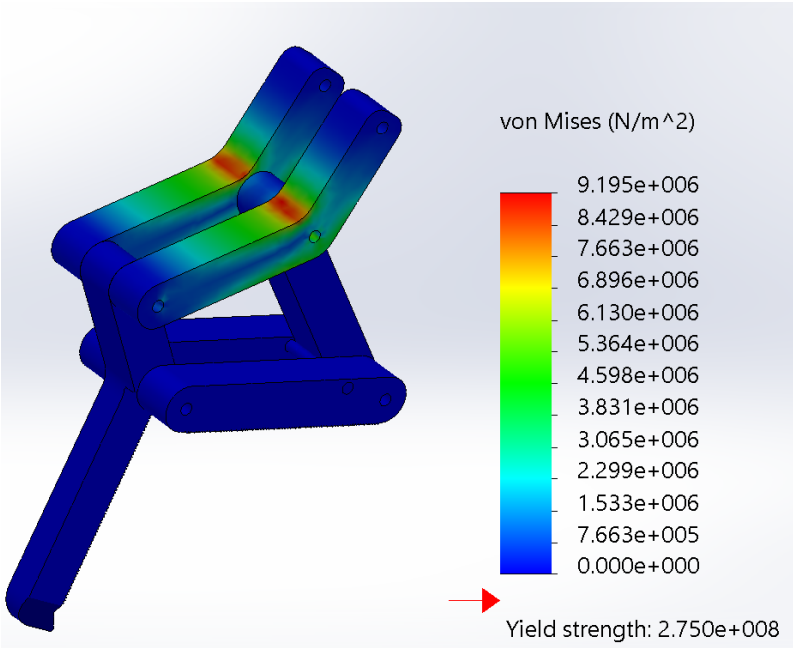

Figure 1.54 Von Mises stress considering only the force acting on the finger.

Von Mises stress considering the force acting on the finger together with a temperature load of -150C are reported in Fig.1.55.

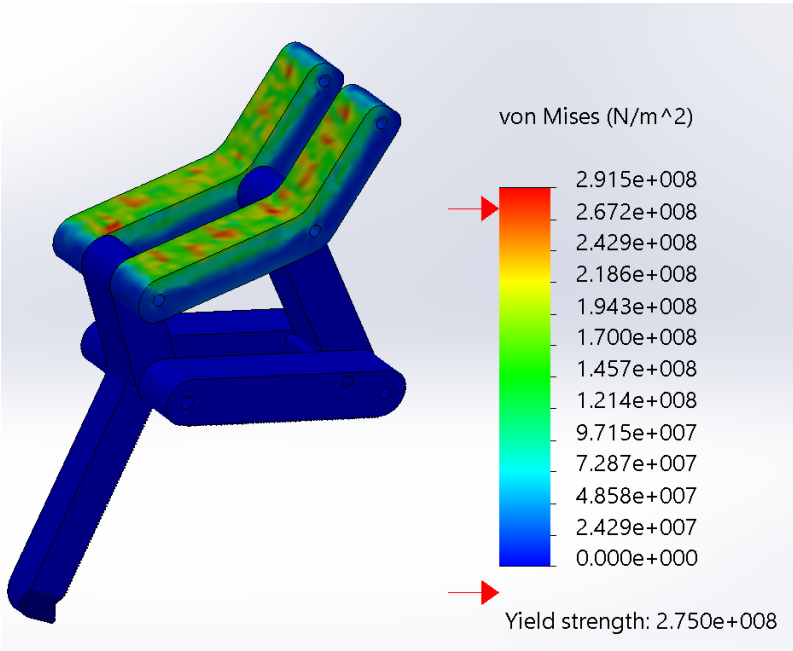

Figure 1.55 Von Mises stress considering the force acting on the finger together with a temperature load of -150C.

Von Mises stress considering the force acting on the finger together with a temperature load of +150C are reported in Fig.1.56.

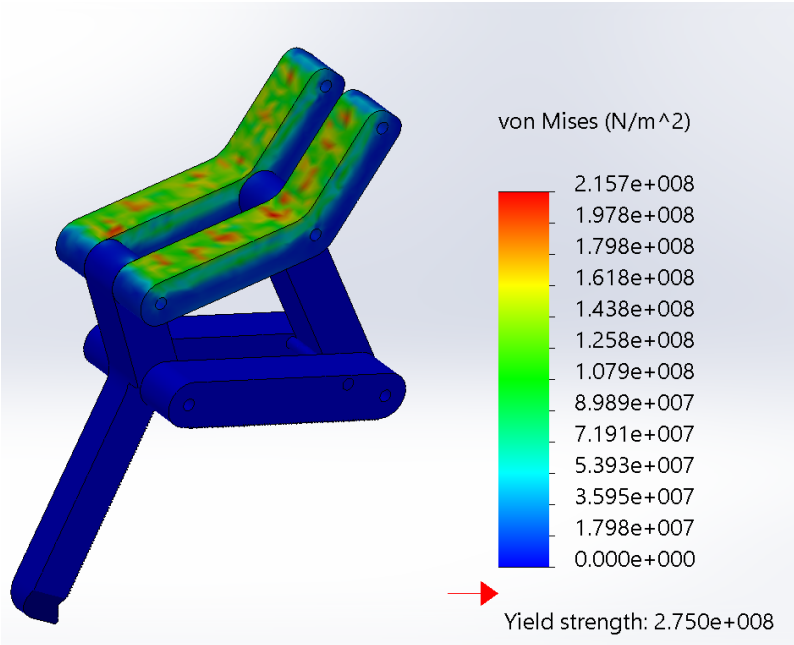

Figure 1.56 Von Mises stress considering the force acting on the finger together with a temperature load of +150C.

There were some areas on the top surfaces of the l-structures where, after having applied a temperature change, the Von Mises stress were higher than the Al-T6061 yield stress value (2.75×10^8N/m^2 see [65]). However, after having performed a section study, it was possible to conclude that these areas are only 0.1mm thick and so they did not affect the whole finger reliability.

1.10.2 Blocking Bar FEA Analysis

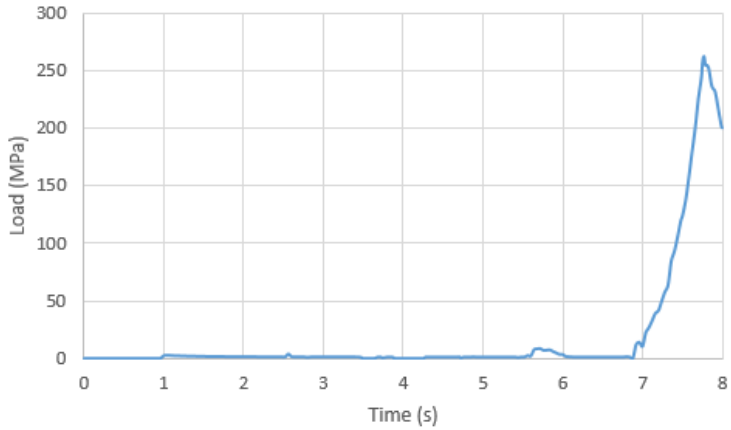

Figure 1.57 Blocking bar compression load as a function of time for the entire grasping maneuver. 300-MPa load was considered as the worst case scenario with a short duration (<1 s).

The blocking bar FEA analysis was taken into account. A finger detail identifying the blocking bar is reported in Fig.1.57. Some constraints were defined: both the nearest phalanx were considered fixed, a uniform pressure of 300MPa was applied on the cylindrical surface of the blocking bar (pink arrows), see Figg.1.58 and 1.59. 300-MPa load was considered as the worst case scenario with a short duration (<1s).

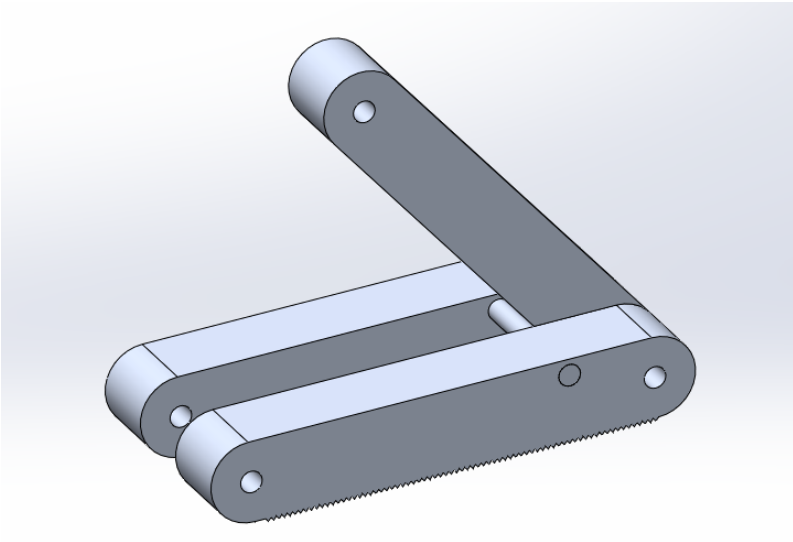

Figure 1.58 Gripper finger detail, from bottom to top: nearest phalanxes, blocking bar and medium beam.

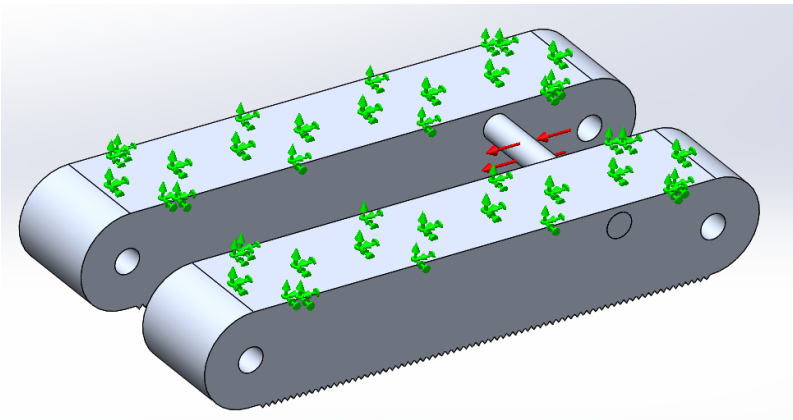

Figure 1.59 Blocking bar FEA analysis. Some constraints were defined: both the nearest phalanx were considered fixed, a uniform pressure of 300MPa was applied on the cylindrical surface of the blocking bar (pink arrows).

Von Mises stress considering only the pressure acting on the blocking bar are reported in Fig.1.60.

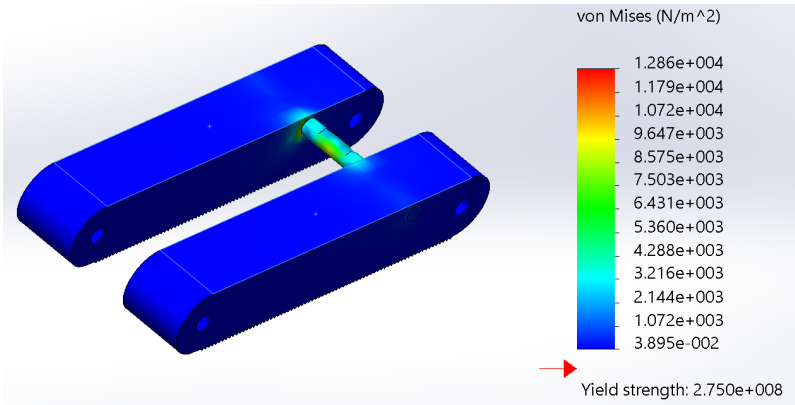

Figure 1.60 Von Mises stress considering only the pressure acting on the blocking bar.

To run a more accurate FEA analysis only the blocking bar structural analysis was taken into account. Some constraints were defined (see Fig.1.61): both the cylindrical faces were considered fixed, a uniform pressure of 300MPa was applied on the cylindrical surface of the blocking bar (orange arrows), and a temperature load was considered (blue arrows).

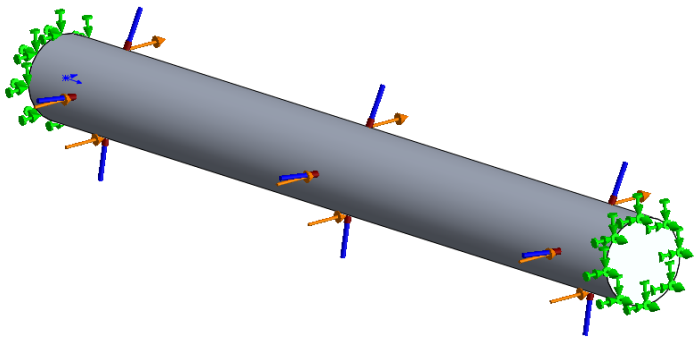

Figure 1.61 Only blocking bar FEA analysis. Some constraints were defined: both the cylindrical faces were considered fixed, a uniform pressure of 300MPa was applied on the cylindrical surface of the blocking bar (orange arrows), and a temperature load was considered (blue arrows).

Von Mises stress considering only the pressure acting on the blocking bar are reported in Fig.1.62.

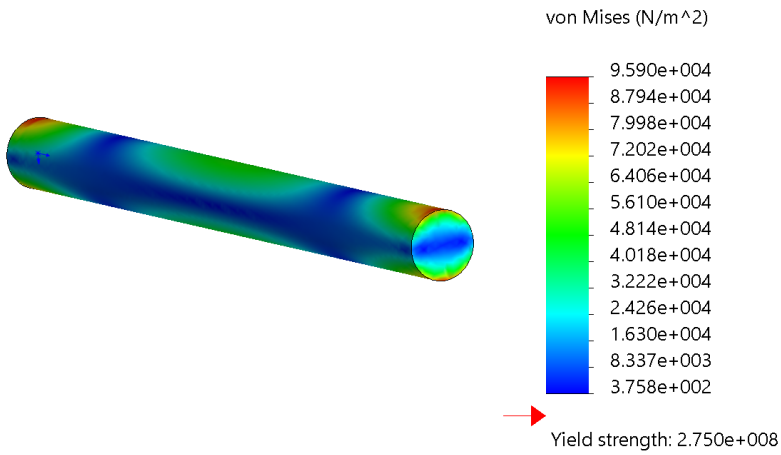

Figure 1.62 Von Mises stress considering only the pressure acting on the blocking bar.

Von Mises stress considering the pressure acting on the blocking bar together with a temperature load of -150C are reported in Fig.1.63.

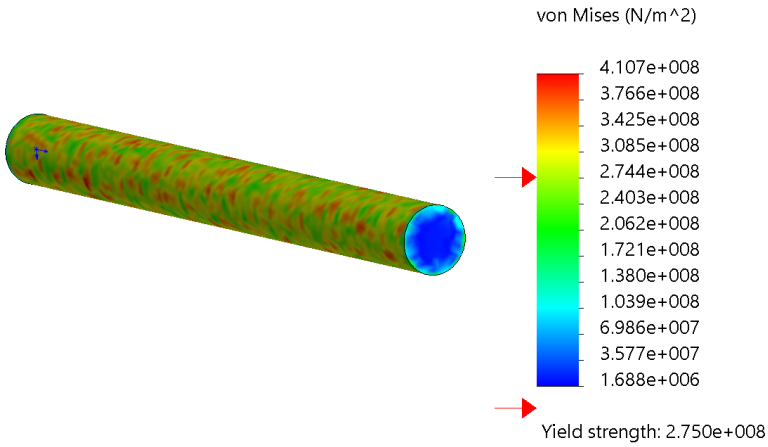

Figure 1.63 Von Mises stress considering the pressure acting on the blocking bar together with a temperature load of -150C.

Von Mises stress considering the pressure acting on the blocking bar together with a temperature load of +150C are reported in Fig.1.64.

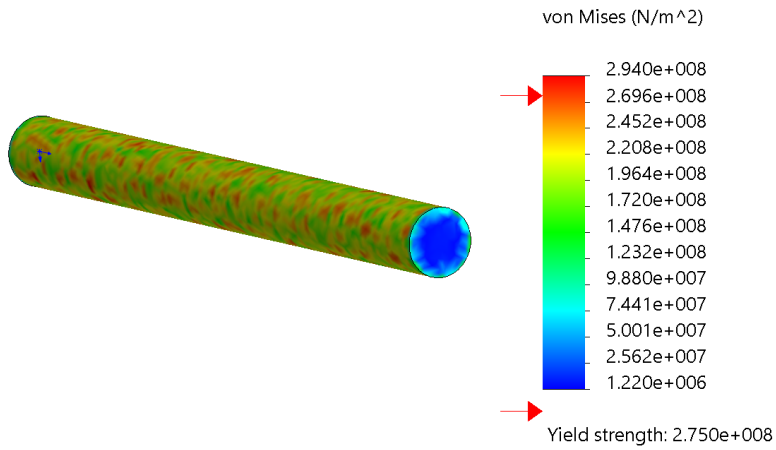

Figure 1.64 Von Mises stress considering the force acting on the finger together with a temperature load of +150C.

There are some areas on the top surfaces of the blocking bar where, after having applied a temperature change, the Von Mises stress were higher than the Al 6061-T6 yield stress value. However, after having performed a section study, it was possible to conclude that these areas were only 0.1mm thick and so they did not affect the whole finger reliability.

1.10.3 Handle FEA Analysis

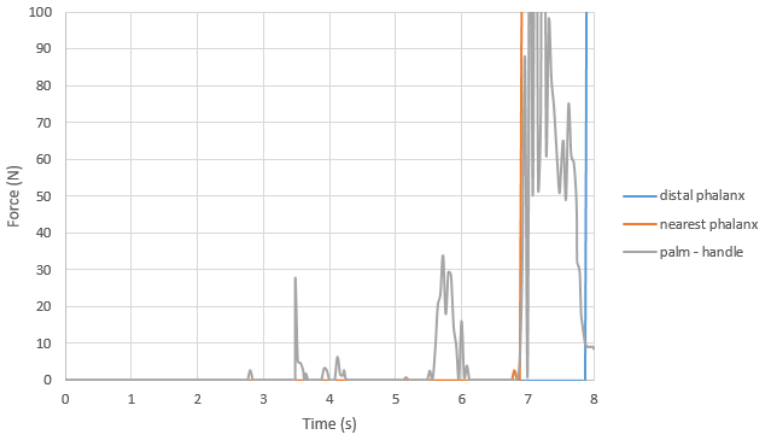

Figure 1.65 Gripper palm-handle contact force as a function of time for the entire grasping maneuver. 100-N force was considered as the worst case scenario with a short duration (<1s). Blue line represents the contact force between the handle and the distal phalanx, orange line represents the contact force between the handle and the nearest phalanx, gray line represents the contact force between the handle and the gripper palm. After the grasping phase the contact force sets to ∼8.5N.

The handle FEA analysis was taken into account. Some constraints were defined (see Fig.1.66): the surface attached to the payload was considered fixed (green arrows), a force of 100N (see Fig.1.65) was applied on the external surfaces and on the internal surface (pink arrows), and a temperature load was considered on the whole handle body. 100-N force was considered as the worst case scenario with a short duration (<1s).

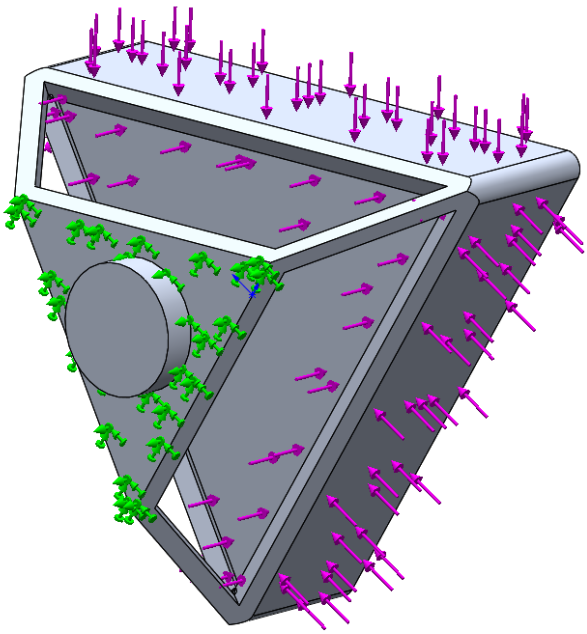

Figure 1.66 Handle FEA analysis. Some constraints were defined: the surface attached to the payload was considered fixed (green arrows), a force of 100N was applied on the external surfaces and on the internal surface (pink arrows), and a temperature load was considered on the whole handle body.

Von Mises stress considering only the force acting on the external and internal surfaces are reported in Fig.1.67.

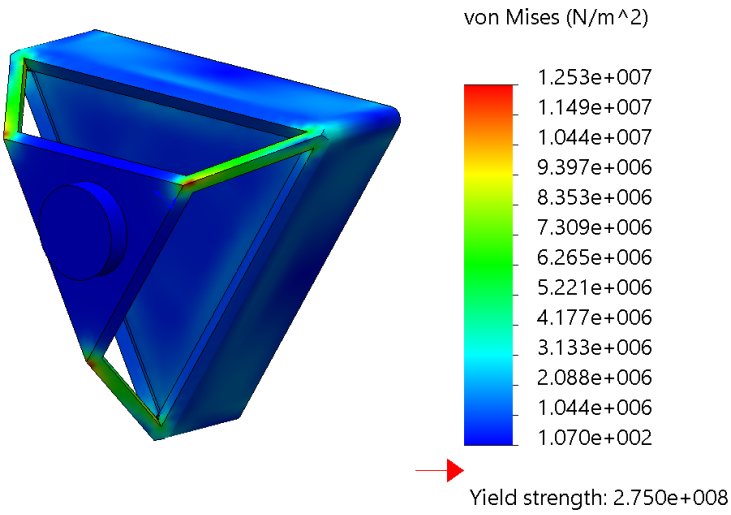

Figure 1.67 Von Mises stress considering only the force acting on the external and internal surfaces.

Von Mises stress considering the force acting on the external and internal surfaces. together with a temperature load of -150C are reported in Fig.1.68.

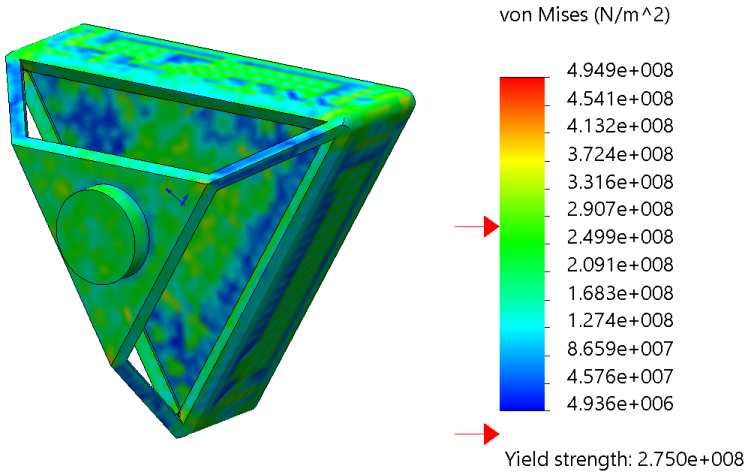

Figure 1.68 Von Mises stress considering the force acting on the external and internal surfaces. together with a temperature load of -150C.

For completeness and to assure that this structure will bear the actual loads, due to the fact that large areas of the handle experience large stress, a factor of safety (FOS) study was carried on. FOS represents a factor applied to the limit load to obtain the design load for the purpose of decreasing the chance of failure [65]. FOS considering the force acting on the external and internal surfaces together with a temperature load of -150C are reported in Fig.1.69.

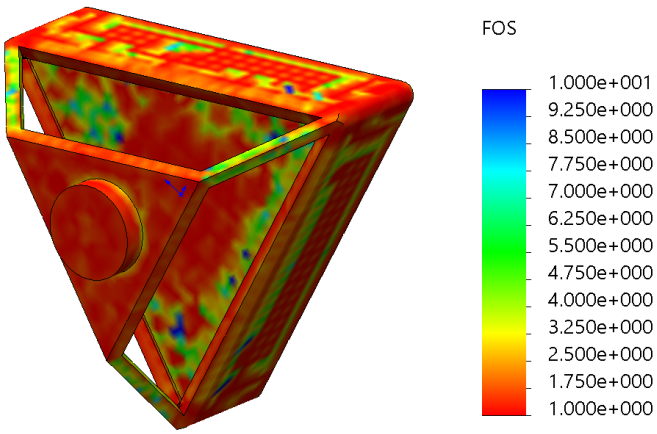

Figure 1.69 Factor of safety (FOS) considering the force acting on the external and internal surfaces together with a temperature load of -150C.

There were some areas on the top surfaces of the blocking bar where, after having applied a temperature change, the FOS is ∼1. These areas were not the most critical ones such as the connecting beams between the handle palm and the handle-payload attachment, where the FOS is ∼5. Moreover, after having performed a section study, it was possible to conclude that these areas were only 0.1mm thick and so they did not affect the whole handle reliability.

Von Mises stress considering the force acting on the external and internal surfaces. together with a temperature load of +150C are reported in Fig.1.70.

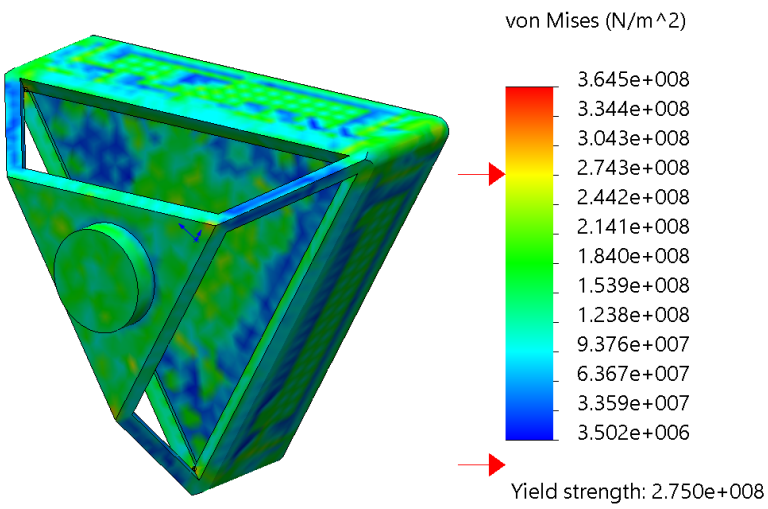

Figure 1.70 Von Mises stress considering the force acting on the external and internal surfaces. together with a temperature load of +150C.

Also in this case, FOS considering the force acting on the external and internal surfaces. together with a temperature load of +150C are reported in Fig.1.71.

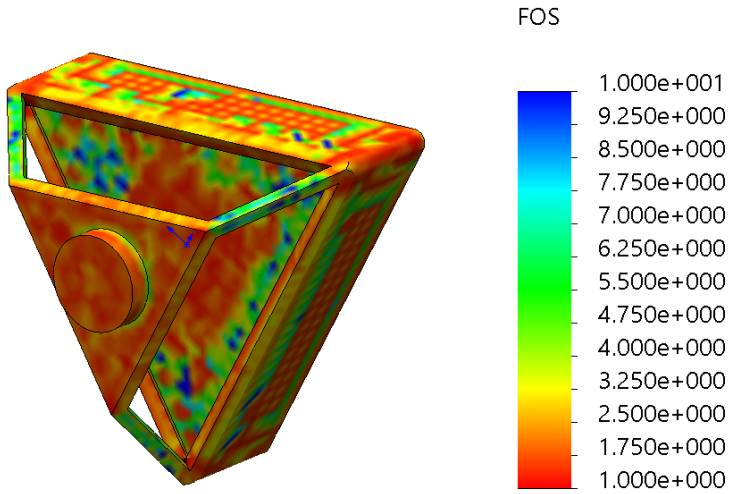

Figure 1.71 Factor of safety (FOS) considering the force acting on the external and internal surfaces. together with a temperature load of +150C.

Also in this case, there were some areas on the top surfaces of the blocking bar where, after having applied a temperature change, the FOS is ∼1. These areas were not the most critical ones such as the connecting beams between the handle palm and the handle-payload attachment, where the FOS was ∼5. Moreover, after having performed a section study, it was possible to conclude that these areas were only 0.1mm thick and so they did not affect the whole handle reliability.

1.11 Acknowledgments

I would like to acknowledge Mrs. Simona Ferraris, Ms. Genny Scalise, Mr. Pasquale Pellegrino, and all the Thales Alenia Space in Turin personnel for their support and availability such as their professionalism in working together.

This research was carried out at Politecnico di Torino, under SAPERE and STRONG projects within a collaboration with Thales Alenia Space in Turin and Applied Mechatronic Engineering and Technologies. These projects are under a contract with the Italian Ministry of Education, Research and University. Copyright 2018. All rights reserved.

Chapter 2

A Potential Mars Sample Return: Science and Technology

This chapter deals with the reasons why the exploration of Mars and the success of a potential Mars Sample Return (MSR) mission architecture is the scientific key to try to answer to the questions related to the origin of life.

2.1 Current Knowledge of Mars

As reported in [11] Mars is a unique place in solar system exploration: it holds keys to many compelling planetary science questions and it is accessible enough to allow rapid, systematic exploration to address and answer these questions. The scientific objectives for Mars center on understanding the evolution of the planet as a system, focusing on the interplay between the tectonic and climatic cycles and the implications for habitability and life.

Mars presents an excellent opportunity to investigate the major question of habitability and life in the solar system. Conditions on Mars, particularly early in its history, are thought to have been conducive to formation of prebiotic compounds and potentially to the origin and continued evolution of life. Mars has also experienced major changes in surface conditions, driven by its thermal evolution, orbital evolution, and by changes in solar input and greenhouse gases, that have produced a wide range of environments. Of critical significance is the excellent preservation of the geologic record of early Mars, and thus the

potential for evidence of prebiotic and biotic processes and how they relate to evolution of the planet as a system. This crucial early period is when life began on Earth, an epoch largely lost on our own planet. Thus, Mars provides the opportunity to address questions about how and whether life arose elsewhere in the solar system, about planetary evolution processes, and about the potential coupling between biological and geological history. Progress on these questions, important to both the science community and the public, could be made more readily at Mars than anywhere else in the solar system.

2.2 Exploration of Mars

The idea that humans could reach Mars is quite old and was advocated by many pioneers of spaceflight. Apart from fictional descriptions, sometimes bypassing completely the problem of getting there, and of pioneristic work dealing with the general aspect of the problem, the first detailed study of a human Mars mission was done by Wernher von Braun who published in 1949 *Das Mars Projekt*, a technically sound project, demonstrating that it was possible to reach Mars with a technology predictable for a not too far future. This project, although technologically consistent, did not take in due account the relevant costs and, as perhaps unavoidably with a first attempt to put the problem in a rational way, was not sustainable. Since then many projects were published by space agencies, individual researchers and companies from many different countries, but after 65 years human Mars exploration seems to be still a goal far in the future [13]. The International Space Exploration Coordination Group (ISECG) produced a Global Exploration Roadmap (GER) in which three destinations for exploration missions are contemplated: the Moon, the cislunar space and the asteroids, and Mars. While in the roadmap the goal of human Mars exploration is left as a goal to be achieved in a more distant future, several stepping stones are stated, among which there is a strong program of Mars robotic exploration.

The spacecraft exploration of Mars began in 1965 with an exploration strategy of flybys, followed by orbiters, landers, and rovers with kilometers of mobility. This systematic investigation has produced a detailed knowledge of the planet's character, including global measurements of topography, geologic

structure and processes, surface mineralogy and elemental composition, the near-surface distribution of water, the intrinsic and remnant magnetic field, gravity field and crustal structure, and the atmospheric composition and time-varying state, see Fig.2.1. The orbital surveys framed the initial hypotheses and questions and identified the locations where in situ exploration could test them. The surface missions the Viking landers, Pathfinder, Phoenix, and the Mars Exploration Rovers have acquired detailed information on surface morphology, stratigraphy, mineralogy, composition, and atmosphere-surface dynamics and confirmed what was strongly suspected from orbital data: Mars has a long-lasting and varied history during which water has played a major role [14].

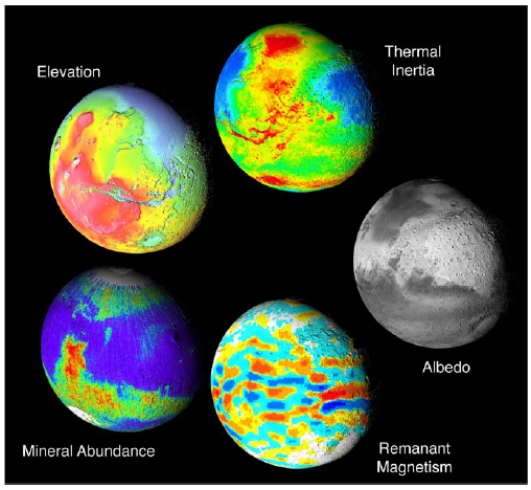

Figure 2.1 Examples of globally data sets highlight major accomplishments from multiple recent missions [14].

A new phase of exploration began with the Mars Express and Mars Reconnaissance (MRO) orbiters, which carry improved instrumentation to pursue the questions raised in the earlier cycles of exploration. Among the discoveries, see Tab.2.1, is the realization that Mars is a remarkably diverse planet with a wide range of aqueous environments, see Fig.2.2. The role of water and the habitability of the ancient environment has been further investigated by the Mars Science Laboratory (MSL), launched in 2011, which carried the most advanced suite of instrumentation ever landed on the surface of a planetary object. The program of Mars exploration over the past 20 years has provided a framework for systematic exploration, allowing hypotheses to be formulated and

tested and new discoveries to be rapidly and effectively pursued with follow-up observations. In addition, the program has produced missions that support each other both scientifically and through infrastructure, with orbital reconnaissance and site selection, data relay, and critical event coverage significantly enhancing the quality of the in situ missions [15].

Major Accomplishment	**Mission and/or Technique**
Provided global mapping of surface composition, topography, remanent magnetism, atmospheric state, crustal structure	Mars Global Surveyor, Odyssey, Mars Express, Mars Reconnaissance Orbiter
Mapped the current distribution of near-surface ice and the morphologic effects of recent liquid water associated with near-surface ice deposits	Odyssey
Confirmed the significance of water through mineralogic measurements of surface rocks and soils	Mars Exploration Rovers, Phoenix
Demonstrated the diversity of aqueous environments, with major differences in aqueous chemistry, conditions, and processes	Mars Express, Odyssey, Mars Reconnaissance Orbiter, Mars Exploration Rovers
Mapped the three-dimensional temperature, water vapor, and aerosol properties of the atmosphere through time; found possible evidence of the presence of methane	Mars Global Surveyor, Odyssey, Mars Express, Mars Reconnaissance Orbiter and ground-based telescopes
Assessing the habitability of geochemical environments identified from orbit where water-rock interactions have occurred and preservation of biosignatures is possible. The sky crane precision landing system, long-term surface operations, and long-range mobility. Capability for sample acquisition and in situ sample analysis	Mars Science Laboratory

Table 2.1 Major Accomplishments of Studies of Mars in the Past Decade [15].

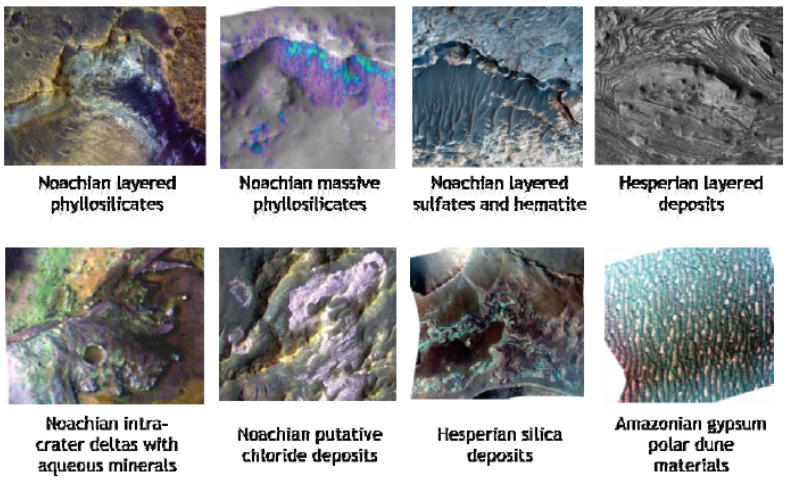

Figure 2.2 Examples of the diversity of environments and their mineralogy and morphology [66].

Finally, this program has allowed the Mars science community to construct a logical series of missions that are each modest in scope and systematically advance the scientific understanding of Mars. Over the past decade the Mars science community, see [16] and [67], has formulated four major science themes that pertain to understanding Mars as a planetary system:

- Determine If Life Ever Arose on Mars - Does life exist, or did it exist, elsewhere in the universe? This is perhaps one of the most compelling questions in science, and Mars is the most promising and accessible place to begin the search. If successful it would be important to know where and for how long life evolved, and how the development of life relates to the planet's evolution.

- Understand the Processes and History of Climate - Climate and atmospheric studies remain a major objective of Mars exploration. They are key to understanding how the planet may have been suited for life and how major parts of the surface have been shaped. In addition, studying Mars's atmosphere and the evolution of its climate at various timescales is directly relevant for our understanding of the past, present, and future climate of Earth. Finally, characterizing Mars's environment is also necessary for the safe implementation of future robotic and human spacecraft missions.

- Determine the Evolution of the Surface and Interior - Insight into the composition, structure, and history of Mars is fundamental to understanding the solar system as a whole, as well as providing context for the history and processes of our own planet. Geological and geophysical investigations would shed light on critical environmental aspects such as heat flow, loss of a global magnetic field, pathways of water-rock interaction, and sources and cycling of volatiles including water and carbon species (e.g., carbon dioxide and hydrocarbons). In contrast to Earth, Mars appears to have a rich and accessible geological record of the igneous, sedimentary, and cratering processes that occurred during the early solar system history. Geophysical measurements of Mars's interior structure and heat flow, together with detailed mineralogic, elemental, and isotopic data from a diverse suite of martian geological samples, are essential for determining the chemical and physical processes that have operated through time on this evolving, Earth-like planet.

- Prepare for human exploration - This goal encompasses the use of robotic flight missions (to Mars) to prepare for potential human missions (or sets of missions) to the Martian system. In broadest context, Mars is a partially unknown place, and partial or missing knowledge creates risk to the design and implementation of a human mission. Many important risks could be brought down by means of acquiring precursor information, which allows for better-informed architectural, design, and operational decisions. In the same way that the Lunar Orbiters, Ranger, and Surveyor landers paved the way for the Apollo Moon landings, the robotic missions of the Mars Exploration Program could help chart the course for potential future human exploration of Mars. It is also worth noting that preparing for the human exploration of Mars would involve precursor activities in several venues other than Mars, including on Earth (e.g., in laboratories, by computer modeling, and from field analogs), in low Earth orbit (including the International Space Station), and probably on nearby celestial objects such as the Moon and asteroids.

From these themes, MEPAG has derived key, overarching science questions that drive future Mars exploration. These include the following:

- What are the nature, ages, and origin of the diverse suite of geologic units and aqueous environments evident from orbital and landed data, and were any of them habitable?
- How, when, and why did environments vary through Mars history, and did any of them host life or its precursors?
- What are the inventory and dynamics of carbon compounds and trace gases in the atmosphere and surface, and what are the processes that govern their origin, evolution, and fate?
- What is the present climate and how has it evolved on time scales of 10 million years, 100 million years, and 1 billion years?
- What are the internal structure and dynamics and how have these evolved over time?
- What is needed to prepare for humankind's first steps on the red planet?

The next decades hold great promises for Mars exploration to address in detail the questions of habitability and the potential origin and evolution of life on Mars. The major focus of the next decade would be to initiate a Mars sample-return campaign, beginning with a rover mission to collect and cache samples, followed by missions to retrieve these samples and return them to Earth. It is widely accepted within the Mars science community that analysis of carefully selected samples from sites that have the highest scientific potential that are returned to Earth for intense study using advanced analytical techniques would provide the highest scientific return on investment for understanding Mars as a planetary system. These samples could be collected and returned to Earth in a sequence of three missions that collect the samples, place them into Mars orbit, and return them to Earth. This modular approach is scientifically, technically, and programmatically robust, with each mission possessing a small number of discrete engineering challenges, and resiliency against failure of the different elements. This modular approach also allows the sample return campaign to proceed at a pace determined by prioritization within the solar system objectives and by available funding.

2.3 Determine if life ever arose on Mars

If life was there the resources that support or supported it have to be understood, see [16] and [67]. If life never existed yet conditions appear to have been suitable for formation and/or maintenance of life, a focus would then be to understand why life did not originate. A comprehensive conclusion about the question of life on Mars would necessitate understanding the planetary evolution of Mars and whether Mars is or could have been habitable, using multi-disciplinary scientific exploration at scales ranging from planetary to microscopic. The strategy adopted to pursue this goal has two sequential science steps: assess the habitability of Mars on an environment-by-environment basis using global remote sensing observations; and then test for prebiotic processes, past life, or present life in environments that could be shown to have high habitability potential. A critical means to achieve both objectives is to characterize martian carbon chemistry and carbon cycling. Therefore, the committee's specific objectives to pursue the life goal are to as follows:

- Assess the past and present habitability of Mars;
- Assess whether life is or was present on Mars in its geochemical context;
- Characterize carbon cycling and prebiotic chemistry.

2.4 Importance of Mars Sample Return

For the past three decades, the scientific community has consistently advocated the return of geological samples from Mars. Summaries of the literature on this topic appear in the extensive writings of the National Research Council (NRC) [68], several major recent reports by MEPAG, [16] and [67], and a significant recent contribution by the International Mars Exploration Working Group. Numerous white papers submitted to the NRC Decadal Survey indicated substantial community support via signatories and addressed the importance and significance of Mars sample return as the keystone of future Mars exploration. The Mars sample return would have significantly high science return and a much higher science-to-dollar ratio.

2.4.1 Sample Return is the Next Step

The analysis of carefully selected and well documented samples from a well characterized site would provide the highest scientific return on investment for understanding Mars in the context of solar system evolution and addressing the question of whether Mars has ever been an abode of life. The purpose and context of a Mars sample return has changed significantly since the early concepts that focused solely on reconnaissance. At that time the key questions centered on bulk planetary geochemistry, petrology, and geochronology, for which a wide range of sample types would be acceptable. Today the emphasis is on well characterized and carefully selected rocks, with the recognition of the critical importance of sedimentary rocks that provide clues to aqueous and environmental conditions. While it is widely accepted that we have samples of Mars on Earth in the form of the Shergottiti, Nakhliti and Chassigniti meteorites, they are not representative of the diversity of Mars. They are all igneous in origin, whereas recent observations have shown the occurrence of chemical sedimentary rocks of aqueous origin as well as igneous, metamorphic, and sedimentary rocks that have been aqueously altered. It is these aqueous and altered materials that would provide the opportunity to study aqueous environments and potential prebiotic chemistry. Two approaches exist to study martian materials: in situ measurements or through returned samples. Returning samples allows for the analysis of elemental, mineralogic, petrologic, isotopic, and textural information using state-of-the-art instrumentation in multiple laboratories. In addition, it allows for the application of different analytical approaches using technologies that advance over a decade or more, and, most importantly, the opportunity to conduct follow-up experiments that are essential to validate and corroborate the results. On an in situ mission, only an extremely limited set of experiments could be performed because of the difficulty of miniaturizing state-of-the-art analytical tools within the limited payload capacity of a lander or rover. In addition, these discrete experiments must be selected years in advance of the mission's launch. Finally, calibrating and validating the results of sophisticated experiments could be challenging in a lab, and would be significantly more difficult when done remotely. The Viking and the ALH84001 martian meteorite experiences underscore the differences in these approaches. Discoveries by MSL could provide additional justification for sample return, but are unlikely to alter the basic architecture of sample return,

in which the primary system variables such as the sample site and the samples that are collected are not constrained in the proposed architecture. Similarly, the lack of major new discoveries by MSL would not impact the importance of getting samples back to Earth, and may well increase the importance of collecting and studying samples in terrestrial labs where a much broader suite of measurements could be obtained. Experience based on previous studies (e.g., of meteorites, the Moon, cometary dust, and the solar wind) strongly supports the importance of sample analysis. Such a diversity of techniques, analysis over time, improvements in sensitivity, and new approaches available in terrestrial labs are expected to revolutionize our understanding of Mars in ways that simply could not be done in situ or by remote sensing. For more information refer to [69] - [82].

Site Selection and Context

The information needed to select a sample return site that would address high-priority science objectives has been, or could be, acquired with current assets. Mars is a remarkably diverse planet with a wide range of aqueous environments preserved in its rock record. As a result of two decades of orbital and in situ exploration of Mars, a large number of excellent candidate sample return sites, where water played a major role in the surface evolution, have already been identified. significantly, the geologic setting of these sites as identified through mineralogic and stratigraphic mapping indicate that there were major differences in water chemistry and temperature, weathering processes, and sediment transport and deposition processes across Mars, providing a diversity of environments from which to collect samples. The known sites also contain diverse sedimentary and igneous terrains within the roving range of existing spacecraft. The site would be selected on the basis of compelling evidence in the orbital data for aqueous processes and a geologic context for the environment (e.g., fluvial, lacustrine, or hydrothermal). The sample collection rover must have the necessary mobility and in situ capability to collect a diverse suite of samples based on stratigraphy, mineralogy, composition, and texture [83].

Sample Criteria

Selecting and preserving high quality samples is essential to the success of the sample return effort. MEPAG, [16] and [67], identified 11 scientific objectives for MSR and specified the minimum criteria for the sample to meet these objectives. The collection of Mars samples would be most valuable if they are collected as sample suites chosen to represent the diverse products of various planetary processes (particularly aqueous processes), and addressing the scientific objectives for MSR would require multiple sample suites. A full program of science investigations is expected to require samples of >8g for bedrock, loose rocks and finer-grained regolith and 2g to support biohazard testing, each for an optimal size of 10g [84]. Textural studies of some rock types might require one or more larger samples of ∼20g. The number of samples needed to address the MSR scientific objectives effectively is 35 (28 rock, 4 regolith, 1 dust, 2 gas). In order to retain scientific value, returned samples must be fully isolated and sealed from the martian atmosphere, each sample must be linked uniquely to its documented field context, and rocks should be protected against fragmentation during transport. The encapsulation of at least some samples must retain any released volatile components [84].

Technical Implementation and Feasibility

A three-element, step-by-step sample return campaign would reduce scientific, technical and cost risks, see [85]. It builds on technologies developed over the last decade of Mars exploration, though major technical challenges remain that must be addressed in a technology development effort that would be an integral part of the sample return campaign. The proposed strategy would conduct sample return as a campaign with three separate steps:

1. A rover, the Mars 2020 rover, followed by;
2. A sample return lander that would include a rover to fetch the sample cache and an ascent vehicle to loft it into orbit or a Solar / Radioisotope Thermoelectric Generator (RTG) mobile MAV rover;
3. A rendezvous and return by a sample return orbiter.

This campaign would be scientifically robust, with the flexibility to return to a previously visited site (e.g., if motivated by an MSL discovery), go to a new site, or fly a second rover if the first mission was unsuccessful for any reason. It would also be technically and programmatically robust, with a modular approach and multiple tubes left on the surface by to recover from a failure of the previous elements without requiring a reflight of the rover. The Mars Exploration Program has made significant strides in developing the technologies needed for this multi-element sample return scenario. In particular:

- Mars Pathfinder and the Mars Exploration Rovers (MER) have demonstrated surface mobility, and MER has demonstrated much of the basic instrumentation needed to select high-priority samples.
- MER and Phoenix have provided valuable experience in sample handling and surface preparations; MSL has gone significantly further.
- The MSL Sky Crane entry, descent, and landing system design supported MSR. It could deploy a rover and could accommodate the next mission with a fetch rover and Mars Ascent Vehicle.
- Technologies that could be adapted to orbital rendezvous and sample capture have been demonstrated in Earth orbit.
- Sample-return protocols and Earth-return entry encapsulation have been validated by the Stardust and Genesis missions.

Critical technologies still need to be developed [86]. These include sample collection and handling, the Mars Ascent Vehicle, orbital acquisition, and back planetary protection. The MAV, in particular, is a system with significant development risk, pointing to the need for an early start to perform trade studies, retire technology risks, and develop and flight-test a flight-like engineering unit in a relevant environment. Key technology elements for the orbiter include autonomously actuated mechanisms for orbital capture; optical sensors; orbital radio beacon; autonomous rendezvous guidance, navigation and control; and ground validation tests. An initial demonstration of this technology has been performed by the Defense Advanced Research Projects Agency's Orbital Express mission, which performed detection and rendezvous in Earth orbit under similar

conditions [87]. The MSR capture-basket concept has been demonstrated on zero-g aircraft flights [88].

2.5 A Potential Mars Sample Return Mission Architecture

2.5.1 Overview

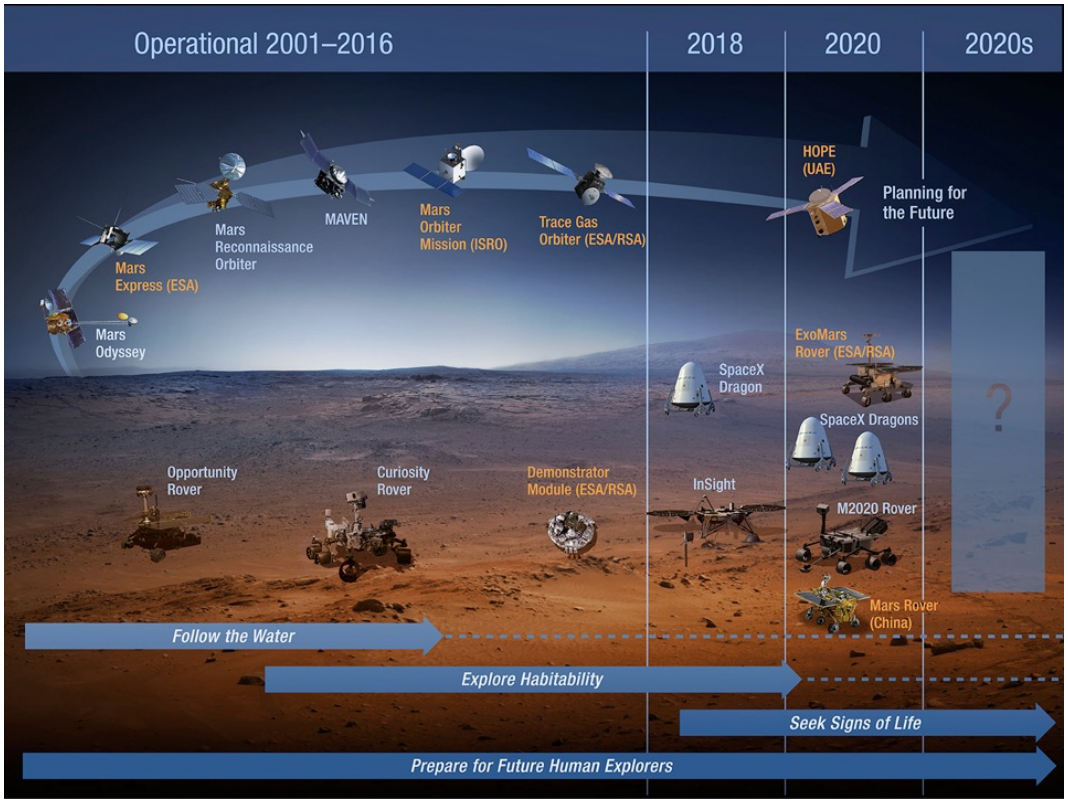

Figure 2.3 Notional MSR architecture, see [89] and [90].

The Orbiter Mission is one of three missions comprising the proposed MSR campaign [91]. Samples would be collected and cached by the first mission, the Mars 2020 rover. A sample cache would be left on the surface of Mars for possible later retrieval. The orbiter would be launched on a medium-class vehicle reaching Mars in ∼9 months. The orbiter would insert into a highly elliptical orbit and aerobrake down to a 500km circular orbit over 6-9 months.

The third mission of the proposed MSR campaign, the lander, which would be the next opportunity to get to Mars. Approximately 6 months after lander arrival, an OS container would be launched by the MAV and an OS would be released in a 500km orbit comparable with the orbiter. This is all part of the Lander Mission concept. The orbiter would provide critical event coverage of the MAV ascent and OS release and capture. Using an optical camera, the orbiter would detect and track an OS. While maneuvering to rendezvous an OS would be captured via a basket, sealed into an outer container, and placed in an EEV. Nominally, within ∼3 months, the orbiter would leave Mars on a non-impact trajectory to Earth, and shortly before arrival, would target Earth, release the EEV, and then divert away from Earth. The EEV would enter and hard land at a recovery site to be determined. This could be Utah Test and Training Range (UTTR). This return trajectory and EDL sequence is similar to the Genesis and Stardust missions, except it would not have a parachute. The Mars Returned Sample Handling (MRSH) facility would then be responsible for safe transport of the EEV to a Sample Receiving Facility (SRF), where the hardware and samples would remain in quarantine until they are determined to be safe (either by their nature or sterilized). A testing protocol would be applied to the samples to determine if they are safe for release. This might take approximately one year and is considered part of the MRSH element. If the samples are determined to be non-hazardous to Earth's biosphere, the samples would be released to a curation facility for safe keeping and distribution to the international science community. While they are not costed in this study, options for conducting science in the SRF are being considered in the event the samples are not deemed safe to release. The orbiter was designed and costed by JPL [92], assuming an in-house build. Alternatively, the orbiter could be built by an industry partner, or provided by an international partner as part of an ongoing international partnership on Mars missions. MRSH would be implemented by NASA with potential help from other agencies for safe transport of the EEV. A new SRF is planned, but augmentation to an existing bio-safety level-4 (BSL-4) lab would be considered.

2.5.2 Technology Maturity

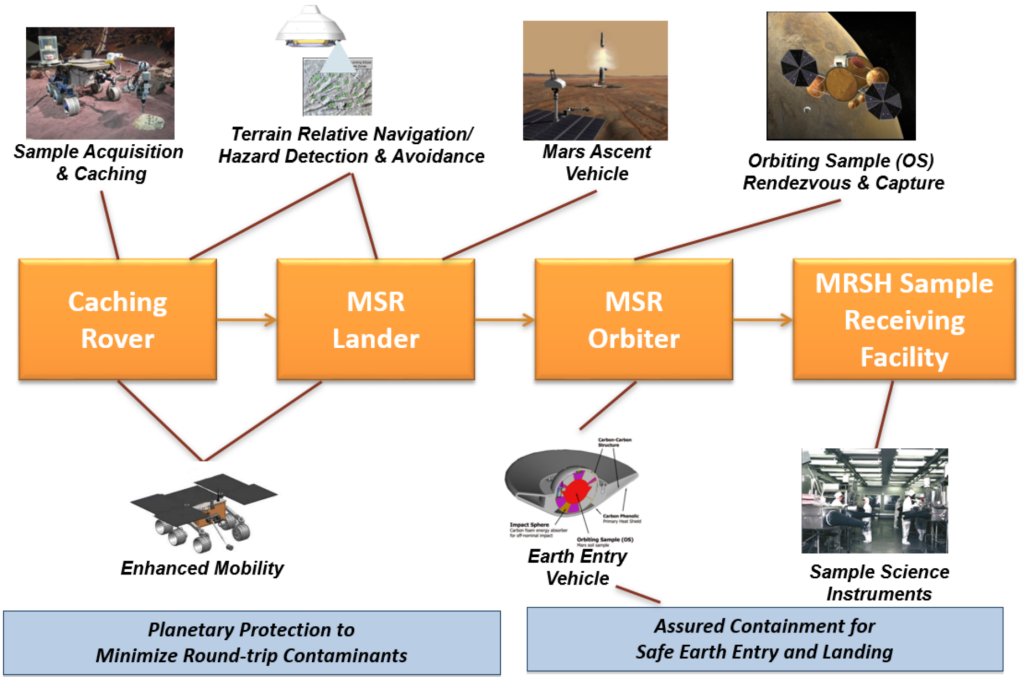

Figure 2.4 Potential MSR Mission: Key Technologies, see [89] and [90].

The Orbiter Mission would use the heritage and experience from a decade of orbiters at Mars. The orbiter bus, per se, would have no new technologies. Rendezvous and capture at Mars would be new, but concerns are mitigated by the experience of the Defense Advanced Research Projects Agency (DARPA) Orbital Express mission [87], which performed detection, rendezvous, and capture in Earth orbit under very similar conditions, and demonstration of a MSR capture basket concept on a zero-g aircraft campaign [88]. While the required rendezvous components have heritage from prior programs, integration as a system would still be required. The capture system would still need further development and integration with the rendezvous system would need to be demonstrated to reach TRL 6 by Preliminary Design Review (PDR). Early development and testing of the EEV concept has taken the design far enough to mitigate concerns. One of the biggest challenge ahead is meeting the planetary protection requirements for a restricted Earth return mission. A probabilistic risk assessment has indicated where development is needed, some of which has been satisfied by the EEV concept. While basic techniques have

been demonstrated in labs, components for sealing, leak detection, and dust mitigation still need to be brought up to TRL 6. In addition, the design of the EEV needs to be refreshed and the system developed to the point that it could be flight tested, if needed, by PDR.

2.5.3 Key Trades

Many trade studies for MSR have been performed over the last decade, e.g., [16], [67], [69], [72], [78]. For the orbiter concept, main trades have included potential use of solar electric propulsion, a rendezvous location (500km circular being a good match for the proposed MAV capability vs deep space or high-altitude), direct entry at Earth (vs returning to the Space Station or Earth orbit, neither of which meets the reliability needed for planetary protection), and passive optical rendezvous sensing (simple, reliable and adequate vs active systems). Orbiter implementation approach details still have open trades, which would be resolved after selection of the implementer (a NASA center, industry, or an international partner). The largest looming trade is staging of the propulsion system, either after Mars Orbit Insertion (MOI), Trans-Earth Injection (TEI), or both. The main trades of MRSH implementation would involve the SRF and curation facility. The SRF might either be a new stand-alone facility or an augmentation to an existing BSL-4 laboratory (budget assumes a new facility). Potential partnership with an international partner might lead to their support to either, or even provision of parallel labs.

2.6 A Potential Mars Sample Return Campaign Technical Overview

The current NASA MSR architecture is being viewed as a campaign, rather than a single mission or flight project. NASA has adopted a four-element campaign architecture [17]:

1. A collecting rover;
2. An MSR Lander to fetch the cache and launch the samples into Mars orbit;

3. An MSR Orbiter for return of samples to Earth;

4. The MRSH components, including the SRF.

Fig.2.5 reports the proposed MSR campaign, while Fig.2.6 reports the MSR elements, functions, and sample states.

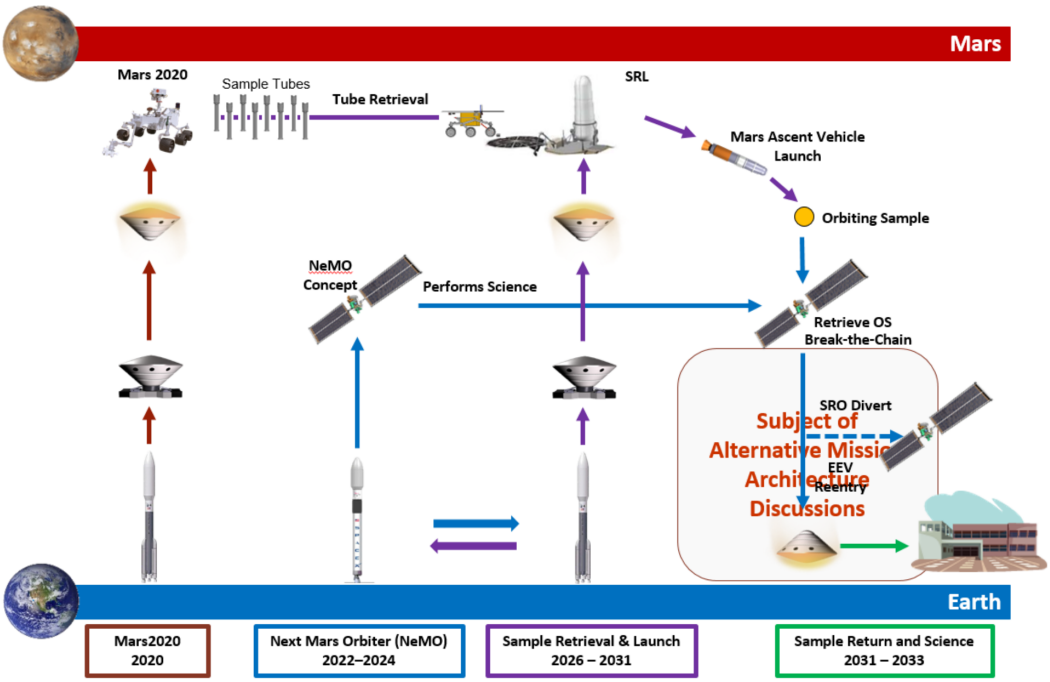

Figure 2.5 Proposed MSR Campaign, see [89] and [90].

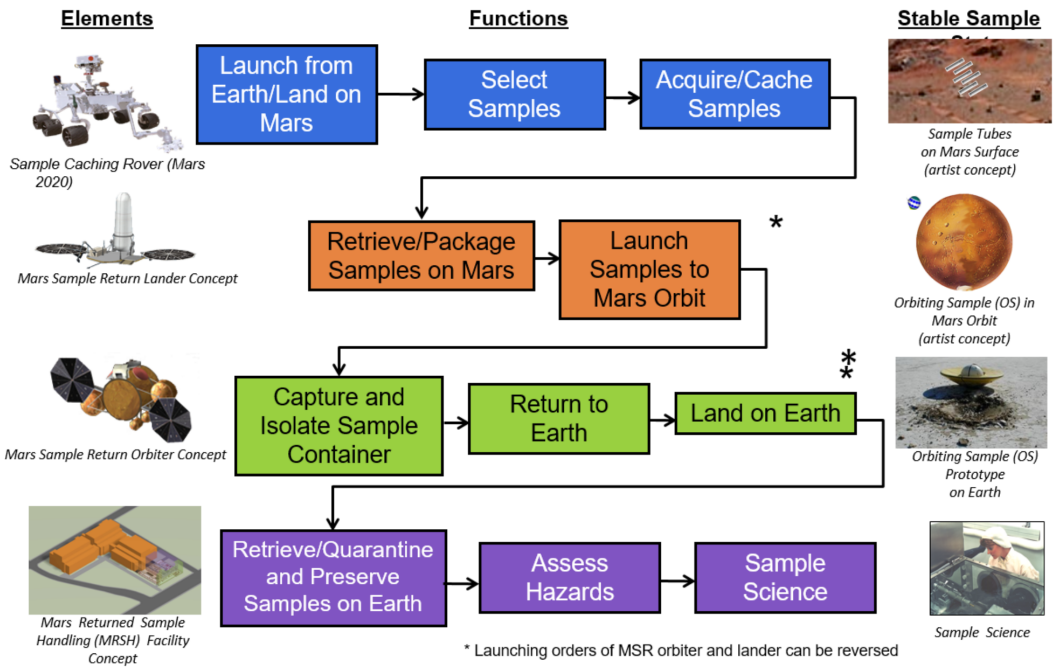

Figure 2.6 Potential MSR Elements, Functions, and Sample States, see [89] and [90].

2.6.1 Mars 2020

Mars 2020 [93] is expected to collect a cache of somewhere between 19 and 37 rock cores. The potential for adding regolith samples is also currently being studied. The mission would be required to last 1.5 Mars years and the NASA rover would be expected to traverse at least 20km. A suite of in situ instruments is planned, which would locate, target, and document the context of samples for possible return to Earth. The sensors would be located on the rover's remote sensing mast (RSM) and at the end of a 5-degree-of-freedom arm with the corer and a rock abrasion tool. The samples would be acquired and encapsulated by the NASA rover's sampling handling system and deposited in the cache. The rover would return to its landing site, if it has gone outside the landing ellipse for sample collection. It would place the cache on the surface of Mars to await retrieval by a fetch rover from the proposed MSR Lander Mission targeted to land at roughly the same landing site some years in the future. The current rover concept would weigh approximately 300kg. As a pioneering step toward how humans on Mars would use the Red Planet's natural resources, the rover would do an experiment to extract oxygen from the

Martian atmosphere. Fig.2.7 comes from computer-assisted-design work on the 2020 rover. The design leverages many successful features of NASA's Curiosity rover, which landed on Mars in 2012, but it adds new science instruments and a sampling system to carry out the new goals for the mission. The European Space Agency (ESA) ExoMars Rover (see [94] and [95]) is expected to access subsurface samples to potentially 2m below the surface and then perform extensive analytical analysis of the samples. Studies are currently underway investigating whether the ESA ExoMars Rover could contribute subsurface samples to the MSR cache. The current rover mass allocation is 300kg.

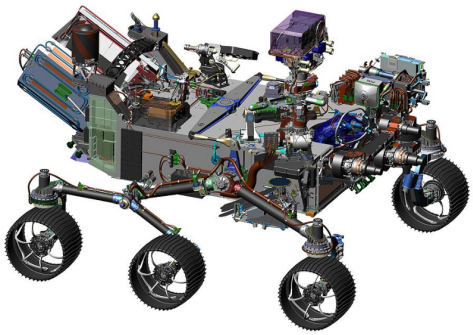

Figure 2.7 NASA's 2020 Mars rover mission would go to a region of Mars thought to have offered favorable conditions long ago for microbial life, and the rover would search for signs of past life there. It would also collect and cache samples for potential return to Earth, for many types of laboratory analysis [96].

The Sample Cache is inserted in a spherical enclosure named Orbiting Sample. The current OS baseline design introduces new concepts and refines upon previous concepts. It consists of two main sub-assemblies: an OS Shell and an OS canister as shown in Fig.2.8. It could accommodate up to 36 soil sample tubes, and two atmospheric sample tanks. It also has accommodations for a Ultra High Frequency (UHF) tracking beacon, which is isolated from the samples but integrated into an OS Shell structure [97]. The current best estimate of the total mass of an OS with beacon hardware and 31 sample tubes is 12kg, and the overall diameter is 28cm.

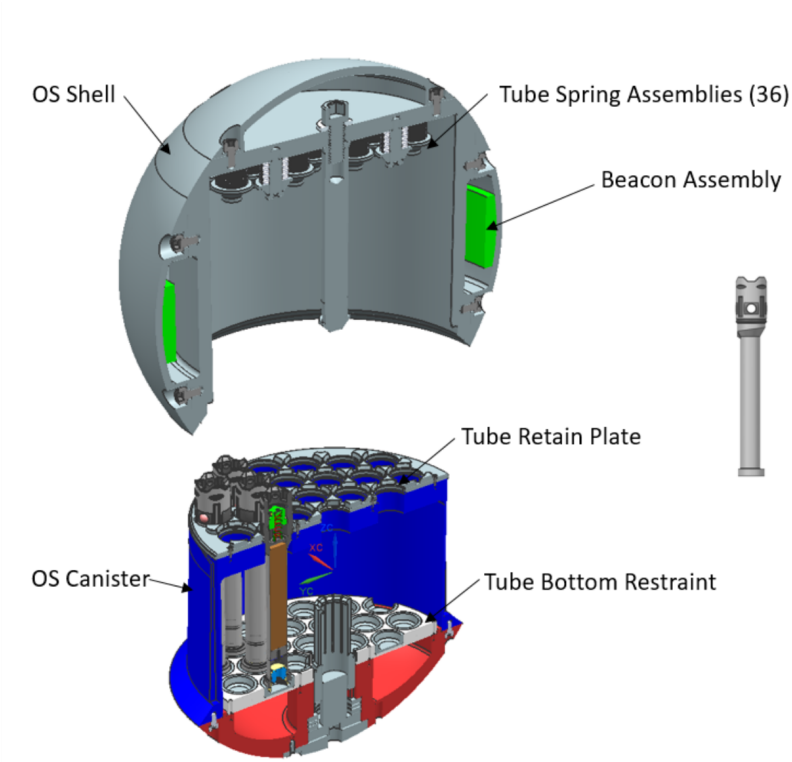

Figure 2.8 OS concept baseline design: exploded view [97].

Fig.2.9 reports the current OS baseline with a detail of the sample tube. An OS would be inserted inside the EEV upside down. Fig.2.10 shows the current OS FEM with close up image of flexure claw structure [97]. It is possible to notice that the sample tubes are upside down with respect to Fig.2.9. The hermetic seal seals the caging plug and the sample inside each tube.

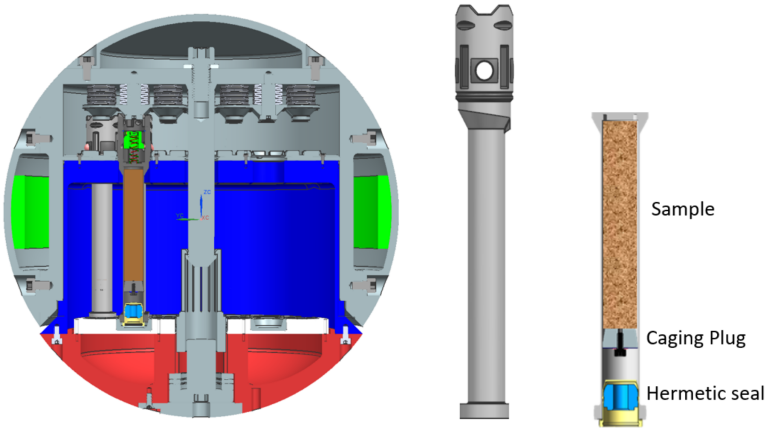

Figure 2.9 OS concept design with a detail of the sample tube [89].

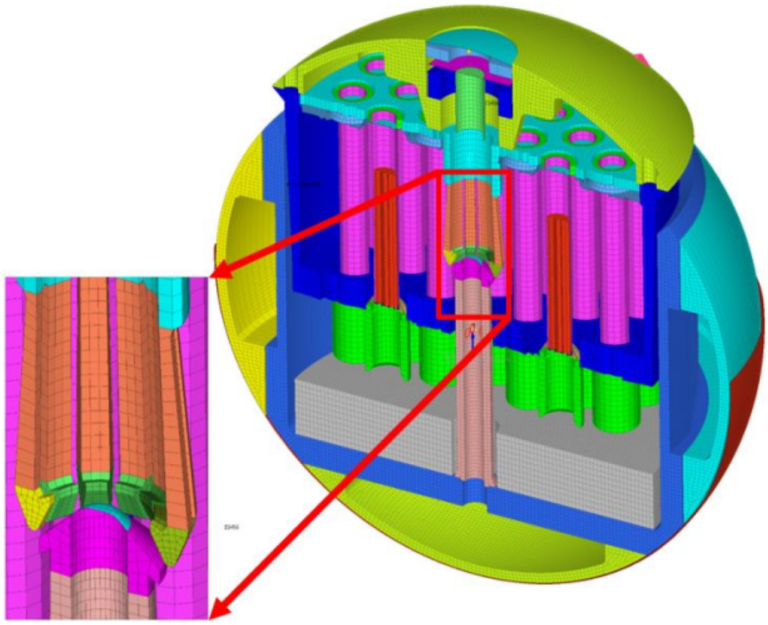

Figure 2.10 OS concept FEM with close up image of flexure claw structure [97].

2.6.2 The Lander Mission

The objective of the proposed MSR Lander Mission would be to retrieve a cache of rock cores left by the NASA Rover Mars 2020, collect local samples of regolith and atmosphere, package them in a container suitable for orbit (an OS), and launch this package into orbit for subsequent capture by the MSR Orbiter

Mission. The proposed MSR Lander would launch from Cape Canaveral on an intermediate-class launch vehicle with a C3 of approximately 12.2. On a Type II trajectory, the lander would arrive at Mars, under the control of a cruise stage. It would then enter directly into the martian atmosphere and achieve touchdown using the MSL-heritage EDL system that would have also been used for the proposed Joint NASA/international partner Mars Mission, see [89] and [90]. The lander, see Fig.2.11, would carry a fetch rover and a MAV and would have some capability to locally collect bulk regolith and atmosphere samples. The proposed NASA Rover Mars 2020 would have deposited sample tubes on the surface for pickup. The MSR Lander would target a landing ellipse containing the cache and would dispatch its single-purpose fetch rover to retrieve and return the cache to the lander. This process is projected to take approximately three months and would involve a round-trip traverse of up to 14km. The fetch rover would be similar in size to the Mars Exploration Rovers (MER), weigh approximately 150kg, and be optimized for efficient driving. The cache pickup concept is via a single degree-of-freedom arm. While the fetch process is underway, regolith samples would be collected via a scoop on the lander's arm. The sample cache, regolith, and atmosphere samples would then be packaged into an OS for transfer to orbit. The MAV would then launch an OS into an 500km circular orbit, releasing an OS with a significant separation velocity. The MSR Orbiter, which would have been in orbit for several years and would have monitored these events, would then assume responsibility for rendezvous and capture of an OS for return to Earth. The baseline MAV is a two-stage solid motor concept, with thrust vector control on the first stage and cold gas attitude steering of the second stage, see Fig.2.12. This concept, as well as others studied in 2002, are described in [98]. This baseline MAV would be stored in a thermal igloo until its launch to keep the propellant from freezing.

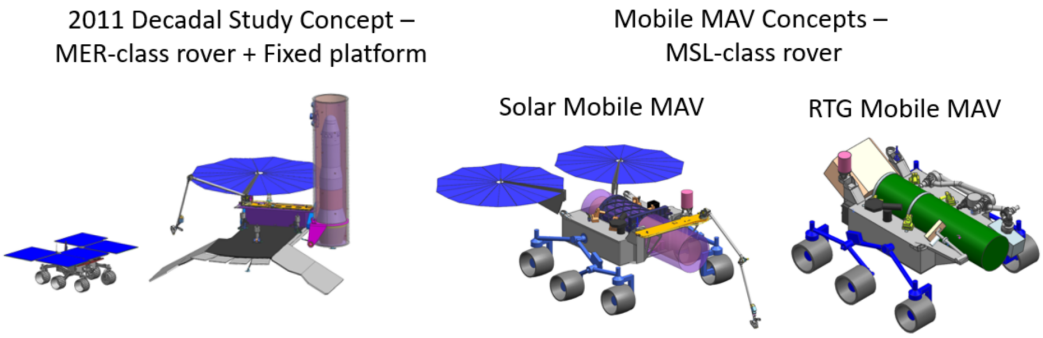

Figure 2.11 Lander System Concepts, see [89] and [90].

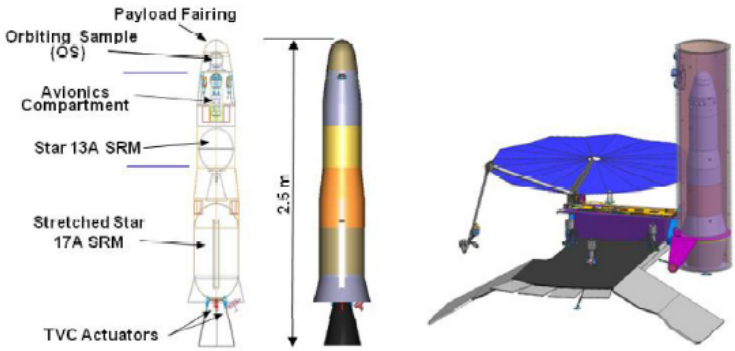

Figure 2.12 Two-Stage Solid Rocket MAV Concept in Proposed Launch Configuration, see [70] and [98].

2.6.3 Flight System

The description is divided into two flight systems: the orbiter bus with a rendezvous / capture subsystem and the notional EEV.

Orbiter

The series of Mars orbiters (Mars Global Surveyor (MGS), Odyssey (ODY), Mars Reconnaissance Orbiter (MRO)) over the last decade lay the foundation for the proposed MSR Orbiter, including bus subsystems, complex operations at Mars, aerobraking (needed to reduce fuel requirements), and telecomm relay for assets on the surface [71]. The primary function of the orbiter would be to detect, rendezvous, and capture an OS, transfer an OS to an EEV, then

target and release the EEV to Earth for entry [91]. This would all need to be performed in a manner consistent with the planetary protection of Earth. Depending on whether there are adequate telecomm assets at Mars for critical event coverage and surface vehicle telecomm relay, the orbiter might need to provide this function, in which case it would have to be early in the mission sequence as baselined. The orbiter would have redundant Electra telecomm relay systems and an X-band Small Deep Space Transponder Earth link with a 2-axis gimbaled 1m high-gain antenna. Electra is the standard programmable radio that has flown on MRO. It has a highly sensitive broadband-receiving mode originally designed for monitoring a potential UHF beacon on an OS, which might be included for backup. Fig.2.13 shows the baseline orbiter concept developed by JPL.

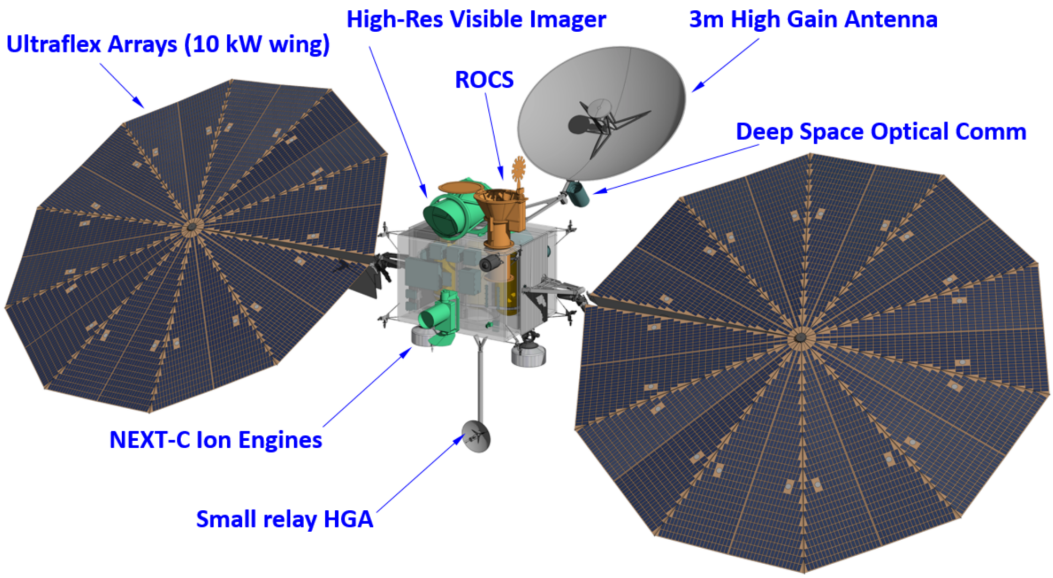

Figure 2.13 Preliminary Orbiter Configuration, see [89] and [90].

Rendezvous and capture of a free-orbiting OS would be performed by the orbiter. An optical navigation (OpNav) camera, demonstrated on MRO would be used to find and track an OS, while a very-low duty cycle UHF beacon on-board an OS could be used as a backup aid if the location is grossly unknown. The camera was designed to detect the orbiting OS from a distance of as far as 10,000km. After the orbiter closes in on an OS in a safe, non-colliding, co-elliptical orbit, the last tens of meters would have to be

performed autonomously. Coupled Reaction Control System (RCS) thrusters would provide fine control of the orbiter state vector for closure on an OS with millimeter/sec granularity. In 2007, DARPA's Orbital Express demonstrated optical tracking and autonomous rendezvous and capture of a passive small satellite in Earth orbit with conditions representative of those that would be needed by MSR at Mars [99]. The process and algorithms confirmed those planned for MSR. Capture would be accomplished via a capture basket as shown in Fig.2.14. The JPL capture basket design concept has been demonstrated on the NASA C-9 zero-g aircraft flight campaign with more than 100 zero-gravity parabolic runs [88]. After capture, an OS would be transferred to the EEV for return to Earth. In that process, an OS could be sealed in a brazed container, in a way that the transfer to the EEV would be Mars-contaminant free. The capture and transfer hardware would be ejected prior to leaving Mars, if analysis indicates that this would be necessary to break the chain of contact with Mars.

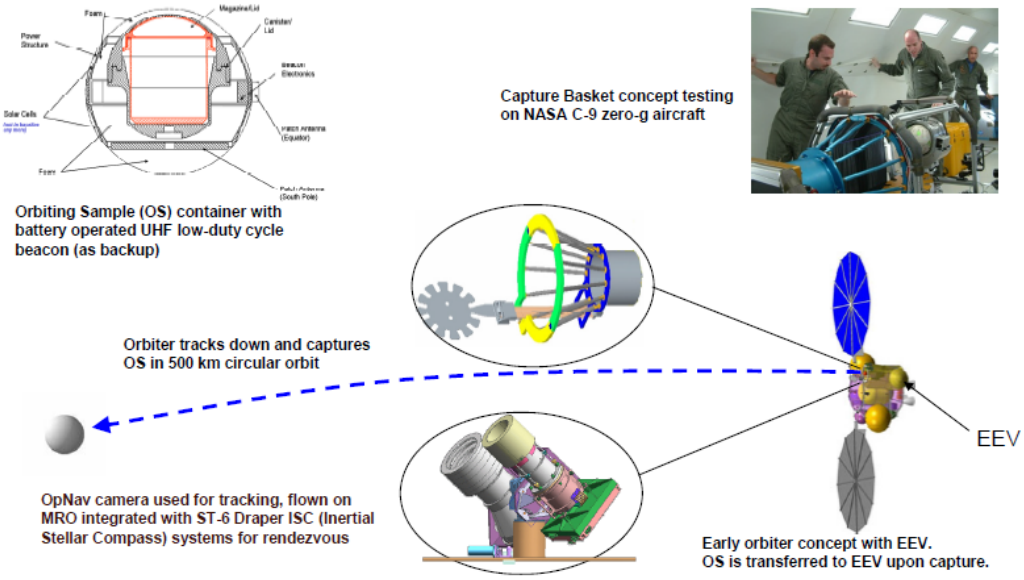

Figure 2.14 Rendez-vous and Capture System Concept [88].

Fig.2.15 reports the update operational phases of the rendezvous of an OS with a potential Solar Electric Propulsion (SEP) Orbiter, see [89] and [90].

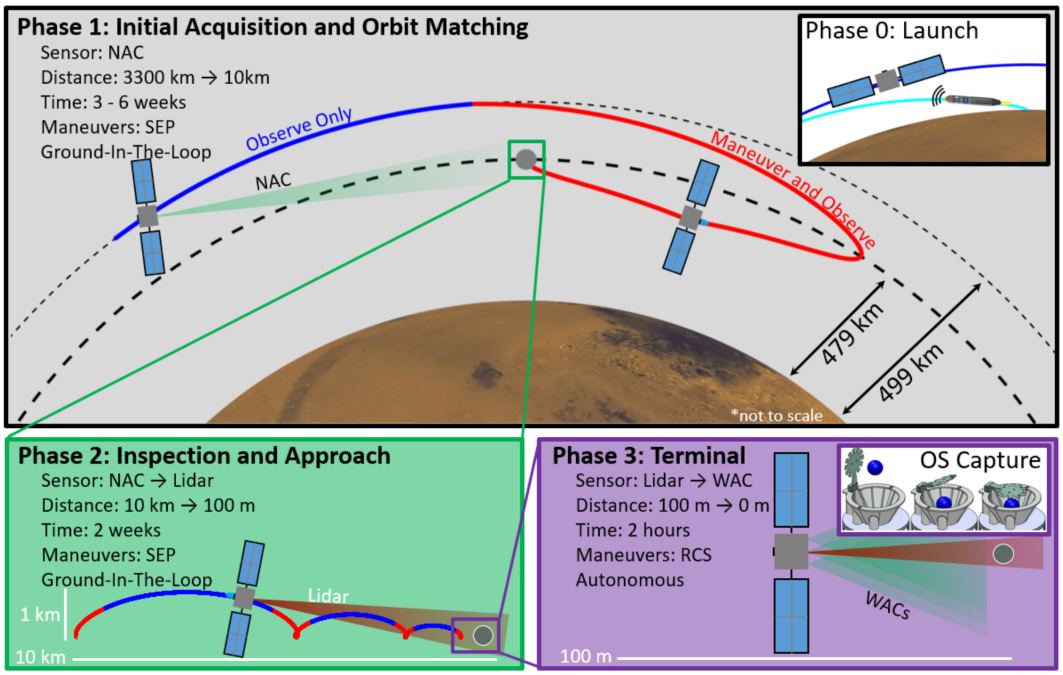

Figure 2.15 Rendezvous with a potential Solar Electric Propulsion (SEP) Orbiter, see [89] and [90].

Earth Entry and the Earth Return Module Preliminary Design

The return to Earth would be via a biased non-Earth-impact trajectory [91]. The orbiter would target toward Earth several days prior to EEV release, nominally entry-minus-4 hours, and then divert away from Earth following EEV release. The return and entry process is modeled after the Stardust and Genesis missions that successfully landed at the UTTR. However, steps would be taken to guarantee a higher degree of reliability (such as added redundancy and cross-checking trajectory planning by multiple teams). Unlike Genesis and Stardust, the MSR EEV would also be parachute-less and self-righting (tumble-free) during atmospheric entry, eliminating these failure modes. A full-scale (0.9m diameter) developmental model was impact tested at UTTR, dropped from high-altitude, reaching terminal velocity, see Fig.2.16. In addition, wind-tunnel testing and high-fidelity simulations have been performed that show that the vehicle would right itself into a stable orientation prior to the entry heat-pulse, even if released backwards or tumbling. The technology program would refresh the design and finish development by PDR. The EEV design

would be ready for flight testing by PDR if determined necessary; however, flight testing is currently considered optional. The EEV would be completely passive, except for self-contained range beacons that would be initiated at entry. An OS would fit in the center of the EEV, inside a 5mm-thick flexible rubberized Kevlar containment vessel that would be sealed in Mars orbit before return toward Earth. Mechanical latches would be used to secure the lid (top half) of the EEV, once an OS is inserted.

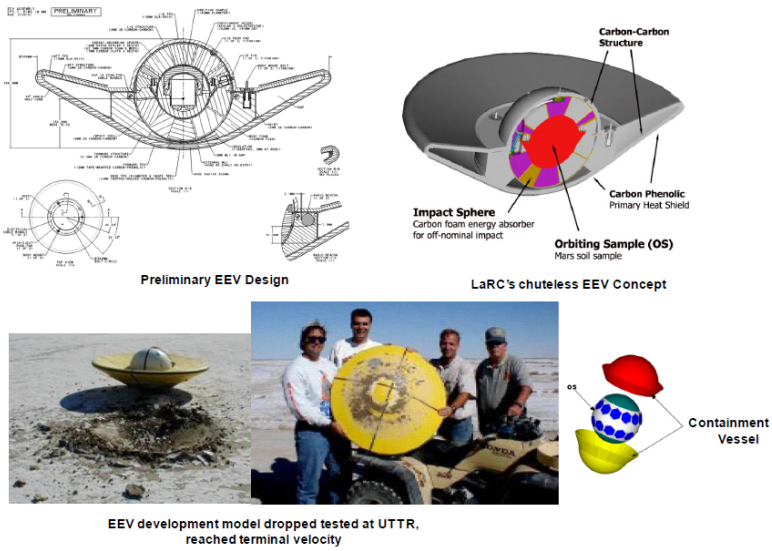

Figure 2.16 Earth Entry Vehicle Design concept [91].

2.6.4 Mars Returned Sample Handling Concept

MRSH denotes the ground segment of the proposed MSR mission, i.e., the activities occurring after landing of the sample return capsule on Earth. The most recent NRC study, Assessment of Planetary Protection Requirements for Mars Sample Return Missions [100], as well as previous studies referenced therein, included high-level recommendations for MRSH. Discussion of the ground segment of MSR often emphasizes the planetary protection aspects, which take the form of policy. However, the ground segment represents a broad multifaceted element of MSR, and would include landing site operations, Earth surface transportation, the SRF (one or more), and curation (e.g., the formal record-keeping, storage, and distribution) of the samples over time, see Fig.2.17. After landing, MSR would require that the whole EEV be put in a quarantine

vault with cooling (to maintain sample integrity) as soon as possible, and be securely transported to the SRF. The SRF represents the facility and processes that would be needed to:

- Handle the samples (and vehicle) in a manner as if they are potentially hazardous materials;
- Keep the samples isolated from Earth-borne contaminants;
- Apply a rigorous protocol to determine if there is any hazard in potentially releasing samples to other laboratories outside the facility.

The NASA Planetary Protection Officer commissioned the development of a draft test protocol that would represent one necessary and sufficient approach to evaluate the safety of the samples while safeguarding the purity of the samples from terrestrial contamination. A Draft Test Protocol for Detecting Possible Biohazards in Martian Samples Returned to Earth was published in October 2002 [101]. In 2003, three architectural design teams independently examined the scope, approach, cost, and technology required for the SRF, using the Draft Test Protocol for requirements. The approaches varied from all robotic handling of samples to more traditional glove box implementations. The studies indicated that the principles and techniques required are generally mature.

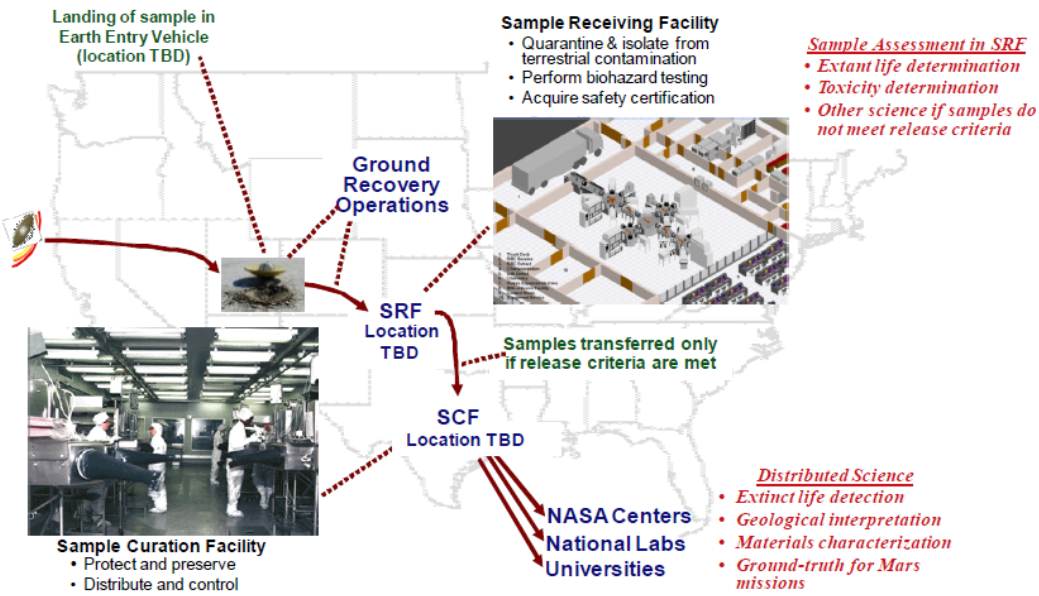

Figure 2.17 Mars Returned Sample Handling Concept [100].

As continues today with the Apollo lunar samples, the Martian samples would be amongst the most carefully studied materials in history, not only by biologists, but also by geologists, geochemists, and atmospheric scientists.

2.6.5 Planetary Protection

The orbiter would likely need to meet the requirements for Category III (forward planetary protection and contamination control). This level of requirements has been implemented in all past Mars orbiters, with procedures like trajectory biasing, analysis, and selected bake-out of subsystems, all included in the cost.

The main challenge for the proposed Orbiter Mission would be to meet the Planetary Protection requirements of Category V, restricted Earth return. Preventing contamination of Earth by potentially bio-hazardous Martian material would require highly reliable sample containment and ultra-safe entry and landing on Earth, as well as breaking-the-chain-of-contact with Mars in a way that would preclude return of Mars organisms outside of the sample containment. A Probabilistic Risk Analysis has been used to guide selection of techniques and would continue to be updated as trades and technology alternate paths are selected. Breaking-the-chain-of-contact has several features to it, including ensuring that the samples would be sealed in a reliable container. Nominally, an OS would be sealed into a container that would be brazed shut at the orbiter. In addition, there could not be any Mars organisms outside the sealed container that could return to Earth. This could be implemented by minimizing Mars dust transfer from the MAV by keeping it in a non-contaminated cocoon, shedding atmospheric dust during launch, and allowing time for an OS to be in free-space before contact with the orbiter. The equipment deck of all the capture and transfer hardware could be ejected prior to leaving Mars if analysis determines it necessary. The potential EEV would be in a biobarrier, which would also provide micrometeoroid protection. A multifaceted approach is planned, diverting the orbiter into a non-Earth impact trajectory and designing the EEV so that all external surfaces reach sterilization temperatures upon entry [102].

Chapter 3

SE Approach to the OS CRR Problem

This chapter deals with the System Engineering (SE) approach to qualify the evaluation criteria related to the mechanism responsible for a potential OS capture, reorientation and retain (CRR) focusing in particular on the reorientation phase. The analysis considers this subsystem as part of Rendezvous Orbiting Capture System (ROCS) on a Mars Sample Return Orbiter (SRO) spacecraft concept and interacting with other subsystems such as Break-The-Chain (BTC) and the notional EEV.

Parts of this chapter were published in:

- Concepts for Mars On-Orbit Robotic Sample Capture and Transfer Mukherjee R., Chamberlain-Simon B., Abcouwer N., Mc Cormick R., Smith R., Frederick T., **Dolci M.**, 2017 IEEE Aerospace Conference, Montana, USA, 04-11 March 2017.

- Concepts for a potential Mars Sample Return On-Orbit Robotic Manipulation System **Dolci M.**, Mukherjee R., Chamberlain-Simon B., Smith R., McCormick R., Ohta P., Mayo J., USC Robotics Symposium, 14 April 2017.

- An Orbiting Sample Capture System Architecture for Proposed Mars Sample Return Younse P., **Dolci M.**, Lalla K., Ohta P., Olds E., Strahle

L., accepted to the 2018 IEEE Aerospace Conference, Montana, USA, 03-10 March 2018.

- Systems Architecting using Bloom's Taxonomy to Promote Creative Engineering Synthesis Younse P., **Dolci M.**, Lalla K., Ohta P., Olds E., Strahle L., accepted to the 2018 IEEE Aerospace Conference, Montana, USA, 03-10 March 2018.

3.1 NASA Mission Concept Approach

There are two approaches how NASA decides to develop a new mission:

- Assigned mission, i.e., NASA decides new goals and new missions in order to reach them, e.g., Mars Science Laboratory, Mars 2020, and Europa projects.
- Competitive mission, i.e., NASA releases some Announcement of Opportunity (AO) to solicit Principal Investigator (PI)-led space science investigations for different-money-size missions, e.g., Nuclear Spectroscopic Telescope Array (NuSTAR), Galaxy Evolution Explorer (GALEX), and Orbiting Carbon Observatory 2 (OCO-2) missions.

Mars sample return mission concept could possibly be a decision-based NASA-funded mission. NASA adopts a method to design a mission in terms of both engineering and scientific sides to minimize costs, risks and to maximize scientific return. It is based on Concept Maturity Level (CML), see [103] and [104].

This chapter refers to CML 3 Trade Space to analyze the subsystem. In the next chapter, this concept would be made more mature and it would reach CML 5 thanks to the test bed implementation and the related tests. The future flight design would bring this concept to CML 6.

3.2 System Engineering Approach

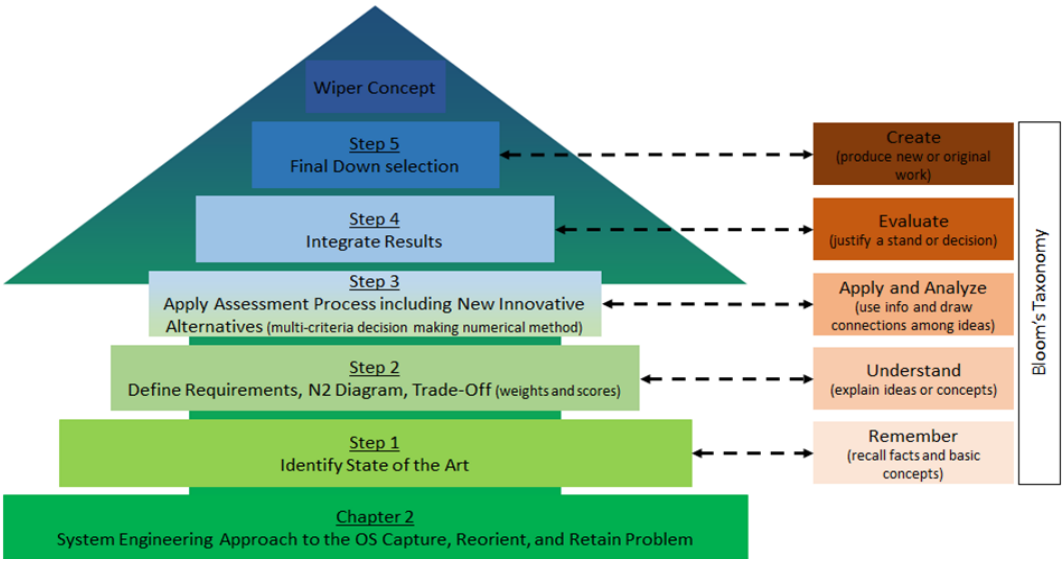

Figure 3.1 System engineering approach diagram.

Fig.6 (in the Introduction) reports the thesis strategic map. Each chapter generates output data adopted in the next chapter as inputs. For what concerns this chapter, Fig.3.1 reports the system engineering approach diagram. This chapter describes the system engineering approach to a notional OS capture, reorient, and retain problem and delivers as output the Wiper concept, mainly related to the reorientation mechanism. Moreover, in Fig.3.1 also a parallelism with the Bloom's taxonomy is reported, see [105] and [106].

3.3 Problem Statement

This subsystem is responsible to perform the following actions with the minimum number of actuators:

- Capture the OS. In this context the term capture is used as synonymous of constrain the OS in a confined space. This aspect is very important because the success of this operation could lead to an independent-contact-dynamics capture cone. This could be considered also from the OS perspective: the OS could assume shapes almost spherical but

not completely inscribed in a sphere. This gives to the designer the possibilities to play with possible OS features, both negative and positive with a proper size to be contained within the OS diameter.

- Reorient the OS. As described in Ch.2 during a potential EEV hard impact on Earth the sample tubes are within the OS with the hermetic seal sealing the caging plug and the sample. Some tests and analysis were run [97] reporting that in order for the hermetic seal to survive the impact the sample tube seals have to be located at least above the OS equator. Due to other system uncertainties the OS presents the potential requirement to be properly reoriented before being inserted inside the EEV. A correct orientation guarantees the survivability of the hermetic seals, avoiding a possible biohazard threat, and the integrity of the samples pledging a posterior pristine scientific analysis. The OS is captured without the knowledge of its orientation. Determine its orientation using sensors makes the system more complex and requires additional masses and power. There is the strong need to design a mechanical system able to reorient the OS against its initial orientation. Orienting the OS in a well-determined orientation before to proceed with the OS encapsulation in the EEV was envisioned. The correct OS orientation is fundamental in terms of the sample tubes orientation and the relative load distributions they experience during a Earth hard landing.

- Retain the OS. Using the OS features it is necessary to retain the OS in a way that during Earth hard landing (expected accelerations of 1300g) the OS remain in its original position without exposing the sample tubes to unconsidered load distributions with the possibility of damage. The retain considered is about the OS three translational degrees of freedom and about the OS two rotational degrees of freedom. The only axis on which the OS is allowed to spin is the tubes vertical symmetry axis.

The OS considered in this study has the following notional features:

- OS mass 12kg;
- OS Thermal Protection System (TPS) external diameter 28cm;
- OS container external diameter 60cm;

- OS incoming velocity 10cm/s;
- OS rotational speed 10rpm;
- OS initial orientation unknown;
- OS position error at the cone inlet ±10cm;
- OS spherical shape: northern hemisphere is the TPS during Mars ascension as part of the MAV, southern hemisphere is the Modifiable Surface (MS). Two cases are considered: 1. The two hemispheres have the same radii, see Fig.3.2(a) 2. The TPS hemisphere and the MS hemisphere have different diameters. The TPS diameter is 10mm longer than the MS side, see Fig.3.2(b). The two hemispheres are concentric. They are made of two different materials: Al 6061 for the MS side and Ceramic for the TPS side. There are three holes (negative features) on the bottom part of the MS, they are the MAV connection features. Positive and negative features are allowed on the MS, none on the TPS side. Sample tubes are inside the OS and they lie on the both sides of a plane coplanar with the intersection between the two hemispheres. During this thesis work, when the author refers to *the OS*, the author refers only to one of the two potential OS configurations reported here.

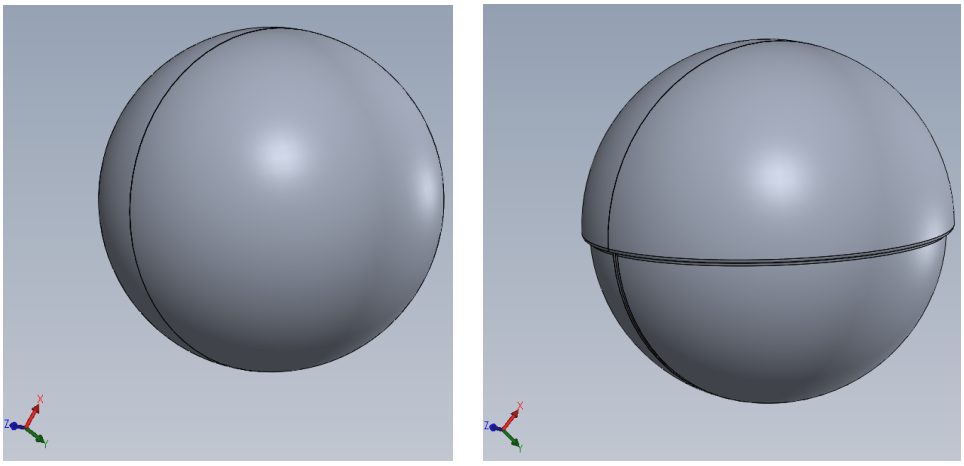

(a) CAD of the spherical OS, the TPS and the MS side have the same radii (28cm).

(b) CAD of the non-spherical OS, the TPS diameter is 10mm longer than the MS side.

Figure 3.2 CADs of notional OS configurations. During this thesis work, when the author refers to *the OS*, the author refers only to one of the two potential OS configurations reported in this figure.

The OS features would keep evolving during the actual design study for this mission. The presented features are a frozen picture of this evolutionary process. They are going to remain constant during the whole thesis work.

3.3.1 Symmetry Conservation

This problem deals with the capture of a six degrees of freedom OS. A spherical (or quasi-) OS shape was assumed due to the fact that it maximizes the symmetry in space for capture. For this same reason in all the evaluated concepts a conical capture cone was considered. It exploits the natural symmetry of the OS. Obviously, a spherical OS is more complex to be manipulated (reorientation and retain operations), and this is a interesting mechanism-design challenge. The problem has its own symmetry. The symmetry preservation could be a key point in the system design to answer to the CRR problem.

3.4 State of the Art - Previous Study

This section captures all the relevant previous studies related to a system that is able to capture and retain a spherical OS.

In the current literature it is not possible to find any end-to-end system able to capture, reorient and retain a OS. In particular, the results of the studies performed by NASA and ESA are reported. They focus on the capture part of the system and not on the reorientation aspect. A conical capture mechanism is a symmetrical capture geometry that works properly within a symmetrical OS domain. This was analyzed, designed and tested both by NASA [88], [92], and [111] and ESA [112] and [113]. Both NASA and ESA consider a rigid capture cone. There are also some projects that have deep analyzed the possibility to adopt a non-rigid capture cone mainly to save mass. Due to the fact that mass saving is counterbalanced by a higher system complexity and so higher risks, a rigid capture cone have always been adopted in this mission scenario. Once the capture was carried out, the ejection of the rigid capture cone through a pyrotechnic fastener (e.g., frangibolts) is a possible option to make the whole vehicle lighter and so to optimize the on-board fuel. Both NASA and ESA approaches to the OS problem are similar. Even if they use different technologies in terms of sensors and actuators, they both use a 1-dof retain system. Both NASA and ESA run some zero-g flight tests in order to validate their models and to enhance the TRL to TRL 6 that means system / subsystem model or prototype demonstration in a relevant environment. Once this happens, this mechanism could be taken into consideration for a real flight mission.

3.4.1 NASA OS Capture Previous Study and Test

In the work of [88] NASA focuses on a system that carries a capture cone to capture and retain the OS. Understanding the capture dynamics between the sample canister and capture cone in the zero gravity environment is paramount to designing an effective capture mechanism. Moreover, testing and validating the sample capture event in a zero gravity environment is a crucial, though challenging, element to ensure mission success.

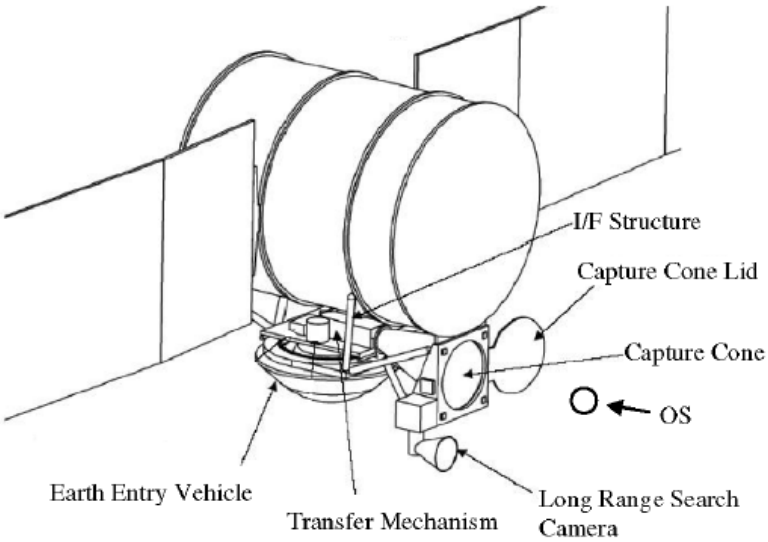

Figure 3.3 NASA rendezvous and sample capture design concept, see [92].

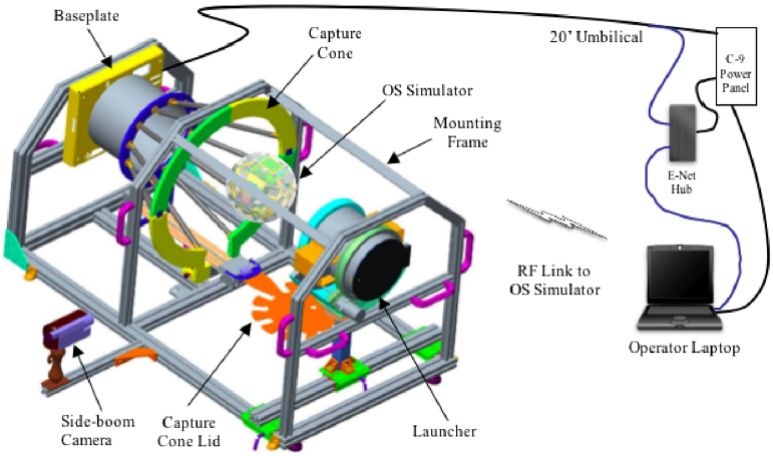

Figure 3.4 NASA test setup overview, see [88].

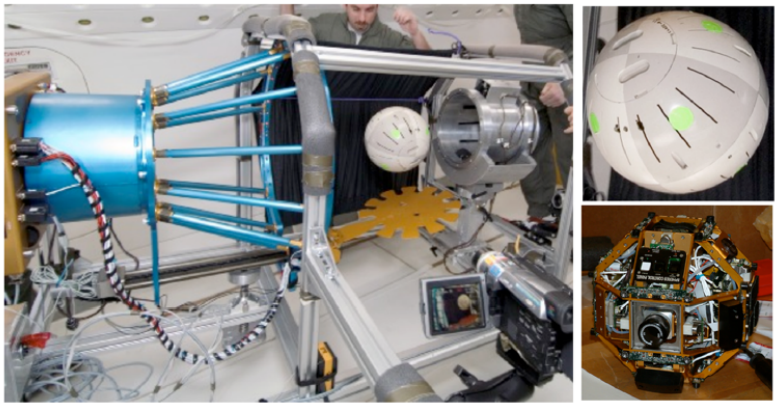

Figure 3.5 Test hardware. Left: frame, capture cone, and launcher. Top right: OS simulator with shell. Bottom right: OS simulator without shell, see [88].

This paper describes a novel, efficient, and cost-effective way to test and validate the last-meter rendezvous problem. It relies on NASA's C-9 parabolic aircraft as a platform to provide short periods of zero gravity. A novel test setup allows the exploration of various capture conditions in a controlled manner and enables the efficient evaluation of capture cone designs. The flight campaign described herein served as a pathfinder for investigating capture dynamics and capture cone efficacy. A total of 160 parabolas were flown, half of which resulted in successful test runs, matching preflight predictions. The overall test setup performed as expected, though a number of shortcomings were identified. Parabolic flight offers a feasible simulation environment to study OS contact dynamics. It offers true zero-g, 6-dof contact conditions for up to 20-25s, although zero-g durations of 5-10s are more typical for the test setup used in this campaign. The test venue (to raise the system TRL to 6) is cost effective by orders of magnitude in comparison to space flight (International Space Station or free-flyer in Earth or Mars orbit) and allows repeated tests with marginal additional cost.

3.4.2 ESA OS Capture Previous Study and Test

This ESA work [112] provides recent updates regarding the ESA technology development activity: Sample canister Capture Mechanism Design and Breadboard for Mars Sample Return Mission developed under the ESA Mars Robotic Exploration Preparation (MREP) program. The technology object of the

activity focuses on the Capture Mechanism and tests it in order to reach a Technology Readiness Level objective of TRL 6. An elegant breadboard of such a device was implemented and extensively tested: functional, thermal and mechanical vibration test campaigns were conducted to assess the breadboard functionality, performances and compliance with the mission environmental requirements. In order to raise the technology TRL to 6 the breadboard was also tested on a Parabolic Flight Test Campaign (zero-g environment). The Sample canister capture operations under free-floating conditions were verified and impact forces between free flying Sample canister and the breadboard investigated.

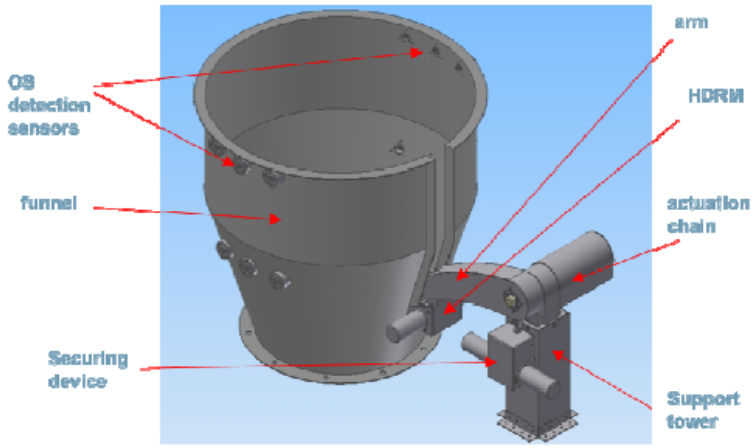

Figure 3.6 ESA Sample canister Capture Mechanism flight model concept, see [113].

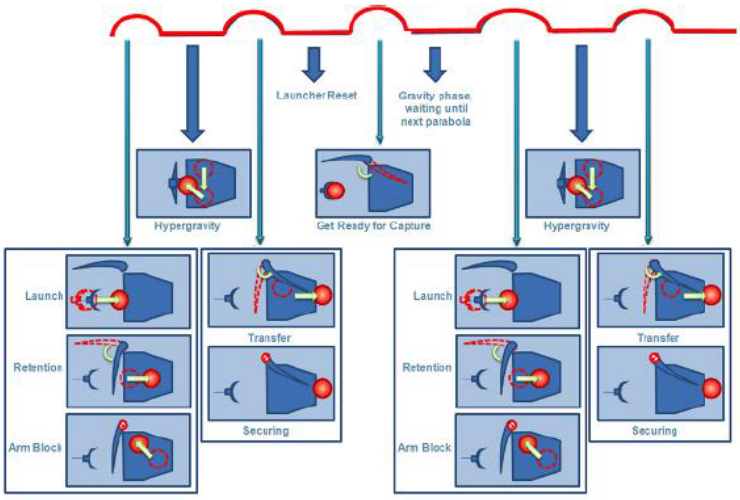

Figure 3.7 ESA complete test schematics, [113].

Figure 3.8 ESA experiment ready for parabolic flight test campaign, [113].

In this last phase, the Sample Canister Capture Mechanism (SCCM) would have to fulfill three different main tasks, the first is to ensnare the OS, the second is to transfer it into a trap, and the third is to secure the OS inside the trap. This SCCM is designed to entrap the OS with spherical or quasi spherical shape having a diameter of 230mm. The SCCM has an overall volume of 800 x 800 x 500mm^3 when in stowed configuration, and foresees four main elements: a funnel, an arm, an actuation chain and an arm support tower, see Fig.3.7. The funnel is represented by a container made in Composite Fibre

Reinforced Polymer (CFRP), aimed at providing the artificial envelope where to capture the Sample canister before its retention and securing inside the trap. Such a funnel was shaped in order to prevent any jamming of the OS during all arm operations. Fig.3.8 shows ESA experiment ready for parabolic flight test campaign.

3.5 Current Study

The study conducted in this dissertation took place at NASA JPL - Caltech. This work is part of the Mars In-Orbit Sample Transfer Technologies (MOSTT) [114]. The principal elements in the ROCS system are reported:

- **ROCS** - Rendezvous Orbiting Capture System is a NASA JPL - Caltech concept study to determine a baseline to realize the third step of the Mars Sample Return mission architecture. It is a payload attached to the SRO mission concept responsible for capturing the OS, sealing it to protect the sample, sterilizing the outside shells and delivering the OS inside the OS container to the EEV or to the hand off scenario, see [115].
- **SRO** - Sample Return Orbiter is the technical task related to the spacecraft that would orbit around Mars and would transport the system to capture the OS and to insert it in a way to bring it back to Earth.
- **OS** - Orbiting Sample is the technical task related to determine the OS shape and size, how it deals with the sampling tubes and it reacts to the loads experienced during a hard Earth landing.
- **MOSTT** - Mars In-Orbit Sample Transfer Technologies is the technical task with the specific challenges of capturing the OS in Mars orbit and then transferring it into the EEV. The scope of this task, with respect to the mission time line, starts with the OS within tens of meters of the spacecraft, and ends after the transfer of the OS to the EEV. This task would first define the OS capture, constrain, control, clean, and transfer system architecture, and would identify the key technology developments required for robust OS handling. This task develops complimentary hardware and simulation testbeds with the key physical elements of the

OS handling chain and the capability to simulate the zero-g environment of the capture phase. This task would also use these testbeds to develop the low TRL technologies and to demonstrate end-to-end operation, thus retiring the risk in the CRR and transfer chain. Successful completion of this task would provide a key foundation for the Mars sample return mission.

- **BTC** - Break-The-Chain is the technical task related to determine a mechanical solution able both to enclose the OS in the OS container sterilizing the outside shell and to eject in the outer space all the elements that entered in contact with the contaminated OS. In this way, a clear separation process allows to create a well defined scenarios in terms of contamination assurance.
- **PPO** - The Planetary Protection Office is the NASA entity responsible for the protection of the solar system planets both in term of avoiding harmful contamination of them with elements brought from Earth and in terms of protecting Earth's environment from any adverse effects that could occur from a sample return mission.

3.6 Conceptual Design Solutions

After having described in the previous sections the mission context, a path was developed from high level manipulation scenarios towards the most feasible solution and its conceptual design.

3.6.1 Manipulation Object Scenarios

A path was depicted that goes from an infinity of possible solutions to a class, and later to a specific design. The first step relates to the manipulation methods considered to manipulate the OS. The current grasping and manipulability technologies were collected. To execute a first choice of the gripper configuration parameters, it is important to describe the existing prehension methods and their advantages and disadvantages both from the gripper side and from the grasped object point of view. A literature search was performed about general

architectures and actuation grippers, refer to [4] - [8]. Following [1], there are four possible configurations for prehension scenarios:

- Impactive: The retention force provided by these tools is based on the physical effects of Newtonian mechanics, mainly associated with mass points and forces, and requiring more or less extensive mechanisms.
- Ingressive: Gripping methods which permeate a material surface to some given depth. Used almost exclusively with soft materials and in particular fabric, foam and fibrous components. Ingression could be intrusive or non intrusive.
- Astrictive: A binding force produced by a field. This field may take the form of air movement (vacuum suction), magnetism or electrostatic charge displacement. Almost all forms of astrictive devices rely on some degree of continuous energy supply to maintain object retention Vacuum adhesion, suitable to any relatively rigid, non-porous surface (OS requirements). Magneto adhesion (magnetic field requirements), able to operate in vacuum environments, suitable with magnetically susceptible materials, great power consumption. Electroadhesion, able to operate in vacuum environments, suitable to any material flat low-mass objects.
- Contigutive: Grippers whose surface must take direct contact with the objects surface in order to produce prehension, e.g. chemical, thermal. Velcro adhesion. Chemoadhesion (UV sensitive). Thermoadhesion (environmental dependent).

	Impactve prehension	Ingressive prehension	Astrictive prehension (magneto adhesion)	Contigutive prehension (thermal adhesion)
Gripper reliability				
Damage free grip				
Retention force				
Environmental dependence				
Power consumption				

Legend: suitable, intermediate, unsuitable

Table 3.1 Manipulation scenarios compared to the key features required in a space environment for the present case study. Green represents suitability, orange intermediate level, and red unsuitability.

Tab.3.1 shows the aforementioned manipulation scenarios compared to the key features required in a space environment for the present case study. The evaluated features are:

- Gripper reliability - Ability of the gripper to work properly not only in the defined scenario, but also in perturbed conditions.
- Damage free grip - Ability of the gripper to operate manipulation without damaging the interested object.
- Retention force - Level of force developed by the prehension method, considering the same amount of power consumption.
- Environmental dependence - Ability to the gripper to modify its behavior as less as possible due to the environmental interaction.
- Power consumption - Ability of the gripper to consume less power, providing the same amount of retention force.

3.6.2 Potential System Requirements

The System Requirements relate to the system able to operate the CRR to the OS are:

- The system shall have the required sensors to detect the incoming OS (near field camera/lidar, wide field camera).
- The system shall have the sensor (laser curtain) to detect the OS entering the capture cone inlet.
- The system shall have the possibility to confirm to Earth (downlink) the OS capture.
- The system shall wait for the uplink for the GO/NOGO from Earth in order to proceed to RR the OS.
- The system shall be resettable in case the OS is not captured at the first attempt.
- The system shall behave in a deterministic way, i.e., there would be some pre-determined time-dependent actions that would lead to CRR (e.g., of a non deterministic way: using a net or a pin-hook system).
- The system shall be able to capture the OS through the capture cone inlet, to constrain it in a confined volume being independent from the OS-capture cone dynamic interaction.
- The system shall be able to reorient the OS, making sure that the tubes would be aligned in a preferred direction.
- The system shall be able to move the OS through the capture cone outlet.
- The system shall be able to retain the OS (five degrees of freedom, three translational ones and two rotational ones). The OS could be free to rotate on the last degree of freedom, whose axis would be aligned with tubes axis.
- The system shall accommodate the OS requirements in terms of planetary protection (two levels of encapsulation - shells - and sterilization).
- The system shall be composed by no single point failure hardware and software components.
- The system shall be composed by no single point failure actuation steps in the CRR process.

- The system shall consider geometric constraints before the contact (capture before contact) and the retain phase integrating the lid symmetrical properties in the capture mechanism.
- The system shall be resettable: autonomous triggered events should not be irreversible.
- The system cost shall fit the time schedule and the cost budget.

3.6.3 N^2 Diagram

An N-squared (N^2) diagram is a matrix representation of functional and/or physical interfaces between elements of a system at a particular hierarchical level [116]. The N^2 diagram was used extensively to develop data interfaces, primarily in the software areas. However, it could also be used to develop hardware interfaces. The system components are placed on the diagonal. The remainder of the squares in the NxN matrix represent the interfaces. The square at the intersection of a row and a column contains a description of the interface between the two components represented on that row and that column. The N^2 diagram could be taken down into successively lower levels to the hardware and software component functional levels. In addition to defining the data that must be supplied across the interface, by showing the data flows the N^2 chart pinpoints areas where conflicts could arise in interfaces, and highlights input and output dependency assumptions and requirements [116].

Capture **Constrain the OS in a well-defined space and volume**	• Capture has to keep OS in place to be reoriented • Capture has to be verified before reorientation starts	• Capture has to constrain the OS in a defined space until retention happens • Capture mechanism could activate the OS retention	• Capture cannot be executed using BTC lid	
	Reorientation **Reorient the OS from infinite unknown initial orientations to a well defined one deterministically without friction**	• The OS has to be reoriented properly to be retained • Reorientation mechanism could activate the OS retention	• Reorientation mechanism has to be removed before BTC • Reorientation has to be verified before BTC starts	• The OS has to be reoriented accordingly to the final OS transfer
		Retention **Retain the OS both during BTC (soft retention) and 1300g-hard landing (hard retention)**	• Retention feature shall not interfere with BTC	• Retention shall make the OS not moving during internal transfer
• BTC happens after capture mechanism is ejected	• BTC happens after reorientation mechanism is ejected	• BTC shall not modify the retained OS status	**BTC** **Break-The-Chain to isolate the OS from the outside environment, create a well-defined clean/dirty areas (PPO)**	• BTC has to be concluded and verified before moving the OS
				Internal OS transfer **Transfer the OS from the BTC location to the EEV**

Figure 3.9 N^2 diagram for CRR orbital system.

Fig.3.9 reports the N^2 diagram related to the OS manipulation. Here the functional connections between the different system components are highlighted. The blank spaces represent no functional interconnections. This diagram is particularly useful to make other figures of merit standing out such as:

- Function-dependence architectures.
- All-the-functions-in-the-same-location architectures vs different-location architectures.
- Multi-scope-actuator architectures (redundancy vs risk).

However, this figures of merit are not taken into consideration in this work due to the preliminary architectural design that focuses more on the single subsystems before discussing on the subsystem interconnections, location and actuator-sharing.

3.6.4 Potential System Criteria

Potential system requirements translates into potential system criteria:

- The system has to be kept as simple as possible, low number of actuators $\leq$3.
- The system has to be kept as simple as possible, low number of moving parts $\leq$3.
- The system has to be kept as simple as possible, low number of sensors / active verification steps.
- The system mass has to be as low as possible (accorded to SRO potential requirements).
- The system volume has to be as low as possible (accorded to SRO potential requirements).
- The system has to deal with the system integration to the SRO (accorded to SRO potential requirements).
- The system power has to be as low as possible (accorded to SRO potential requirements).
- The system has to be scalable to accommodate future different size and dimension OS.
- The system cost has to be as low as possible.
- The system shall be able to not use friction to CRR the OS. This because friction requires a normal force (preload), it is environmental dependent and increases the level of risk. Form closure approach is preferred to force closure approach.

- The system should minimize the number of the components that would remain inside the OS shell after the CRR.
- As few modifications as possible related to the OS non-TPS side.
- The system should be able to retain the OS with a different mechanical component with respect to the one used to capture the OS (for Planetary Protection (PP) purposes).
- OS feature has be to compatible with the MAV system and with the tubes canister attachment.

3.6.5 Conceptual Designs

After having selected a class, the envision working concepts were described. Each of them respects the potential system requirements and answers in a different way to the potential system criteria. To envision these conceptual designs this line of thinking was followed: during the CRR operations the system needs to perform capture, reorientation and retain of the OS. In Tab.3.2 all the possible permutations after the capture are shown. If as first action the initial orientation is known, it could be possible either to reorient the OS or to retain it. However, this system is initial orientation dependent. This implies to use sensors to infer it and so this case has to be disqualified (they are labeled red).

First action after capture	Second and third actions	Mechanical approaches	Remarks
1. Initial orientation			
	2. Re-orient 3. Retain	• Under actuated system • Form closure	Initial orientation dependent
	2. Retain 3. Re-orient	• Form closure • Container rotation	Initial orientation dependent
1. Re-orient			
	2. Retain 3. Final orientation	• Form closure • Geometric constraints	**This concept seems to satisfy all the requirements**
	2. Final orientation 3. Retain	• Sensors / Singularities • Form closure	Use of sensors
1. Retain			
	2. Re-orient 3. Final orientation	• Gears • Geometric constraints / sensors	No deterministic approach / use of sensors
	2. Final orientation 3. Re-orient	• Sensors / Geometric constraints • Gears	Use of sensors / no deterministic approach

Table 3.2 Permutations among all the CRR operations after the capture and possible working concepts.

If the first action is the retain, different cases were developed. The first case is the one depicted in Fig.3.10: ring plus gear thin pattern. In this case the OS is retained through a ring, rotation is caused by gear-thin (less than the TPS edge) square pattern surface interaction. After having run some dynamic simulations in MSC Adams, this working concept present some problems:

- No deterministic surface-gear contact, OS initial orientation dependence.
- Gear-surface contact positioning complexity, OS initial orientation dependence.
- Difficulty to stop its rotation, once the OS lays on the ring.

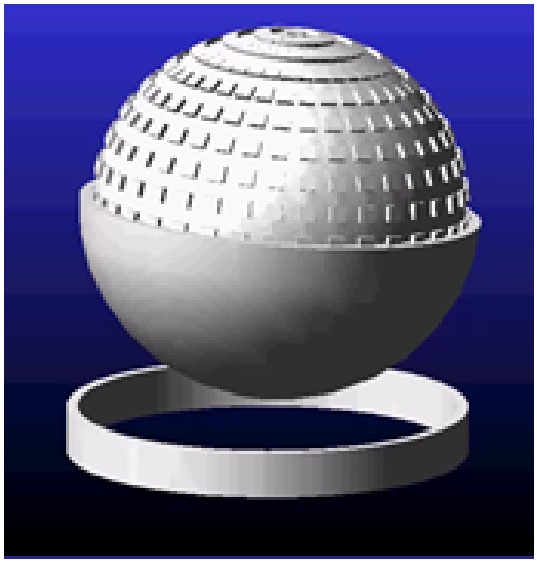

Figure 3.10 Ring plus gear thin pattern working concept.

The second case is the one depicted in Fig.3.11, ring plus gear thick pattern. In this case the OS is retained through a ring, rotation is caused by gear-thick (more than the TPS edge) square pattern surface interaction. After having run some dynamic simulations in MSC Adams, this working concept presents some problems:

- No deterministic surface-gear contact, OS initial orientation dependence.
- Gear-surface contact positioning complexity, OS initial orientation dependence.

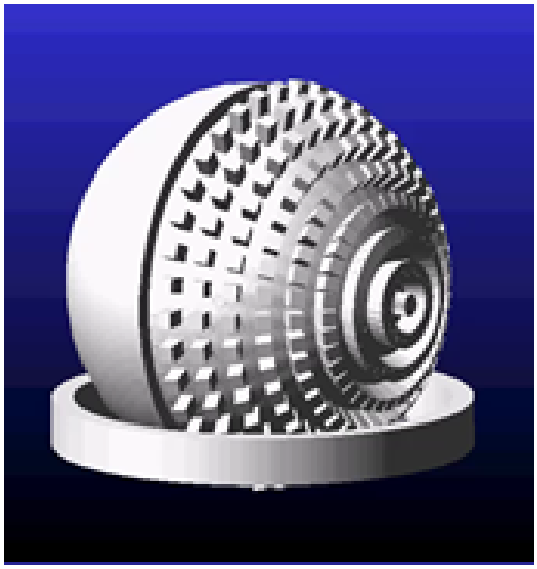

Figure 3.11 Ring plus gear thick pattern working concept.

The third case is the one depicted in Fig.3.12, clump with two-side OS container. In this case the OS is retained using a two-side dodecahedron mold OS container [117]. After having run some dynamic simulations in MSC Adams, this working concept present some problems:

- Friction problem (dodecahedron) to retain.
- Use of sensors / software to infer OS orientation, once retained.
- Consequent rotation of OS container.
- Possibility to use icosahedron (> number of faces).

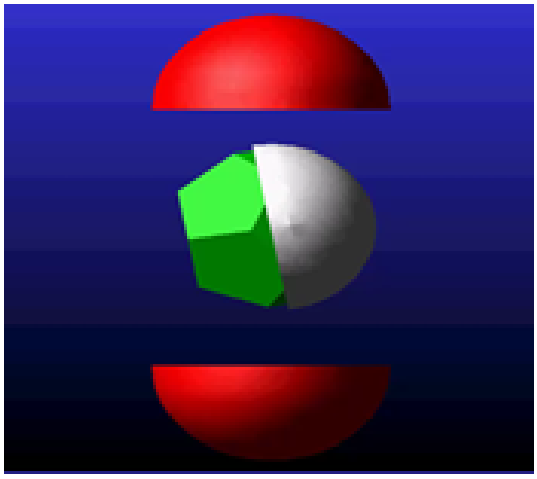

Figure 3.12 Clump with two side OS container [117].

All the cases related to the retain as first action (they are labeled red) have to be disqualified. Here reorientation is considered as first action. In this case, as second step either an evaluation of the current orientation or a retain could be operated. First, evaluation of the orientation was considered. This method consists of three main steps:

1. OS enters a cylinder with a flat surface.

2. OS enters a cylinder with a chamfered wall. With the exact same size, there is no possible chamfer that could accommodate the OS. In this case the OS made up of two hemispheres with different radii. There are infinite possible initial orientations. In Fig.3.13 the power spectrum density (PSD) as a function of spatial frequencies is reported. The chamfered cylinder OS exact size space frequency range is shown together with the chamfered cylinder OS exact size plus margin space frequency range. The second one is larger than the first one and this could allow the OS to rotate until it fits the chamfered cylinder. This problem was evaluated as a space frequency problem approach. In doing that a margin of 0.5cm was added to the chamfered cylinder.

3. This is an OS symmetrical problem. Breaking the symmetry could oblige the OS to rotate. To reach this goal a single degree-of-freedom linear actuator was considered.

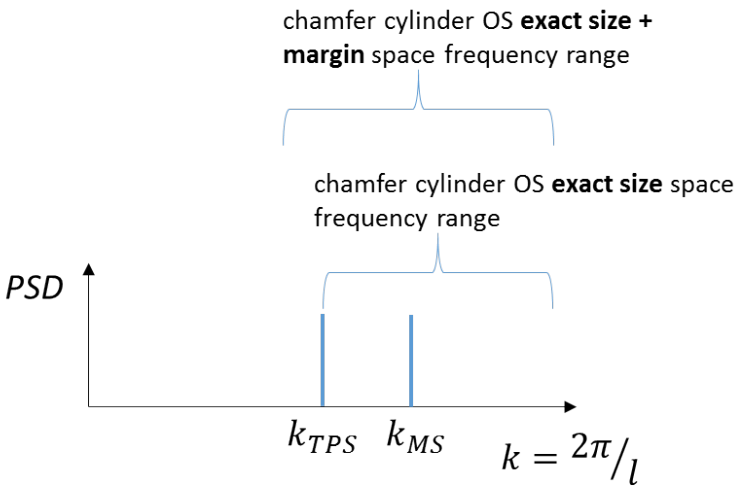

Figure 3.13 Power spectrum density (PSD) as a function of spatial frequencies.

Fig.3.14 reports the main components that characterize this case.

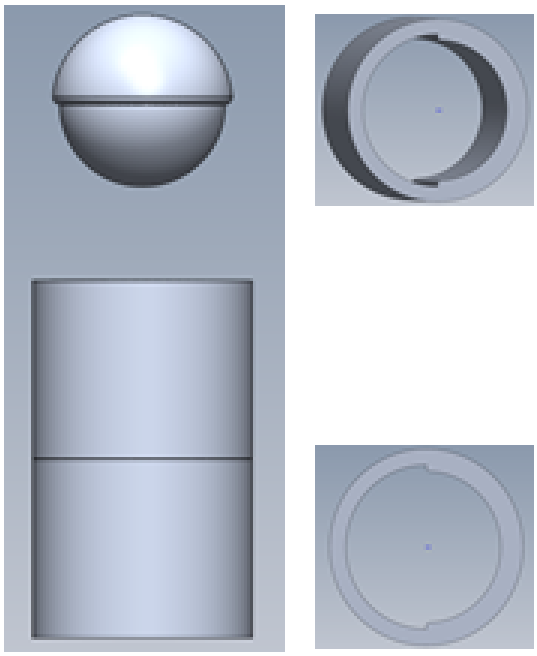

Figure 3.14 Components that characterize this case. Left: complete system with OS. Top right: chamfered cylinder. Bottom right: flat cylinder.

In this case, once the OS is reoriented (passing from ∞^3 to ∞^2 possible rotations), the OS is reoriented (passing from ∞^2 to ∞^1 possible rotations) and then retained using a form closure approach, passing from ∞^1 to the final orientation. In this case, gear positioning problem and sensors / software are avoided. It is based only on mechanical interface through a generated torque. It is a more deterministic procedure, but not complete yet. An orientation limit time could be set. It would be time deterministic, but no action deterministic. A whole system is reported in Fig.3.15 [117]. In this case the single one degree of freedom actuator is constituted by three fingers, the central one allows the OS to rotate and the other two prevent the OS to escape. After having designed an actuator that could operate the three fingers (another mechanism could be a crank shaft, more efficient and more mechanically reliable), some dynamic simulations in MSC Adams were run.

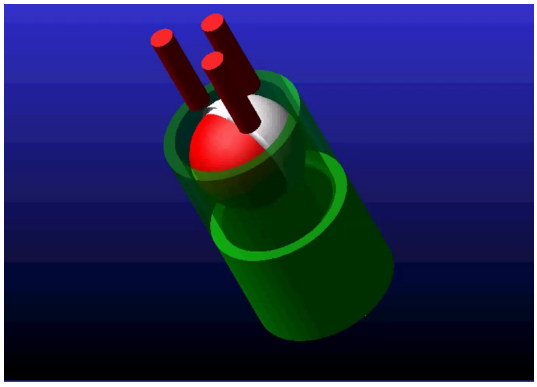

Figure 3.15 Chamfered wall tunnel OS interaction complete system [117].

A story board in Fig.3.16 is reported. This working concept presents some problems:

- The finger interaction on the OS is considered friction.
- The finger interaction on the OS TPS could scratch or damage it.
- There are some singularity cases in which the OS reorientation within 100 seconds does not succeed. They are classified as failures.

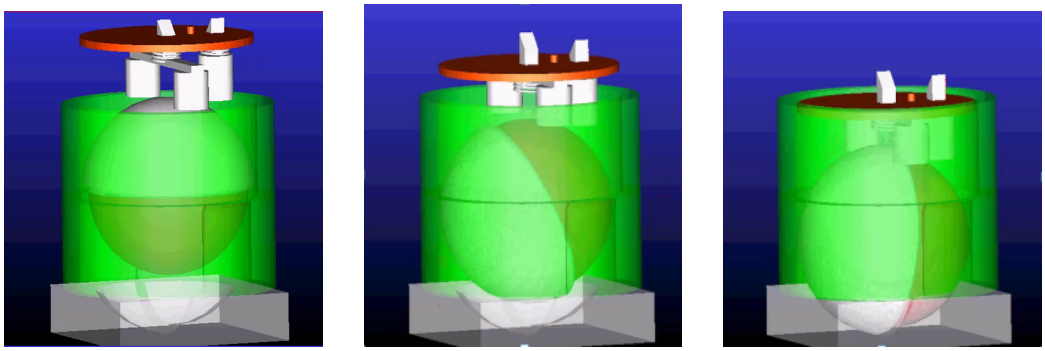

Figure 3.16 Story board of the Chamfered wall tunnel OS interaction complete system using MSC Adams [117].

All the cases related to the reorientation as first action and evaluation of the current orientation as second action have to be disqualified (they are labeled red). It seems that, after a reorientation, the only viable strategy is conducting the OS retain. This working concept is the one that would work properly. The selected cells in Tab.3.2 are labeled green.

Looking at Tab.3.2 the only class that remains (green labeled) is the one concerning a reorientation as first action, followed by a retain that leads to the correct OS final orientation. This class supports two concepts the author and members of the MOSTT team have developed [117]:

1. Space cup with the OS that presents a positive annular ring.
2. Wiper system with the OS that presents a positive feature (pin).

In Fig.3.17 the space cup concept with the OS that presents a positive annular ring is depicted. In this case a cup pushes the OS to enter in the capture cone and thanks to a u-joint connection the cup aligns the OS symmetry axis to the capture cone vertical symmetry axis. It keeps pushing the OS towards the capture cone bottom where the cup creates a torque to reorient the OS with the horizontal plane of the bottom of the capture cone. The OS was captured, reoriented and retained.

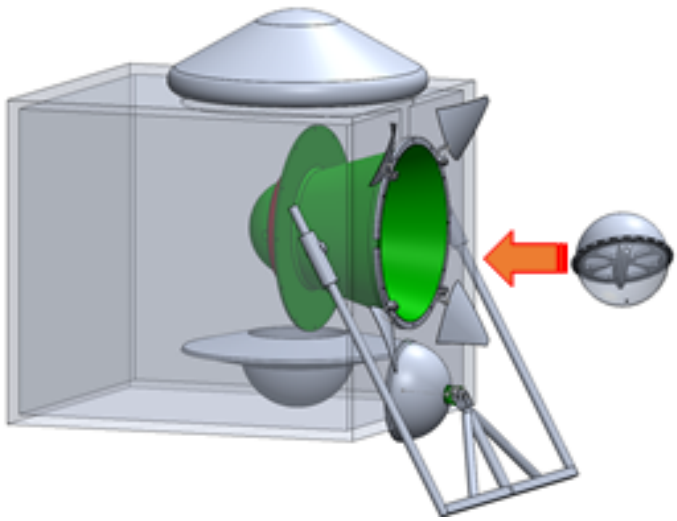

Figure 3.17 Space cup with the OS that presents a positive annular ring, see [117].

In Fig.3.18 the Wiper concept with the OS that presents a positive feature (pin) is shown [117]. The OS comes with a position error of ±10cm and a rotational rate of 10rpm. The OS enters in the capture cone. The four symmetrical leaves push the OS, avoiding it to escape. The cup capture the OS and pushes it toward the bottom of the capture cone. The cup constrain the OS to stay in a specific volume between the cup and the bottom part of the capture cone. A Wiper starts to rotate and explores the OS surface in search of the positive feature. The Wiper keeps rotating to explores the OS surface in search of the positive feature. The Wiper pushes the OS positive features towards the bottom of the below shell, where a positive extrusion allows the capture of the positive feature. The OS positive feature is engaged by the Wiper. It is retained in between then Wiper and the shell positive extrusion. After that the Wiper rotates back 90° and would be ejected together with the capture cone and all the other components that interact with the OS (BTC process). The OS positive feature remains attached to the bottom of the shell thanks to a simple clamping device (e.g, a clip). The OS was captured, reoriented and retained.

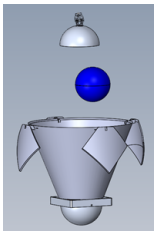

(a) The OS comes with a position error of ±10cm and a rotational rate of 10rpm.

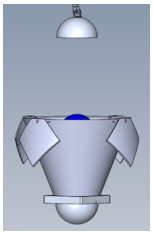

(b) The OS enters in the capture cone.

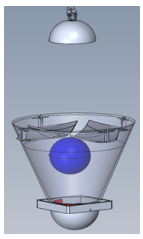

(c) The four symmetrical leaves push the OS, avoiding it to escape.

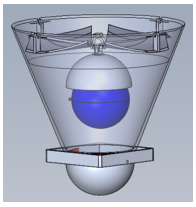

(d) The cup capture the OS and pushes it toward the bottom of the capture cone.

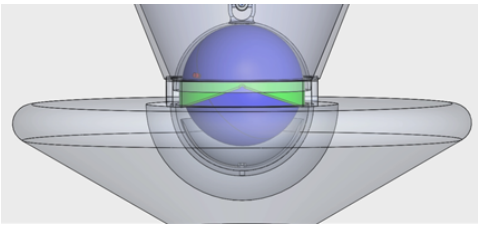

(e) The cup constrain the OS to stay in a specific volume between the cup and the bottom part of the capture cone.

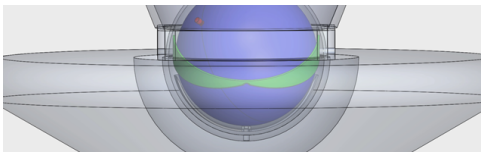

(f) A Wiper starts to rotate and explores the OS surface in search of the positive feature.

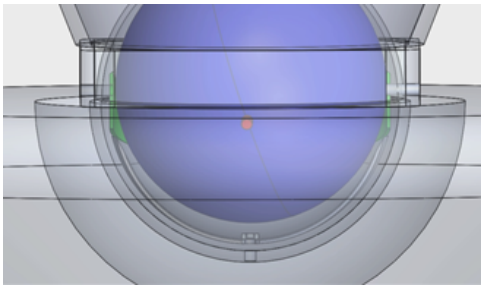

(g) The Wiper keeps rotating to explores the OS surface in search of the positive feature.

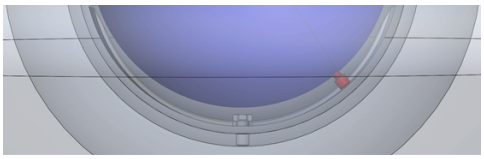

(h) The Wiper pushes the OS positive features towards the bottom of the below shell, where a positive extrusion allows the capture of the positive feature.

3.7 Assessment Process - Trade-off Study

After having shown all the concepts in the previous sections, a trade-off study to determine the most feasible one was run. In Tab.3.3 the trade-off study is illustrated. As system figures of merit are considered what system criteria should be taken into consideration in evaluating candidate capture / reorientation / lid placement approaches. Each of them was weighted with a weight:

- 1 was considered a low weight. This figure of merit is interesting to be considered, but not fundamental to the ultimate goal.
- 2 was an intermediate weight. The figure of merit is relevant for that particular design, but no fundamental to the whole system.
- 3 was a high weight. This figure of merit is fundamental to the whole system and does not affect other system components (such as BTC, MAV).

	Analyzed concepts	Ring + gear thin pattern	Ring+ gear thick pattern	Clump with 2 side OSC	Chamfer wall OS 2diamt tunnel	Wiper system + OS with pin	Space cup + OS annular ring
Figures of merit							
what factors should be taken into consideration in evaluating candidate capture / re-orientation / lid placement approaches	**Weights (1-low, 3-high)**						
The system has to be kept as simple as possible • low number of actuators ≤3, concerning mass and power	3	12	12	15	15	12	12
The system has to be kept as simple as possible • low number of moving parts ≤3, concerning reliability	3	12	12	15	9	12	15
The system has to be kept as simple as possible • low number of sensors / active verification steps, concerning harness, SW and power	2	6	6	10	10	10	10
The system should be able to not use friction to CRR the OS. This because friction requires a normal force (preload), it is environmental dependent and increases the level of risk. Form closure approach is preferred to force closure approach	3	15	15	6	6	15	15
The system should behave in a deterministic way, i.e. there would be some pre-determined time-dependent / limited actions that will lead to CRR (defined time window is related to power resources)	3	9	9	9	9	15	15
The system should minimize the number (vs volume) of the components that will remain inside the OS container after the CRR	3	9	9	15	15	15	15
System should ensure a correct locking of the OS to guarantee a normal load of 1000s gs	2	6	6	8	10	10	10
As few modifications as possible related to the OS non-TPS side	1	3	3	3	5	4	4
The system should minimize the volume (diameter) of the OS container used to retain the OS	2	6	4	10	10	10	6
The system should be able to retain the OS with a different mechanical component wrt the one used to capture the OS (PP)	3	12	12	9	9	15	15
The system should ensure that as few components as possible could interact with the OS, and all of them could be ejected afterwards (PP)	3	9	9	15	9	15	15
OS feature has be to compatible with the MAV system and with the tubes canister attachment	3	6	6	12	15	15	9
Total /155		**105**	**103**	**127**	**122**	**148**	**141**

Table 3.3 Trade-off study.

The scores are assigned in a ranking from 1 to 5 using a Analytical Hierarchy Process prioritization matrix [116]:

- ≤ 2 (red cell) was considered the lowest score. In this case the scenario does not answer sufficiently to the figure of merit.
- 3 (orange cell) was considered a low-intermediate score. In this case the scenario answers quite sufficiently to the figure of merit, but there are still some problems.
- 4 (yellow cell) was considered a high-intermediate score. In this case the scenario answers sufficiently to the figure of merit.
- 5 (green cell) was considered the highest score. In this case the scenario answers sufficiently to the figure of merit and interacts properly with other system components (such as BTC, MAV).

As reported in Tab.3.3 the last two columns do not present red cells, i.e., these two scenarios answer sufficiently to all the figures of merit. The most promising concept is the Wiper system with the OS positive feature. This system does not present any orange cells and its associated score is higher.

3.7.1 TOPSIS Approach

Technique for Order Preference by Similarity to Ideal Solution (TOPSIS) is one of the numerical methods of the multi-criteria decision making. This is a broadly applicable method with a simple mathematical model. Furthermore, relying on computer support, it is very suitable practical method, see [118]. The TOPSIS method was first developed by Hwang and Yoon [119] and ranks the alternatives according to their distances from the ideal and the negative ideal solution, i.e., the best alternative has simultaneously the shortest distance from the ideal solution and the farthest distance from the negative ideal solution. The ideal solution is identified with a hypothetical alternative that has the best values for all considered criteria whereas the negative ideal solution is identified with a hypothetical alternative that has the worst criteria values. In practice, TOPSIS was successfully applied to solve selection / evaluation problems with a finite number of alternatives because it is intuitive and easy to understand

and implement. Furthermore, TOPSIS has a sound logic that represents the rationale of human choice and was proved to be one of the best methods in addressing the issue of rank reversal [120]. This method considers three types of attributes or criteria:

- Qualitative benefit attributes/criteria;
- Quantitative benefit attributes;
- Cost attributes or criteria.

In this method two artificial alternatives are hypothesized: the Ideal alternative: the one which has the best level for all attributes considered and the Negative ideal alternative: the one which has the worst attribute values. TOPSIS selects the alternative that is the closest to the ideal solution and farthest from negative ideal alternative. TOPSIS assumes that there are m alternatives (options) and n attributes / criteria and there are the score of each option with respect to each criterion. Let x_{ij} score of option i with respect to criterion j, a matrix $X = (x_{ij})$ $m \times n$ matrix. Let J be the set of benefit attributes or criteria (more is better) and let $J^{'}$ be the set of negative attributes or criteria (less is better). The main steps that describe TOPSIS method procedure are:

1. Construct normalized decision matrix. This step transforms various attribute dimensions into non-dimensional attributes, which allows comparisons across criteria. Normalize scores or data as follows: $r_{ij} = \frac{x_{ij}}{\sum_{i=1}^{i=m} x_{ij}^2}$.
2. Construct the weighted normalized decision matrix. Assume there is a set of weights for each criteria w_j for $j = 1, ..., n$. Multiply each column of the normalized decision matrix by its associated weight. An element of the new matrix is: $v_{ij} = w_j r_{ij}$.
3. Determine the ideal and negative ideal solutions. Ideal solution $A^* = v_1^*, ..., v_n^*$, where $v_j^* = max_i(v_{ij})$ if $j \in J$; $min_i(v_{ij})$ if $j \in J^{'}$. Negative ideal solution $A^{'} = v_1^{'}, ..., v_n^{'}$, where $v_j^{'} = max_i(v_{ij})$ if $j \in J$; $min_i(v_{ij})$ if $j \in J^{'}$.
4. Calculate the separation measures for each alternative. The separation from the ideal alternative is: $S_i^* = [\sum_{j=1}^{j=n} (v_j^* v_{ij})^2]^{0.5}$ with $i = 1, ..., m$.

Similarly, the separation from the negative ideal alternative is: $S_i^{'} = [\sum_{j=1}^{j=n}(v_j^{'} v_{ij})^2]^{0.5}$ with $i = 1, ..., m$.

5. Calculate the relative closeness to the ideal solution C_i^* $C_i^* = \dfrac{S_i^{'}}{S_i^{'} + S_i^*}$, with $0 < C_i^* < 1$. Select the option with Ci* closest to 1.

Results using TOPSIS method

Using the TOPSIS method the C_i^* values obtained for the different candidates are reported in Tab.3.4.

candidates	1	2	3	4	**5**	6
$\boldsymbol{C_i^*}$	0.387	0.493	0.621	0.593	**0.859**	0.758

Table 3.4 TOPSIS method candidate results.

The best candidate is candidate N.5: Wiper system that engages with a pin present on the OS. In the next Chapter further analysis and this solution optimization will be presented.

3.7.2 Reorientation Mechanism Concept Study

Manipulation refers to the process of moving or rearranging objects in the environment [1].

This is a definition for robotic manipulation. What about robotic orientation? What is orientation? How is it described in the robotic field? In order to answer to all these questions it is important to start from the very basics of what orientation is, see [106] - [110] and [121]. Robotic manipulation could be divided into

- Grasping - It deals with 6 degrees of freedom (dofs).
- Positioning - It deals with 3 translational dofs.

- Orienting - It deals with 3 rotational dofs. To perform orientation it is possible to operate on:
  - Changing the rotation axis (ω).
  - Changing the rotation angle (θ).

The goal is identifying methods to manipulate (orient) a spherical object.

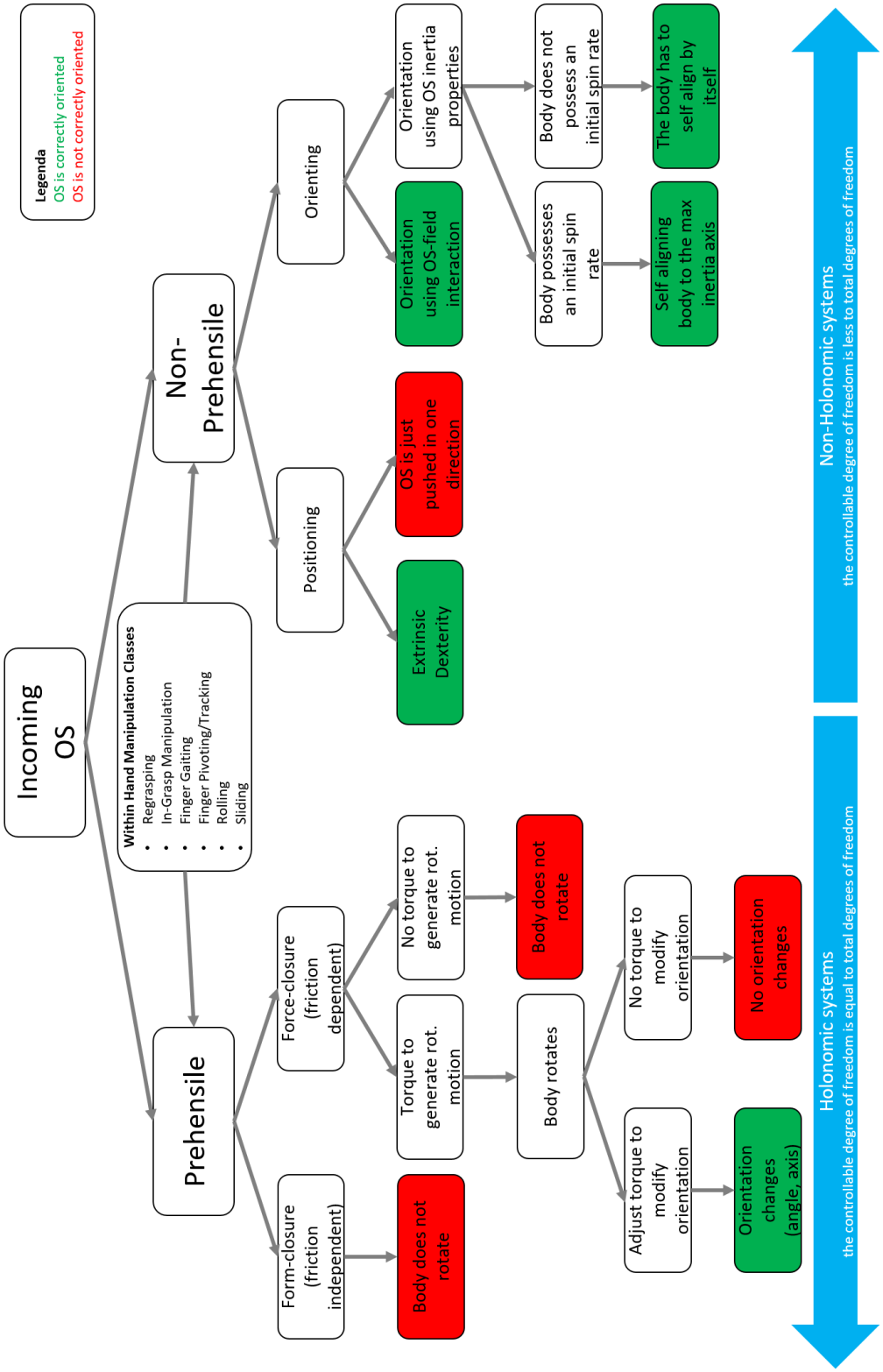

Figure 3.19 Orientation design tree.

Fig.3.19 shows the orientation design tree to collect all possible ways to orient a spherical object, the OS in particular.

1. Prehensile Approach - All the 6 dofs are considered. These systems are considered holonomic systems, where the number of the controllable degree of freedom is equal to the total degrees of freedom.
   (a) Form closure - Friction independent approach brings to a non-reorientation of the OS.
   (b) Force closure - Friction dependent approach brings to
      i. Torque to generate rotational motion - It brings to a reorientation of the OS.
         - If it is possible to adjust the torque to modify the OS orientation - It brings to a reorientation of the OS.
         - If it is not possible to adjust the torque to modify the OS orientation - It brings to a non-reorientation of the OS.
      ii. No enough torque to generate rotational motion - It brings to a non-reorientation of the OS.
2. Non-Prehensile Approach - Either 3 translational dofs or 3 rotational dofs are considered. These systems are considered non-holonomic systems, where the number of the controllable degree of freedom is less than the total degrees of freedom.
   (a) Positioning - It deals with 3 translational dofs.
      i. Extrinsic dexterity [122]. It brings to a reorientation of the OS.
      ii. The OS is just pushed in one direction - It brings to a non-reorientation of the OS.
   (b) Orienting - It deals with 3 rotational dofs.
      i. Orientation of the OS using OS-field interaction [123].
      ii. Orientation using OS inertia properties.
         - If the OS possesses an initial spin rate - It brings to a reorientation of the OS through a self-aligning to the maximum inertia axis (gyroscopic stability).

- If the OS does not possess an initial spin rate - It brings to a reorientation of the OS through a self-aligning operate by the body itself, e.g., using internal Control Moment Gyros.

Accordingly to the aforementioned classification, the Wiper mechanism could be classified as an impactive gripper. In particular, the Wiper could be considered an element of the robotic manipulation field related to Extrinsic Dexterity.

3.8 Conceptual Wiper Design Integrated in the MSR Spacecraft

In Fig.3.20 a potential ROCS design attached to the SRO mission concept is reported. In Fig.3.21 a zoom-in of this system is presented. Its position is the result of a peculiar topology study to be sure to take into account all the requirements for both the spacecraft and the system itself.

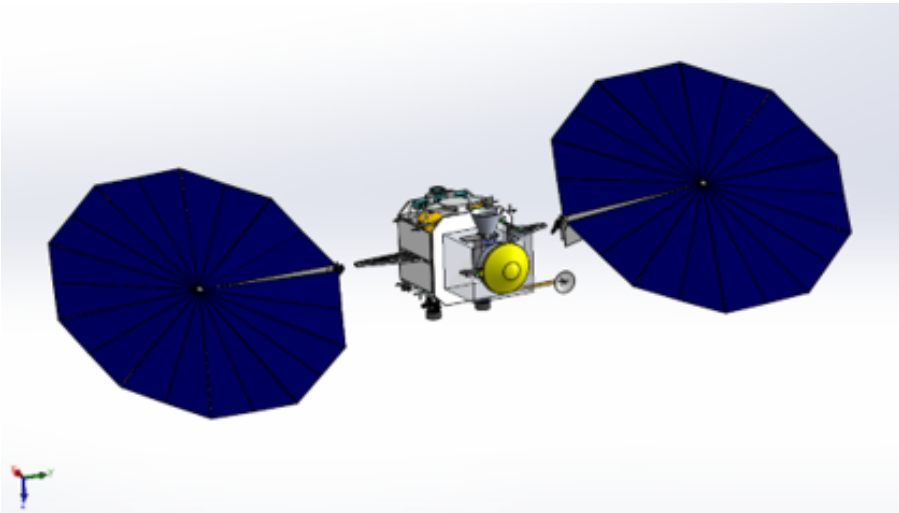

Figure 3.20 Preliminary Wiper system assembly attached to a concept of the SRO spacecraft.

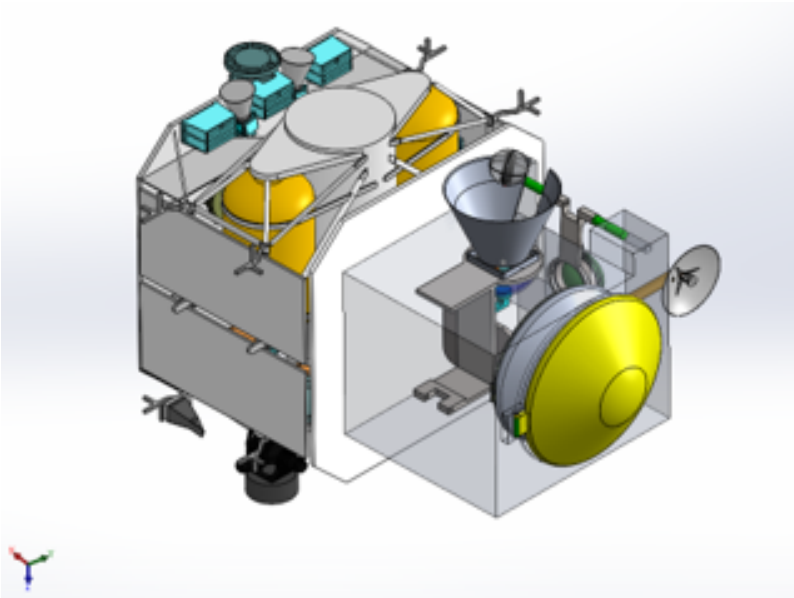

Figure 3.21 Preliminary Wiper system assembly attached to a concept of the SRO spacecraft (zoom-in).

In Figg.3.22 and 3.23 the preliminary Wiper mechanism concept story board on SRO spacecraft is reported. OS enters in the capture cone. Rotational springs are released. Cup coming from above captures the OS. Cup and u-joint align the OS axis to the capture cone axis. Cup pushes the OS to the bottom of the capture cone. Rotational actuator actuates the Wiper. It explores the whole OS surface until it engages with the pin. The Wiper reorients the OS and retains it. Capture cone system is ejected together with the Wiper and all the components that interact with the OS. Rotational actuator moves the BTC platform. BTC process starts. Linear actuator starts to move back the OS container. Linear actuator moves back the OS container. Rotational spring rotates 90° the OS container and the linear actuator. The same linear actuator moves forward the OS container inside the EEV. EEV hold door opens. EEV is ejected.

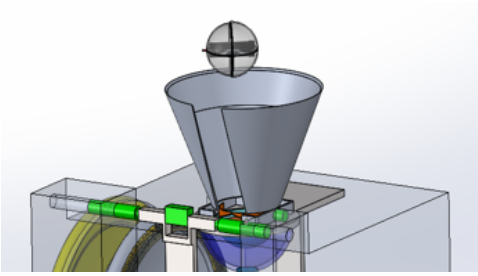

(a) OS enters in the capture cone.

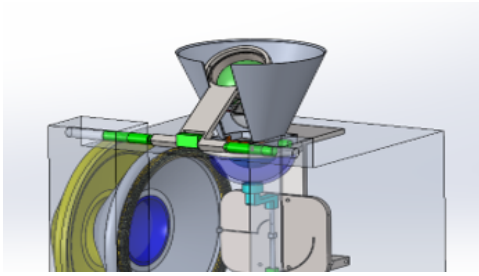

(b) Cup traps the OS inside the capture cone.

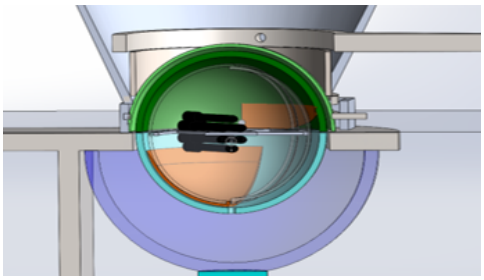

(c) Cup pushes the OS to the bottom of the capture cone.

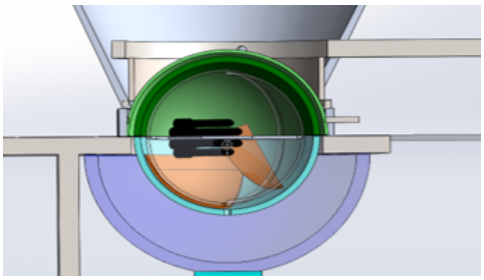

(d) Rotational actuator actuates the Wiper. It explores the whole OS surface until it engages with the pin.

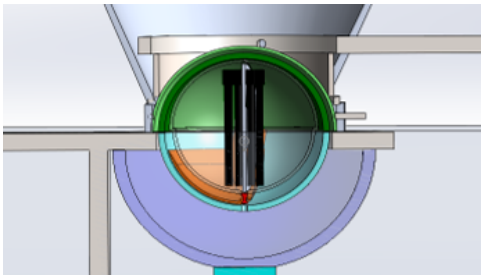

(e) The Wiper reorients the OS and retains it.

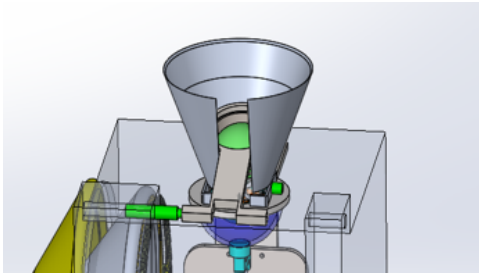

(f) The cup moves away from the capture cone.

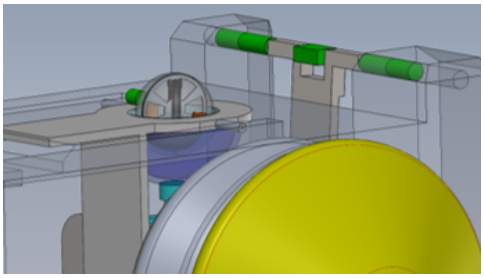

(g) Wiper and capture cone are ejected.

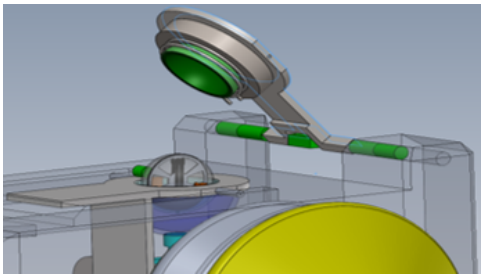

(h) Rotational actuator moves the BTC platform.

Figure 3.22 Conceptual Wiper Design integrated in the SRO spacecraft (to be continued).

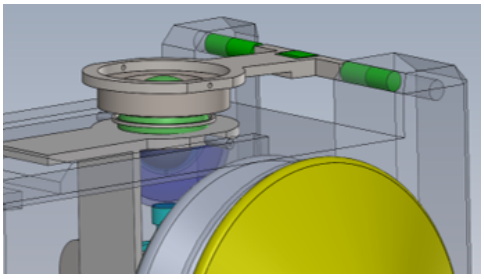

(a) BTC process starts.

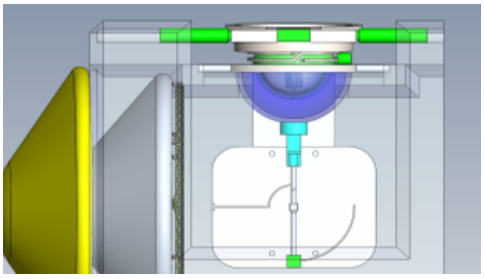

(b) Linear actuator starts to move back the OS container.

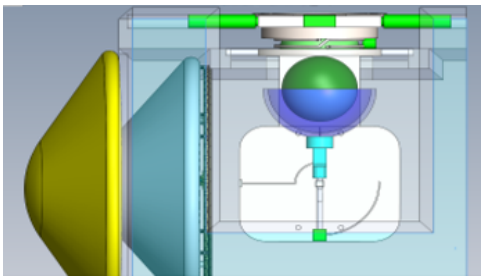

(c) Linear actuator moves back the OS container.

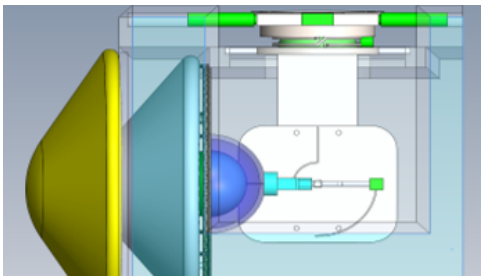

(d) Rotational spring rotates 90 deg the OS container and the linear actuator.

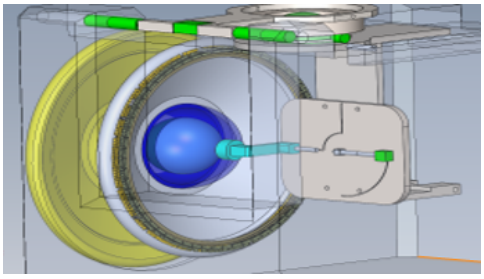

(e) The same linear actuator moves forward the OS container inside the EEV.

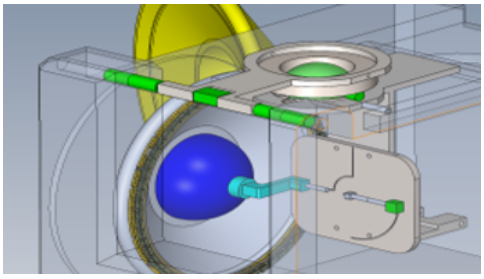

(f) EEV hold door opens.

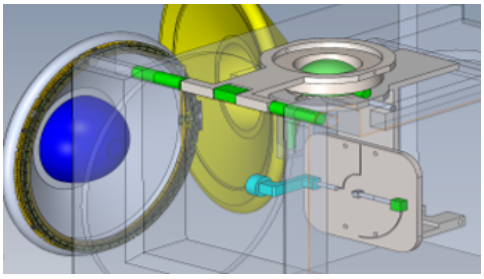

(g) EEV is ejected.

Figure 3.23 Conceptual Wiper Design integrated in the SRO spacecraft.

Chapter 4

Wiper Design and Analysis

This chapter deals with the Wiper design and analysis.

Parts of this chapter were published in:

- Concepts for a potential Mars Sample Return On-Orbit Robotic Manipulation System **Dolci M.**, Mukherjee R., Chamberlain-Simon B., Mc Cormick R., Smith R., Ohta P., Mayo J., SoCal Robotics Symposium, USC, April 14, 2017.
- Electro-Mechanical System to Reorient a Spherical Orbital Sample for a Potential Mars Sample Return Mission Concept **Dolci M.**, Mayo J., Chamberlain-Simon B., Smith R., Kim J., Ubellacker W., Ohta P., Mukherjee R., submitted to Acta Astronautica, August 2017.

The main focus in this chapter is relative to the Wiper profile, the Wiper-pin interaction and the Wiper profile optimization. The Wiper model is described with its relative optimization. The goal is to answer to the following questions:

1. Why should the Wiper present its shape?
2. How do the Wiper manufacture tolerances affect performance?

As illustrated in Ch.3, after the OS is captured, a process starts to reorient the OS and to retain it. The the reorientation mechanism is discussed. In this operational scenario the OS presents a positive feature (pin). This Wiper mechanism consists of three main components:

- A contact-less Wiper that explores the surface of the OS looking for engaging with the pin;
- A positive feature present on the OS-capturing-bottom shell that collaborates with the Wiper to move the pin toward the center of the mechanism (home location);
- An OS positive feature (pin), located on the OS with assigned shape and dimensions (length and diameter).

4.1 Testbed Design

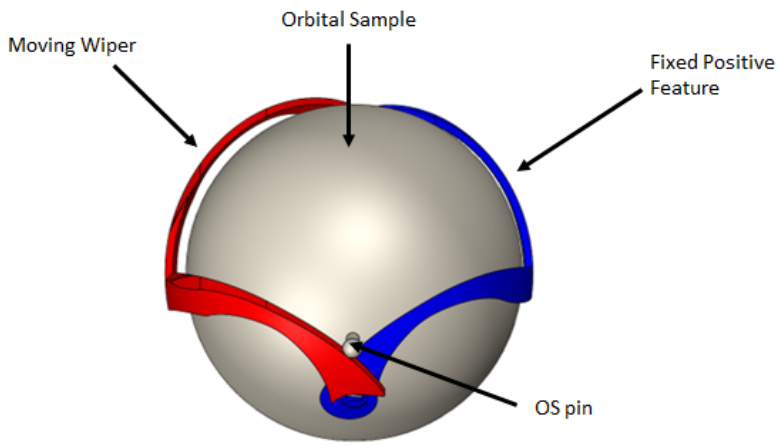

Figure 4.1 Wiper mechanism system. The Wiper sweeps a spherical profile around the OS engaging the pin in a converging fashion such that the pin terminates in a predetermined location [124].

Accordingly to the aforementioned classification, see Ch.3, the Wiper mechanism can be classified as an impactive gripper. In particular, the Wiper can be considered an element of the robotic manipulation field of Extrinsic Dexterity [122]. The Wiper interacts with two positive features: the pin on the OS and a static Wiper (fixed positive feature), which is of mirrored geometry. The Wiper rotates around a spherical volume of a diameter larger than the OS but smaller than the OS plus the pin, see Fig.4.1. Therefore along its sweep of the spherical surface, the Wiper engages with the pin and converges the pin to the home location, which is centered between the dynamic and static wipers.

4.1.1 Mechanism Sizing

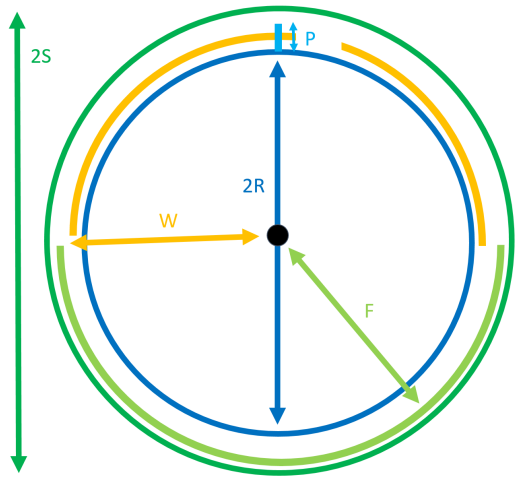

Figure 4.2 Ideal Wiper mechanism system component sizing.

In Fig.4.2 a sketch containing all the main mechanism system components is reported, see Tab.4.1. The equations to obtain a first sizing on the shell / OS / pin dimensions are reported. In this case a max 10mm of radial OS geometric center offset with respect to the shell center was considered. First of all, Eq.4.1 allows the Wiper to not miss the pin

$$P + 2R + W_{cl} > S + W. \tag{4.1}$$

If it was considered that the Wiper lays on the OS surface, Eq.4.2 was obtained

$$P + 2R + W_{cl} = S + W + Wt. \tag{4.2}$$

Calculating the whole assembly height, Eq.4.3 was produced

$$2S = P + 2R + W_{cl} + S_{cl}, \tag{4.3}$$

where W_{cl} is the clearance (2mm) considered in this testbed to allow the Wiper-OS to freely rotate without getting jammed. From Eq.4.2 the Wiper radius was achieved

$$W = P + 2R + W_{cl} - S - Wt. \tag{4.4}$$

while from Eq.4.3 the external shell radius was calculated

$$S = \frac{P + 2R + W_{cl} + S_{cl}}{2}. \tag{4.5}$$

The max clearance between the Wiper and the positive feature could be also related to the maximum sprung Wiper stretch, if a sprung Wiper were considered. The maximum offset the pin can accommodate was expressed in Eq.4.6

$$O_{max} = F - R. \tag{4.6}$$

In Tab.4.2, the actual design dimensions were reported

Variable	**Description**	**Value [mm]**
S	Minimum radius of shell	155
R	Radius of the OS	140
W	Outer radius of the Wiper	148
F	Inner radius of the positive feature	150
P	Pin length off OS surface	25
Wt	Radial width of the Wiper	5
Ft	Radial width of the positive feature	5
W_{cl}	Clearance between the Wiper and the OS	3
F_{cl}	Clearance between the positive feature and the Wiper	2
S_{cl}	Clearance between the shell and the positive feature	2
O_{max}	Offset with maximum pin length	10

Table 4.1 Design dimensions in mm for the testbed system.

In order to respect the constraint of having the OS center offset of maximum 10mm radially away from the shell center, the author and members of the MOSTT team came up with the solution of using flexible fingers to allow the OS to be centered and to allow the Wiper to pass through them, see Fig.4.3 [124].

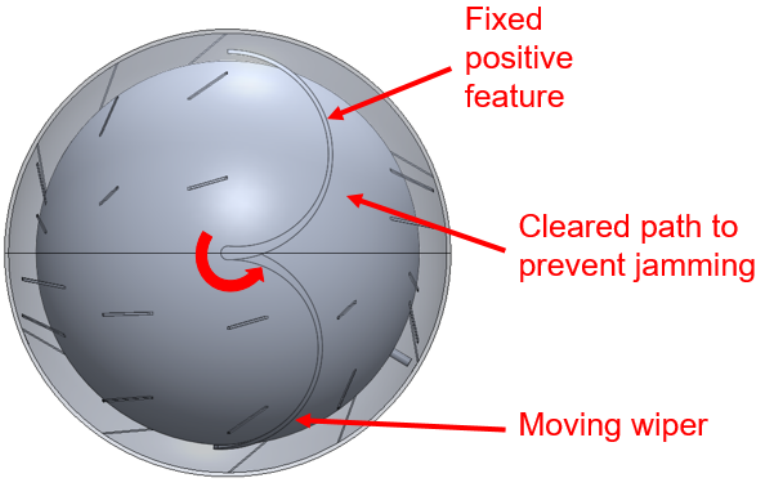

Figure 4.3 CAD of one-way flexure fingers in shell to keep the OS centered [124].

Until here, the OS was considered being a perfect sphere. This system should work also considering the OS as a non-spherical OS with two half-spheres with a radius difference (Δr) of 10mm. In this case the pin and all the other components have to be sized properly (a first value for the pin length could be $P + \Delta r = 35$mm). In this case the pin will be located at the pole of the hemisphere with the smaller diameter. However, the OS fits inside a spherical volume and this mechanism is able to satisfy this requirement even in this case.

4.1.2 Mechanism Modeling

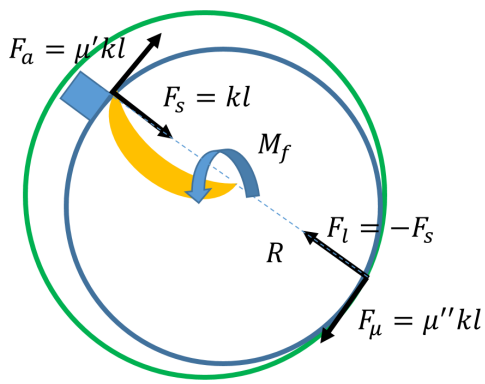

Figure 4.4 Free-body diagram of the OS in space in a zero-g environment. The forces and torques acting on the OS are reported.

Variable	**Explanation**	**Unit**
F_a	Friction force between pin and shell	N
F_s	Sprung Wiper force on the OS	N
F_l	Reaction force between the OS and the shell generated by the sprung Wiper	N
F_μ	Friction force between the OS and the shell	N
k	Wiper spring stiffness	N/m
l	Wiper spring displacement vector	m
M_f	Torque exerted on the OS by the Wiper to reorient it	Nm
$\mu^{'}$	Pin-shell friction coefficient	-
$\mu^{''}$	OS-shell friction coefficient	-
α	Scissor angle	deg

Table 4.2 Variable explanation table.

A 2D model is illustrated describing the side view of the Wiper interacting with the pin and with the positive feature. The free-body diagram of the OS in space in a zero-g environment is reported in Figg.4.4, 4.5 and 4.6. All the main forces and torques acting on the OS are reported. From this diagram the Wiper torque is reported in Eq.4.7

$$M_f = 2Rkl(\mu^{'} + \mu^{''}). \tag{4.7}$$

It was worth noticing the torque is proportional both to the Wiper stiffness (both a sprung and a non-sprung Wiper have been adopted by the the author and members of the MOSTT team in the Wiper testbed), to the Wiper-pin friction and to the OS-shell friction. While the Wiper-pin friction is a parameter possible to be adjusted, the OS-shell friction is a future given value function of the OS and shell materials. Moreover, the OS could be dirty of Martian dust / sand and this can affect unpredictably the friction between the OS and the shell. The friction plane chosen to be represented in this model is the most critical one, because on this plane the angle between the Wiper and the positive feature profiles becomes smaller and so jamming conditions could happen most

likely. When the pin moves on the Wiper profile this plane stays normal to the pin vertical axis.

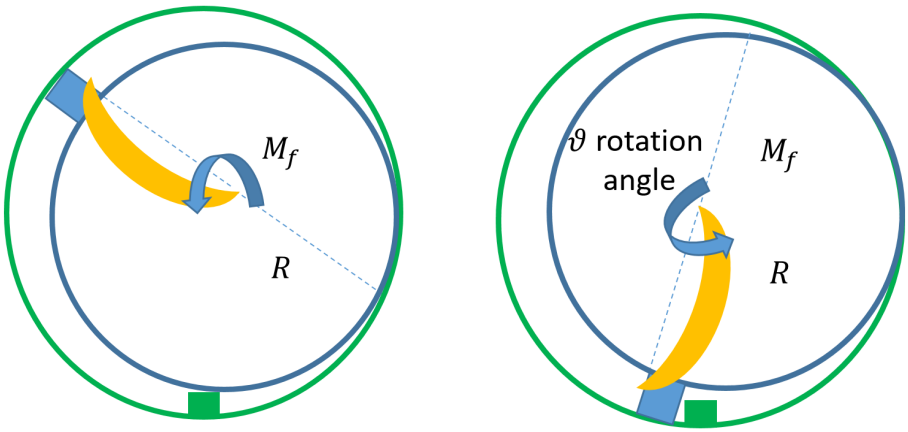

(a) Free-body diagram of the OS in space in a zero-g environment. The Wiper swipes the OS surface until it engages with the pin.

(b) Free-body diagram of the OS in space in a zero-g environment. The Wiper pushes the pin inside the home location working together with the positive feature.

Figure 4.5 Free-body diagram of the OS in space in a zero-g environment.

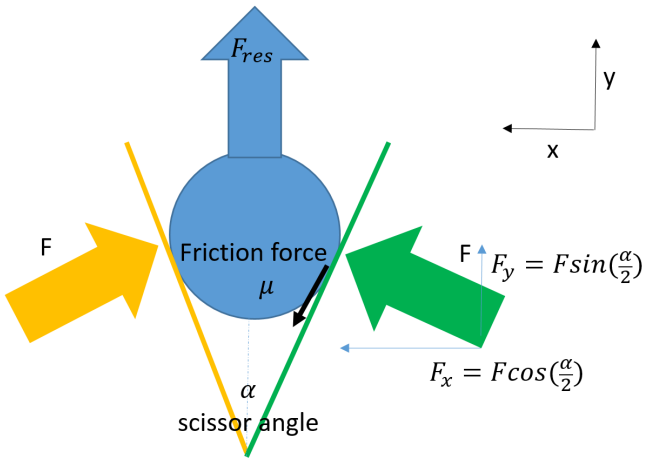

Figure 4.6 Free-body diagram detail of the Wiper-positive feature interaction with the pin.

The effective force that the pin feels to make it moving towards the home location is

$$F_{res} = 2F\sin\left(\frac{\alpha}{2}\right) - 2\mu F\cos\left(\frac{\alpha}{2}\right), \tag{4.8}$$

where α is the scissor angle in the friction plane and $\mu = \mu^{'}$. When the pin moves on the Wiper profile this plane keeps staying normal to the pin vertical axis. This model shows that this situation does not present any jamming conditions and it is worth running a more detailed 3D analysis.

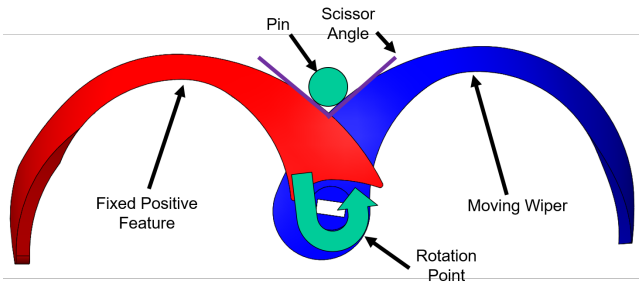

Figure 4.7 Wiper-positive feature interaction with the OS pin has to guarantee a larger scissor angle (3D angle Wiper-positive feature profile angle) for least friction [124]. In this case the rotation angle is 0°. It increases counterclockwise.

The Wiper requires a spherical section geometry, and has a splined contour which is designed to maximize the scissor angle α for minimizing friction between the wipers and the pin, as reported in Fig.4.7. The scissor angle is the angle between the Wiper and the positive feature curves that can accommodate the pin. This angle is fundamental because it can be coupled to the mechanical advantage of this system. The ideal mechanical advantage (MA), or theoretical mechanical advantage, is the mechanical advantage of a device with the assumption that its components do not flex and there is no wear. It is calculated using the physical dimensions of the device and defines the maximum performance the device can achieve, see [125]. The assumptions of an ideal machine are equivalent to the requirement that the machine does not store or dissipate energy; the power into the machine thus equals the power out. The ideal mechanical advantage is the ratio of the force out of the machine (load) to the force into the machine (effort)

$$MA = \frac{F_{out}}{F_{in}}. \tag{4.9}$$

The system mechanical advantage results to be expressed in Eq.4.10

$$MA = 2\sin\left(\frac{\alpha}{2}\right) - 2\mu\cos\left(\frac{\alpha}{2}\right). \tag{4.10}$$

The mechanical advantage of this mechanism was considered as cost function to optimize the Wiper profile. A MA>0.5 was considered enough for the proper working of this mechanism.

4.2 Wiper Analysis

The goal of this section is to create an analytical model to describe the Wiper mechanism profile. This procedure presents the following advantages:

- The whole system can be proofed to have a deterministic behavior (effective closed-form solution).
- An analytical model is easier to be optimized than a numerical model. This helps a lot for what concerns the possible tolerances for manufacturing in case of possible damages and / or dirt caused by unforeseen Martian dust / sand.

This advantages are mitigated by the cost of a more complex and time consuming implementation.

In this model the Wiper profile was identified using the blue color while the positive feature was identified with the green color. The pin model was red. The pin section view was a circle. Assuming that the pin relies also on a contact with the Wiper and the positive feature, the pin center can be described as belonging to the intersecting points between the the normal curves to both the Wiper curve and the positive feature curve.

4.2.1 Potential Wiper Requirements

To obtain the most adequate Wiper shape and profile for the present testbed, the potential requirements were listed:

- Wiper profile shall swipe a fictitious spherical surface around the OS (compactness) to host the incoming OS respectful of all the possible orientations. This translates in the Wiper height being less than the OS radius.

- Wiper rotation shall not relate to the OS surface properties (e.g., friction). The OS could be contaminated with Mars sand or dust and these unpredictable elements could affect the correct Wiper work. Moreover, having a contact-less Wiper can guarantee the properly work considering both a spherical OS and an OS made up of two hemispheres with different diameters (10mm difference).
- Wiper shall be able to engage with the pin and move it to the Wiper center within a 720° (2 complete loops) rotation.
- Wiper and positive feature shape and curvature shall be able to move the pin to the provisional retention mechanism whatever orientation the OS comes in (singularity conditions).
- Wiper and positive feature shape and curvature shall be able to move the pin to the provisional retention mechanism whatever position the pin presents during the actuation of the whole mechanism (jamming conditions).
- Wiper shall be ejectable together with the Wiper support structure on a direction laying on the same plane of the shells contact plane.

To obtain the most adequate Wiper shape and profile and being respectful of all the previous potential requirements, an evolutionary process was developed. This process takes into account the following cost functions:

- Scissor angle - Guarantee that the scissor angle has positive values means that the pin has been engaged by the Wiper avoiding any possible singularity conditions.
- Mechanical advantage - Guarantee that the mechanical advantage is greater than 0 and ideally greater than 0.5 (50% margin on the MA) means avoiding any possible jamming conditions.

4.2.2 Wiper 2D Analysis

First of all, a 2D analysis was executed concerning the most critical friction plane (x-z plane). This is the page plane on which Fig.4.8 is reported. This figure reports both the CAD Wiper model and the 2D Matlab model.

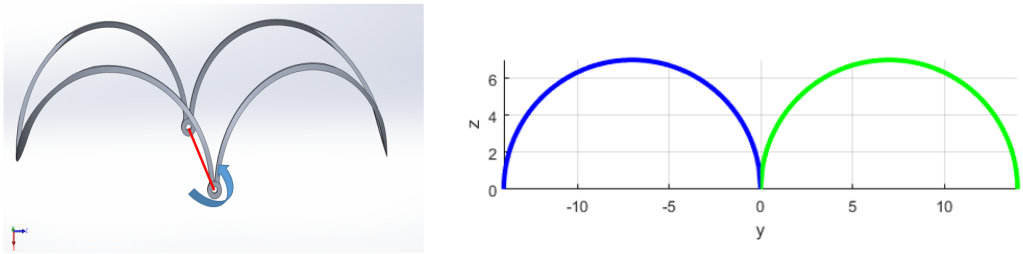

(a) CAD Wiper model. The blue arrow indicates the rotation angle. It is 0° in the shown configuration.

(b) 2D Matlab Wiper model. The rotation angle is 0° in the shown configuration.

Figure 4.8 Wiper 2D analysis.

Fig.4.9 depicts the Wiper 2D analysis results. The rotation angle represents the angle the Wiper rotates whose rotation axis passes through the Wiper-positive feature intersection, see Fig.4.8.

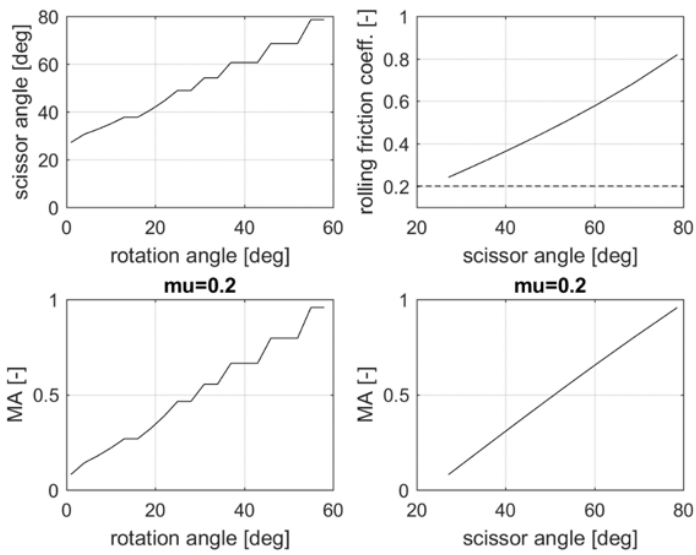

Figure 4.9 Wiper 2D analysis results.

Here a rotation angle range was assumed to be 0-60° because this range represents the most critical jamming condition angles. In the bottom right plot the MA is close to 0. This can bring to a jamming condition and so to the end of the whole MSR mission. The top left plot reports the upper limit static rolling friction coefficient between the Wiper and the pin. This means that

higher this curve is better it is, the system needs to have a friction coefficient lower than the plotted curve. The dashed line represent a value of 0.2. In order to solve this condition, the idea to modify the Wiper profile was considered. Fig.4.10 reports both the modified CAD Wiper model and the 2D Matlab model.

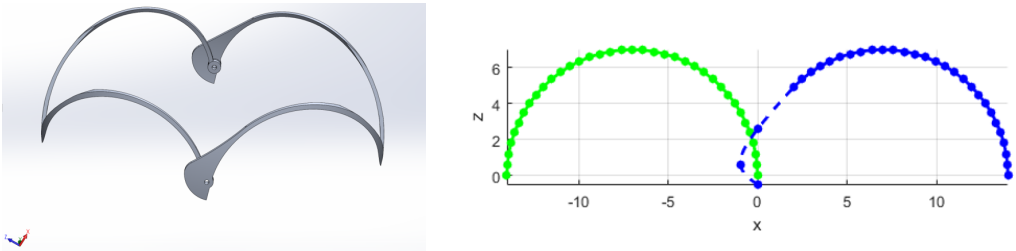

(a) CAD modified Wiper model. (b) 2D Matlab modified Wiper model.

Figure 4.10 Modified Wiper 2D analysis results.

Fig.4.11 depicts the modified Wiper 2D analysis results.

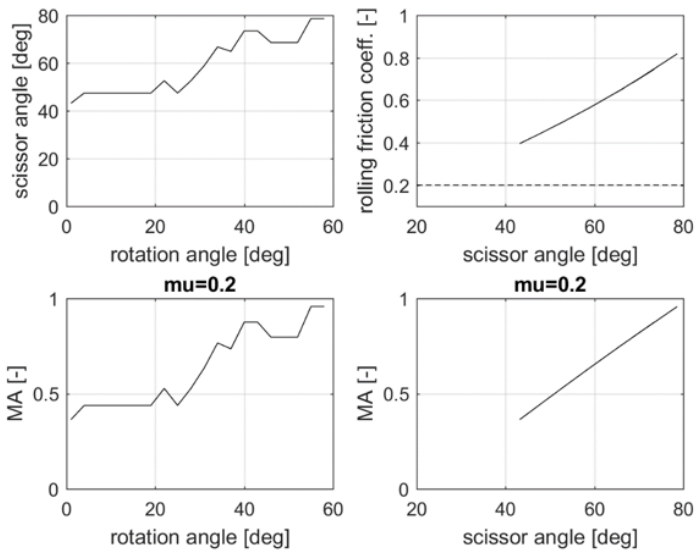

Figure 4.11 Modified Wiper 2D analysis results.

The MA is higher especially at rotational angle closer to 0°. Further analysis adopting 3D models are required to optimize this Wiper profile.

4.3 Wiper 3D Analysis - Evolutionary Process

With respect to the 2D case, for what concerns the 3D analysis a high-level approach was taken into account. To optimize the Wiper-positive feature profile an evolutionary approach was considered to create a general flow going from almost all possible Wiper configurations to the final one. Respectful of all the aforementioned potential requirements, different candidates were examined to obtain the best Wiper in terms of scissor angle and mechanical advantage for all the rotation angles. Fig.4.12 reports the four candidates.

1. Arc-arc scenario;
2. Arc-Wiper scenario;
3. Wiper-Wiper scenario;
4. Optimized Wiper-Wiper scenario.

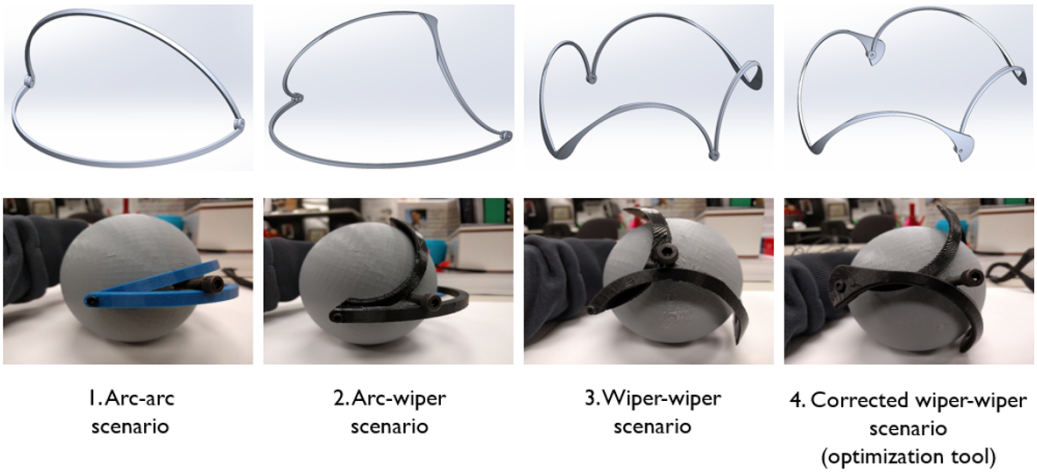

Figure 4.12 Wiper 3D evolutionary process analysis. The four candidates that are discussed in the next Sections. Top line: CAD drawings. Bottom line: Z-Ultra 3D-printed models to have a practical understanding of the problem and for tests [124].

As reported in Fig.4.12, some Z-Ultra 3D-printed models were realized to have a practical understanding of the problem.

4.3.1 Case 1: Arc-Arc Scenario

The first chosen approach was the Arc-Arc scenario. In this case both the Wiper and the positive feature were considered being formed adopting two half circular arcs. 3D simulations and results are reported in Figg.4.13 and 4.14. In Fig.4.13 the 3D Matlab simulation of half of the mechanism is depicted. Only half of the system was reported because of symmetry to reduce the computational time.

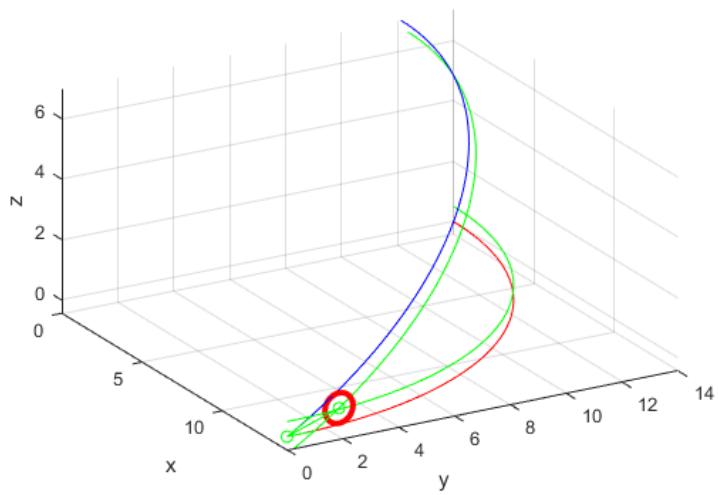

Figure 4.13 Arc-Arc scenario 3D Matlab simulation.

In Fig.4.14 it was possible to notice that both the scissor angle and the MA reach a point in which they become negative. This happens because the two arcs rotate on each other up to a point where the angle between their edges (the scissor angle) becomes so small that the pin jams and cannot move anymore (MA=0).

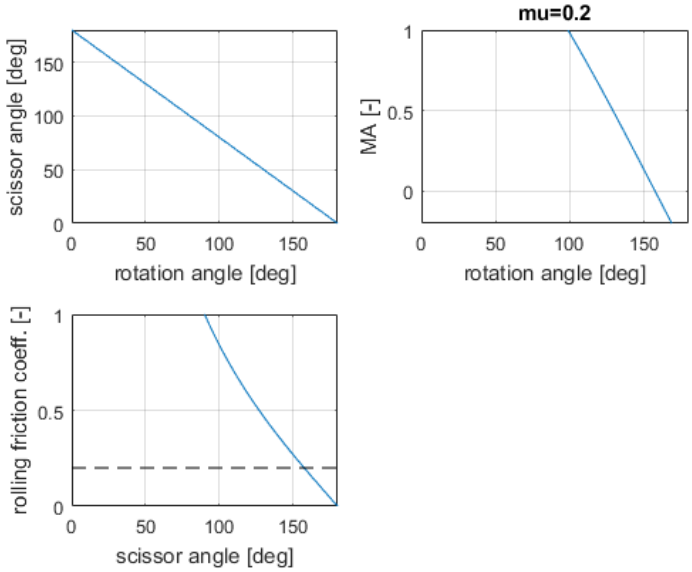

Figure 4.14 Arc-Arc scenario 3D Matlab simulation results as functions of the rotation angles from 0-180°. Top left: scissor angle. Top right: MA. Bottom: static rolling friction coefficient.

This scenario does not guarantee a complete accomplishment of the mechanism goal.

4.3.2 Wiper 3D Analytical Profile

After the failure of scenario 1, 3D curves were considered that can satisfy the potential requirements whose description can be performed analytically.

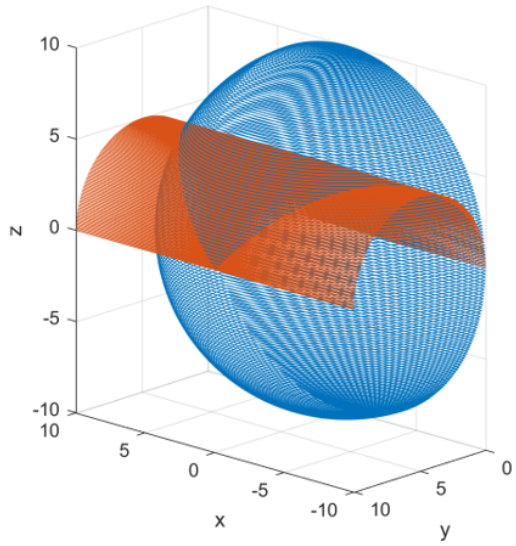

Figure 4.15 From the intersection of the cylinder of radius $\frac{R}{2}$ and center $(\frac{R}{2},0)$ and a sphere with center $(0,0,0)$ and radius R Viviani curve is born.

A possibility would be using Viviani curves, defined by Viviani in 1692, see [126], [127], [128], [130], [131], and [132]. Viviani's curve, sometimes also called Viviani's window, is the space curve giving the intersection of the cylinder of radius $\frac{R}{2}$ and center $(\frac{R}{2},0)$

$$\left(y-\frac{R}{2}\right)^2+z^2=\left(\frac{R}{2}\right)^2 \tag{4.11}$$

and the sphere

$$x^2+y^2+z^2=R^2 \tag{4.12}$$

with center $(0,0,0)$ and radius R, see Fig.4.15 and 4.16.

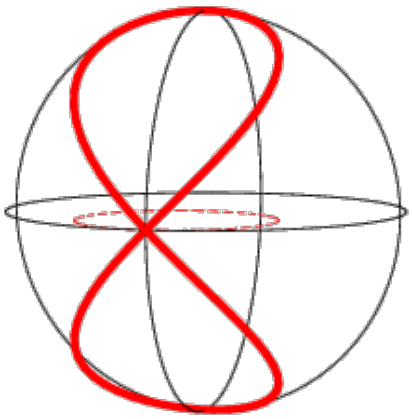

Figure 4.16 Graphical representation of the Viviani curve on a sphere [132].

The equation describing the Viviani's curve is given by

$$f[x(\theta), y(\theta), z(\theta)] = \left[-\frac{R}{2} + \frac{R}{2}\cos\theta, \frac{R}{2}\sin\theta, R\cos\left(\frac{\theta}{2}\right)\right], \tag{4.13}$$

with $\theta \in [0, 2\pi)$. For the scope of this work the whole Viviani's curve was not adopted, but two halves of two Viviani's curves. The relative equation parametrized using the parameter t, from -R (Wiper radius) to R, becomes Eq.4.14

$$f[x(t), y(t), z(t)] = \left[t, \frac{t^2 - R^2}{R}, \sqrt{R^2 - t^2 - \frac{(t^2 - R^2)^2}{R^2}}\right]. \tag{4.14}$$

For what concerns the positive feature curve, the points described by Eq.4.14 were plotted. This curve was rotated of 90° around the x-axis. The vector describing the positive feature curve orientation is depicted in Eq.4.15

$$vec_{PF}(\theta) = [x(\theta), -z(\theta), y(\theta)]^T. \tag{4.15}$$

To describe analytically the shifted normal curve to the positive feature curve to describe the pin motion, the following steps were taken. For a curve with radius vector $\mathbf{r}$(t), the unit tangent vector $\mathbf{T}$(t) is defined by

$$\mathbf{T}(t) \equiv \frac{\dot{\mathbf{r}}}{|\dot{\mathbf{r}}|} = \frac{\dot{\mathbf{r}}}{|\dot{s}|} = \frac{d\mathbf{r}}{ds}, \tag{4.16}$$

where t is a parameterization variable, s is the arc length, and $\dot{\boldsymbol{x}} = \frac{d\boldsymbol{x}}{dt}$. It is also true that

$$\frac{d\hat{\mathbf{T}}}{ds} = k\hat{\mathbf{N}} \tag{4.17}$$

$$\frac{d\hat{\mathbf{T}}}{dt} = k\frac{ds}{dt}\hat{\mathbf{N}} \tag{4.18}$$

where $\mathbf{N}$ is the normal vector and k is the curvature [133]. Finding the intersection point between the Wiper and the positive feature is pretty straightforward. Finding the intersection point that identifies the pin center is more tricky. Some innovative passages are reported to define this intersection point. Let $\mathbf{r}(t)$ be a differentiable vector valued function on $[a,b]$.

$$\mathbf{r}(t) = x(t)\hat{\mathbf{i}} + y(t)\hat{\mathbf{j}} + z(t)\hat{\mathbf{k}}. \tag{4.19}$$

Then the arc length s is defined by Eq.4.20

$$s = \int_a^b \sqrt{\left(\frac{dx}{dt}\right)^2 + \left(\frac{dy}{dt}\right)^2 + \left(\frac{dz}{dt}\right)^2}\, dt, \tag{4.20}$$

where dt is the unit tangent vector. Tangent vectors have slopes equivalent to the instantaneous slope of a curve at the given point, see Eq.4.21

$$\mathbf{T} = \frac{d\mathbf{r}}{dt} \quad \hat{\mathbf{T}} = \frac{\mathbf{T}}{|\mathbf{T}|} = \frac{d\mathbf{r}/dt}{|d\mathbf{r}/dt|}. \tag{4.21}$$

Curvature is a measure of how much the curve deviates from a straight line. Let us assume that the curve is defined in terms of the arc length s to make things easier. Most curves are written in parametric equations in terms of some dummy variable, see Eq.4.22

$$\kappa = \left|\frac{d\hat{\mathbf{T}}}{ds}\right| = \left|\frac{d\hat{\mathbf{T}}}{dt} \cdot \frac{dt}{ds}\right| = \frac{1}{|ds/dt|}\left|\frac{d\hat{\mathbf{T}}}{dt}\right|. \tag{4.22}$$

A unit normal vector of a curve is perpendicular to the curve at given point. This means a normal vector of a curve at a given point is perpendicular to the tangent vector at the same point. Normal vector of a curve is the derivative of

tangent vector of a curve, see Eq.4.23

$$\hat{\mathbf{N}} = \frac{1}{\kappa}\frac{d\hat{\mathbf{T}}}{ds} = \frac{1}{\kappa}\frac{d\hat{\mathbf{T}}}{dt}\cdot\frac{dt}{ds} = \frac{\dfrac{d\hat{\mathbf{T}}}{dt}}{\left|\dfrac{d\hat{\mathbf{T}}}{ds}\right|}\cdot\frac{\left|\frac{ds}{dt}\right|}{\frac{ds}{dt}}. \tag{4.23}$$

Applying this math to the case under study, Eq.4.24 was obtained

$$\mathbf{r}(\mathbf{t}) = \left(-\frac{R}{2}+\frac{R}{2}\cos\theta\right)\hat{\mathbf{i}}+\left(\frac{R}{2}\sin\theta\right)\hat{\mathbf{j}}+\left(R\cos\frac{\theta}{2}\right)\hat{\mathbf{k}}. \tag{4.24}$$

The arc length s was defined by Eq.4.25

$$s = \int_0^t \sqrt{\frac{R^2}{4}\left(1+\sin^2\frac{\theta}{2}\right)}dt. \tag{4.25}$$

This integral is an incomplete elliptic integral of the second kind. The goal was to calculate its derivative with respect to the parameter t:

$$\frac{ds}{dt} = \sqrt{\frac{R^2}{4}\left(1+\sin^2\frac{\theta}{2}\right)}. \tag{4.26}$$

Looking at the fact that $\frac{ds}{dt} > 0$ is always valid, $\frac{\left|\frac{ds}{dt}\right|}{\frac{ds}{dt}} = 1$ was inferred. The Unit Normal Vector becomes was expressed in Eq.4.27

$$\hat{\mathbf{N}} = \frac{\dfrac{d\hat{\mathbf{T}}}{dt}}{\left|\dfrac{d\hat{\mathbf{T}}}{dt}\right|}. \tag{4.27}$$

The Tangent Vector was expressed in Eq.4.28

$$\mathbf{T} = \frac{d\mathbf{r}}{dt} = \left(-\frac{R}{2}\sin\theta\right)\hat{\mathbf{i}}+\left(\frac{R}{2}\cos\theta\right)\hat{\mathbf{j}}+\left(-\frac{R}{2}\sin\frac{\theta}{2}\right)\hat{\mathbf{k}}, \tag{4.28}$$

and the Unit tangent Vector was expressed in Eq.4.29

$$\hat{\mathbf{T}} = \frac{\mathbf{T}}{|\mathbf{T}|} = \frac{d\mathbf{r}/dt}{|d\mathbf{r}/dt|} = \frac{\left(-\frac{R}{2}\sin\theta\right)\hat{\mathbf{i}} + \left(\frac{R}{2}\cos\theta\right)\hat{\mathbf{j}} + \left(-\frac{R}{2}\sin\frac{\theta}{2}\right)\hat{\mathbf{k}}}{\sqrt{\left(\frac{R}{2}\sin\theta\right)^2 + \left(\frac{R}{2}\cos\theta\right)^2 + \left(\frac{R}{2}\sin\frac{\theta}{2}\right)^2}}. \tag{4.29}$$

All the needed calculations to obtain the real aspect of $\hat{\mathbf{N}}$ were shown in Eqq.4.30, 4.31, 4.32, and 4.33

$$\frac{d\hat{T}_1}{dt} = \frac{-A^{1/2}\cos\theta + A^{-0.5}\sin\theta\sin\frac{\theta}{2}\cos\frac{\theta}{2}}{A}, \tag{4.30}$$

$$\frac{d\hat{T}_2}{dt} = \frac{-A^{1/2}\sin\theta - A^{-0.5}\cos\theta\sin\frac{\theta}{2}\cos\frac{\theta}{2}}{A}, \tag{4.31}$$

$$\frac{d\hat{T}_3}{dt} = \frac{-\frac{A^{1/2}}{2}\cos\frac{\theta}{2} + A^{-0.5}\sin^2\frac{\theta}{2}\cos\frac{\theta}{2}}{A}, \tag{4.32}$$

$$\left|\frac{d\hat{\mathbf{T}}}{dt}\right| = \sqrt{\left(\frac{d\hat{T}_1}{dt}\right)^2 + \left(\frac{d\hat{T}_1}{dt}\right)^2 + \left(\frac{d\hat{T}_1}{dt}\right)^2}, \tag{4.33}$$

where $A = 1 + \sin^2\frac{\theta}{2}$. The Unit Normal Vector was so expressed in Eq.4.34

$$\hat{\mathbf{N}} = \frac{\frac{d\hat{T}_1}{dt}\hat{\mathbf{i}} + \frac{d\hat{T}_2}{dt}\hat{\mathbf{j}} + \frac{d\hat{T}_3}{dt}\hat{\mathbf{k}}}{\left|\frac{d\hat{\mathbf{T}}}{dt}\right|}. \tag{4.34}$$

The same steps were taken also for the Wiper curve. It was rotated of an angle β (rotation angle) also around the y-axis expressed in Eq.4.35. This rotation represents the Wiper motion during the mechanism operation.

$$vec_W(\theta) = [-x(\theta)\cos\beta + y(\theta)\sin\beta, -z(\theta), +x(\theta)\sin\beta + y(\theta)\cos\beta]^T. \tag{4.35}$$

To identify the intersection point that describes the pin center, two different approaches were operated:

1. Optimization search algorithm through all the points of the curves (time consuming, less precise, simpler).

2. After having defined analytically the Unit Normal vector equations, solving them numerically using *matlab vpasolve* command to find θ of intersection (less time consuming, very precise, more complex).

First, the first approach was used, then due to time consuming issues necessary to reach a high precision level the second approach was selected. Fig.4.17 reports the search algorithm simulation details. In the (a) plot the center of the circle is not located where the two red lines (normal curves) intersect, while in the (b) plot the cross locates at the exact intersection between the two normal curves.

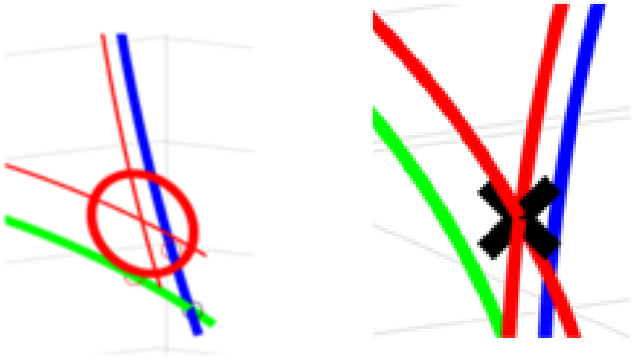

(a) Optimization search algorithm simulation detail (less precise).

(b) Analytical search algorithm simulation detail (more precise).

Figure 4.17 Search algorithm simulation details.

Looking for the intersection point between the two red curves (normal curves to the Wiper and positive feature curves of a distance equals to the pin radius) Eq.4.36 was obtained

$$\cos\theta\left(-a\frac{R}{2}-\frac{R}{2}\right)+\sin\theta b\frac{R}{2}=\frac{R}{2}(-a-1)+R_p(-\hat{N}_1-a\hat{N}_1+b\hat{N}_2), \quad (4.36)$$

where $a=\cos\beta$, $b=\sin\beta$ and R_p is the pin radius. Solving this equation with respect to θ it is possible to find the value of the position of the intersecting point, that is the pin position.

4.3.3 Case 2: Arc-Wiper Scenario

The second chosen approach was the Arc-Wiper scenario. In this case for the Wiper was adopted the whole analytical model depicted in the Subsec.4.3.2 and the positive feature is considered adopting a half circular arc. 3D simulations and results are reported in Figg.4.18 and 4.19. In Fig.4.18 the 3D Matlab simulation of half of the mechanism is depicted. Only half of the system was reported because of symmetry to reduce the computational time.

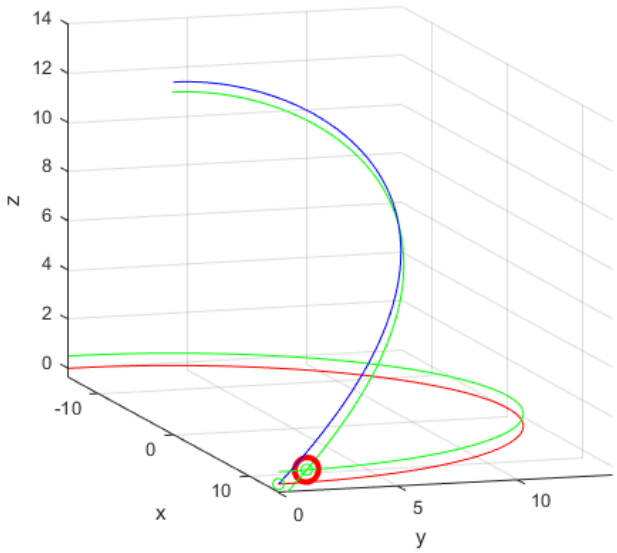

Figure 4.18 Arc-Wiper scenario 3D Matlab simulation.

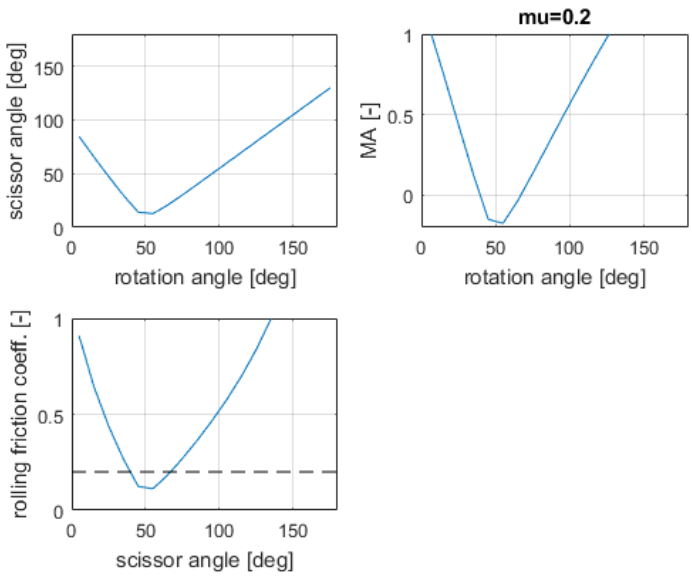

Figure 4.19 Arc-Wiper scenario 3D Matlab simulation results as functions of the rotation angles from 0-180°. Top left: scissor angle. Top right: MA. Bottom: static rolling friction coefficient.

In this case at rotation angles around 50° the scissor angle, the MA and the static rolling friction coefficient reach values closer to zero and below, see Fig.4.19. This means that in these situations the pin jams jeopardizing the whole MSR mission. This scenario does not guarantee a complete accomplishment of the mechanism goal.

4.3.4 Case 3: Wiper-Wiper Scenario

The third chosen approach is the Wiper-Wiper scenario. In this case for both the Wiper and the positive feature is adopted the whole analytical model depicted in the Subsec.4.3.2. In Figg.4.20 and 4.21 the 3D Matlab simulation of half of the mechanism is depicted. Only half of the system was reported because of symmetry to reduce the computational time. The color code adopted is the blue line represents the Wiper, the green line the positive feature, the red lines represent the normal curves to both the Wiper and the positive feature in the 3D space. Their intersection determines the pin position and the scissor angle evaluation (black cross).

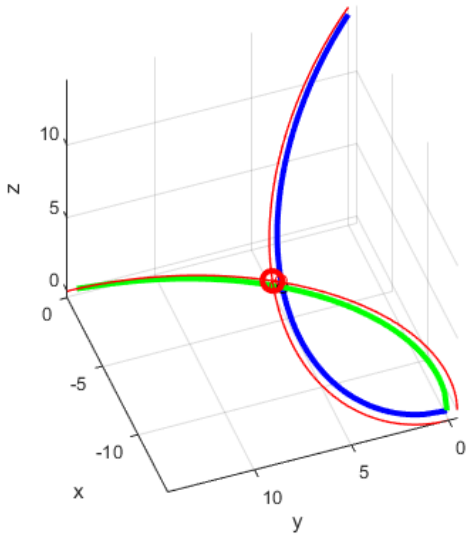

Figure 4.20 Wiper-Wiper scenario 3D Matlab simulation.

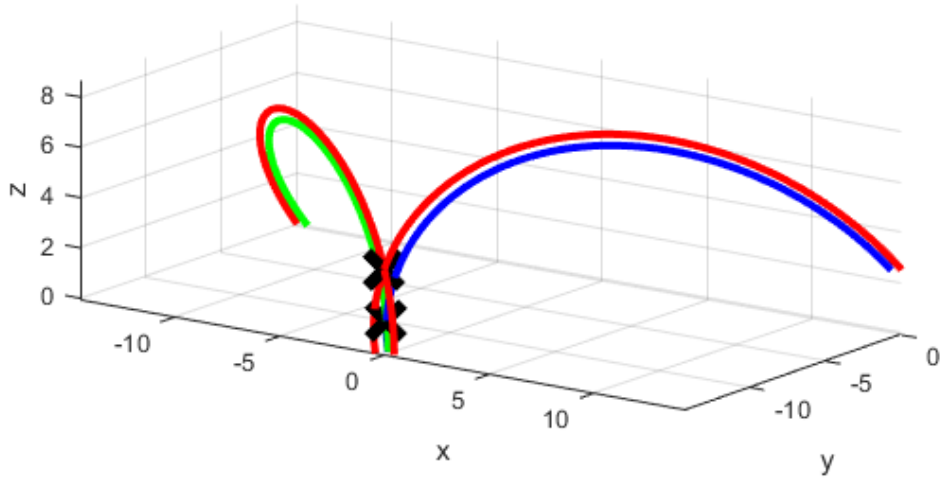

Figure 4.21 Wiper-Wiper scenario 3D Matlab simulation. The blue line represents the Wiper, the green line the positive feature, the red lines represent the normal curves to both the Wiper and the positive feature. Their intersection determines the pin position and the scissor angle evaluation (black crosses).

Fig.4.22 depicts four frames of a video simulation produced using Matlab and ImageJ. It is interesting to notice that the analytical model discussed before results in a precise and correct simulation. The pin moves towards the final home location.

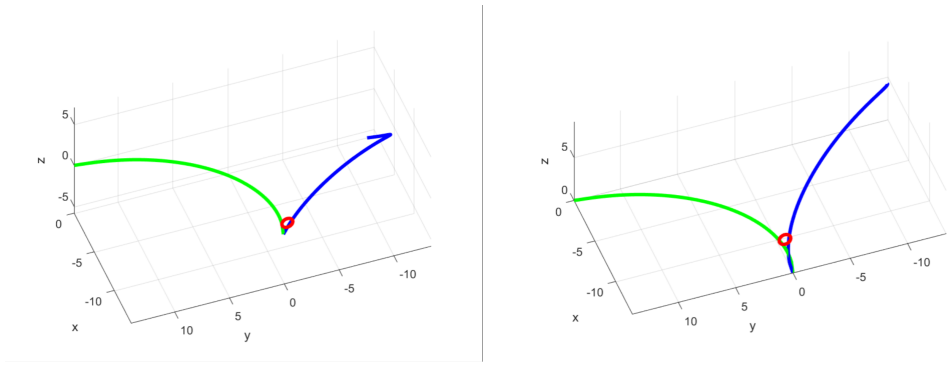

(a) Wiper has been actuated. The pin is located closer to the intersection between the Wiper and the positive feature.

(b) Wiper keep pushing the pin out of the critical area.

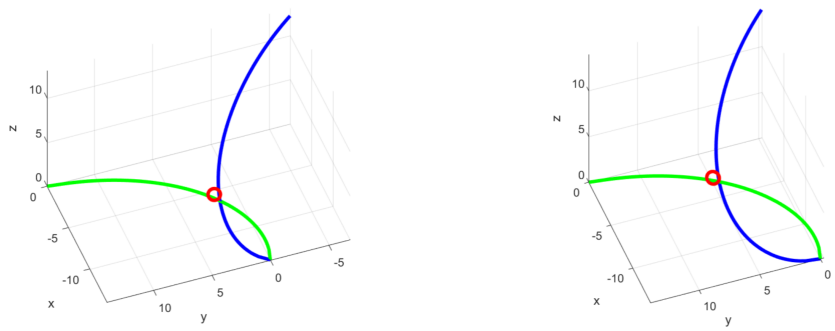

(c) Wiper keeps moving the pin helped by the interaction with the positive feature.

(d) Wiper keeps moving the pin towards the final pin home location.

Figure 4.22 Frames of a video simulation produced using Matlab and ImageJ about the Wiper (blue)-positive feature (green)-pin (red) interaction.

Different Pin Radii

Fig.4.23 shows the simulation analysis results obtained for this specific scenario as functions of the rotation angles and parametrized with respect to the pin radius (blue 5mm, green 10mm, red 15mm). Even in this case, it is possible to notice that both the scissor angle and the MA get to a point in which they become negative. This means that the Wiper mechanism jams. As expected, a higher scissor angle and MA is obtained for higher pin radii. This happens because a larger pin will be able to escape easier from the critical pin location than a smaller pin. The easiness is proportional to the fact that at a given scissor angle, larger the pin is, larger the subtended pin angular diameter is. If

the pin angular diameter becomes larger than the minimum scissor angle the pin will never be in a jamming condition. Unfortunately, this is not possible. The system efficiency has to rely on the Wiper optimized profile.

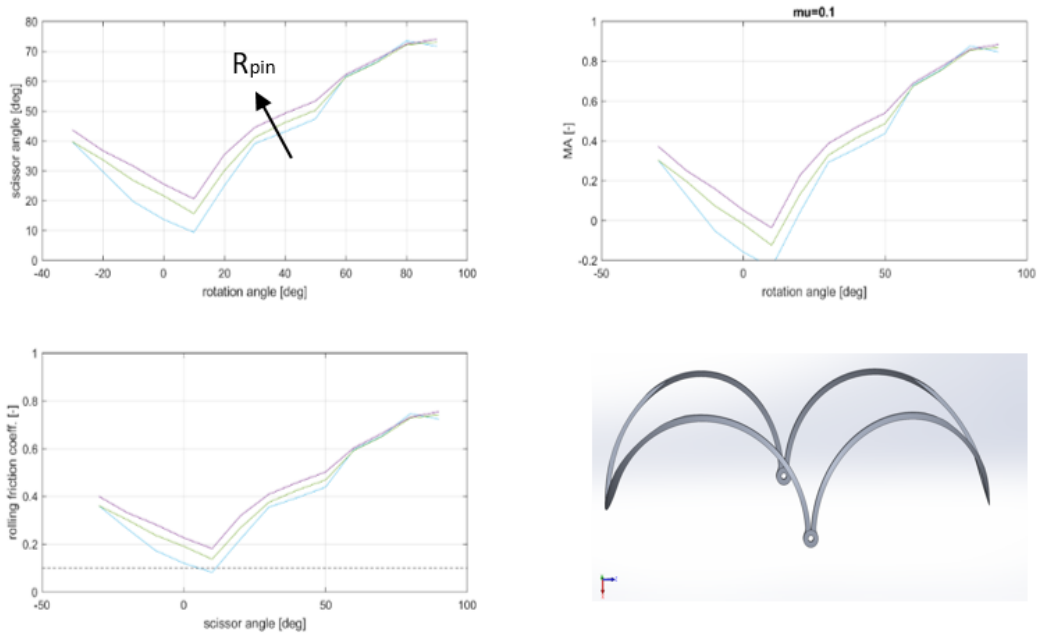

Figure 4.23 Wiper-Wiper scenario 3D Matlab simulation results as functions of the rotation angles and parametrized with respect to the pin radius (blue 5mm, green 10mm, red 15mm). Top left: scissor angle. Top right: MA. Bottom left: static rolling friction coefficient. Bottom right: CAD model.

This scenario does not guarantee a complete accomplishment of the mechanism goal.

A pin thickness of 10mm has been chosen as main baseline for the Wiper optimization scenario. The 10mm pin presents a higher MA with respect to the 5mm pin and a saving in mass with respect to the 15mm pin.

4.3.5 Case 4: Optimized Wiper-Wiper Scenario

The fourth chosen approach was the optimized Wiper-Wiper scenario. In this case as positive feature was adopted the Wiper profile discussed in Subsec.4.3.2, while for what concerns the Wiper the existing Wiper profile was modified. Having the analytical model of the Wiper profile, an optimized Wiper profile

was obtained using as cost function parameters both the MA and the scissor angle. In this case this procedure was followed:

1. Starting from the Wiper-Wiper curve;
2. Introducing three parameters [par1, par2, par3], see Fig.4.24;
3. Make them varying in a well-defined range;
4. Evaluating the scissor angle and the MA (cost function parameters);
5. Geometry relies on a spherical surface ± pin radius, as a constraint;
6. Obtaining the best three parameters with the associated highest MA;
7. Results and final Wiper profile.

For what concerns the three parameters, see Figg.4.24 and 4.25, the parameter variation range was chosen accordingly to a Wiper geometry that:

- The end point of the modified Wiper profile is attached on the same vertical axis of the standard Wiper geometry;
- The Wiper geometry is able to have an initial orientation (rotation angle of 180°) that allows the pin to not jam when OS is initially entering.
- Guarantee compactness of the Wiper shape on a spherical surface. This aspect is really key to the whole OS reorientation mechanism. When the OS will be inserted in this mechanism, the Wiper will start in the rest position (rotation angle of 180°), see Fig.4.26. The red arrow shows the increasing of the value of this parameter. Having a large parameter 1 value brings to have a hole in between the modified Wiper and the positive feature where the pin could remain stuck.
- The first part of the modified Wiper arc should be compact and without long segments and / or vertexes to avoid the pin jamming. In particular, Fig.4.27 shows the system at a rotation angle of 100°. The red arrow shows the increasing of the value of this parameter. A curve too flat (lower parameter 2) or too steep (higher parameter 2) could bring to a possible pin jamming condition.

- No local minima or maxima are required between the modified Wiper part arc and the non-modified Wiper part (the pin could get stuck in these points). This condition was referred as *functional convexity*. In particular, Fig.4.28 shows the system at a rotation angle of 0°. The red arrow shows the increasing of the value of parameter 3. Different curves could present a local minimum (lower parameter 3) or a local maximum (higher parameter 3) and each of them could bring to a possible pin jamming condition.

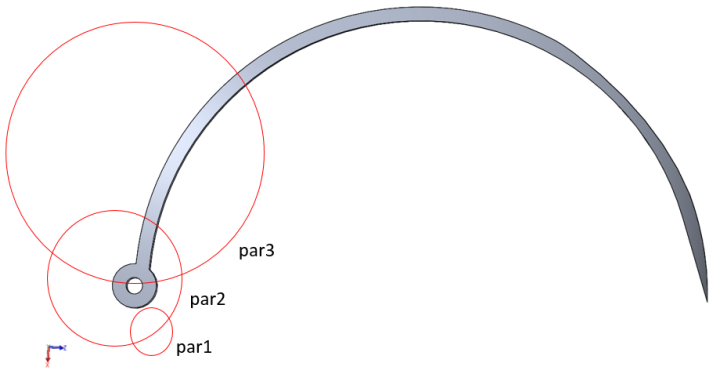

Figure 4.24 The parameters associated to three different parts of the original Wiper (side view).

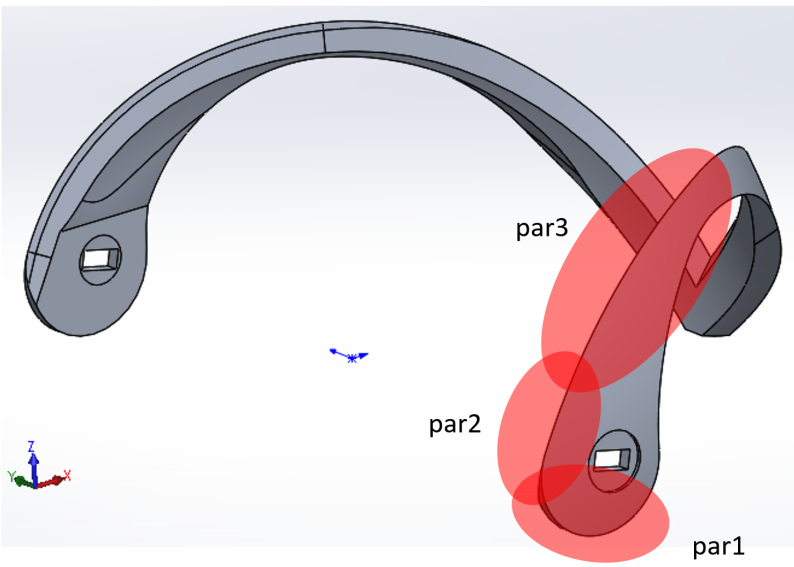

Figure 4.25 The parameters associated to three different parts of the optimized Wiper (3D view) [124].

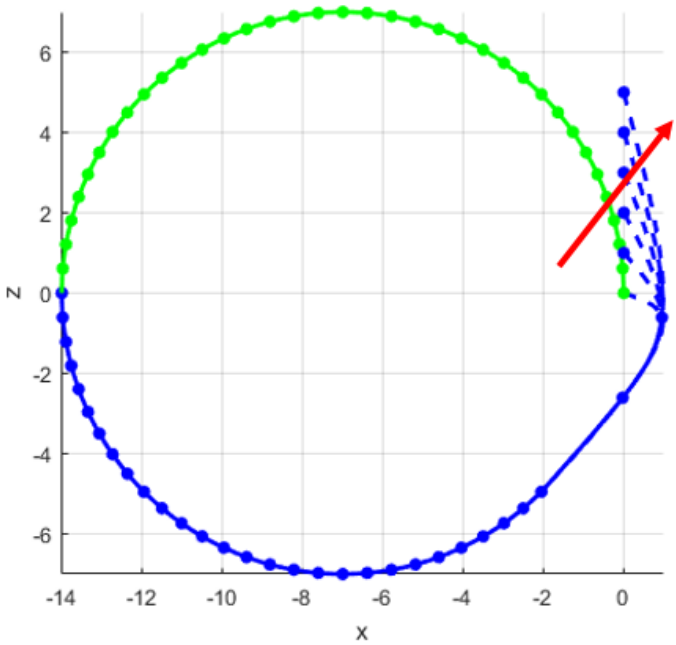

Figure 4.26 When the OS will be inserted in this mechanism, the Wiper will start in the rest position (rotation angle of 180°). The red arrow shows the increasing of the value of this parameter. Having a large parameter 1 value brings to have a hole in between the modified Wiper and the positive feature where the pin could remain stuck.

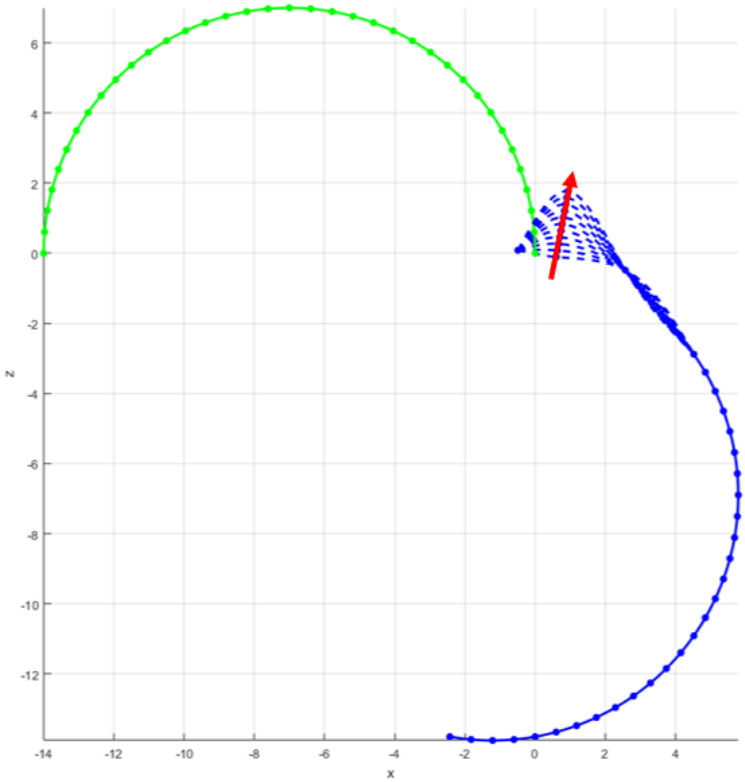

Figure 4.27 The system at a rotation angle of 100°. The red arrow shows the increasing of the value of parameter 2. A curve too flat (lower parameter 2) or too steep (higher parameter 2) could bring to a possible pin jamming condition.

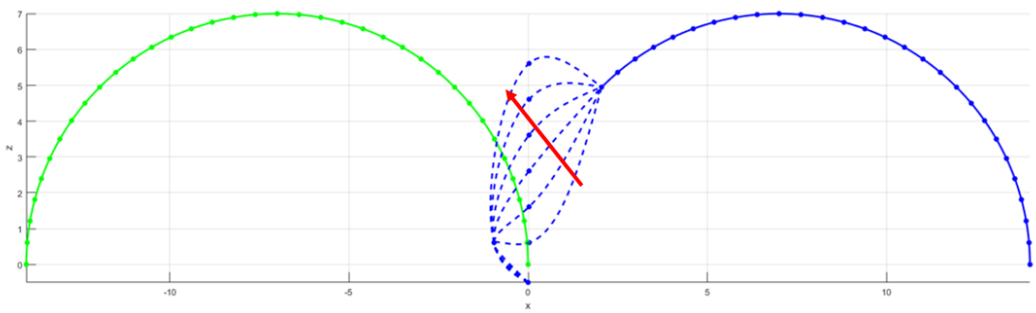

Figure 4.28 System at a rotation angle of 0°. The red arrow shows the increasing of the value of parameter 3. Different curves could present a local minimum (lower parameter 3) or a local maximum (higher parameter 3) and each of them could bring to a possible pin jamming condition.

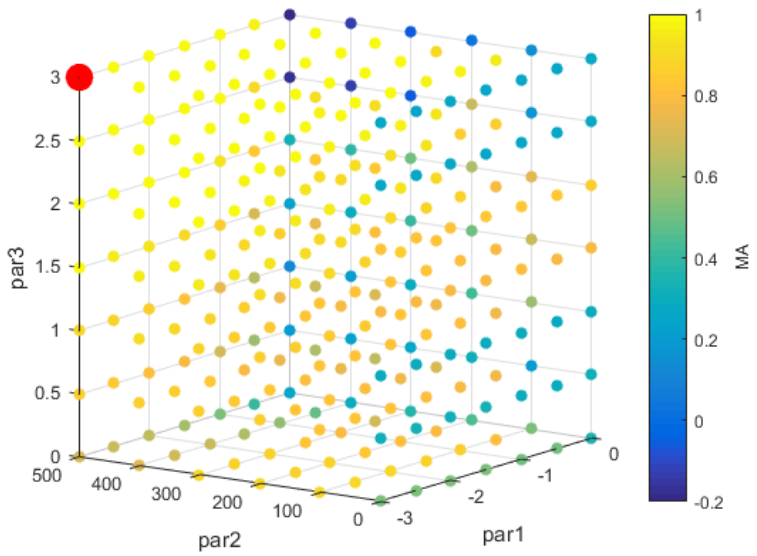

Figure 4.29 Global parameters variation as a function of the MA for a rotation angle of 40°. The red dot indicates the parameter combination that produces the highest MA.

Fig.4.29 reports the global parameters variation as a function of the MA for a rotation angle of 40°. The red dot indicates the parameter combination that produces the highest MA. Fig.4.30 shows the Wiper profile obtained using the parameters that maximize the MA for a rotation angle of 40° (global parameters optimization). Clearly, this method is not winning, because in this way a Wiper that presents a local minimum was obtained and this was a region in which the pin could get stuck. It was better to proceed optimizing one parameter at time on all the rotation angles.

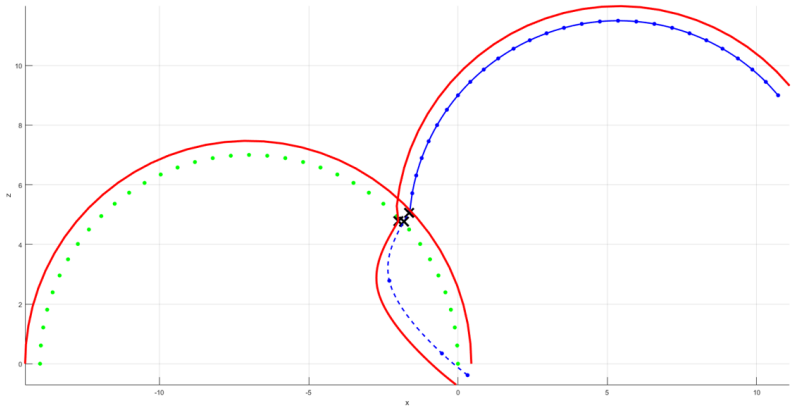

Figure 4.30 Wiper profile obtained using the parameters that maximize the MA for a rotation angle of 40°. The same color code use for Case 3 was adopted here.

After having determined the variation range for the three parameters, the modified Wiper rotation was simulated on the positive feature to estimate the scissor angle and the MA. This procedure helps to select the parameters that optimize the cost functions. When one parameter changes over its range of interest, the other two assume average values within their range of interest.

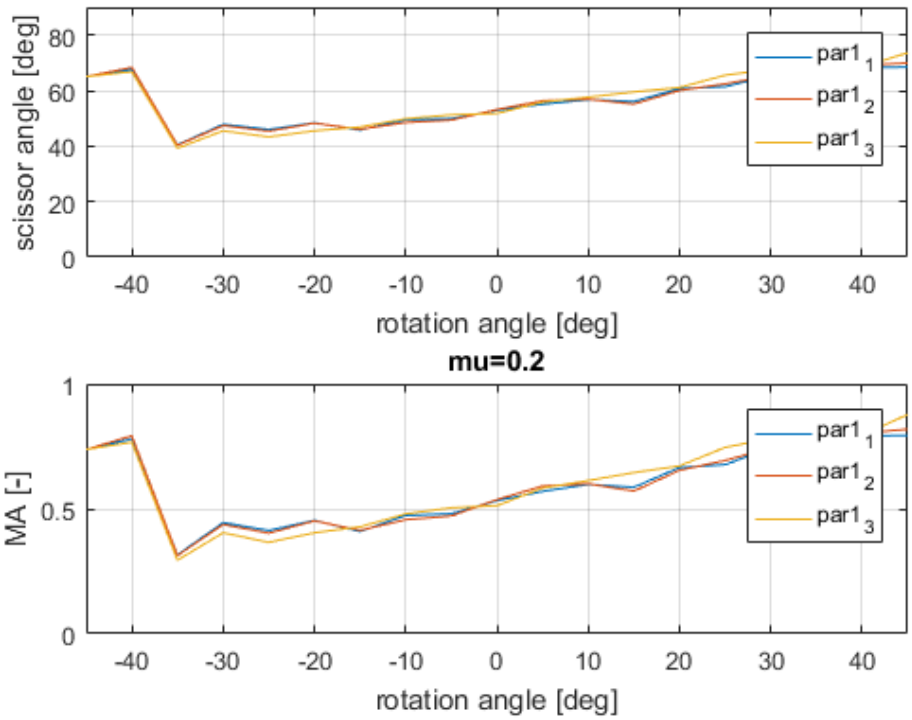

Figure 4.31 Scissor angle and MA as functions of the rotation angle parametrized on different values for parameter 1.

The conclusions obtained by Fig.4.31 is that the parametrization of parameter 1 does not affect substantially the simulation outcomes. Parameter 1_2 was chosen to characterize the modified Wiper profile.

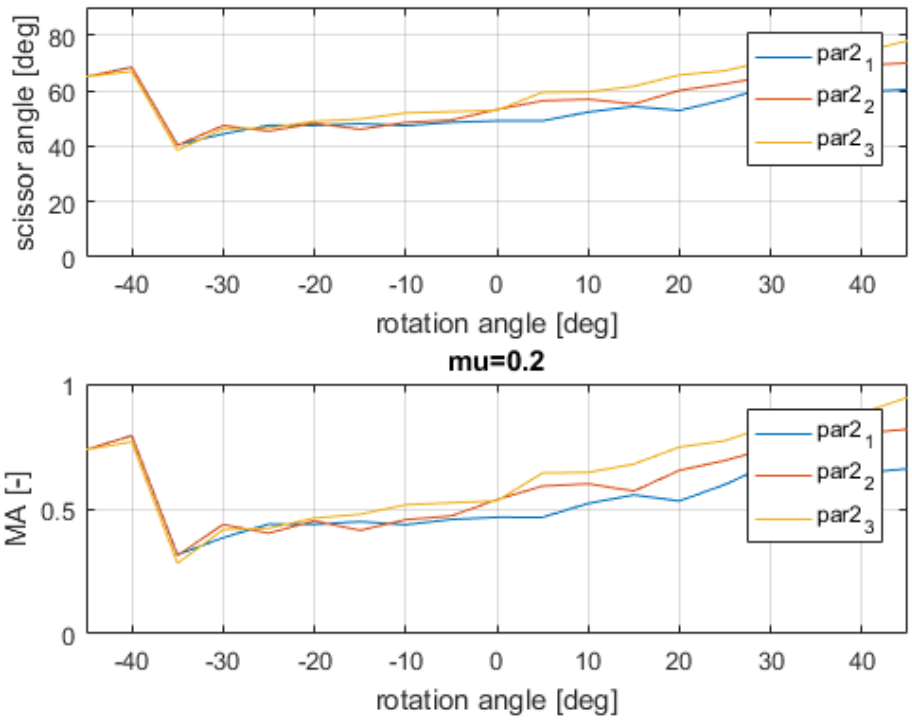

Figure 4.32 Scissor angle and MA as functions of the rotation angle parametrized on different values for parameter 2.

The conclusions obtained by Fig.4.32 is that parameter 2_2 allows to have a higher minimum and a higher value for rotation angles greater than 0°. Parameter 2_2 was chosen to characterize the modified Wiper profile.

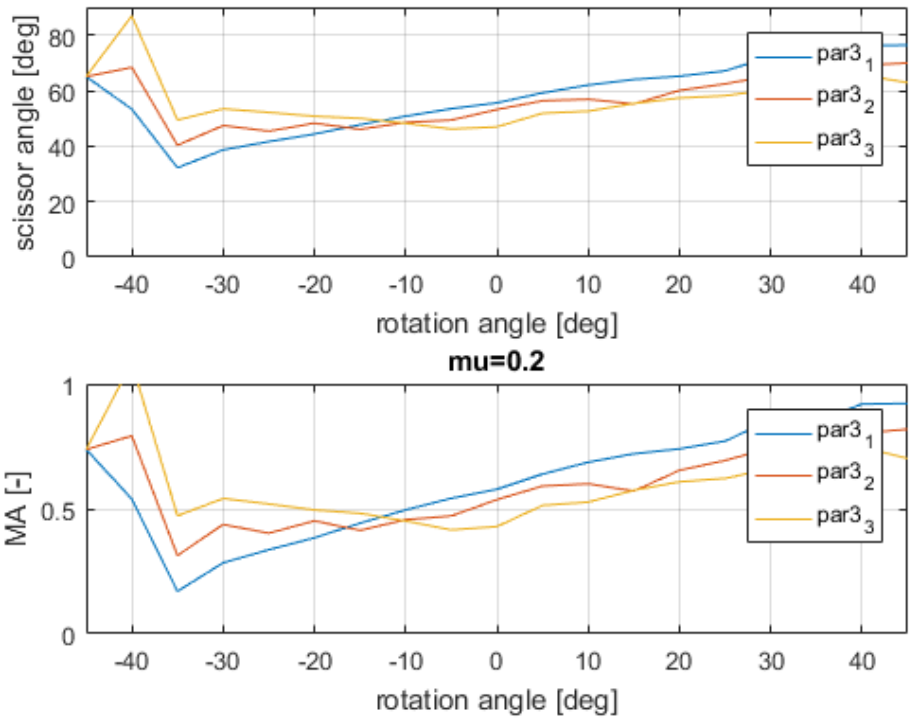

Figure 4.33 Scissor angle and MA as functions of the rotation angle parametrized on different values for parameter 3.

The conclusions obtained by Fig.4.33 is that parameter 3_3 allows to have a higher minimum even if after -10° the associated curve is lower than the other two, but still it allows to have a MA>0.5. Parameter 3_3 was chosen to characterize the modified Wiper profile.

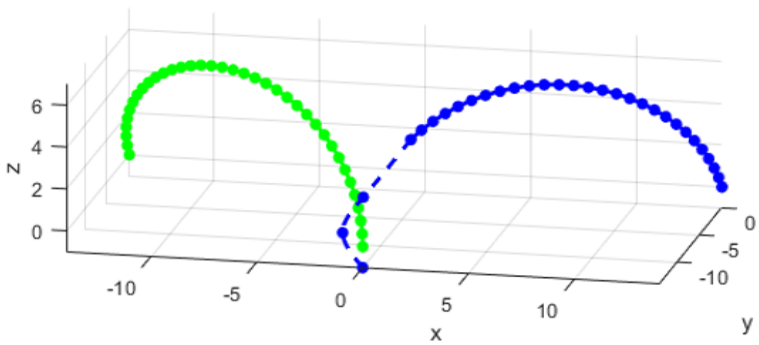

Figure 4.34 Final optimization of the modified Wiper profile.

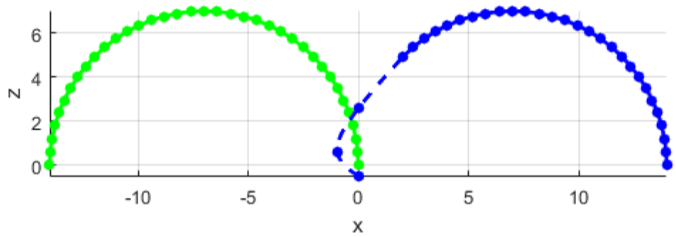

(a) Final optimization of the modified Wiper profile (x-z plane).

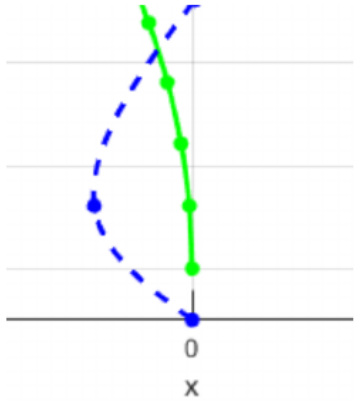

(b) Detail of the longer Wiper profile than the positive feature profile. The last point of the positive feature (last green point) is the location of the rotation axis for the Wiper.

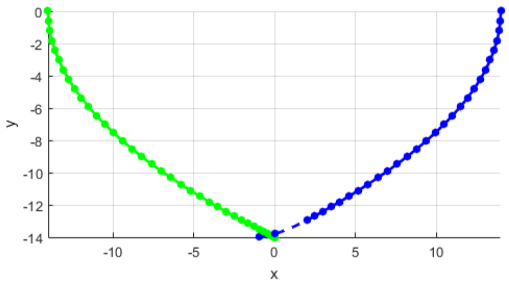

(c) Final optimization of the modified Wiper profile (x-y plane).

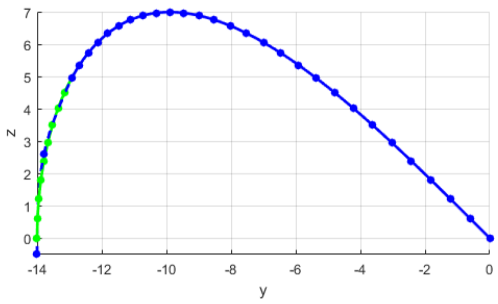

(d) Final optimization of the modified Wiper profile (y-z plane).

Figure 4.35 Different planes of the final optimization of the modified Wiper profile.

Figg.4.34 and 4.35 report the final optimization of the modified Wiper profile. Fig.4.36 shows the upper limit static rolling friction coefficient curve for the optimized Wiper (blue line). This curve represents the minimum value of static rolling friction this mechanism needs. If this system has a friction coefficient that stays below this curve, it will work properly. The dashed line refers to the lower limit friction coefficient of 0.2. It is possible to notice that the blue line is above the dashed black line.

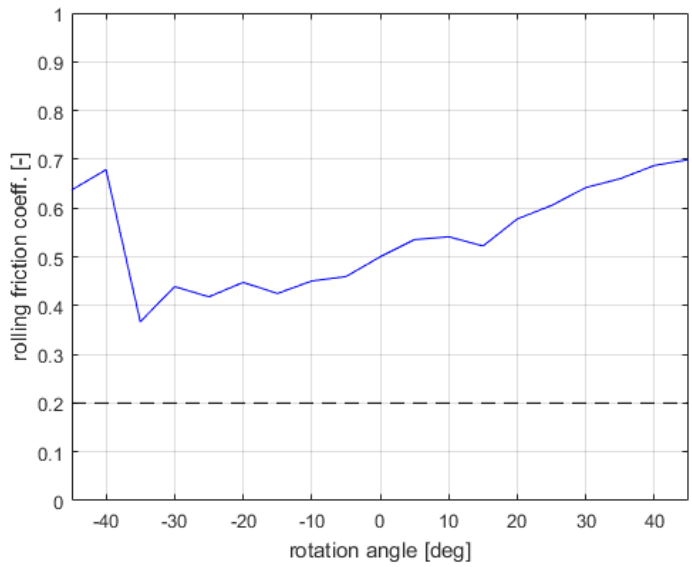

Figure 4.36 Upper limit static rolling friction coefficient curve for the version 4 optimized Wiper (blue line). The dashed line refers to the lower limit friction coefficient of 0.2. The blue line is always above the dashed black line.

Fig.4.37 depicts the Wiper radius as function of the Wiper angle among two lines that represent the Wiper radius ± pin height. Only half of the Wiper is here represented for symmetry reason. This shows that the spherical constraint was respected, i.e., the modified Wiper lays on a spherical surface without exceeding the imaginary curves described by the pin added to the Wiper. There is a small oscillation around 10° due to the fact that the first part of the Wiper is assumed to be flat, see Fig.4.35(b), to prevent incoming OS jamming.

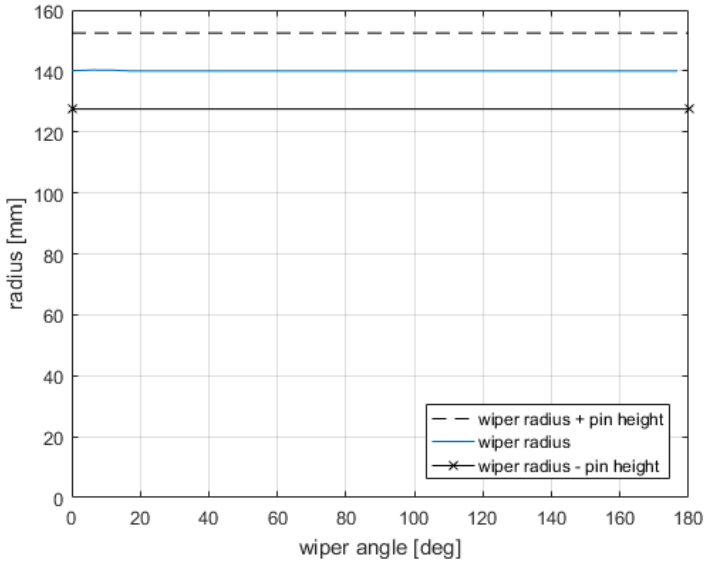

Figure 4.37 Wiper radius as function of the Wiper angle among two lines that represent the Wiper radius ± pin height. This shows that the spherical constraint is respected, i.e., the modified Wiper lays on a spherical surface without exceeding the imaginary curves described by the pin added to the Wiper.

The optimized Wiper is described by Eq.4.37

$$f[x(\theta), y(\theta), z(\theta)] = \begin{cases} \left[\frac{R}{2} - \frac{R}{2}\cos(\theta), \frac{R}{2}\sin(\theta) + par_1, R\cos\left(\frac{\theta}{2}\right)\right] & \text{if } \theta = 0, \\ \left[\frac{par_2}{2} - \frac{par_2}{2}\cos(\theta), \frac{R}{2}\sin(\theta), R\cos\left(\frac{\theta}{2}\right)\right] & \text{if } \theta = 5, \\ \left[-\frac{R}{2} + \frac{R}{2}\cos(\theta), \frac{R}{2}\sin(\theta) + par_3, R\cos\left(\frac{\theta}{2}\right) - \frac{par_3}{10}\right] & \text{if } \theta = 5, \\ \left[-\frac{R}{2} + \frac{R}{2}\cos(\theta), \frac{R}{2}\sin(\theta), R\cos\left(\frac{\theta}{2}\right)\right] & \text{if } \theta \geq 45. \end{cases} \tag{4.37}$$

This equation is divided in four parts: the first three refer to the first three points respectively at θ=0° and θ=5°, while the last one refers to Eq.4.13 that describes the whole Wiper profile. After having analytically simulated the Wiper points in Matlab environment, a spline fits the Wiper points (use the *cscvn* Matlab command, which provides a parametric natural cubic spline curve) and the mechanism actuation rotates around the y axis.

However, from the Figg.4.31, 4.32, and 4.33, it was possible to notice a scissor angle and MA minimum at rotation angle of -35°. This was due mainly by the fact that the Wiper profile was modified up to 45° (operational angle), as showed in Eq.4.37. Other simulations were run moving back the operational angle from 45° to 70° to obtain better results. Analysis were performed moving back this angle up to 90° too, but proceeding further, worst the whole Wiper profile optimization becomes in terms of scissor angle and MA. As reported from Case 3 results the only part to be modified in this Wiper is the part described by angles <90° and in this case ≤70°.

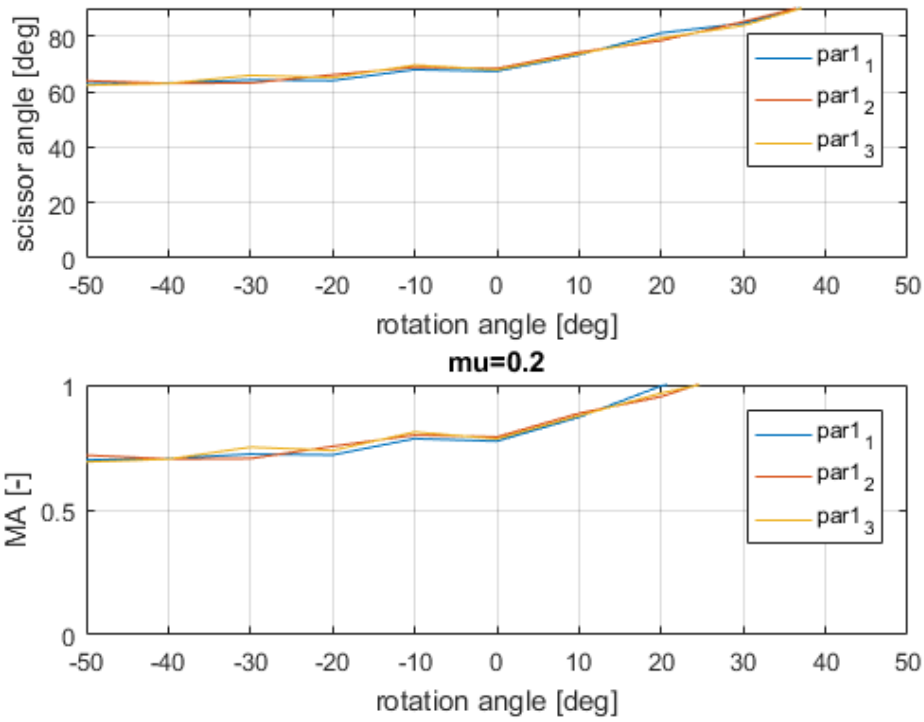

Figure 4.38 Scissor angle and MA as functions of the rotation angle parametrized on different values for parameter 1 for operational angle of 70°.

The conclusions obtained by Fig.4.38 is that the parametrization of parameter 1 does not affect substantially the simulation outcomes. Parameter 1_2 was chosen to characterize the modified Wiper profile.

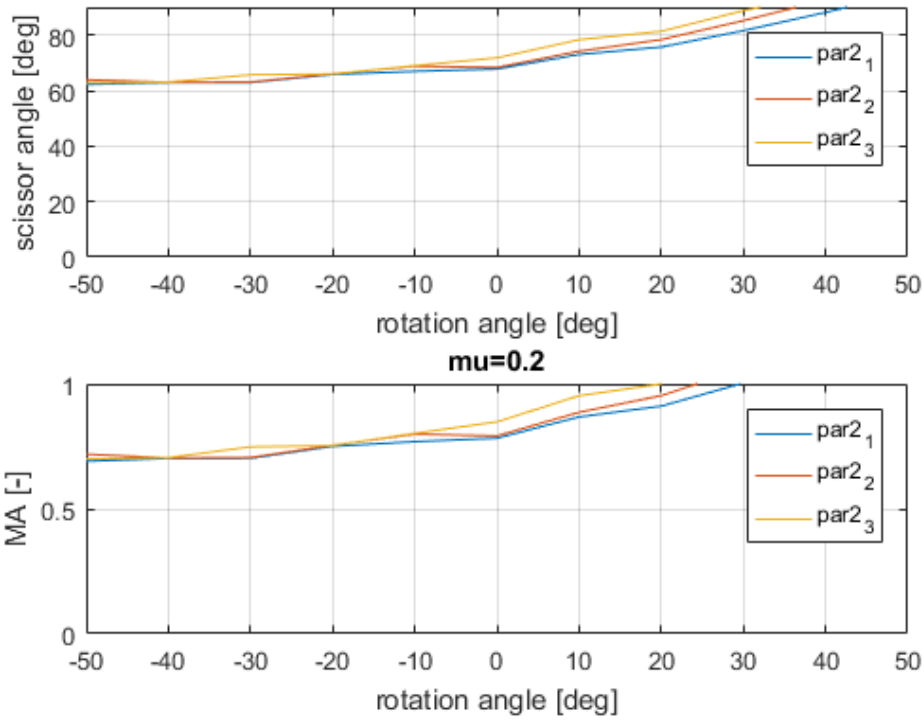

Figure 4.39 Scissor angle and MA as functions of the rotation angle parametrized on different values for parameter 2 for operational angle of 70°.

The conclusions obtained by Fig.4.39 is that parameter 2_3 allows to have a higher minimum and a higher value for rotation angles greater than 0°. Parameter 2_3 was chosen to characterize the modified Wiper profile.

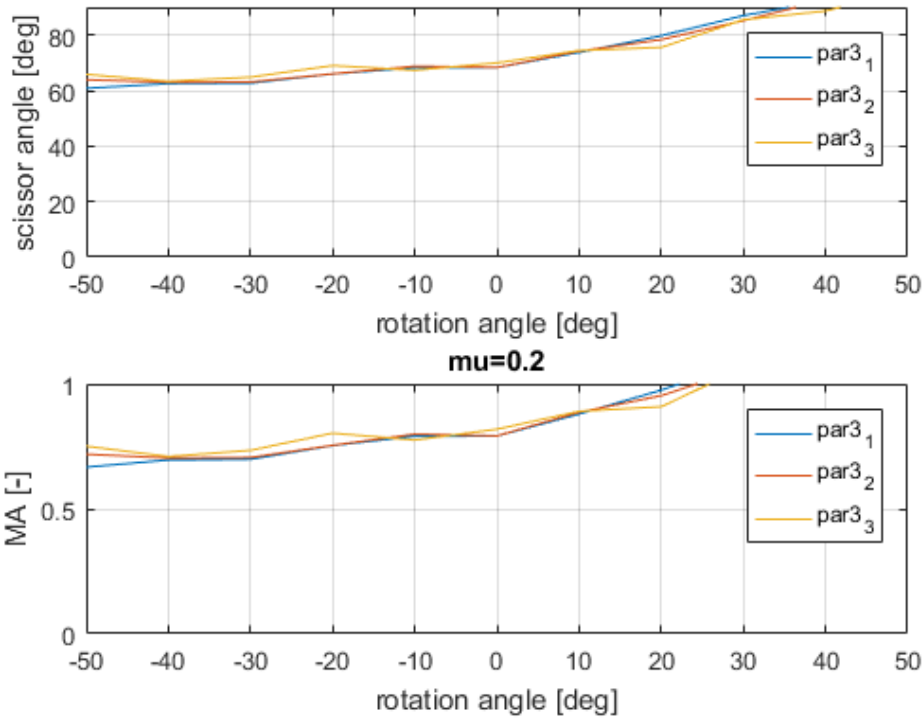

Figure 4.40 Scissor angle and MA as functions of the rotation angle parametrized on different values for parameter 3 for operational angle of 70°.

The conclusions obtained by Fig.4.40 is that the parametrization of parameter 3 does not affect substantially the simulation outcomes. Parameter 3_2 was chosen to characterize the modified Wiper profile.

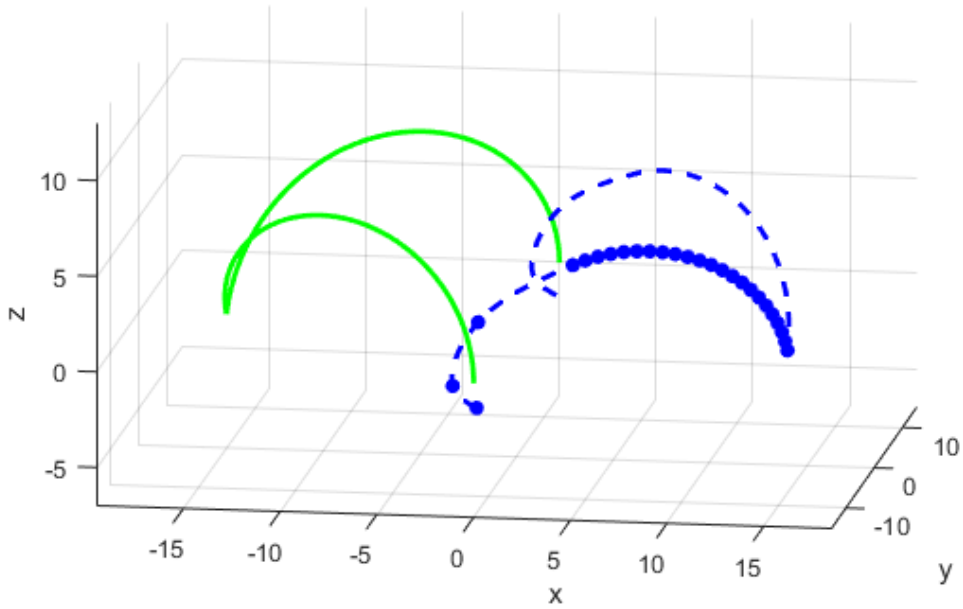

Figure 4.41 Final optimization of the modified Wiper profile for operational angle of 70°.

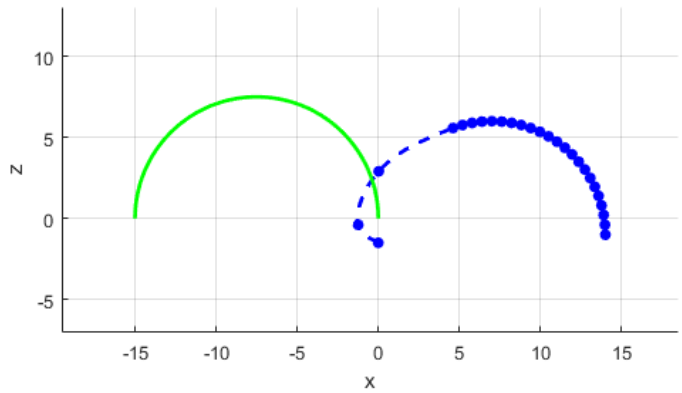

(a) Final optimization of the modified Wiper profile (x-z plane).

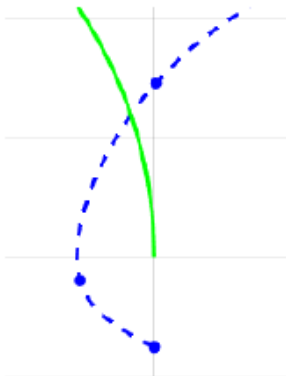

(b) Detail of the longer Wiper profile than the positive feature prodile. The last point of the positive feature (last green point) is the location of the rotation axis for the Wiper. This axis passes through the Wiper shape and not to the last Wiper point.

Figure 4.42 Different planes of the final optimization of the modified Wiper profile for operational angle of 70°.

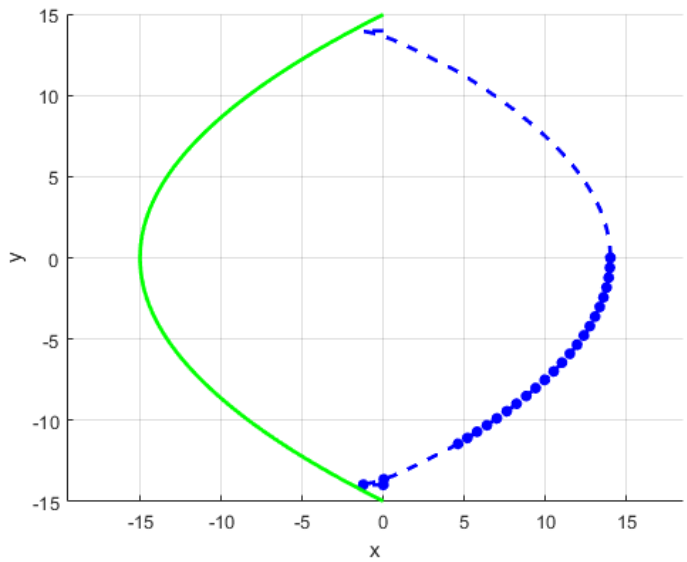

(a) Final optimization of the modified Wiper profile (x-y plane).

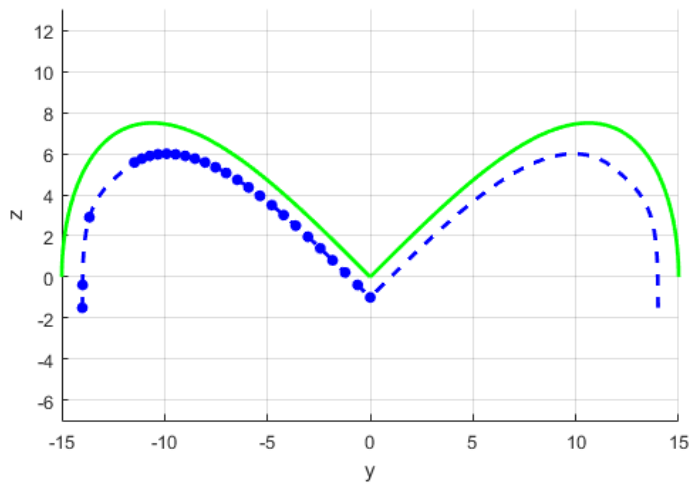

(b) Final optimization of the modified Wiper profile (y-z plane).

Figure 4.43 Different planes of the final optimization of the modified Wiper profile for operational angle of 70°.

Figg.4.41, 4.42, and 4.43 report the final optimization of the modified Wiper profile. Fig.4.44 shows the upper limit static rolling friction coefficient curve for the optimized Wiper (blue line). This curve represents the minimum value

of static rolling friction this mechanism needs. If this system has a friction coefficient that stays below this curve, it will work properly. The dashed line refers to the lower limit friction coefficient of 0.2. It is possible to notice that the blue line is above the dashed black line and higher than 0.5.

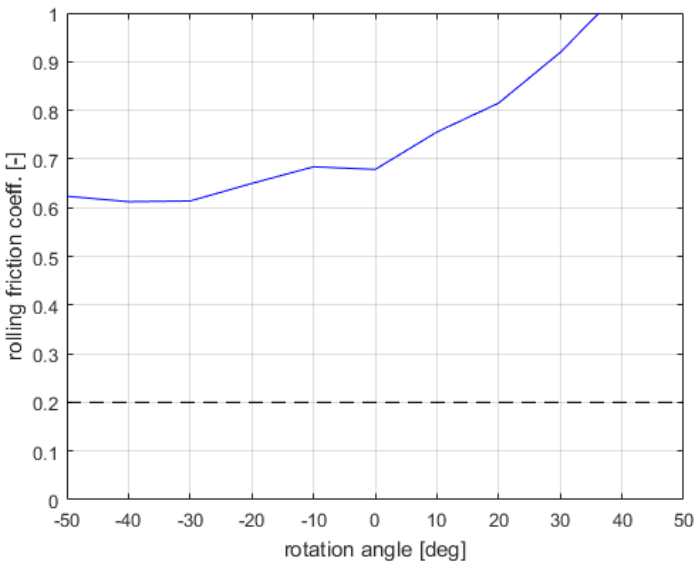

Figure 4.44 Upper limit static rolling friction coefficient curve for the version 4 optimized Wiper (blue line). The dashed line refers to the lower limit friction coefficient of 0.2. Note that the blue line is always above the dashed black line [124].

Fig.4.45 depicts the Wiper radius as function of the Wiper angle among two lines that represent the Wiper radius ± pin height. This shows that the spherical constraint is respected, i.e., the modified Wiper lays on a spherical surface without exceeding the imaginary curves described by the pin added to the Wiper. There is a small oscillation around 10° due to the fact that the first part of the Wiper is assumed to be flat, see Fig.4.42(b), to prevent the OS jamming.

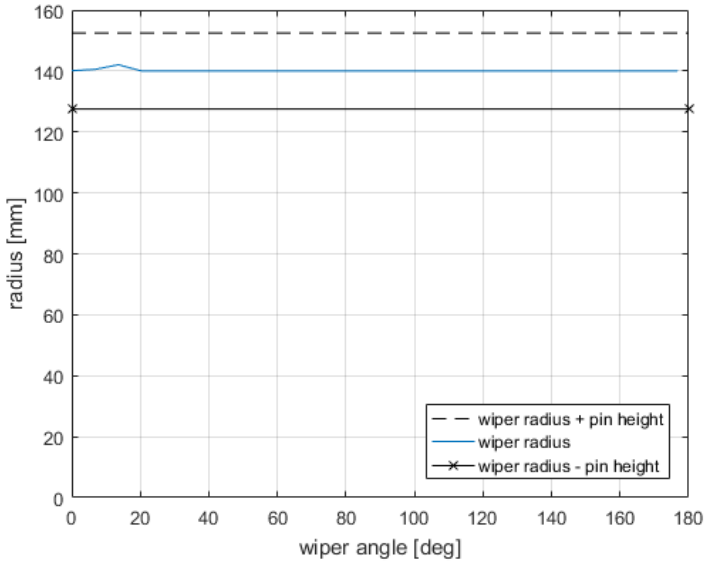

Figure 4.45 Wiper radius as function of the Wiper angle among two lines that represent the Wiper radius ± pin height. Only half of the Wiper is considered for symmetry reason. This shows that the spherical constraint is respected, i.e., the modified Wiper lays on a spherical surface without exceeding the imaginary curves described by the pin added to the Wiper.

The final optimized Wiper is described by Eq.4.38

$$f[x(\theta),y(\theta),z(\theta)] = \begin{cases} \left[\frac{R}{2} - \frac{R}{2}\cos(\theta), \frac{R}{2}\sin(\theta) + par_1, R\cos\left(\frac{\theta}{2}\right)\right] & \text{if } \theta = 0, \\ \left[\frac{par_2}{2} - \frac{par_2}{2}\cos(\theta), \frac{R}{2}\sin(\theta), R\cos\left(\frac{\theta}{2}\right)\right] & \text{if } \theta = 5, \\ \left[-\frac{R}{2} + \frac{R}{2}\cos(\theta), \frac{R}{2}\sin(\theta) + par_3, R\cos\left(\frac{\theta}{2}\right) - \frac{par_3}{10}\right] & \text{if } \theta = 5, \\ \left[-\frac{R}{2} + \frac{R}{2}\cos(\theta), \frac{R}{2}\sin(\theta), R\cos\left(\frac{\theta}{2}\right)\right] & \text{if } \theta \geq 70. \end{cases} \tag{4.38}$$

Tab.4.3 reports the final optimized parameters values at different rotation angles together with their scissor angles and MAs. Fig.4.46 reports the scissor angle and the MA as a function of the rotation angle for Case 4 optimized Wiper with respect to Case 3 [124]. It is interesting to notice that close to $\sim 0°$

both the scissor angle and the MA increase to completely eliminate the pin singularity condition.

Rot. Angle (°)	Parameter 1	Parameter 2	Parameter 3	Scissor angle (°)	MA (-)
-50	-0.5	700	3.2	64	0.7
0	-0.5	700	3.2	68	0.8
+50	-0.5	700	3.2	98	1

Table 4.3 Optimized parameters values at different rotation angles together with their scissor angles and mechanical advantage.

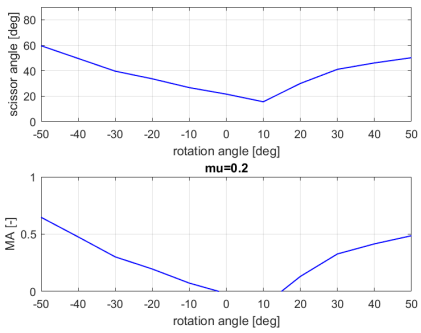

(a) Scissor angle and the MA as a function of the rotation angle for version 3 Wiper.

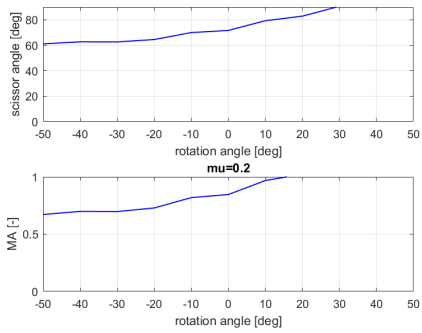

(b) Scissor angle and the MA as a function of the rotation angle for Case 4 optimized Wiper.

Figure 4.46 Final scissor angle and the MA as a function of the rotation angle for Case 4 optimized Wiper with respect to Case 3 [124].

Wiper/Pin Potential Materials

From Fig.4.44 it was possible to infer that the minimum upper limit dry static friction coefficient relating to the Wiper / pin interaction is 0.6. From [134] some possible selections could be:

- Hard Carbon - Hard Carbon, 0.16;
- Hard Carbon - Steel, 0.14;
- Steel - Cast Iron, 0.4;

- Titanium Alloy Ti-6Al-4V(Grade 5) - Aluminium Alloy 6061-T6, 0.41;
- Titanium Alloy Ti-6Al-4V(Grade 5) - Titanium Alloy Ti-6Al-4V(Grade 5), 0.36;
- Another possibility would be to cover either the Wiper, the pin, or both, with Teflon / Kapton cover to decrease the dry static friction.

Wiper Manufacture Tolerance

Another open question was related to the necessary Wiper manufacture tolerance (W_{mt}) in the 3D space to make the whole mechanism working properly. Considering that the pin radius (P_r) was 5mm and the clearance between the positive feature and the Wiper (F_{cl}) was 2mm, the required Wiper manufacture tolerance should follow Eq.4.39

$$W_{mt} < F_{cl} < P_r. \tag{4.39}$$

Having a typical Computer Numerical Control tolerance of ±0.127mm [135] should guarantee the correct Wiper operation.

4.4 3D-Printed Wiper

At the same speed with the optimization analysis, different wipers, each of them with a different profile, were built using a 3D printer Objet250 Connex3 by Stratasys [136] at NASA JPL - California Institute of Technology. Finally, in Fig.4.47 depicts the CAD drawings of the final optimization of the modified Wiper profile.

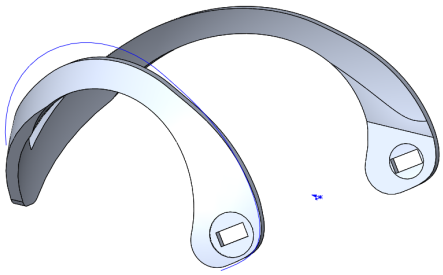

(a) Final optimization of the modified Wiper profile. The blue line is the profile generated by the Matlab optimization.

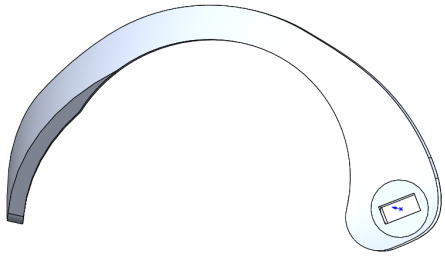

(b) Final optimization of the modified Wiper profile (side view).

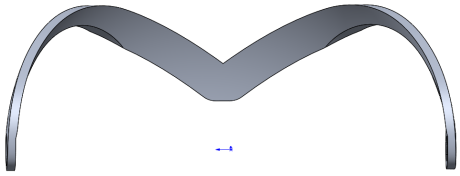

(c) Final optimization of the modified Wiper profile (front view).

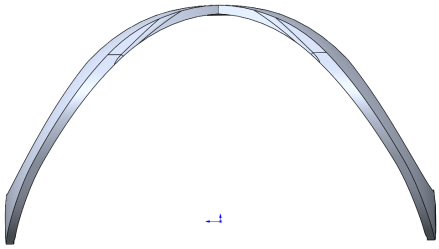

(d) Final optimization of the modified Wiper profile (top view).

Figure 4.47 Final Wiper optimized CAD drawings (Case 4).

The optimized Wiper was manufactured using also out of E-beam Titanium EOS M290 Laser Powder Bed at California Institute of Technology 316L Stainless Steel Post machining on 5 axis mill. Wiper and positive feature nominal thickness was 5mm. Both Matlab and Stainless Steel 3D-printed Wiper views are reported in Figg.4.48, 4.49, 4.50, and 4.51 [124].

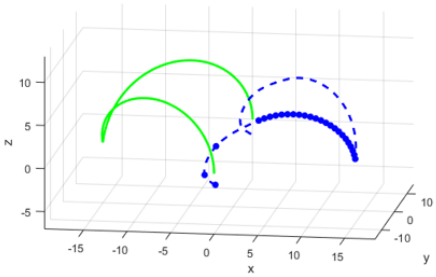

(a) Matlab Wiper model. The blue line is the moving Wiper. The green line represents the static positive feature.

(b) Stainless Steel 3D-printed Wiper.

Figure 4.48 Optimized Wiper model [124].

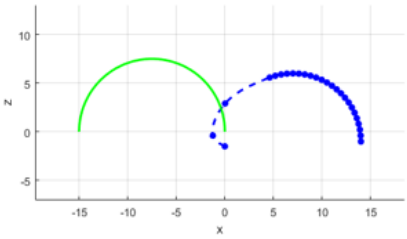

(a) Matlab Wiper model (side view). The blue line is the moving Wiper. The green line represents the static positive feature.

(b) Stainless Steel 3D-printed Wiper (side view).

Figure 4.49 Optimized Wiper model (side view) [124].

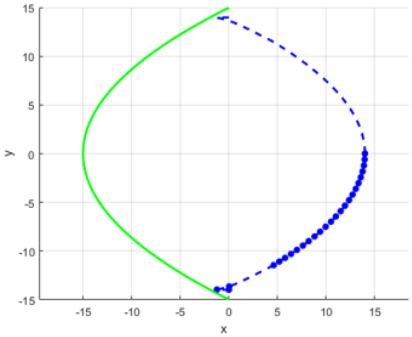

(a) Matlab Wiper model (top view). The blue line is the moving Wiper. The green line represents the static positive feature.

(b) Stainless Steel 3D-printed Wiper (top view).

Figure 4.50 Optimized Wiper model (top view) [124].

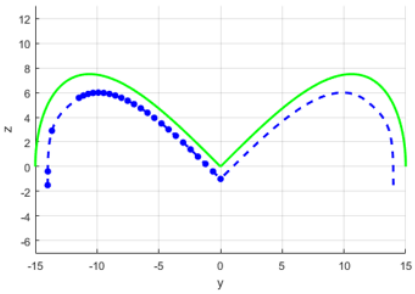

(a) Matlab Wiper model (front view). The blue line is the moving Wiper. The green line represents the static positive feature.

(b) Stainless Steel 3D-printed Wiper (front view).

Figure 4.51 Optimized Wiper model (front view) [124].

Chapter 5

Testbed Design and Analysis

In this chapter the work related to the testbed designs and simulations are reported. The testbeds were put together by the author and members of the MOSTT team. The role of the author will be highlighted and reported in this work.

Parts of this chapter were published in:

- Electro-Mechanical System to Reorient a Spherical Orbital Sample for a Potential Mars Sample Return Mission Concept **Dolci M.**, Mayo J., Chamberlain-Simon B., Smith R., Kim J., Ubellacker W., Ohta P., Mukherjee R., submitted to Acta Astronautica, August 2017.

The current testbeds were designed to test and to characterize:

1. Wiper-pin interaction
    - Model properly the Wiper (in terms of material and geometry) to make the pin migrating towards the center of the Wiper;
    - Select the pin material and geometry.
2. Positive feature-pin-Wiper interaction
    - Proof the pin migration towards the center of the Wiper using the positive feature as support. The final pin location will be between the Wiper and the positive feature centers where the retention mechanism will guarantee its locking.

3. Capability to reorient the OS
    - Proof success and repeatability in the OS orientation thanks to interaction with the pin, independently from the OS initial orientation.
4. Retention mechanism
    - Show retention mechanism concepts that satisfy all the potential requirements. Identify a reasonable candidate, execute its design and test it.
5. Testing the whole reorientation and retain mechanism
    - Add other structural elements (e.g., the shells around the OS fro the BTC process) to test the whole mechanism in a qualified environment (i.e., Water Testbed, parabolic flight).

5.1 Testbed N.1: Three-Roller Wiper Testbed Description

This testbed consists of three ball transfers, which gravitationally offload the OS. The low OS-roller friction nearly simulates the zero-g case in which the OS is free to rotate without preloading into the containment vessel. Both the three-roller Wiper testbed CAD and the real testbed are reported in Fig.5.1 [124]. The testbed is limited by a 280° range of motion, a constant gravity force, and friction at the ball transfers. Additionally, the OS is translationally constrained which is not representative of the notional zero-g operating case.

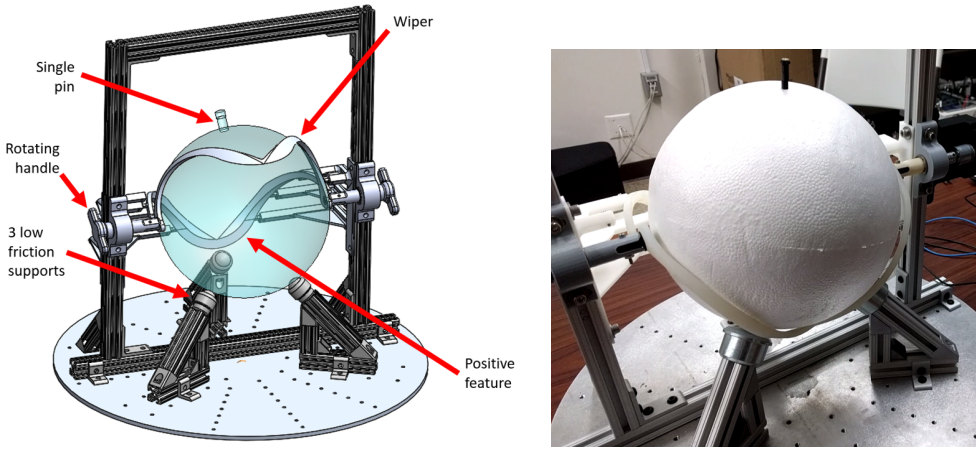

(a) Three-roller Wiper testbed CAD. (b) Three-roller Wiper testbed.

Figure 5.1 Testbed N.1: Three-roller Wiper testbed [124].

Using this testbed the Wiper was consistently able to capture and to center the pin. Moreover, the friction with rollers enables the Wiper to center the pin before contact with positive feature.

In Fig.5.2 the Solidworks CAD of the testbed is illustrated. Three different views are shown: (a) front view, (b) side view and (c) top view. The author personal contributions discussed in the next sections are related to the green highlighted components. The author took care of:

- Characterization of the Wiper-positive feature shape and profile and their interaction with the pin;
- Characterization of the pin dimensions (length and diameter);
- Design and 3D printing of the actuator housing support;
- Design and 3D printing of the connection between the motor shaft and the Wiper;
- Electronic system wiring, to the motor and to power supply (E-switch);
- Motion control of the actuator;
- Assembling of the 80 / 20 structural frame in the testbed;
- Alignment of the testbed;

- Actuation of the testbed to record data;
- Analysis of the obtained data.

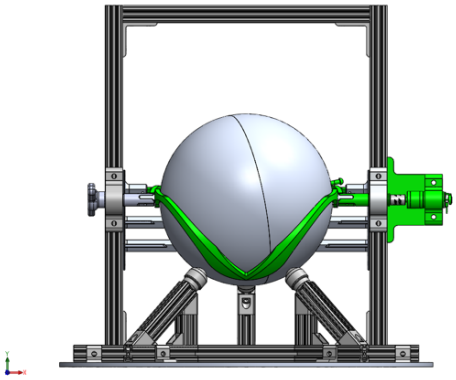

(a) Testbed CAD front view.

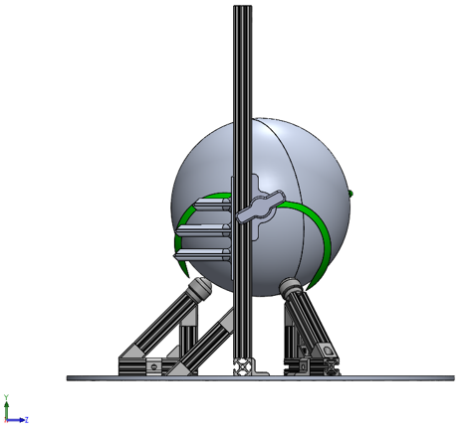

(b) Testbed CAD side view.

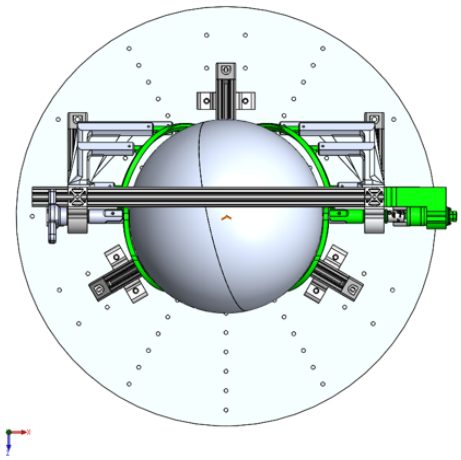

(c) Testbed CAD top view.

Figure 5.2 The Solidworks CAD of the testbed is illustrated. Three different views are shown: (a) front view, (b) side view and (c) top view. The author personal contributions discussed in the next sections are related to the green highlighted components.

5.1.1 Wiper - Positive Feature Shape and Profile

The study related to the Wiper - positive feature interaction to determine their shapes, profiles, and material was described in Ch.4.

5.1.2 Pin Dimensions

The pin is the positive feature this mechanism uses to reorient the OS. It is composed by structural elements and bearing elements. Fig.5.3 reports the SolidWorks CAD drawing of a possible pin configuration envisioned by the author. Left: pin isometric view. Right: pin top view, lateral and bottom view. The pin is constituted by two different elements:

- Head of the pin, it corresponds to the first part of the left plot in Fig.5.3. It is characterized by a l_h length (from the base to the top), by a D neck diameter and by a D_h diameter, that is the diameter of the circle at the base of the head.
- Neck of the pin, it corresponds to the second part of the left plot in Fig.5.3. It is characterized by a l_n length (from the base to the top) and by a D neck diameter.

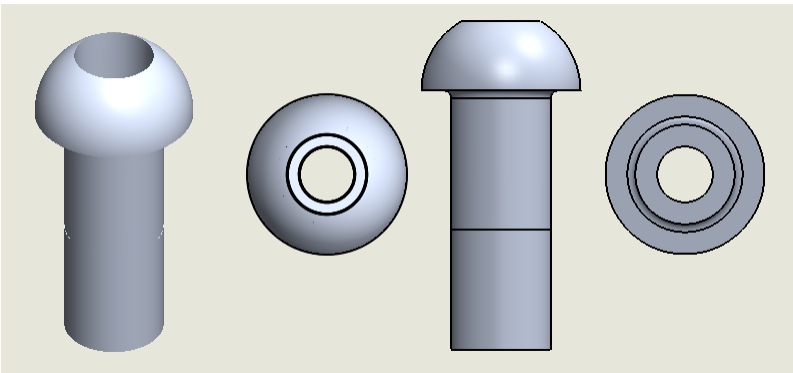

Figure 5.3 SolidWorks CAD drawing of a possible pin configuration. Left: pin isometric view. Right: pin top view, lateral and bottom view.

Determining the total length of the pin $L = l_h + l_n + D_h/2$ and in particular its thickness D are two very interesting aspects. In this testbed $5-10-15$mm were considered as possible diameters D. The material for the 3D-printed prototype was Z-Ultra, a Zortrax M200 printer was adopted.

5.1.3 Actuator Housing Support

Fig.5.4 shows the SolidWorks CAD drawing of the actuator housing support connected to the 80 / 20 structural frame. Left: pin isometric view. Right: support front, top, back, and lateral view. The material for the 3D-printed prototype was Z-Ultra, a Zortrax M200 printer was used.

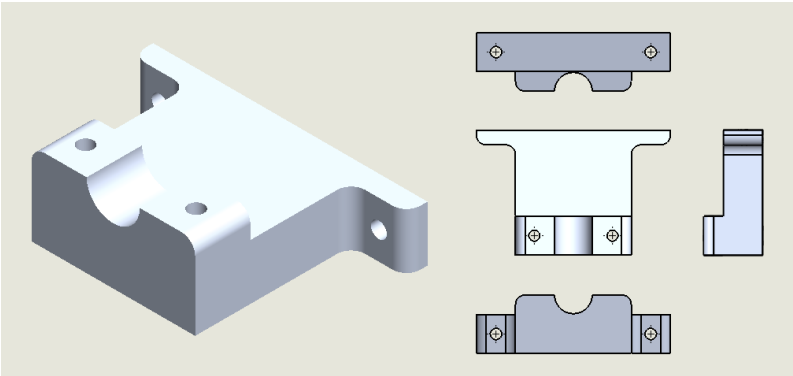

Figure 5.4 SolidWorks CAD drawing of the actuator housing support connected to the 80 / 20 structural frame. Left: support isometric view. Right: support front, top, back, and lateral view.

This support holds up the actuator and aligns the motor shaft to the Wiper rotation axis transmitting the torque to guarantee the proper working of the mechanism. Fig.5.5 shows the SolidWorks CAD drawing of the actuator housing support motor holder. Left: support isometric view. Right: support holder front, top, back, and lateral view. The material for the 3D-printed prototype was Z-Ultra, a Zortrax M200 printer was adopted.

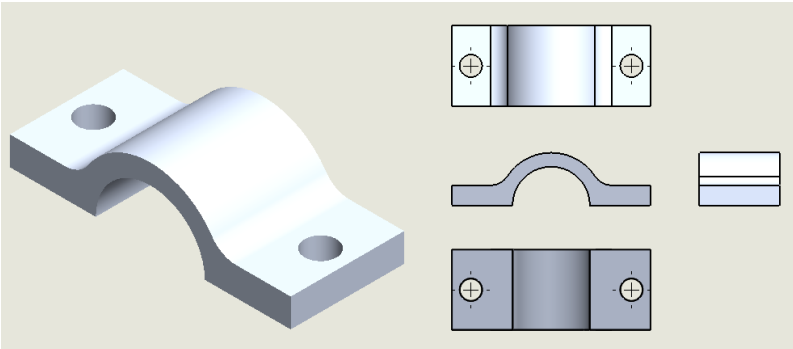

Figure 5.5 SolidWorks CAD drawing of the actuator housing support motor holder. Left: support holder isometric view. Right: support holder front, top, back, and lateral view.

Fig.5.6 shows the SolidWorks CAD assemble drawing of the actuator housing support motor and the holder.

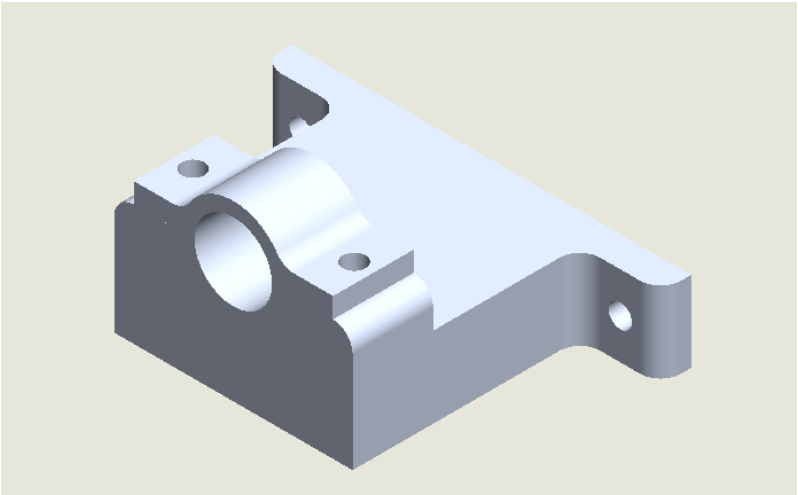

Figure 5.6 SolidWorks CAD assemble drawing of the actuator housing support motor and the holder.

5.1.4 Motor Shaft-Wiper Connection

Fig.5.7 shows the SolidWorks CAD drawing of the motor shaft-Wiper connection. Left: isometric view. Right: connection front, top, back, and lateral view. It is possible to notice the feature to connect to the Wiper, the two grooves to host two retaining rings and a d-profile shaft to be connected to a shaft coupler. The material for the 3D-printed prototype was Z-Ultra, a Zortrax M200 printer was adopted.

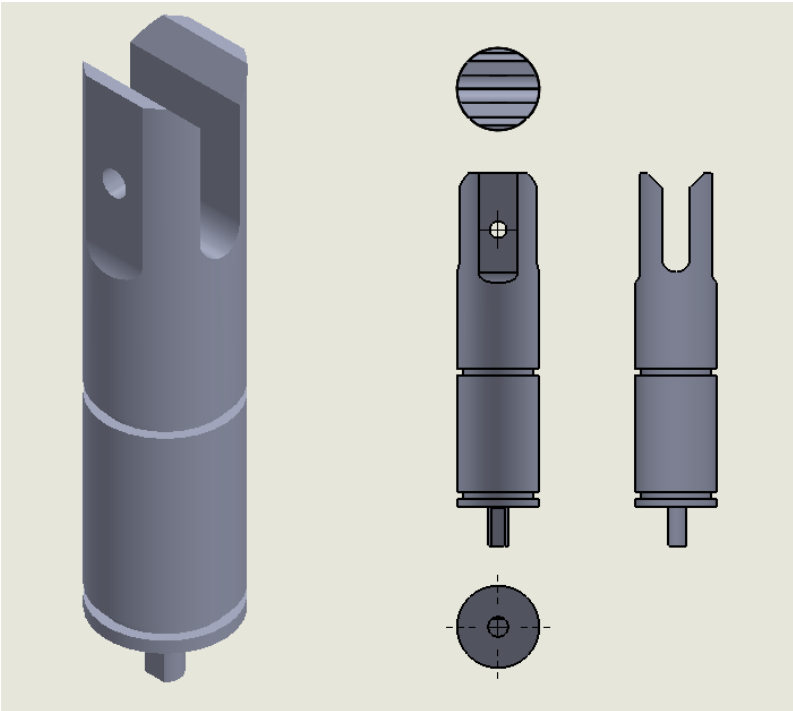

Figure 5.7 SolidWorks CAD drawing of the motor shaft-Wiper connection. Left: isometric view. Right: connection front, top, back, and lateral view.

As retaining ring to hold the shaft axially in position, one from McMaster [137] was selected: Side-Mount External Retaining Ring (E-Style). Two of them were inserted on the two grooves present on the motor shaft-Wiper connection to guarantee the correct lateral system alignment (motor actuation rotation axis direction). The material of this retaining ring was Stainless Steel. Drawings are reported inf Fig.5.8 and specifications in Tab.5.1.

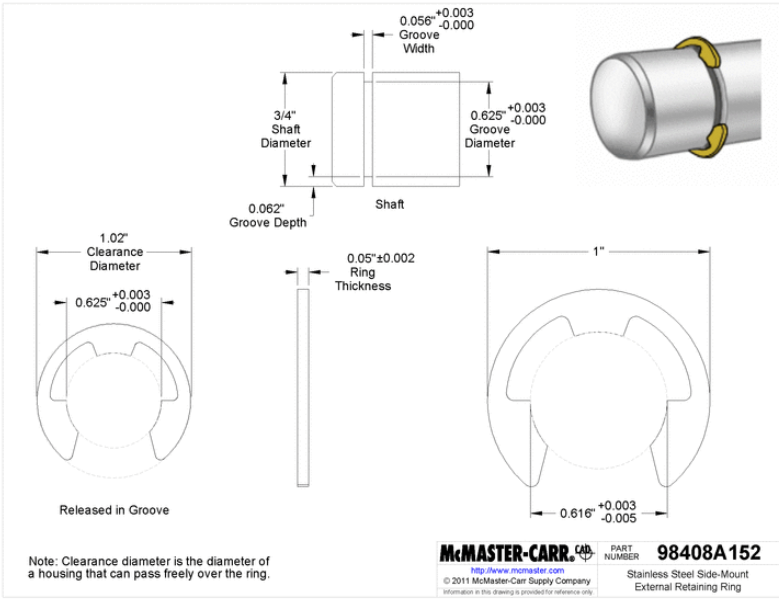

Figure 5.8 McMaster SolidWorks CAD drawing of shaft coupler between the motor shaft and the Wiper connection [137].

Specifications	**Values [mm]**
For Shaft Diameter	19.05
Fits Groove Diameter	15.87
Fits Groove Width	1.42
Ring Size (A)	25.40
Ring Size Thickness	1.27

Table 5.1 Clamp-on Helical Flexible Shaft Coupling features and values from McMaster [137].

Shaft Coupler

A shaft coupler was selected from McMaster [137]: Clamp-on Helical Flexible Shaft Coupling. This shaft coupler was chosen because it couples correctly to the motor shaft with the Wiper connection shaft. Moreover, its flexibility helps to recover existing misalignment between the motor shaft and the Wiper rotation axis. The material of this shaft coupler is Aluminum. Drawings are reported inf Fig.5.9.

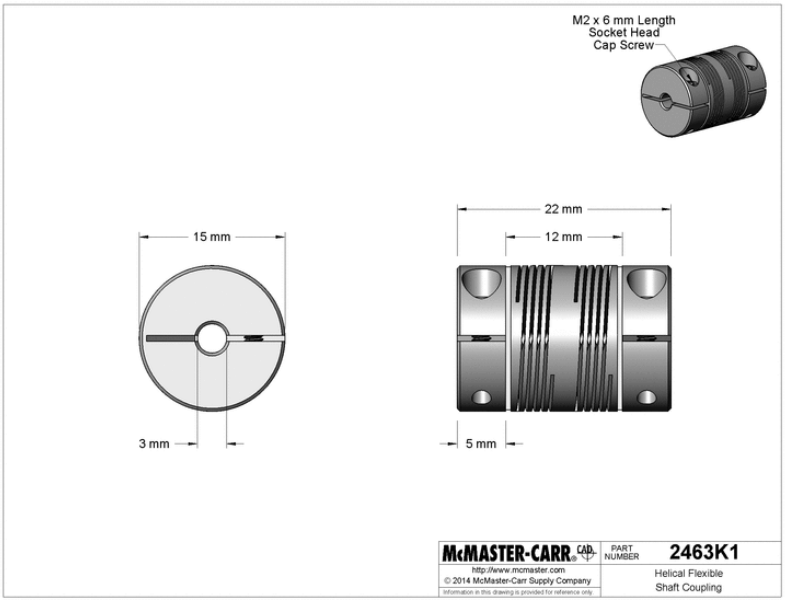

Figure 5.9 McMaster SolidWorks CAD drawing of shaft coupler between the motor shaft and the Wiper connection [137].

Tab.5.2 reports the Clamp-on Helical Flexible Shaft Coupling features and values from McMaster website.

Specifications	**Values**	**Units**
For Shaft Diameter (A)	3	mm
For Shaft Diameter (B)	3	mm
Length	22	mm
OD	15	mm
Maximum rpm	6,000	rpm
Maximum Torque	0.79	Nm
Maximum Misalignment Parallel	0.2	mm
Maximum Misalignment Angular	3	°
Maximum Misalignment Axial	0.12	mm

Table 5.2 Clamp-on Helical Flexible Shaft Coupling features and values from McMaster [137].

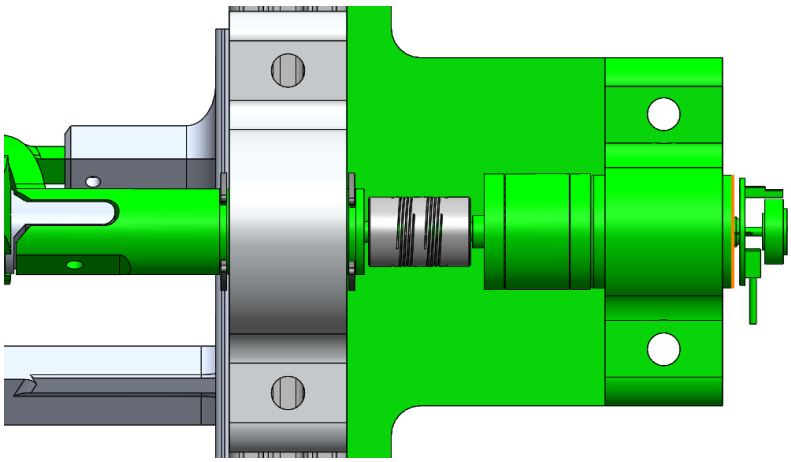

Figure 5.10 SolidWorks CAD assembly detail. It is possible to notice (from right to left) the actuator, its housing, the shaft coupler, the motor shaft-Wiper connection and the two retaining rings on the both sides of the connection support to the 80 / 20 frames.

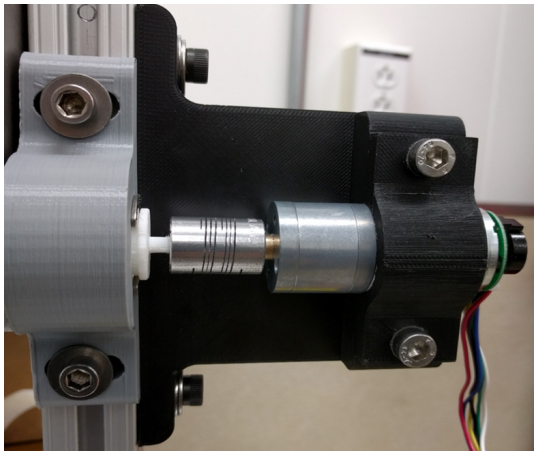

Figure 5.11 Mechanical hardware assembly detail.

Fig.5.10 shows the motor housing support SolidWorks CAD assembly detail. Fig.5.11 shows the motor housing support mechanical hardware assembly detail.

5.1.5 Electronic System

For what concerns the electronic system, the elements shown in Fig.5.12 were wired up. From the top left to the bottom right, a E-switch connected to

a breadboard, an Arduino Micro processor, a Motor Driver Carrier. This elements were connected to a Polulu Actuator.

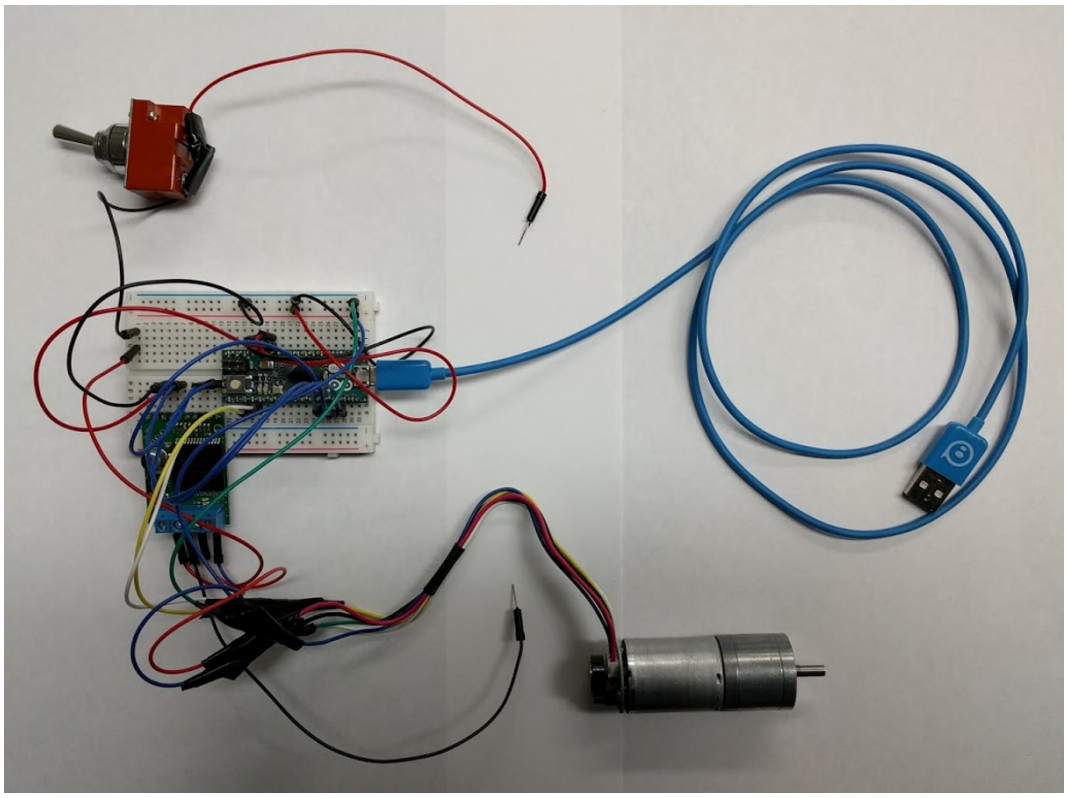

Figure 5.12 Electronic system. From the top left to the bottom right, it is possible to notice a E-switch connected to a breadboard, a Arduino Micro processor, a Motor Driver Carrier. This elements were connected to a Polulu Actuator.

In Fig.5.13 a schematic using Eagle PCB design software [138] was shown. Five elements were present: the Arduino Micro processor, the power supply, the motor driver, the breadboard, the E-switch, the DC motor.

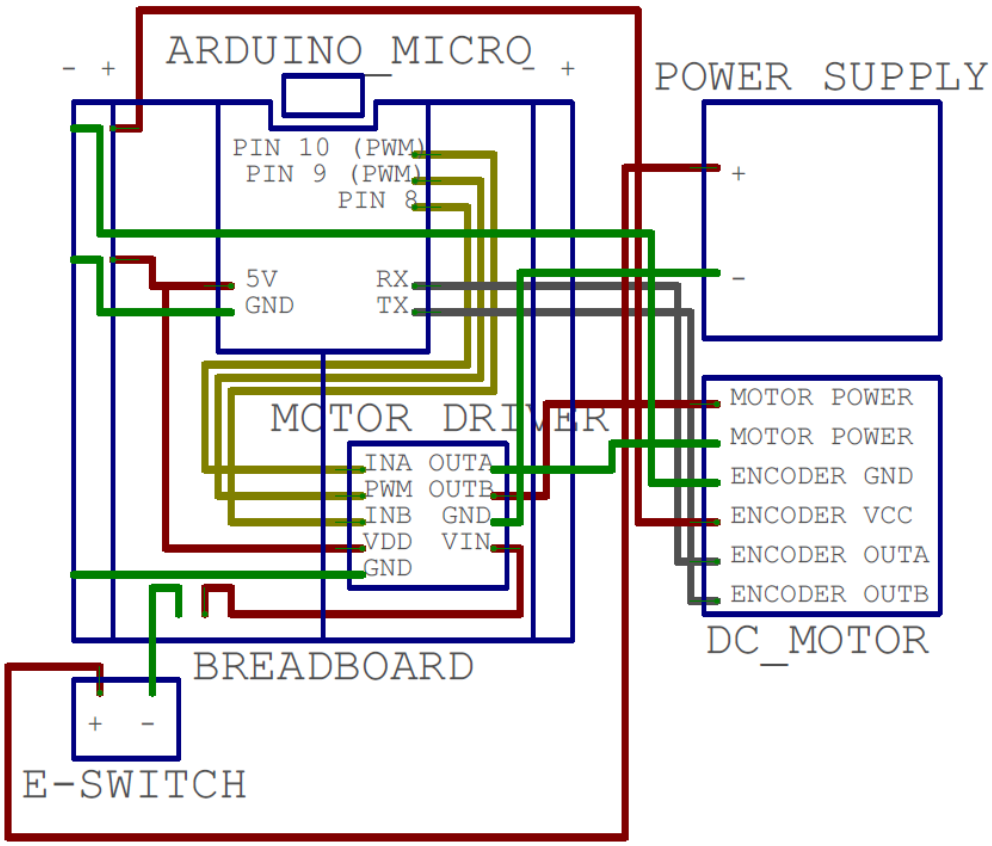

Figure 5.13 Electronic system schematic using Eagle PCB design software [138]. Five elements were present: the Arduino Micro processor, the power supply, the motor driver, the breadboard, the E-switch, the DC motor.

Motherboard: Arduino Micro

As microprocessor an Arduino Micro was used. Fig.5.14 depicts a picture of Arduino Micro (USA only) and Genuino Micro (outside USA) [139].

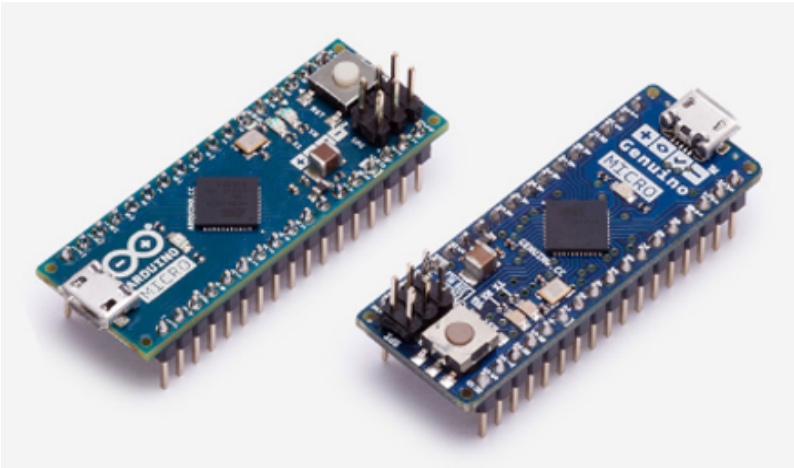

Figure 5.14 Arduino Micro (USA only) and Genuino Micro (outside USA) [139].

The Micro is a micro controller board based on the ATmega32U4, developed in conjunction with Adafruit. It has 20 digital input / output pins (of which 7 can be used as PWM outputs and 12 as analog inputs), a 16 MHz crystal oscillator, a micro USB connection, an ICSP header, and a reset button. It contains everything needed to support the micro controller; simply connect it to a computer with a micro USB cable to get started. It has a form factor that enables it to be easily placed on a breadboard. The Micro board is similar to the Arduino Leonardo in that the ATmega32U4 has built-in USB communication, eliminating the need for a secondary processor. This allows the Micro to appear to a connected computer as a mouse and keyboard, in addition to a virtual (CDC) serial / COM port. In Fig.5.15 the Arduino micro schematic is reported.

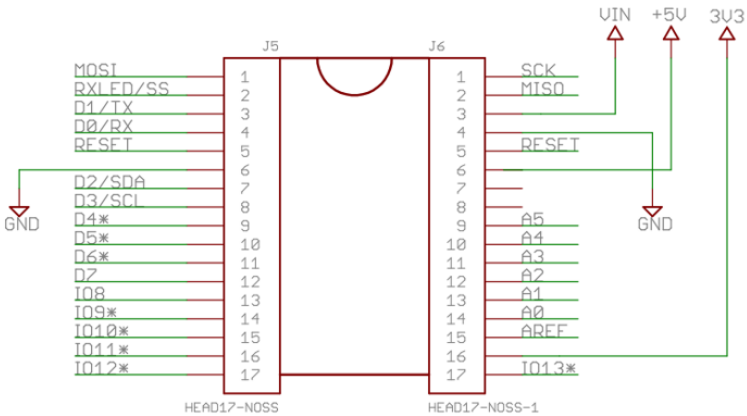

Figure 5.15 Arduino Micro schematic [139].

In Tab.5.3 the Arduino micro specifications are reported.

Specifications	**Values**	**Units**
Microcontroller	ATmega32U4	-
Operating Voltage	5	V
Input Voltage (recommended)	7-12	V
Input Voltage (limit)	6-20	V
Digital I/O Pins	20	-
PWM Channels	7	-
Analog Input Channels	12	-
DC Current per I/O Pin	20	mA
DC Current for 3.3V Pin	50	mA
Flash Memory	32 (ATmega32U4)	KB
SRAM	2.5 (ATmega32U4)	KB
EEPROM	1 (ATmega32U4)	KB
Clock Speed	16	MHz
LED-BUILTIN	13	-
Length	48	mm
Width	18	mm
Weight	13	g

Table 5.3 Arduino micro specifications from Arduino [139].

Motor Driver Carrier

A VNH5019 Motor Driver Carrier [140] was adopted to deliver the necessary power (high current) to the actuator to make it work correctly. This carrier board for ST's VNH5019 motor driver IC operates from 5.5 to 24V and can deliver a continuous 12A (30A peak). It works with 2.5 to 5V logic levels, supports ultrasonic (up to 20kHz) PWM, and features current sense feedback (an analog voltage proportional to the motor current).

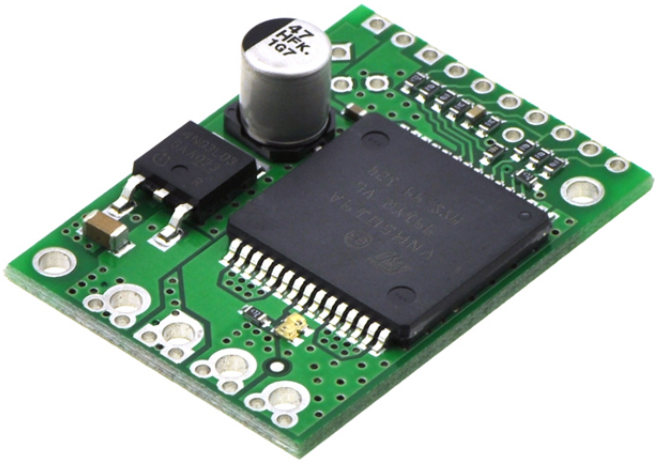

Figure 5.16 Polulu VNH5019 motor driver carrier [140].

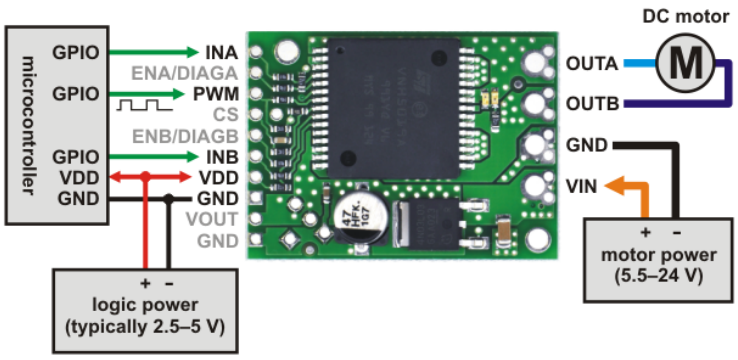

Figure 5.17 Polulu VNH5019 motor driver carrier schematic, labeled top view [140].

Specifications	Values	Units
Motor driver	VNH5019	-
Motor channels	1	-
Minimum operating voltage	5.5	V
Maximum operating voltage	24	V
Continuous output current per channel	12	A
Peak output current per channel	30	A
Current sense	0.14	V/A
Maximum PWM frequency	20	kHz
Reverse voltage protection	Yes	-
Size	38.1 x 27.94 x 9.65	mm
Weight	6.5	g

Table 5.4 VNH5019 motor driver carrier specifications [140].

Actuator

As actuator (motor and gear box) a 75:1 Metal Gearmotor 25Dx54L mm LP 6V with 48 CPR Encoder [140] was adopted. Fig.5.18 depicts a Polulu 75:1 Metal Gear motor 25Dx54L mm LP 6V with 48 CPR Encoder. This gear motor consists of a low-power, 6 V brushed DC motor combined with a 74.83:1 metal spur gearbox, and it has an integrated 48 CPR quadrature encoder on the motor shaft, which provides 3591.84 counts per revolution of the gearbox's output shaft. The gear motor is cylindrical, with a diameter just under 25mm, and the D-shaped output shaft is 4mm in diameter and extends 12.5mm from the face plate of the gearbox.

(a) Polulu 75:1 Metal Gearmotor 25Dx54L mm LP 6V with 48 CPR Encoder.

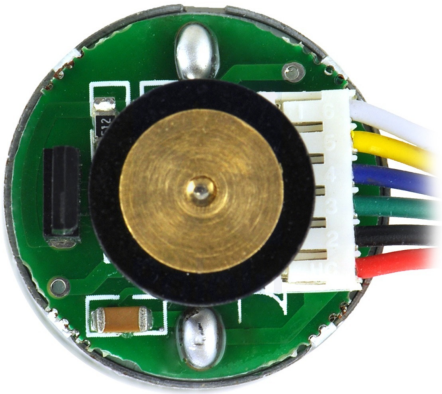

(b) 25D mm metal gearmotor with 48 CPR encoder: close-up view of encoder.

Figure 5.18 Left: Polulu 75:1 Metal Gearmotor 25Dx54L mm LP 6V with 48 CPR Encoder. Right: close-up view of encoder [140].

Tab.5.5 reports Polulu 75:1 Metal Gearmotor 25Dx54L mm LP 6V with 48 CPR Encoder specifications.

Specifications	**Values**	**Units**
Size	25D x 66L	mm
Weight	104	g
Shaft diameter	4	mm
Gear ratio	74.83:1	-
Free-run speed @ 6V	78	rpm
Free-run current @ 6V	250	mA
Stall current @ 6V	2400	mA
Stall torque @ 6V	0.67	Nm
Lead length	203.2	mm
Motor type	2.4A stall @ 6V (LP 6V)	-
Encoders	Yes	-

Table 5.5 Polulu 75:1 Metal Gearmotor 25Dx54L LP 6V with 48 CPR Encoder specifications [140].

Fig.5.19 shows the MATLAB plot motor performance curves for Pololu brushed DC gearmotors [140].

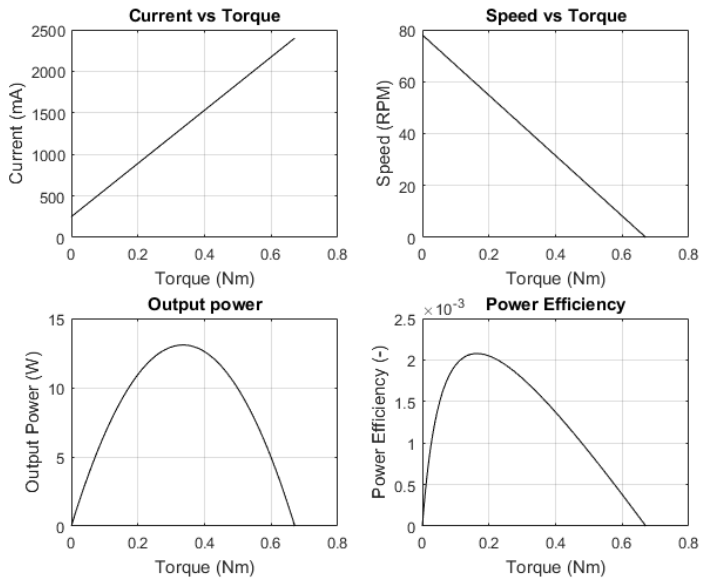

Figure 5.19 MATLAB plot motor performance curves for Pololu brushed DC gear motors.

Actuation Motion Control

For the actuation, a proportional motor control both in direct and reverse motion was adopted. The control code was written using Arduino interface. In Fig.5.20 a screen shot of the Arduino control (left) and the user window to insert the desired rotation in degrees (right) are displayed.

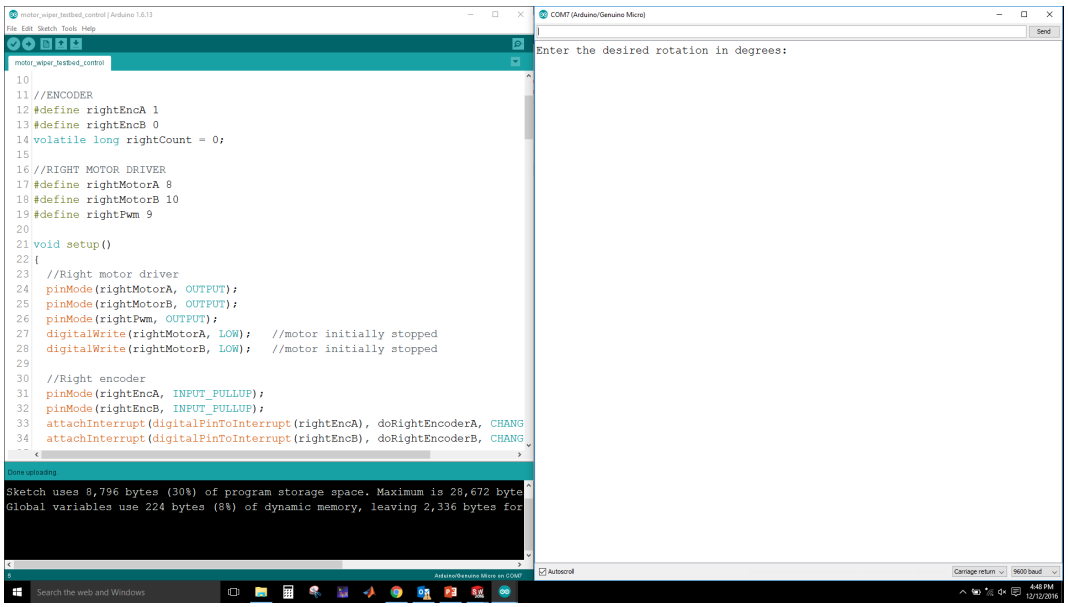

Figure 5.20 Screen shot of the Arduino control (left) and the user window to insert the desired rotation in degrees (right) are displayed.

Fig.5.21 shows the proportional motor control diagram implemented in Arduino.

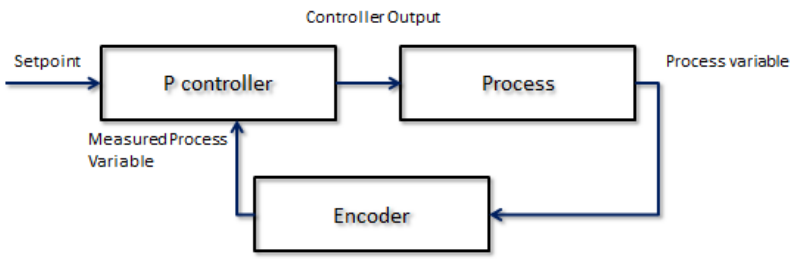

Figure 5.21 Proportional motor control diagram implemented in Arduino.

5.1.6 Testbed Assembling

To assemble this testbed 80 / 20 frames [141] were used. 80 / 20 is a framing system using extruded beams of 6105-T5 aluminum alloy. It provides a wide range of aluminum T-slot, Ready Tube, and Quick Frame profiles. T-slot aluminum profiles offer several benefits. The shape of the profile creates modularity, meaning it is easily assembled and reassembled to conform to evolving needs. The T-slot also provides the ability to add connections and

join profiles to captive ends. This allows to change the design without having to start from scratch and also enables easy expansion and retraction of your build for modifications down the road. The T-slot profile concept is designed to allow movement while staying secure within the T-slot. Moving on from the T-slot concept, let us consider the benefits of aluminum. There are several advantages to T-slot aluminum profiles. Some of the biggest are:

- Strong;
- Light;
- High strength-to-Iight ratio;
- Resilient;
- Modularity;
- Easily machined;
- All 80/20 profiles come standard with a clear anodize which helps prevent oxidation and corrosion while providing a matte finish.

Main 80 / 20 structural assembly components are reported in Fig.5.22.

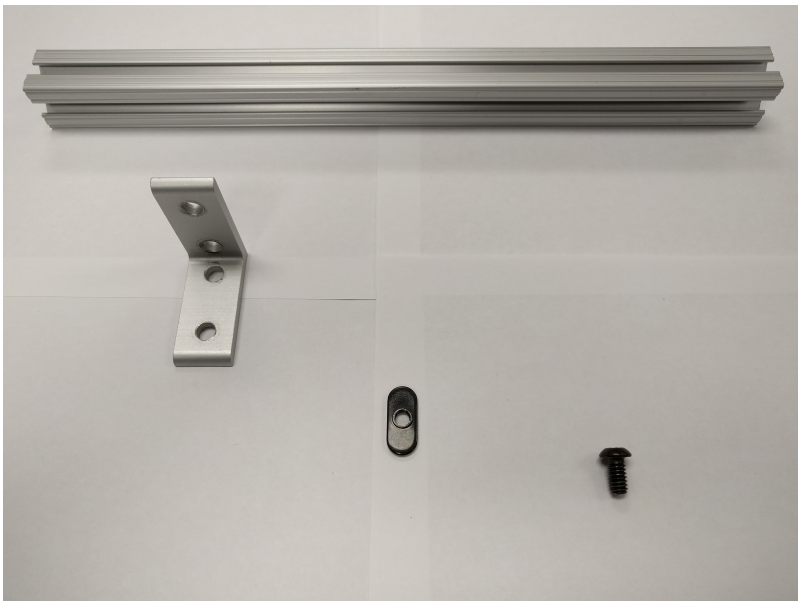

Figure 5.22 Main 80 / 20 structural assembly components. From left to right: T-slot profile, bolt, slide-in T-nut centered thread, angle bracket.

5.1.7 Testbed Alignment

To align all the mechanical components on the testbed Allen keys were used together with wrenches, pincers, rulers, and level using eye view. All the minor contact / friction issues were fixed operating the mechanism first manually and then using the motor. In particular, a special care was devoted to:

- The interaction contact between the Wiper and the pin;
- The gap between the Wiper and the positive feature during a whole loop (360°);
- The no interaction between the whole testbed structure and the Wiper during a whole loop (360°).

5.2 Testbed Apparatus

In the testbed apparatus some elements were grouped together:

- The structural platform including the OS with the pin;
- The electronic system including the E-switch;
- The PC laptop to send commands to the electronic system to control the actuator;
- The power supply provides the correct amount of power for the whole mechanism to work properly.

The testbed apparatus is reported in Fig.5.23, while Fig.5.24 shows the testbed architectural flow and connections. The double-headed arrows indicate connections in both ways, both forward and backward.

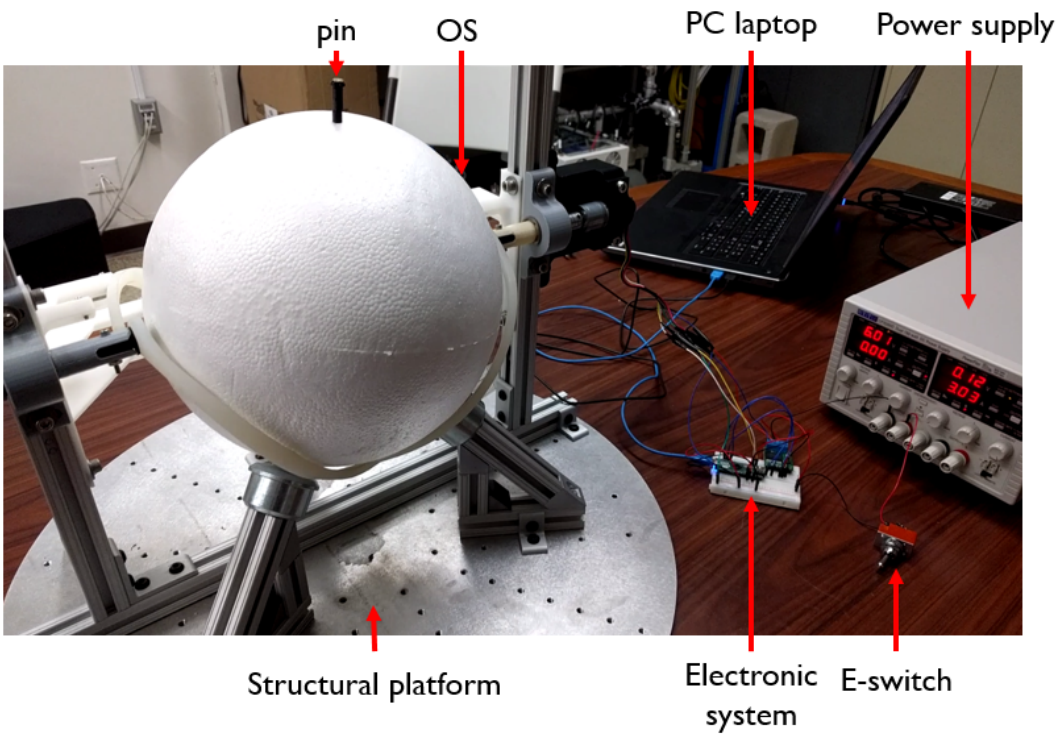

Figure 5.23 Testbed apparatus [124].

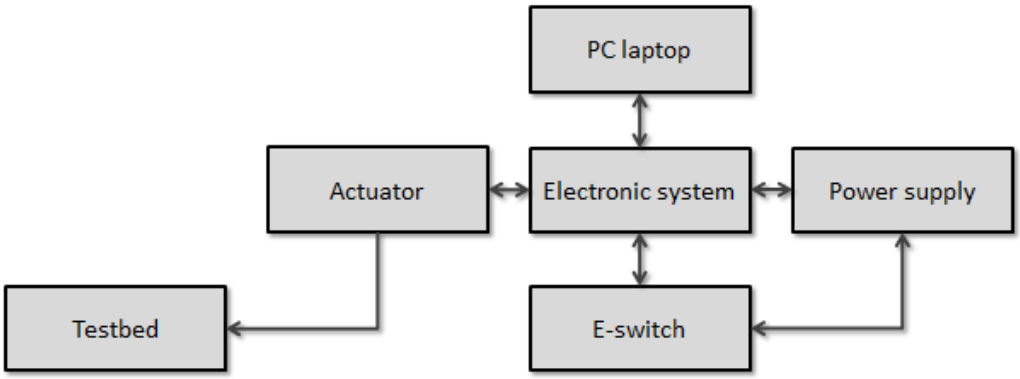

Figure 5.24 Testbed architectural flow and connections. The double-headed arrows indicate connections in both ways, both forward and backward.

5.2.1 Testbed Apparatus Actuation

Fig.5.25 displays four phases of the testbed apparatus actuation with the OS initial orientation with the pin located opposite to the retention mechanism:

a) The pin is located opposite to the retention mechanism. The Wiper has not started to rotate yet;

b) The Wiper starts to rotate. It interacts with the pin. The pin is already in the final position within the Wiper arc;

c) The Wiper brings the pin down correctly;

d) The Wiper brings the pin to the final location where the retention mechanism is placed. The shaft coupler-Wiper connection shaft was made voluntarily slipping inside the shaft coupler once the OS orientation was terminated with the pin trapped. In this case the actuator tries to rotate the Wiper that cannot, because it is physically constrained. The slipping reflects the fact that the initial OS orientation is unknown. It is possible to reorient the OS within two loops, the actuator control gives more than two loops rotation to the Wiper, and the slipping guarantees that the mechanism will not brake.

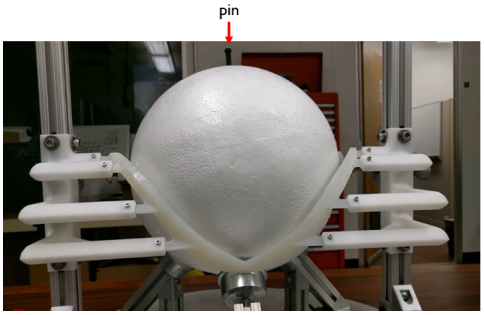

(a) The pin is located opposite to the retention mechanism. The Wiper has not started to rotate yet.

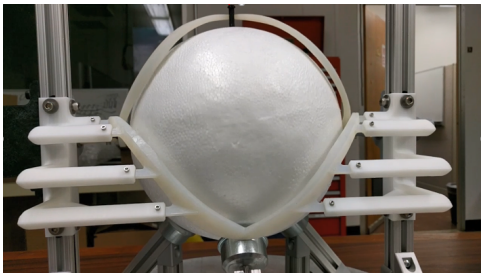

(b) The Wiper starts to rotate. It interacts with the pin. The pin is already in the final position within the Wiper arc.

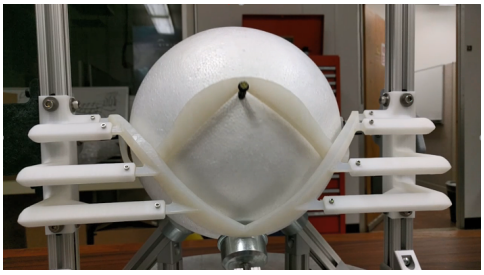

(c) The Wiper brings the pin down correctly.

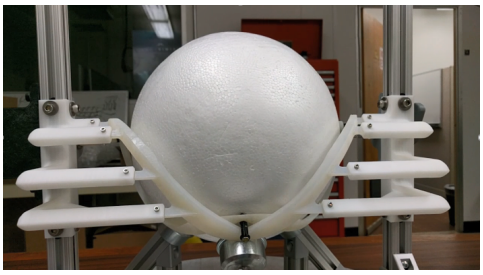

(d) The Wiper brings the pin to the final location where the retention mechanism is placed.

Figure 5.25 Testbed apparatus actuation with the OS initial orientation with the pin located opposite to the retention mechanism.

Fig.5.26 displays four phases of the testbed apparatus actuation with a random OS initial orientation:

a) The pin is located randomly with respect to the retention mechanism. The Wiper has not started to rotate yet;

b) The Wiper starts to rotate. It interacts with the pin;

c) The Wiper brings the pin down correctly;

d) The Wiper brings the pin to the final location where the retention mechanism is placed.

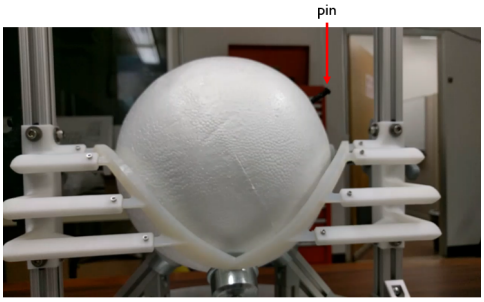

(a) The pin is located randomly with respect to the retention mechanism. The Wiper has not started to rotate yet.

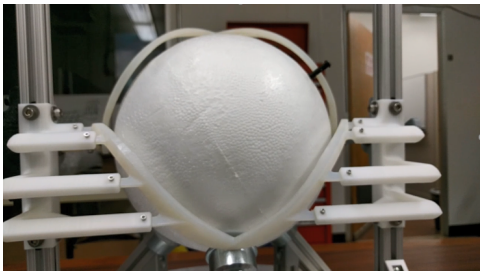

(b) The Wiper starts to rotate. It interacts with the pin.

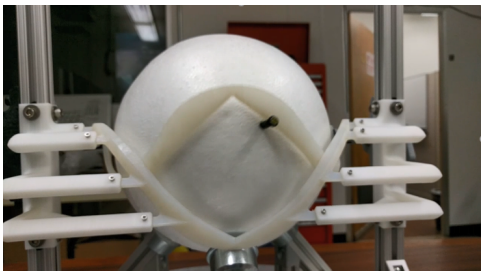

(c) The Wiper brings the pin down correctly.

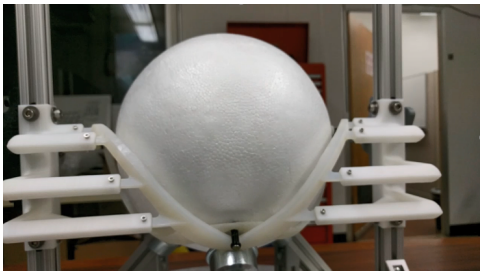

(d) The Wiper brings the pin to the final location where the retention mechanism is placed.

Figure 5.26 Testbed apparatus actuation with a random OS initial orientation.

Fig.5.27 displays a detail of the most critical configuration where the pin locates between the Wiper and the positive feature and where a jamming condition could happen caused by a small scissor angle.

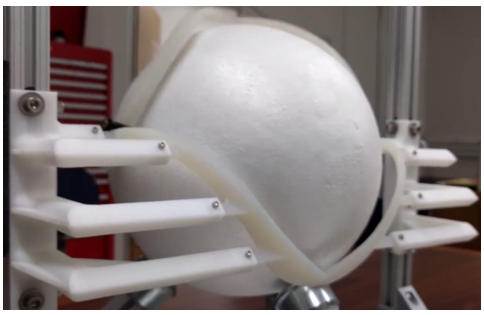

(a) Critical configuration.

(b) Critical configuration detail.

Figure 5.27 Detail of the most critical configuration where the pin locates between the Wiper and the positive feature and where a jamming condition could happen caused by a small scissor angle.

Fig.5.28 displays four phases of the testbed apparatus actuation related to this critical configuration.

a) The pin is located between the Wiper and the positive feature and where a jamming condition could happen caused by a small Wiper angle. The Wiper has not started to rotate yet;

b) The Wiper starts to rotate. It interacts with the pin;

c) The Wiper brings the pin down correctly;

d) The Wiper brings the pin to the final location where the retention mechanism is placed.

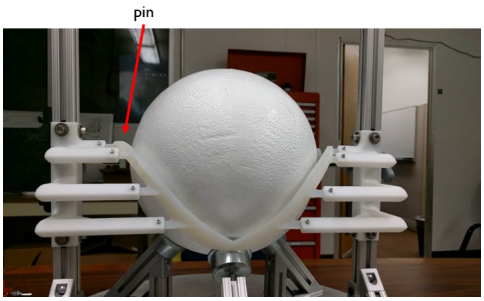

(a) The pin is located between the Wiper and the positive feature and where a jamming condition could happen caused by a small scissor angle. The Wiper has not started to rotate yet.

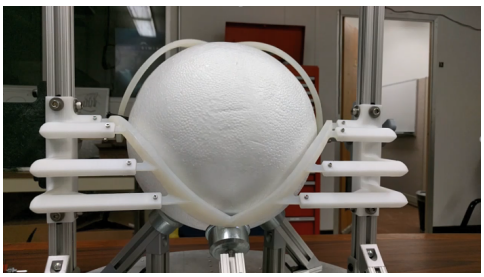

(b) The Wiper starts to rotate. It interacts with the pin.

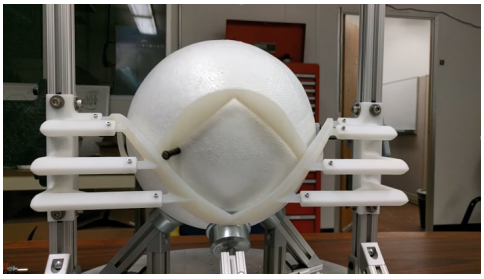

(c) The Wiper brings the pin down correctly.

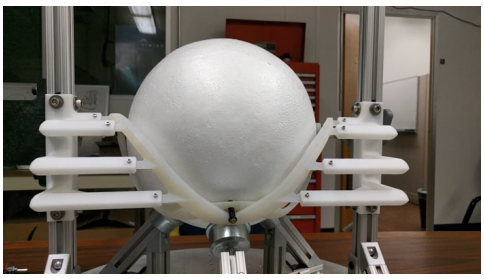

(d) The Wiper brings the pin to the final location where the retention mechanism is placed.

Figure 5.28 Testbed apparatus actuation related to the most critical configuration where the pin locates between the Wiper and the positive feature and where a jamming condition could happen caused by a small scissor angle.

Moreover, Fig.5.29 shows that the actuation can be controlled in reverse too. This makes the testbed easier to be used.

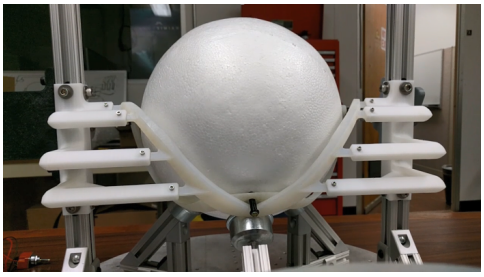

(a) The Wiper is retaining the pin in the final position.

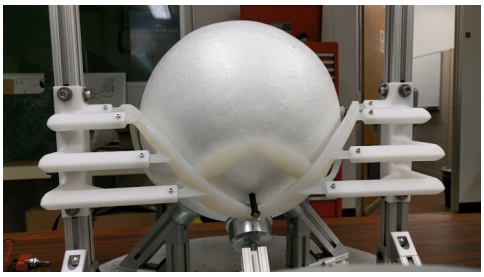

(b) The Wiper starts to rotate backwards.

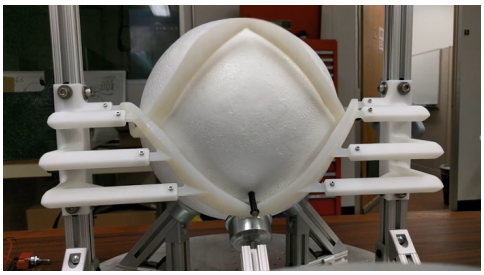

(c) The Wiper continues to rotate backwards.

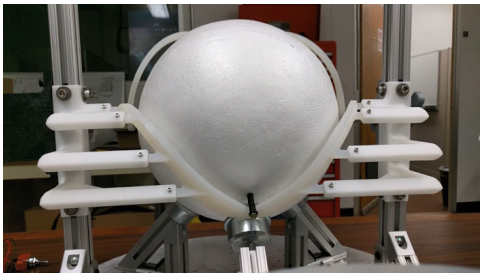

(d) The Wiper rotates backwards until it engages with the positive feature support.

Figure 5.29 Testbed apparatus actuation controlled in reverse.

5.2.2 Results

In this case the success is 100%. The mechanism works in all the possible pin locations (OS initial orientation) and especially in the most critical one. In this testbed the Wiper cannot rotate 360° and the ball bearing support with low friction represent the absence of gravity. These two elements are better represented in the upgrade of this testbed using water to support the styrofoam ball OS to allow a 360°-Wiper rotation and to adopt the buoyant force against the gravitational one.

5.3 Testbed N.2: Water Wiper Testbed Description

This testbed consists of a semi-spherical shell filled with water where a buoyant OS was placed. The water supports the OS and more closely simulates a zero-g environment [124]. For this testbed, using water to offset gravity force was considered. The Water Wiper testbed is reported in Fig.5.30. A Phidgets motor with 24:7 reduction drives the mechanism. It develops a total of 2.2Nm constant torque. With respect to the Testbed N.1, less dynamic motion is present, the positive feature location is adjustable, the Wiper can spin freely 360° plus, it does not artificially center the OS in all directions and a low friction rotation surface is present. While the Water Testbed is not a hard translational constraint, it behaves like a sprung damper system which translationally biases the OS. In zero-g, the OS would have no translational bias. In essence this testbed gives the OS a translational soft constraint.

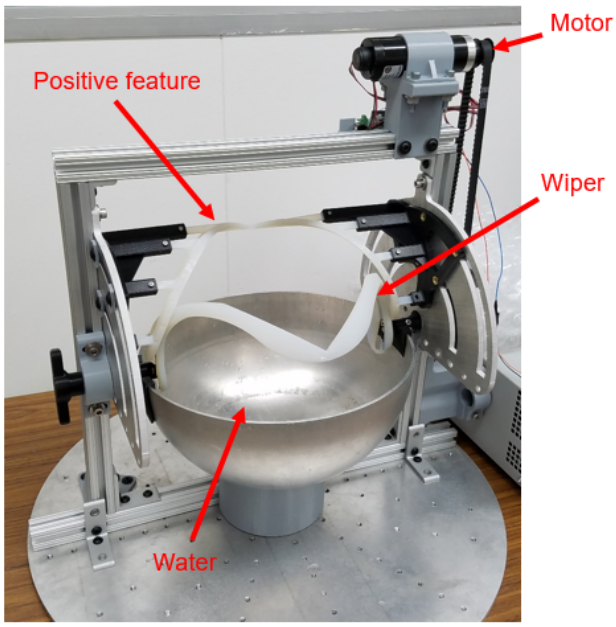

Figure 5.30 Water Wiper testbed [124].

The main disadvantages are that water only offsets gravity in plane and an unbalanced OS causes undesired extra forces during reorientation.

In Fig.5.31, 5.32, and 5.33 the Solidworks CAD of the testbed is illustrated together with the real testbed. Three different views are shown: (a) front view, (b) side view and (c) top view. The author personal contributions discussed in the next sections are related to the green highlighted components. In particular:

- Characterization of the Wiper-positive feature shape and profile and their interaction with the pin;
- Characterization of the pin dimensions (length and diameter);
- Electronic system wiring to the motor and to the power supply;
- Motion control of the actuator.

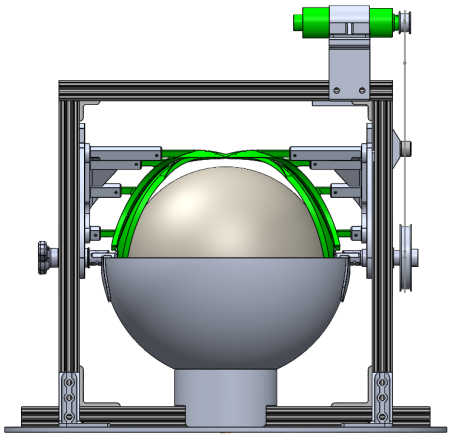

(a) CAD model testbed front view.

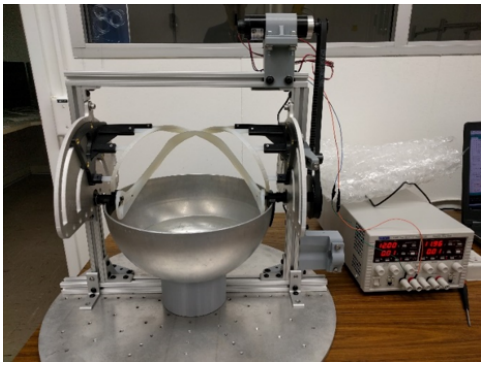

(b) Wiper Water Testbed front view [124].

Figure 5.31 Water Testbed front view.

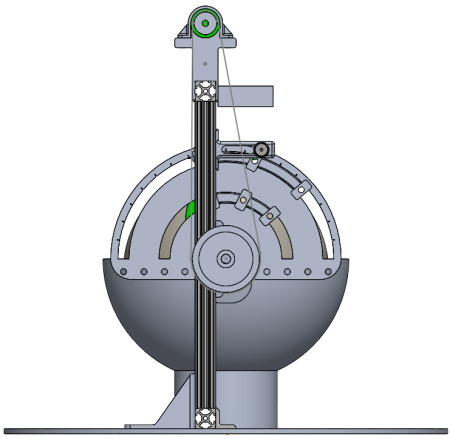

(a) CAD model testbed side view.

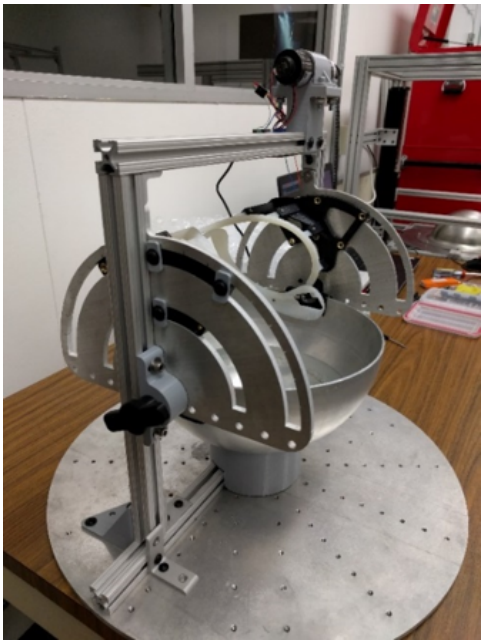

(b) Wiper water Testbed side view [124].

Figure 5.32 Water Testbed side view.

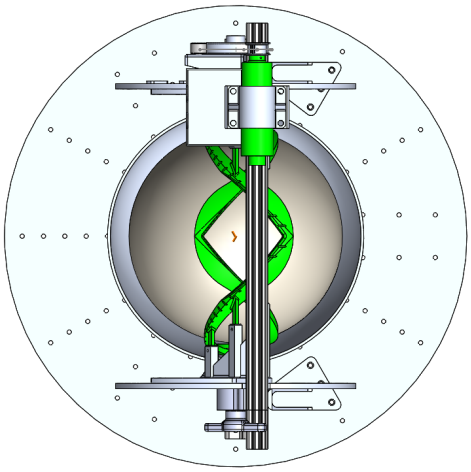

(a) CAD model testbed top view.

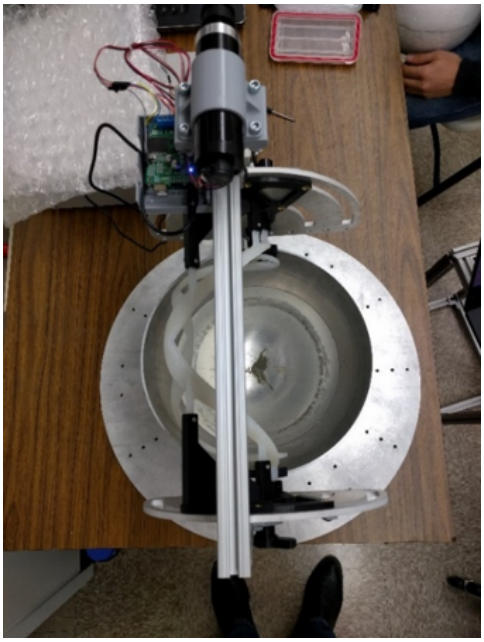

(b) Wiper Water Testbed top view [124].

Figure 5.33 Water Testbed top view.

Fig.5.34 shows the testbed architectural flow and connections. The double-headed arrows indicate connections in both ways, both forward and backward. With respect to Fig.5.24, two other blocks are present: IMU and the electronic system, both inside the OS. In this case, data regarding the actual OS motion in real time are collected, see Ch.6.

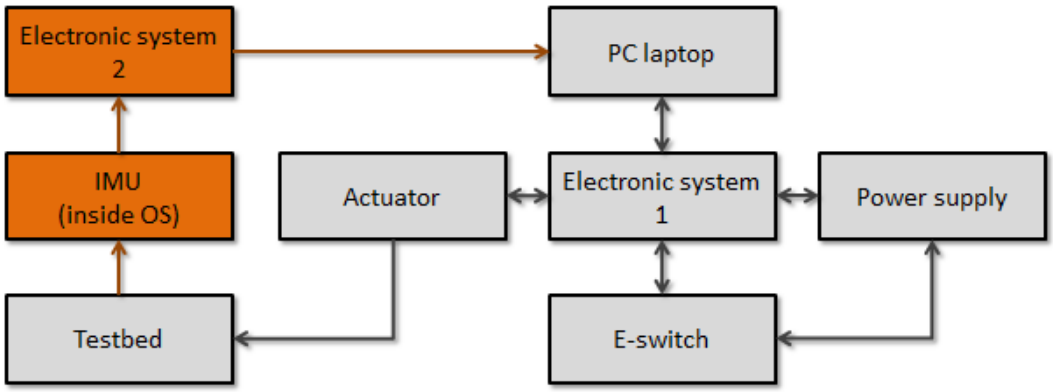

Figure 5.34 Testbed architectural flow and connections. The double-headed arrows indicate connections in both ways, both forward and backward. Two other blocks are present (in orange): IMU and the electronic system, both inside the OS to collect data regarding OS motion in real time.

5.3.1 Electronic System

In Fig.5.35 a schematic using Eagle PCB design software [138] is shown. Four elements are present: the Arduino Uno processor, the power supply, the motor driver, the breadboard, the DC motor. The electronic physical hardware is reported in Fig.5.36.

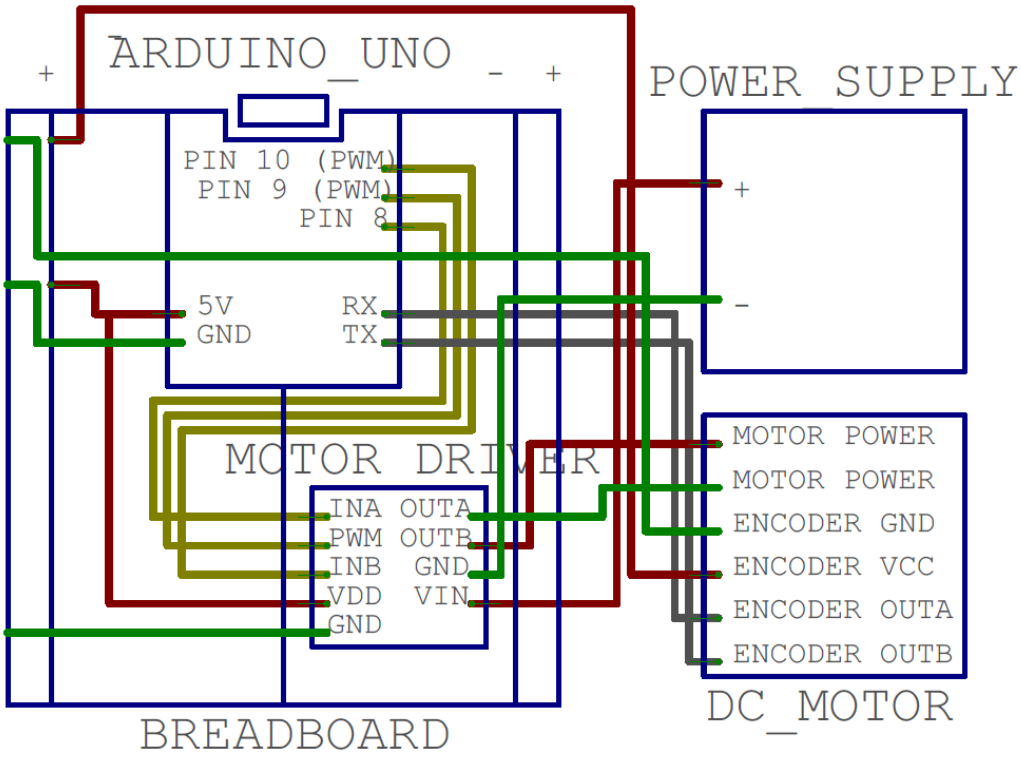

Figure 5.35 Electronic system schematic using Eagle PCB design software [138]. Four elements are present: the Arduino Uno processor, the power supply, the motor driver, the breadboard, the DC motor.

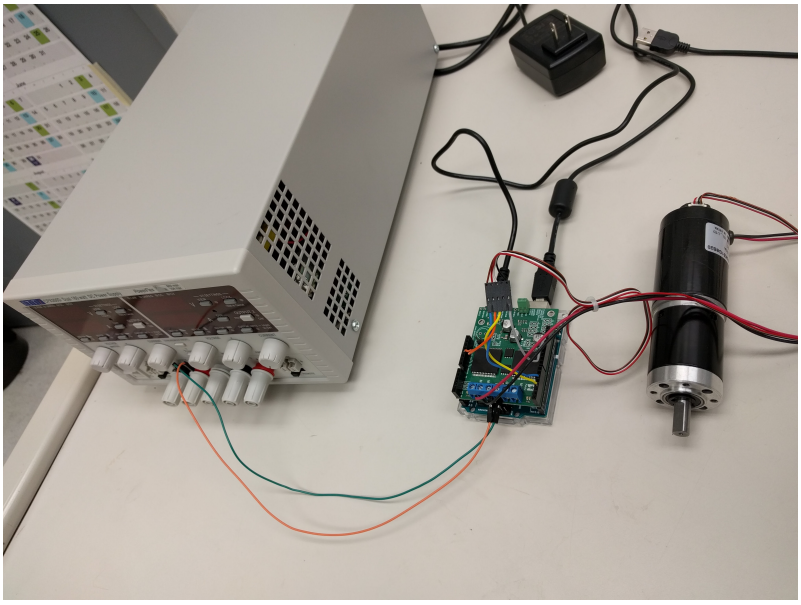

Figure 5.36 Electronic physical hardware, from left to right: Power Supply, Arduino Uno and Motor Driver and DC motor.

Figure 5.37 Arduino Uno R3 USB Microcontroller [139].

Motherboard: Arduino Uno

The Arduino Uno R3 USB Microcontroller is a microcontroller board based on the ATmega328 microchip. It has 14 digital input/output pins (of which 6

can be used as PWM outputs), 6 analog inputs, a 16MHz crystal oscillator, a USB connection, a power jack, an ICSP header, and a reset button. It contains everything needed to support the microcontroller; simply connect it to a computer with a 1.5m USB Cable Type A to B or power it with an Wall Adapter Power Supply - 9VDC 650mA or DFRobot 7.4V Lipo 2200mAh Battery (Arduino Power Jack) to get started [139]. The Arduino Uno can be powered via the USB connection or with an external power supply. The power source is selected automatically. External (non-USB) power can come either from an AC-to-DC adapter (wall-wart) or battery. The adapter can be connected by plugging a 2.1mm center-positive plug into the board's power jack. Leads from a battery can be inserted in the Gnd and Vin pin headers of the POWER connector. The board can operate on an external supply of 6 to 20V. The Arduino Uno can be programmed with the Arduino software. The board can operate on an external supply of 6 to 20V. If supplied with less than 7V, however, the 5V pin may supply less than five volts and the board may be unstable. If using more than 12V, the voltage regulator may overheat and damage the board. The recommended range is 7 to 12V. The power pins are as follows:

- VIN. The input voltage to the Arduino board when it's using an external power source (as opposed to 5V from the USB connection or other regulated power source). It is possible to supply voltage through this pin, or, if supplying voltage via the power jack, access it through this pin.
- 5V. This pin outputs a regulated 5V from the regulator on the board. The board can be supplied with power either from the DC power jack (7 - 12V), the USB connector (5V), or the VIN pin of the board (7-12V). Supplying voltage via the 5V or 3.3V pins bypasses the regulator, and can damage the board.
- 3V. A 3.3V supply generated by the on-board regulator. Maximum current draw is 50mA.
- GND. Ground pins.
- IOREF. This pin on the Arduino board provides the voltage reference with which the microcontroller operates. A properly configured shield

can read the IOREF pin voltage and select the appropriate power source or enable voltage translators on the outputs for working with the 5V or 3.3V.

Motor Driver Carrier

A Pololu Dual VNH5019 Motor Driver Shield was adopted for Arduino [140] to deliver the necessary power (high current) to the actuator to make it work correctly. This motor driver carrier has the same characteristic of the one shown in Subsec.5.1.5.

Actuator

The previous actuator was substituted due to:

- Necessity to study the Wiper-OS interaction at lower speed and higher torque.
- Passing from a dynamic OS balancing condition to a quasi-static OS balancing condition, closer to zero-g space environment.

As actuator (motor and gear box) a 3267E 0 - 12V/6.6Kg-cm/49RPM 51:1 DC Gear Motor w/Encoder was adopted [142]. Fig.5.38 depicts this actuator. The 3267E is a 12V gear motor, generating 0.65Nm of torque at 49rpm. Since this motor has a lower power output for its size, it has a longer lifespan than other motors. This motor comes equipped with an E4P US Digital Encoder, which keeps track of the motor's rotation, allowing to control the motor precisely. The planetary gearbox on this motor is more sophisticated than a typical spur gearbox and provides greater efficiency, higher torque, and quieter motor operation.

Figure 5.38 3267E actuator with encoders [142].

Tab.5.6 reports 3267E actuator with encoder specifications.

Specifications	**Values**	**Units**
Wire length	350	mm
Weight	529	g
Shaft diameter	8	mm
Gear ratio	50.895	-
Free-run speed @ 12V	49	rpm
Free-run current @ 12V	650	mA
Stall current @ 12 V	2400	mA
Stall torque @ 12V	4.59	Nm
Output Power (Mechanical)	3.8	W
Motor type	DC Motor with Encoder	-
Encoders	Yes	-

Table 5.6 3267E actuator specifications [142].

Fig.5.39 shows the MATLAB plot motor performance curves for 3267E actuator.

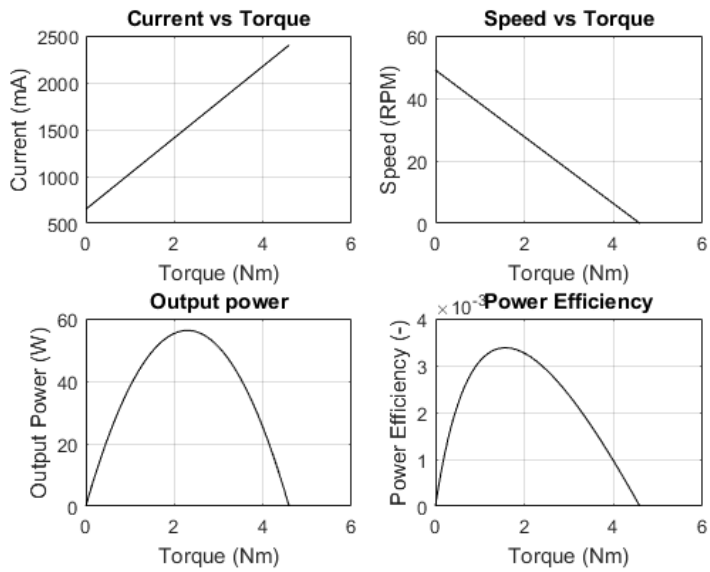

Figure 5.39 MATLAB plot motor performance curves for 3267E actuator.

Actuation Motion Control

For the actuation control a PID-control for direct motion was implemented. The control code was written using Arduino interface. Fig.5.40 shows the PID motor control diagram implemented in Arduino.

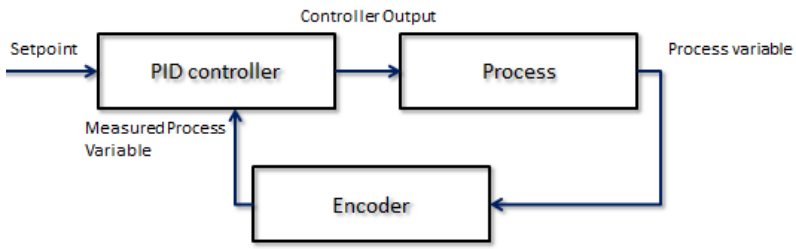

Figure 5.40 PID motor control diagram implemented in Arduino.

5.3.2 Results

The results concerning the proper working of this testbed to validate the Wiper-pin concept are reported together with the full description of the Designs of Experiment in Ch.6.

5.3.3 Water Testbed Considerations

There are some aspects to be discussed about Water testbed:

- The OS was made of styrofoam and its mass is about 0.5kg. The mass such as the friction properties were not representative of a real OS in space. Moreover, the OS was not perfectly balanced on the three inertia axis as it would happen in zero-g or using a magnetic-levitation testbed. Some expedients about that were considered, they will be briefly discussed in Ch.6.
- On the z-axis (gravity axis) the OS was balanced between the gravity force pulling downward and the water buoyant force pushing upward. This brings the OS spherical center to be almost always in the center in the outer shell for what concerns the z-axis. Testing demonstrates proper operation of the mechanism even with a OS misalignment of up to 10mm of its nominal centered position within the mechanism.
- The motor torque adopted for the Water Testbed was limited. This could bring to some jamming conditions considering the OS was made of styrofoam and both the Wiper, the positive features and the pin were plastic-3D printed components.

The main goal of this testbed was to test the Wiper concept profile and the Wiper-pin interaction. All the precautions were taken to guarantee the validation of this mechanism.

5.4 Final MOSTT Wiper Testbed

For completeness, in Fig.5.41 the final MOSTT Wiper testbed is reported [124].

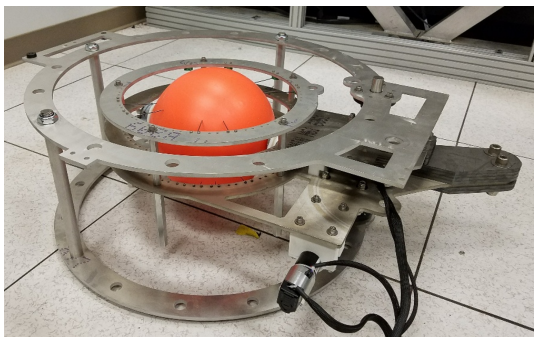

Figure 5.41 Final MOSTT Wiper testbed [124].

The final testbed was designed to test a strategy to both keep the OS centered in a spherical volume and to ensure the Wiper can sweep the full surface of the OS. Flexible fingers mechanically keep the OS centered to avoid Wiper binding conditions. Being flexible is what allows the moving Wiper to pass in one-way direction with little resistance until it engages with the pin. The ability to operate the Wiper mechanism within this testbed opens to the possibility to validate it in a one-g terrestrial laboratory.

5.5 OS Retention Mechanism

After the reorientation phase, another critical aspect was the OS Retention Mechanism (ORM) that retains the OS before inserting it inside the EEV, see detail in Fig.5.42.

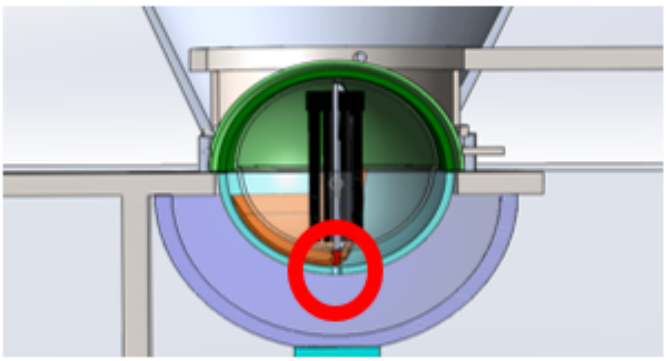

Figure 5.42 The Wiper reorients the OS and retains it through a retention mechanism (red circle).

In this work, the OS is retained through its positive feature, i.e., the pin. A retention mechanism concept design was evaluated and here proposed. It has to be respectful of the following objectives:

- The ORM shall retain the OS after reorientation (providing a soft retention feature) and during the entire landing event on Earth ($\sim$1300g) (providing a hard retention feature).
- The ORM volume has to be considered inside the OS container and to be minimized as much as possible.
- The ORM shall be able to recover the OS insertion from all the possible insertion errors ($\sim 10°$).

An ORM concept named Spring Loaded Trap was developed. As reported in Fig.5.43, (a) this mechanism hosts the incoming pin with against incoming inclination error ($\sim 10°$), (b) the pin makes the three clumps opening (each clump base is radially sprung to the center of the mechanism), (c) the pin enters in the mechanism, (d) as soon as the pin head enters completely in the mechanism the three springs cause the three clumps to move back to trap the pin. This mechanism relies on:

- Passive pre-sprung system with no necessity of actuators to hold the pin inside the trap.
- Three linear springs (stiffness $\sim$ 10N/mm).
- The interaction among the three clumps is a key aspect. The retention mechanism works correctly if there are no spaces in between the clump edges.
- Pin / clump incidence angle (15° in this case) is another key feature to be sure the pin does not jam when it enters in the trap.
- It allows to recover from possible insertion errors.

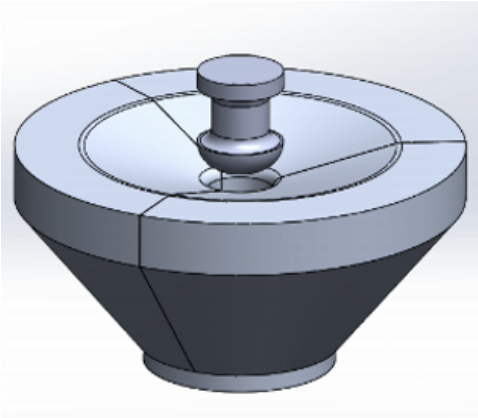

(a) This mechanism hosts the incoming pin with a possible incoming inclination error ($\sim 10°$).

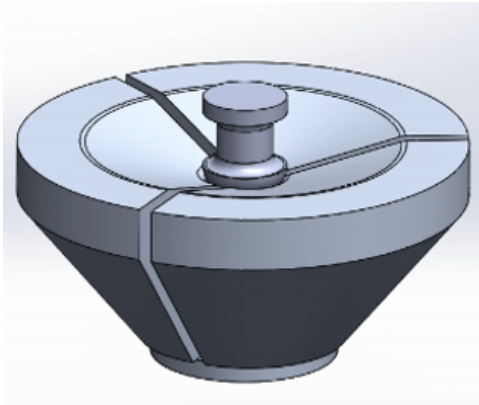

(b) The pin makes the three clumps opening (each clump base is radially sprung to the center of the mechanism).

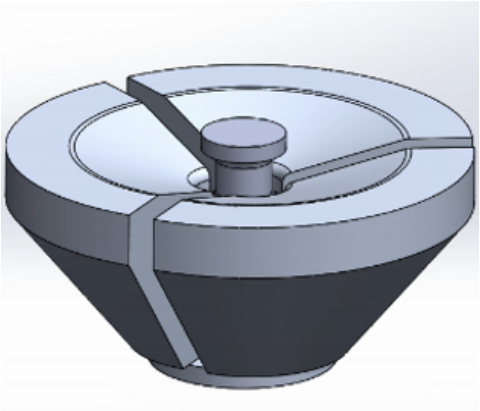

(c) The pin enters in the mechanism.

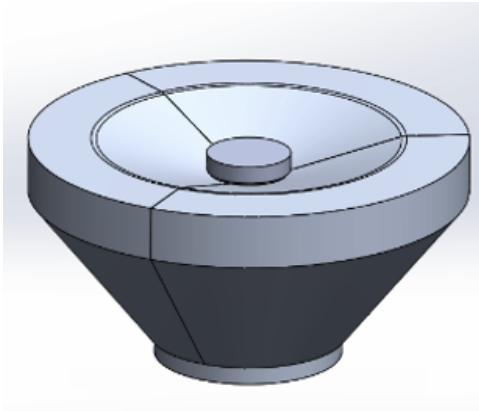

(d) As soon as the pin head enters completely in the mechanism the three springs cause the three clumps to move back to trap the pin

Figure 5.43 OS retention mechanism concept design: Spring Loaded Trap.

Some drop-off dynamic simulations were also executed to verify if the presented concept could survive the worst condition scenario that is a hard landing with accelerations around 1300g drop test at 44m/s of impact speed. In Fig.5.44 the SolidWorks results of these simulations are reported. In this case both the pin and the retention mechanism were constituted of Al 6061-T6. The results indicate that the mechanism survives under the considered loads and the OS will be safely retained through the pin.

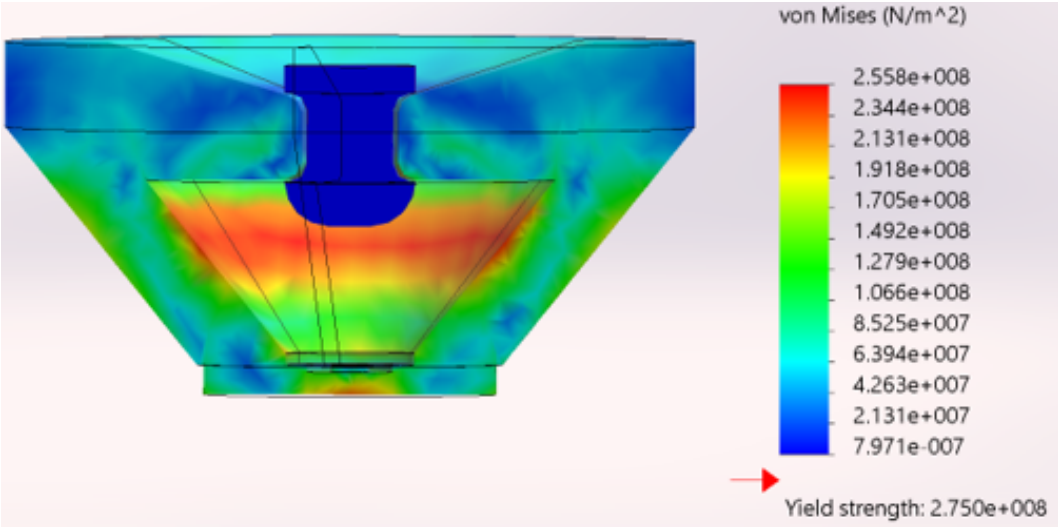

Figure 5.44 SolidWorks drop-off dynamic simulations to verify if the presented concept could survive the worst condition scenario that is a hard landing with accelerations around 1300g drop test at 44m/s of impact speed. The stress reported are below the Al 6061-T6 yield stress.

Chapter 6

Experimental Setup

6.1 Apparatus Description

The goal of this chapter is to illustrate the experimental setup through the design of experiment (DOE) using the Water Wiper Testbed to validate the concept through data acquisition.

Parts of this chapter were published in:

- Electro-Mechanical System to Reorient a Spherical Orbital Sample for a Potential Mars Sample Return Mission Concept **Dolci M.**, Mayo J., Chamberlain-Simon B., Smith R., Kim J., Ubellacker W., Ohta P., Mukherjee R., submitted to Acta Astronautica, August 2017.

The main goals of the experimental setup were:

- Obtaining OS angles (roll, pitch, yaw) during the reorientation to show that the mechanism was able to reorient the OS, even in critical locations.
- Acquire data to have an esteem about the minimum torque amount required to reorient the OS.

Fig.6.1 describes the OS designed for the DOE both CAD and the real hardware.

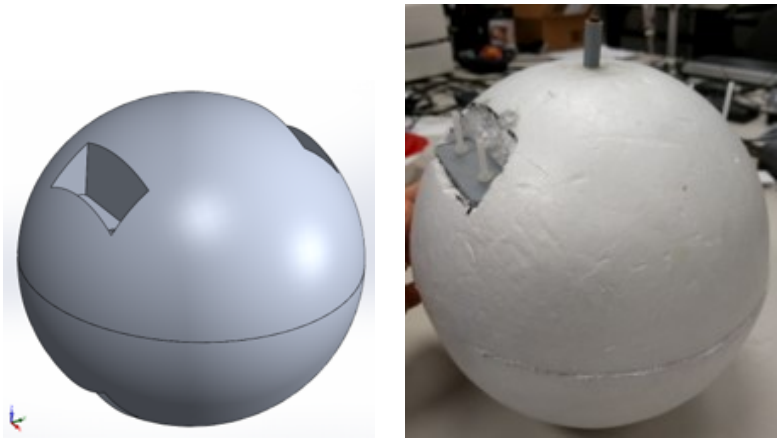

(a) Styrofoam OS CAD. (b) Styrofoam OS real hardware.

Figure 6.1 OS designed for the DOE.

A water proof electronic box, with sensors inside, was inserted inside the OS. A motheboard was connected to a IMU and to a bluetooth wireless module. Fig.6.2 shows OS inserting water proof electronic box [124].

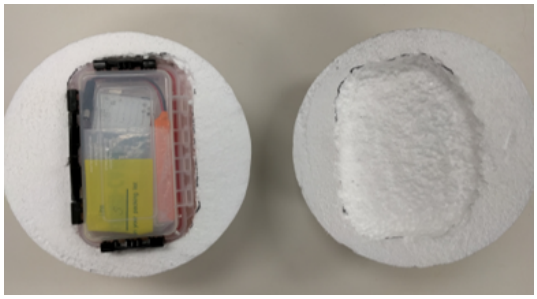

Figure 6.2 OS inserting water proof electronic box [124].

Fig.6.3 shows the closed water proof electronic box.

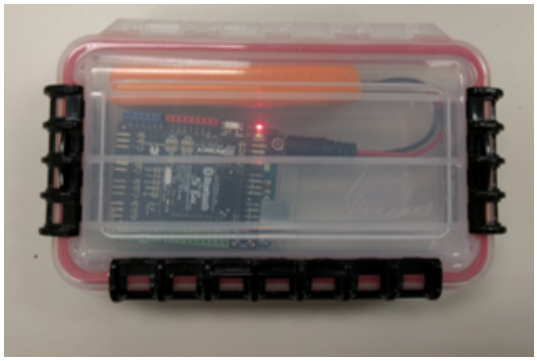

Figure 6.3 Water proof electronic box (close).

Fig.6.4 shows the open water proof electronic box [124]. There are three main elements: water-proof box, the electronics and the battery.

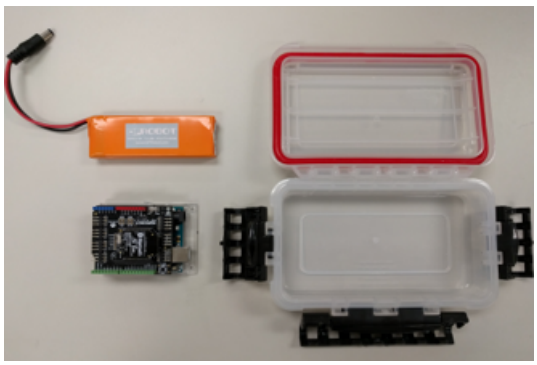

Figure 6.4 Water proof electronic box (open) [124].

The procedure followed consists of two main steps:

- IMU communicate through Bluetooth to the PC adopting Python.
- Extended Kalman Filter (EKF) sensor fusion of IMU (accelerometer and gyro) data adopting Python.

6.1.1 Electronics

An Arduino Uno R3 USB Microcontroller board was adopted for this design of experiment with the same features of the one already reported in Ch.5.

6.1.2 Inertial Mass Unit (IMU)

Figure 6.5 Inertial Mass Unit [143].

The 6-dof IMU Arduino Shield with XBee Headers is a 6-dof IMU shield for Arduino, using the ADXL345 accelerometer and the ITG-3200 gyro [143], see Fig.6.5. This IMU Combo shield also embeded a xbee sockets. So it is suitable for a project that needs bluetooth, wifi or Zigbee wireless communication. The shield extends a pair of the encoders, the motor driver interface and 4 analog input connectors. The IMU specifications are:

- 6-dof IMU shield for Arduino;
- Working voltage: 5v and 3.3v;
- Interface: I2C (SCL, SDA);
- Connectors:
  - 2 way encoder connectors by using D2, D3, D8, D9;
  - 2 way motor driver connector by using D4, D5, D6, D7;
  - 4 way analog input connector (A0∼A3).

- Embeded the ADXL345 accelerometer and the ITG-3200 gyro;
- Directly support Xbee and XBee form factor wi-fi, bluetooth and RF modules.

ADXL345 accelerometer

Tab.6.1 reports possible sources of error to characterize the accelerometer within the EKF.

Source	**Value**	**Unit**
Non linearity	± 0.5	%
Cross axis sensitivity	± 1	%
Sensitivity	-0.10 / +0.12	g
Noise performance	± 0.006	g

Table 6.1 Possible sources of error to characterize the accelerometer within the EKF.

Assuming that the accelerations involved in this problem are ∼1g. The total error affecting this sensor results to be $\sigma^2_{acc} = \pm 0.12$g on all three axis.

ITG-3200 gyro

Tab.6.2 reports possible sources of error to characterize the gyro within the EKF.

Source	**Value**	**Unit**
Sensitivity scale factor tolerance	± 6	%
Non linearity	± 0.2	%
Cross-axis sensitivity	± 2	%
Power-supply sensitivity (120-250 Hz)	± 0.2	$^\circ/s$
Total RMS noise	± 0.38	$^\circ/s$

Table 6.2 Possible sources of error to characterize the gyro within the EKF.

Assuming that the angular velocities involved in this problem are $\sim 10°/s$. The total error affecting this sensor (without considering the sensitivity scale factor variation over temperature) results to be $\sigma^2_{gyro} = \pm 0.765°/s$ on all three axis.

6.1.3 DFRobot Bluetooth Bee

Figure 6.6 DFRobot Bluetooth Bee wireless module [143].

The DFRobot Bluetooth Bee wireless module adapts XBEE design. It features compact size and the pinout is compatible with XBEE which is suitable for all kinds of microcontroller systems having 3.3V output power. Its specifications are:

- Fully qualified bluetooth V2.0 + EDR;
- Sensitivity: </= (-84dBm) @0.1% BER;
- Comes with an on-board antenna;
- Pinout is compatible with XBEE;
- Default baud rate: 9600;
- Bluetooth chip: CSR BC417143;
- USB Protocol: USB v1.1/2.0;
- Operating frequency: 2.4-2.48GHz;

- Modulation: GFSK;
- Transmit Power: = 4dBm, Class-2;
- Transmission distance: 20m-30m (free space);
- Transfer rate:
  - Asynchronous: 2.1Mbps (Max)/160 kbps;
  - Synchronous: 1Mbps/1Mbps.
- Safety features: Authentication and encryption;
- Support profiles: Bluetooth serial port;
- Serial port settings: 1200-1382400/N/8/1;
- Input voltage: +3.3 DC/50mA;
- Operating temperature: -20°C to +55°C.

This module communicates to a PC laptop through Arduino first and then adopting Python to collect and process the IMU data.

6.2 Extended Kalman Filter - Sensor Fusion

6.2.1 Tait-Bryan Angles

Following [144], [145], [146] using Tait-Bryan angles the state equation is Eq.6.1

$$x = (\theta_x, \theta_y, \theta_z, \omega_x, \omega_y, \omega_z, b_x, b_y, b_z), \tag{6.1}$$

where θ_x, θ_y, θ_z represent the Tait-Bryan angles, ω_x, ω_y, ω_z the angular velocities b_x, b_y, b_z are the gyro bias.
The measurements vector is represented by Eq.6.2

$$z = (\tilde{\omega_x}, \tilde{\omega_y}, \tilde{\omega_z}, \bar{a_x}, \bar{a_y}, \bar{a_z}), \tag{6.2}$$

where $\tilde{\omega_x}, \tilde{\omega_y}, \tilde{\omega_z}$ represent raw gyro measurements and $\bar{a_x}, \bar{a_y}, \bar{a_z}$ normalized accelerometer vector. The rotation ψ, θ, ϕ was adopted, as expressed by Eq.6.3

$$R_{tot} = R_\psi R_\theta R_\phi = \begin{bmatrix} \cos(\psi)\cos(\theta) & -\sin(\theta)\sin(\phi)\cos(\psi)+\sin(\psi)\cos(\phi) & \cos(\psi)\sin(\theta)\cos(\phi)+\sin(\phi)\sin(\psi) \\ -\sin(\psi)\cos(\theta) & +\sin(\psi)\sin(\theta)\sin(\phi)+\cos(\psi)\cos(\phi) & \sin(\theta)\sin(\psi)\cos(\phi)-\cos(\psi)\sin(\phi) \\ -\sin(\theta) & -\sin(\phi)\cos(\theta) & \cos(\theta)\cos(\phi) \end{bmatrix}, \tag{6.3}$$

where $\theta_x = \psi$, $\theta_y = \theta$ and $\theta_z = \psi$. The EKF predict step considers assuming a linear process model (velocity and bias stay constant)

$$x_{t+1} = Ax_t + B_t u_t + \omega_t, \tag{6.4}$$

where the system dynamics (control inputs $B_t u_t$) is unknown. Eq.6.4 becomes Eq.6.5.

$$x_{t+1} = Ax_t + \tilde{\omega_t}, \tag{6.5}$$

where

$$\tilde{\omega_t} = \omega_t + g_t = N(0,Q) + N(0,G), \tag{6.6}$$

in which the control inputs were considered as noise. G was obtained through simulations. From probability theory if X and Y are independent random variables that are normally distributed, then their sum is also normally distributed [147]. This means that the sum of two independent normally distributed random variables is normal, with its mean being the sum of the two means, and its variance being the sum of the two variances (i.e. the square of the standard deviation is the sum of the squares of the standard deviations). Q matrix assumes the shape expressed in Eq.6.7

$$Q = \begin{bmatrix} \Delta t^2 & 0 & 0 & 0 & 0 & 0 & 0 & 0 & 0 \\ 0 & \Delta t^2 & 0 & 0 & 0 & 0 & 0 & 0 & 0 \\ 0 & 0 & \Delta t^2 & 0 & 0 & 0 & 0 & 0 & 0 \\ 0 & 0 & 0 & 0.01\Delta t & 0 & 0 & 0 & 0 & 0 \\ 0 & 0 & 0 & 0 & 0.01\Delta t & 0 & 0 & 0 & 0 \\ 0 & 0 & 0 & 0 & 0 & 0.01\Delta t & 0 & 0 & 0 \\ 0 & 0 & 0 & 0 & 0 & 0 & 0.03\Delta t & 0 & 0 \\ 0 & 0 & 0 & 0 & 0 & 0 & 0 & 0.03\Delta t & 0 \\ 0 & 0 & 0 & 0 & 0 & 0 & 0 & 0 & 0.03\Delta t \end{bmatrix}, \tag{6.7}$$

where Δt^2 are responsible for the integration error from Taylor truncation, $0.01\Delta t$ are the estimated error of angular velocity (constant approximation), and $0.03\Delta t$ are the estimated error of bias (constant approximation). Matrix

G is expressed in Eq.6.8

$$G = \begin{bmatrix} \frac{L_x}{J_{xx}} & 0 & 0 & 0 & 0 & 0 & 0 & 0 & 0 \\ 0 & \frac{L_y}{J_{yy}} & 0 & 0 & 0 & 0 & 0 & 0 & 0 \\ 0 & 0 & \frac{L_z}{J_{zz}} & 0 & 0 & 0 & 0 & 0 & 0 \\ 0 & 0 & 0 & \frac{M_x}{J_{xx}} & 0 & 0 & 0 & 0 & 0 \\ 0 & 0 & 0 & 0 & \frac{M_y}{J_{yy}} & 0 & 0 & 0 & 0 \\ 0 & 0 & 0 & 0 & 0 & \frac{M_z}{J_{zz}} & 0 & 0 & 0 \\ 0 & 0 & 0 & 0 & 0 & 0 & 0 & 0 & 0 \\ 0 & 0 & 0 & 0 & 0 & 0 & 0 & 0 & 0 \\ 0 & 0 & 0 & 0 & 0 & 0 & 0 & 0 & 0 \end{bmatrix} \tag{6.8}$$

where $\frac{L_x}{J_{xx}}$ represents the angular momentum divided by inertia axis (angular speed), $\frac{L_x}{J_{xx}}$ represents the torque divided by inertia axis (angular acceleration). These σ values come from simulations, while bias were not possible to be measured (guess values).

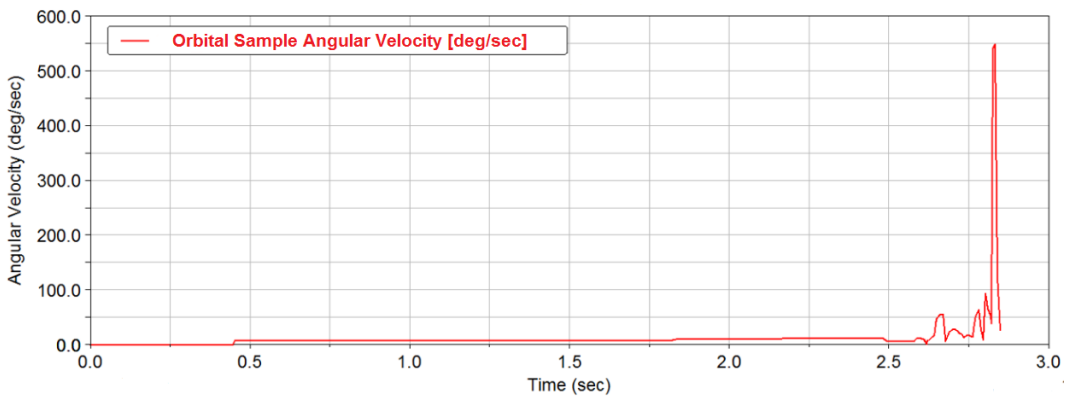

Figure 6.7 OS orientation velocity was considered constant, but during the pin trap (multi-body MSC Adams simulation software).

From multi-body MSC Adams simulation software sigma squares were obtained, see Fig.6.7. Related to angular velocities $\sigma^2 = 0.1$ were assumed, angular accelerations $\sigma^2 = 0.0003$ were assumed and bias $\sigma^2 = 0.0$ were assumed.

To perform the EKF some steps were taken into account [146]:

1. Prediction step:

$$x_{t|t-1} = Ax_{t-1|t-1}, \tag{6.9}$$

where

$$A = \begin{bmatrix} 1 & 0 & 0 & \Delta t & 0 & 0 & -\Delta t & 0 & 0 \\ 0 & 1 & 0 & 0 & \Delta t & 0 & 0 & -\Delta t & 0 \\ 0 & 0 & 1 & 0 & 0 & \Delta t & 0 & 0 & -\Delta t \\ 0 & 0 & 0 & 1 & 0 & 0 & 0 & 0 & 0 \\ 0 & 0 & 0 & 0 & 1 & 0 & 0 & 0 & 0 \\ 0 & 0 & 0 & 0 & 0 & 1 & 0 & 0 & 0 \\ 0 & 0 & 0 & 0 & 0 & 0 & 1 & 0 & 0 \\ 0 & 0 & 0 & 0 & 0 & 0 & 0 & 1 & 0 \\ 0 & 0 & 0 & 0 & 0 & 0 & 0 & 0 & 1 \end{bmatrix} \tag{6.10}$$

that represents a linear process model (assumes velocity and bias stay constant). Evaluate covariance estimate:

$$P_{t|t-1} = AP_{t-1|t-1}A^T + Q_t \tag{6.11}$$

2. Update step:

   (a) Innovation or measurement residual:

$$y_t = z_t - H(x_{t|t-1}), \tag{6.12}$$

   where

$$H(x) = \begin{pmatrix} \omega_x + b_x \\ \omega_y + b_y \\ \omega_z + b_z \\ -\sin(-\theta_z)\cos(-\theta_x) \\ \cos(-\theta_z)\cos(-\theta_x) \\ \cos(-\theta_x) \end{pmatrix} \tag{6.13}$$

   that represents a nonlinear measurement model.

   (b) Innovation covariance:

$$S_t = J_H^{(x_{t|t-1})} P_{t|t-1} J_H^{(x_{t|t-1})^T} + R_t, \tag{6.14}$$

   where $J_H^{(x_{t|t-1})}$ is the Jacobian of the state $x_{t|t-1}$ and R_t includes the σ_{acc}^2 and σ_{gyro}^2.

(c) Kalman gain:

$$K_t = P_{t|t-1} J_H^{(x_{t|t-1})^T} S_t^{-1} \tag{6.15}$$

(d) Update state estimate:

$$x_{t|t} = x_{t|t-1} + K_t y_t \tag{6.16}$$

(e) Update covariance estimate:

$$P_{t|t} = (I - K_t J_H^{(x_{t|t-1})}) P_{t|t-1} \tag{6.17}$$

6.2.2 Quaternions

There are a lot IMU data sensor fusion applications in the recent literature, see [148]-[159]. The same problem stated before was approached using quaternions because they represent global rotation parameters interdependently from the magnitude of the rotation angle and from the order of axis rotation. Knowing that quaternions are defined by Eqq.6.18 and 6.19

$$\beta_\nu = \beta_1, \beta_2, \beta_3 \qquad \& \qquad \beta_4, \tag{6.18}$$

$$\dot{\beta}_\nu = \frac{1}{2}(\beta_4 \omega + \beta_\nu \times \omega) \qquad \& \qquad \dot{\beta}_4 = -\frac{1}{2}\beta_\nu^T \omega. \tag{6.19}$$

Using Eqq.6.18 and 6.19 the whole system will be non linear and it will be more difficult to be represented. To simplify it and to make it linear, the state vector was reduced from seven values (β_i, ω_i) to only four values (β_i). This was also possible because ω_i are not states, but outputs coming from the IMU

$$\begin{pmatrix} \dot{\beta}_1 \\ \dot{\beta}_2 \\ \dot{\beta}_3 \\ \dot{\beta}_4 \end{pmatrix} = \frac{1}{2} \begin{pmatrix} 0 & \omega_3 & -\omega_2 & \omega_1 \\ -\omega_3 & 0 & \omega_1 & \omega_2 \\ \omega_2 & -\omega_1 & 0 & \omega_3 \\ -\omega_1 & -\omega_2 & -\omega_3 & 0 \end{pmatrix} \begin{pmatrix} \beta_1 \\ \beta_2 \\ \beta_3 \\ \beta_4 \end{pmatrix}, \tag{6.20}$$

$$z = \begin{pmatrix} \tilde{\omega}_1 \\ \tilde{\omega}_2 \\ \tilde{\omega}_3 \\ \bar{a}_x \\ \bar{a}_y \\ \bar{a}_z \end{pmatrix} = \begin{pmatrix} \omega_1 + b_1 \\ \omega_2 + b_2 \\ \omega_3 + b_3 \\ -2(\beta_4\beta_2 + \beta_1\beta_3) \\ -2(\beta_2\beta_3 - \beta_4\beta_1) \\ -(\beta_4^2 - \beta_1^2 - \beta_2^2 + \beta_3^2) \end{pmatrix}, \tag{6.21}$$

where also all the ω_i were added to the gyroscopic bias values and the values for the accelerations come from the rotation matrix (same procedure used for Tait-Bryan angles) applied to quaternions. For what concerns the Jacobian matrix J_H, it is reported in Eq.6.22

$$J_H = \begin{pmatrix} 0 & 0 & 0 & 0 \\ -2\beta_3 & -2\beta_4 & -2\beta_1 & -2\beta_2 \\ 2\beta_4 & -2\beta_3 & -2\beta_2 & 2\beta_1 \\ 2\beta_1 & 2\beta_2 & -2\beta_3 & -2\beta_4 \end{pmatrix}. \tag{6.22}$$

Both the Prediction Step and the Update Step were run as illustrated in Subsec.6.2.1 to obtain the correct quaternion values. After that, they were translated into Tait-Bryan angles as expressed in Eqq.6.23, 6.24, and 6.25

$$\theta_x = \phi = \arctan\left[\frac{2(\beta_4\beta_1 + \beta_2\beta_3)}{1 - 2(\beta_1^2 + \beta_2^2)}\right], \tag{6.23}$$

$$\theta_y = \theta = \arcsin[2(\beta_4\beta_2 - \beta_3\beta_1)], \tag{6.24}$$

$$\theta_z = \psi = \arctan\left[\frac{2(\beta_4\beta_3 + \beta_1\beta_2)}{1 - 2(\beta_2^2 + \beta_3^2)}\right]. \tag{6.25}$$

6.2.3 Sampling Rate

For what concerns the communication between the different platforms the sampling rate for the accelerometer was 3.2kHz, while the sampling rate of the gyroscope was 8kHz. In this case the sampling rate of the IMU was dominated by the slowest one (3.2kHz). The IMU communicates to the Arduino Uno using I^2C protocol that works at 400kHz. The system sampling rates was 3.2kHz. Arduino communicates Blueetooth to the PC. The Bee V2 standard baud rate was 9600. The baud rate is the sampling rate divided by the number of output

characters. To increase it a SparkFun XBee Explorer Dongle was adopted. The comm baud rate was 230400. Arduino needs to print on the screen the received data. The system sampling rate was 500Hz due to the internal Arduino computational time and monitor serial printing. This was a sampling rate that works properly in accord with this experiment. Fig.6.8 depicts a schematic view of the experimental setup system communication protocols.

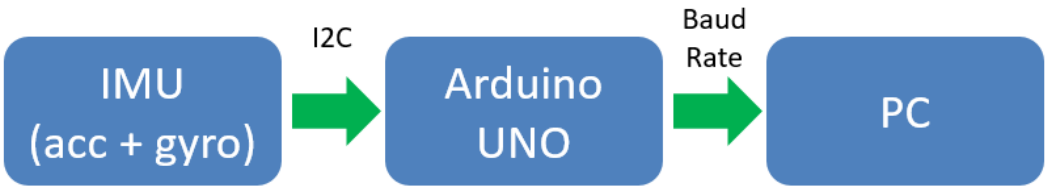

Figure 6.8 Experimental setup system communication protocols.

6.2.4 Data Low-Pass Filter: Moving Average

In statistics, a moving average (rolling average or running average) is a calculation to analyze data points by creating series of averages of different subsets of the full data set [160]. It works as a finite impulse response / low pass filter. Given a series of numbers and a fixed subset size, the first element of the moving average is obtained by taking the average of the initial fixed subset of the number series. Then the subset is modified by shifting forward; that is, excluding the first number of the series and including the next number following the original subset in the series. This creates a new subset of numbers, which is averaged. This process is repeated over the entire data series. The plot line connecting all the (fixed) averages is the moving average. A moving average is a set of numbers, each of which is the average of the corresponding subset of a larger set of datum points. A moving average is commonly used with time series data to smooth out short-term fluctuations and highlight longer-term trends or cycles.

In this experimental setup a moving average was adopted to eliminate the possible data spikes and too smooth out short-term fluctuations. A window of 100 was adopted for this low-pass filter application.

6.3 Tests and Data Acquisition

In this Section the followed test procedures are described to acquire data and the following data analysis.

6.3.1 Procedure

The followed procedure was characterized by these steps:

1. Acquisition of IMU data (both accelerometer and gyro data);
2. Application of a low-pass filter to cancel out the existing data spikes due to sudden external perturbations;
3. Linear spline interpolation of gyro angular velocities and derivative to obtain angular accelerations, and OS torques from IMU data;
4. Execution of EKF on IMU data (sensor fusion) to obtain quaternions and then Tait-Bryan angles;
5. Current sensing to obtain a quantitative evaluation of the power required by this mechanism.

6.3.2 Data Handling

Fig.6.9 reports the sensor reference frame with respect to the testbed reference frame. The latter one acts as an inertia reference frame.

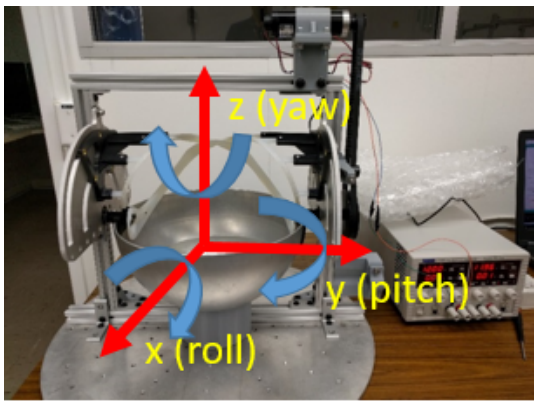

Figure 6.9 Body frame sensors with respect to testbed reference frame (inertia reference frame) [124].

Fig.6.10 reports the Water Wiper Testbed angular reference frame considered during tests. (a) shows the θ polar coordinate from 0° to 180°. (b) shows the ϕ longitudinal coordinate from 0° to 360°. Due to the system symmetry, the variation range from 0° to 180° was considered. It is interesting to notice that the final resting spot of the OS is ∼43° from straight up. This reflects either in roll angle plot or in pitch angle plot, not having direct control on this degeneracy.

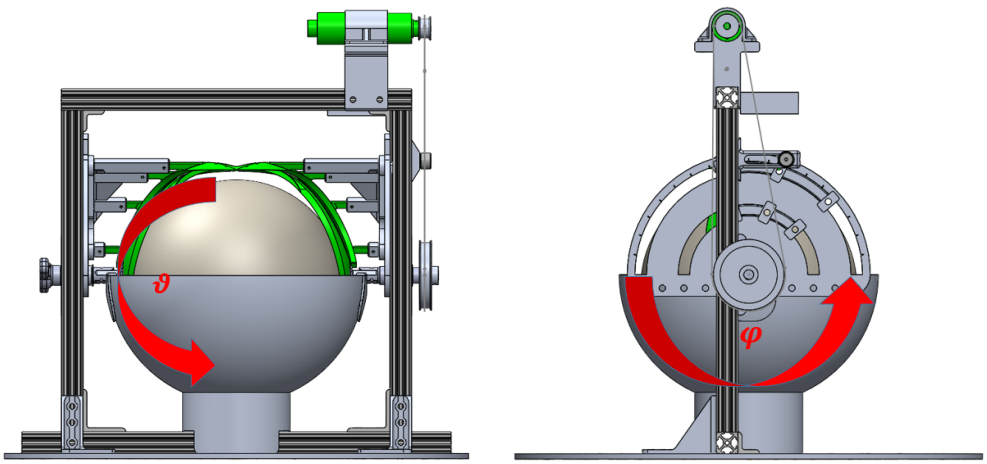

(a) θ polar coordinate from 0° to 180°.

(b) ϕ longitudinal coordinate from 0° to 360°. Due to the system symmetry, the variation range from 0° to 180° was considered.

Figure 6.10 Testbed angular reference frame considered during tests.

Water Testbed Performances

In Fig.6.11 a measure of the absolute error of the Water Testbed initial OS positioning is reported. A sampling resolution angle of 30° both in azimuth and elevation was considered. The absolute error represents the root sum square of the errors both in azimuth and elevation. Both at 180°, at 0°, and at -180° in elevation the absolute error was lower due to the aptitude to position the OS in these discrete cases.

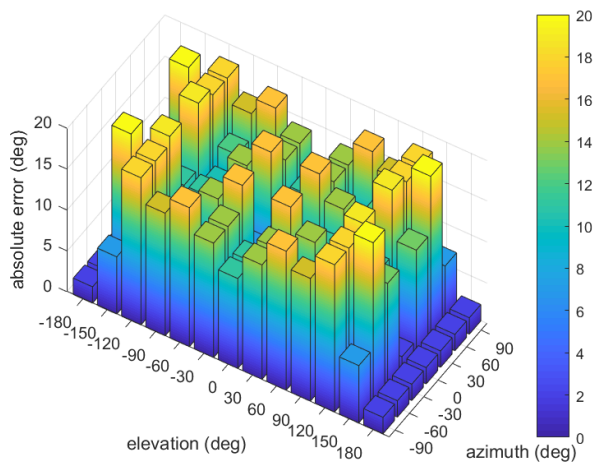

Figure 6.11 Water testbed initial OS positioning performances. The absolute angular error (root sum square of the azimuth and elevation errors) as function of the azimuth and elevation angles.

The average absolute error was 10° over all the azimuth and elevation angles. This translates into an average error in positioning of 7° both for azimuth and elevation angles. Considering the OS was initially centered using either a hand or a magnetic pick up stick, the OS was positioned better than the angular variation of 30°.

Testbed Operation Example

An example is reported to illustrate the testbed operations, the data filtering, and the final results concerning the Tait-Bryan angles. In this case the pin is located at a position of (θ=90°, ϕ=0°).

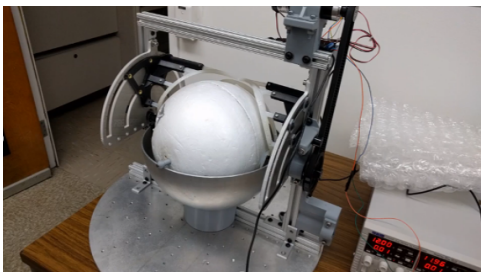

(a) Wiper starts to move. OS stays in position.

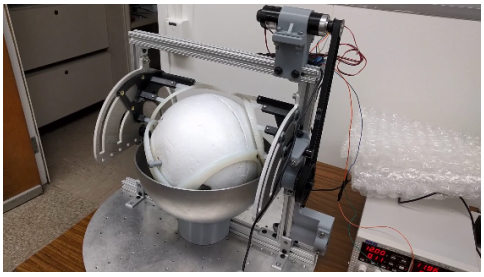

(b) Wiper interacts with tye OS and subsequentley with the pin.

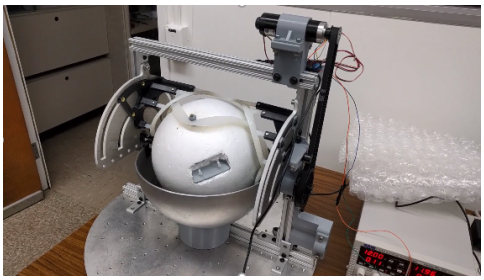

(c) Wiper capture the OS pin and start to reoerient the OS.

(d) OS reorientation has been successfully performed.

Figure 6.12 Example test to illustrate the testbed operations. In this case the pin is located at a position of (θ=90°, ϕ=0°) [124].

The coordinate data (respectively x, y, z) are reported in Figg.6.13, 6.14, and 6.15 coming from both gyroscope and accelerometer. The red line is the filtered line used as actual data, while the black line on the background represents the real IMU data [124].

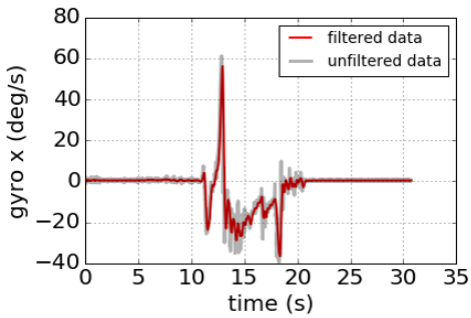

(a) Gyro angular velocity around x axis.

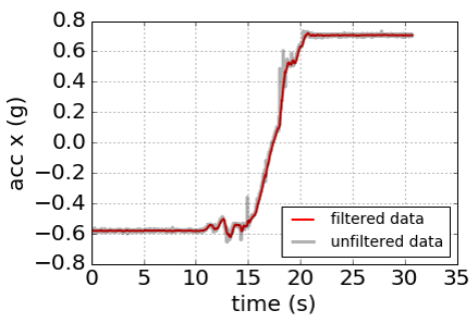

(b) Accelerometer data along x axis.

Figure 6.13 Coordinate x data [124].

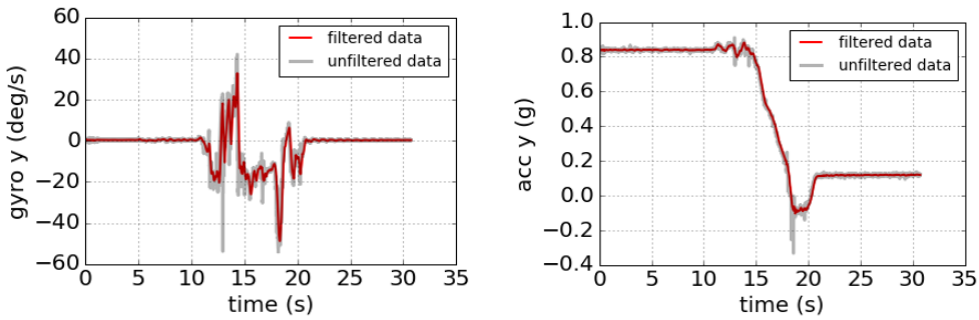

(a) Gyro angular velocity around y axis. (b) Accelerometer data along y axis.

Figure 6.14 Coordinate y data [124].

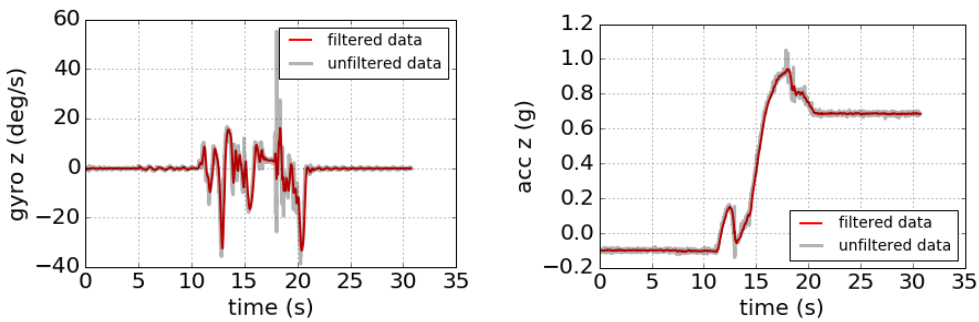

(a) Gyro angular velocity around z axis. (b) Accelerometer data along z axis [124].

Figure 6.15 Coordinate z data.

The quaternions obtained from the EKF are shown in Fig.6.16. The system was initialized at the quaternion state $\boldsymbol{\beta_0} = [0,0,0,1]^T$. Once the system detects the true OS orientation, the angles assume the correct values.

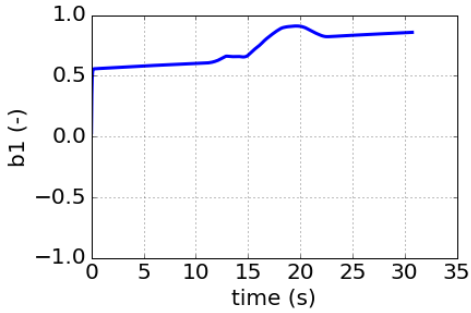

(a) β_1 quaternion. It was initialized to 0.

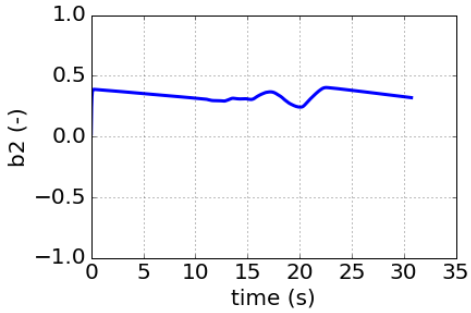

(b) β_2 quaternion. It was initialized to 0.

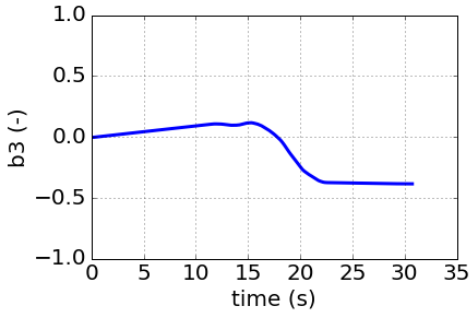

(c) β_3 quaternion. It was initialized to 0.

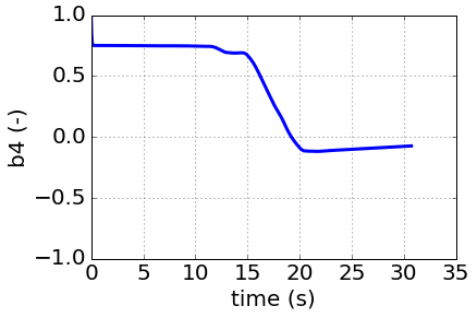

(d) β_4 quaternion. It was initialized to 1.

Figure 6.16 Quaternions as a function of time obtained through the EKF.

Roll, pitch, and yaw angles obtained from the EKF based on the quaternions are shown in Fig.6.17.

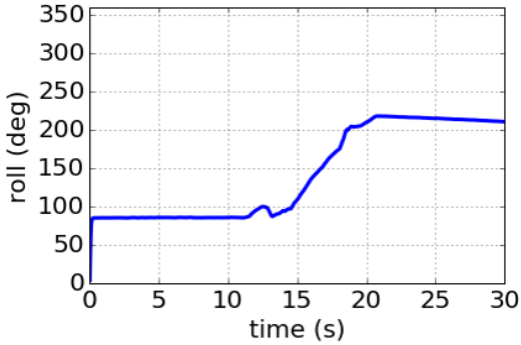

(a) Roll angle.

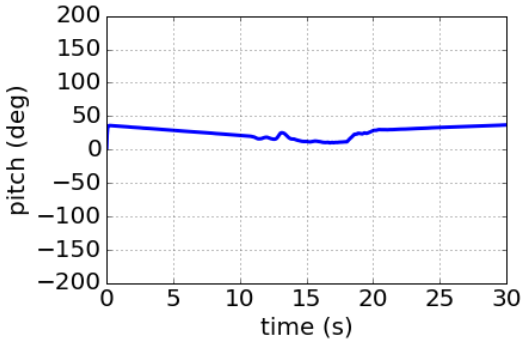

(b) Pitch angle.

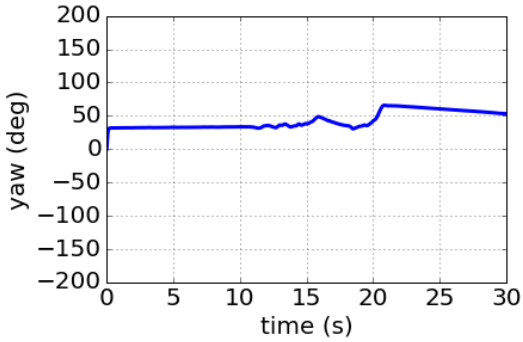

(c) Yaw angle.

Figure 6.17 Tait-Bryan angles as a function of time obtained through the EKF.

6.3.3 Test Considerations

Some considerations were adopted during the tests:

- To properly center the OS, the pin position was determined and then either hand or magnetic pick up stick was used to hold the pin in place

until it interacts with the Wiper. The OS hand holding is depicted in Fig.6.18, while Fig.6.19 reports the magnetic pick up stick holding.

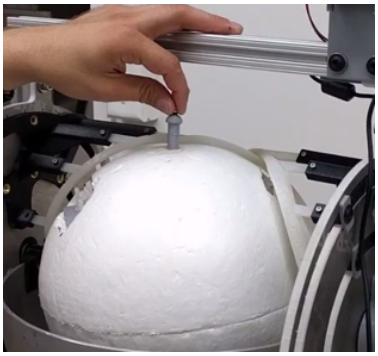

Figure 6.18 Pin OS hand holding.

Figure 6.19 Pin OS magnetic pick up stick holding.

- Kapton tape was used around the pin to lower the pin-shell friction. The Kapton-wrapped pin is depicted in Fig.6.20.

Figure 6.20 Kapton-wrapped pin.

- During the tests, the OS starts from different initial orientation (pin location) with an angular variation of 30°.

- Due to the high complexity of balancing a sphere in water, it was preferred to bias intentionally the OS inertia properties (adding two weights, ∼55g each) and to exploit this asymmetry to try to avoid the OS to react to its inertia as much as possible. Fig.6.21 reports the electronic box and the location of the two weights (red circles) adopted to create an intentionally inertial asymmetry.

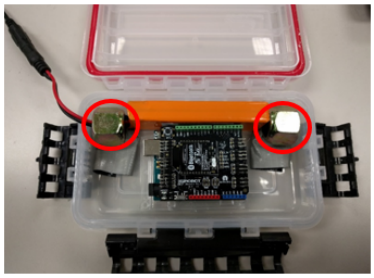

Figure 6.21 Electronic box and the location of the two weights (red circles) adopted to create an intentionally inertial asymmetry.

6.3.4 Motor No.1 Approach

In Ch.5, the use of the rolling bearing testbed was described, in that case a particular motor was used. Using that motor (called Motor No.1) on the Water Wiper testbed was proposed. The Water Wiper testbed with the motor described in Ch.5 (red circle) is shown in Fig.6.22.

Figure 6.22 Water Wiper testbed with the Motor No.1 location (red circle).

The lowest Wiper speed using Motor No.1 was about 20rpm adopting PID control. This Wiper speed interacting with the OS generates a dynamic

OS balancing condition that is not something that it will happens in zero-g. Fig.6.23 reports a case that shows this dynamic condition caused by the Wiper high speed.

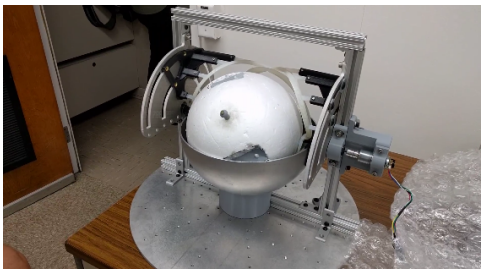

(a) Wiper starts its motion.

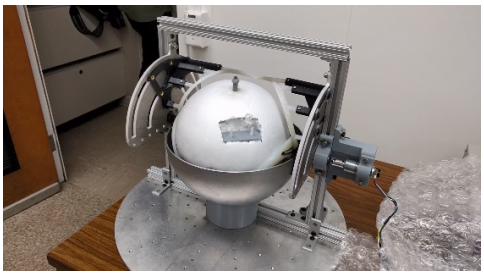

(b) Wiper interacts with the OS and makes it rotating.

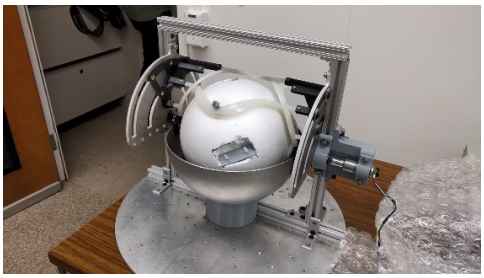

(c) OS moves back instead of moving forward.

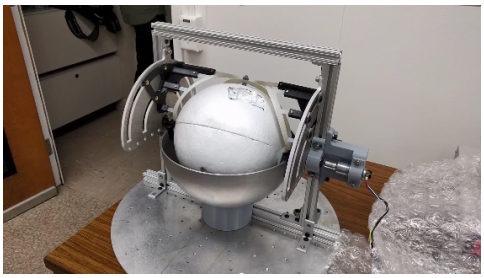

(d) Wiper brings the pin to its home location.

Figure 6.23 Case that shows the OS dynamic condition caused by the Wiper high speed.

6.3.5 Motor No.2 Approach

Adopting the same motor described in Ch.5 for the Water Wiper testbed, Motor No.2, this allows the minimum Wiper speed to be about 5rpm. This makes possible passing from a dynamic OS balancing condition to a quasi-static OS balancing condition, that is closer to a zero-g space environment. A case that shows this quasi-dynamic condition caused by the Wiper slower speed is shown in Fig.6.24, with the OS in the same initial orientation of Fig.6.23 using Motor No.1.

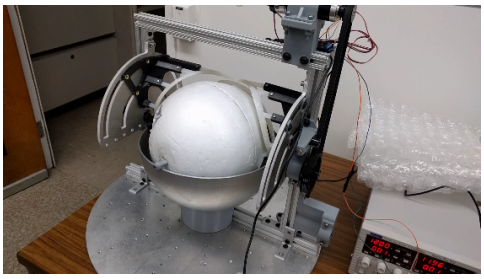

(a) Wiper starts its motion.

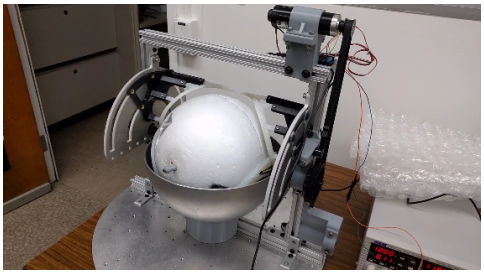

(b) Wiper interacts with the OS and makes it slightly rotating.

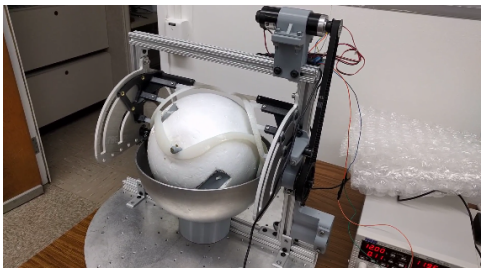

(c) Wiper engages with the pin and rotate the OS forward.

(d) Wiper brings the pin to its home location.

Figure 6.24 Case that shows the OS quasi-static condition caused by the Wiper slower speed.

6.4 Representative Results

Some of the collected test results are reported to validate the Wiper model using the Water Wiper testbed with Motor N.2.

6.4.1 Design Of Experiment

The Wiper experiment was a series of tests in which the input variables were changed accordingly to a given rule in order to identify the reasons for the changes in the output response [129]. As input variables OS Tait-Bryan angles (pin locations) and pin radius were considered. The output response was given by the OS Tait-Bryan angles describing the pin going to the final location interacting with the Wiper during the proper OS reorientation.

OS Type	Test Name	Factors under Test	Range of Variability
Spherical OS	OS reorientation Non-CPL	OS roll, pitch, yaw	(0°:30:180°, 0°:30:90°)
	OS reorientation CPL	OS roll, pitch, yaw	(90°, 90°)
	OS reorientation at CPL Different Pin Diameters	OS roll, pitch, yaw Pin radius	(90°, 90°) 5mm:5:15mm
Non-spherical OS	OS reorientation Non-CPL	OS roll, pitch, yaw (visual inspection)	(90°:90:180°, 0°:90:90°)
	OS reorientation CPL	OS roll, pitch, yaw (visual inspection)	(90°, 90°)

Table 6.3 Wiper design of experiment test matrix. Critical Pin Locations (CPL) is (90°, 90°) where the pin was located between the Wiper and the positive feature at rotation angle ∼0°.

Tab.6.3 reports the Wiper design of experiment test matrix. Tests related both to the spherical OS and to the non-spherical OS were performed. Tests considered OS reorientation both in Critical Pin Locations (CPL) and non-CPL. The factors under tests were the Wiper profile and the pin radius. These factors translated operationally into the OS Tait-Bryan angles change induced by the Wiper profile change during the OS reorientation. The goal of this DOE was to show that at different OS initial orientations and with different pin radii the Wiper mechanism could work correctly.

6.4.2 Results

Motor No.2 test ($\theta = 0°$, $\phi = 30°$)

The test results are reported considering the OS initial position (pin location) to be θ=0°, ϕ=30°. Testbed operations are reported in Fig.6.25. Tait-Bryan angles as a function of time obtained through the EKF are depicted in Fig.6.26.

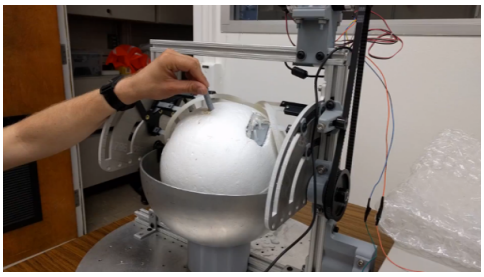

(a) Wiper starts its motion.

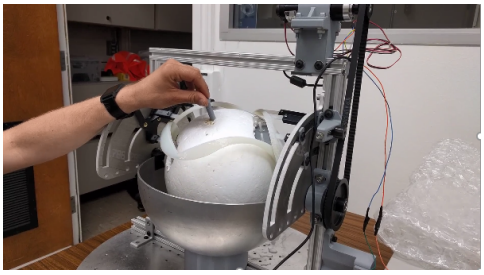

(b) Wiper interacts with the OS.

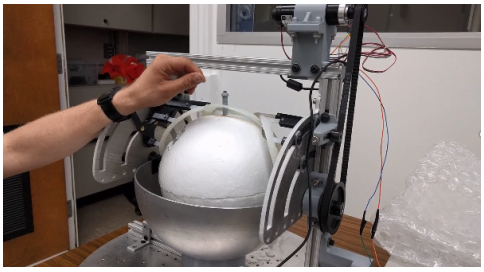

(c) Wiper engages with the pin and rotates the OS forward.

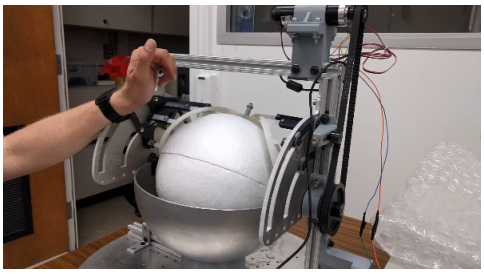

(d) Wiper brings the pin to its home location.

Figure 6.25 Example test to illustrate the testbed operations. In this case the pin was located at a position of (θ=0°, ϕ=30°).

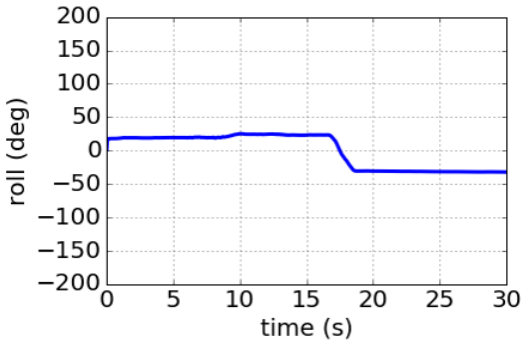

(a) Roll angle.

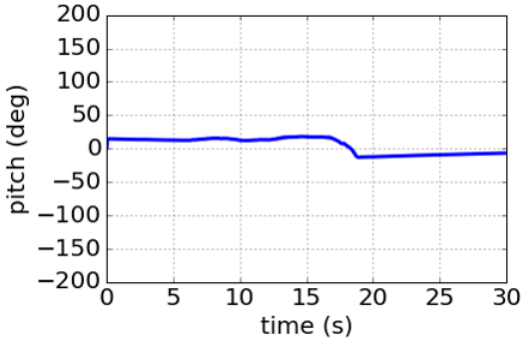

(b) Pitch angle.

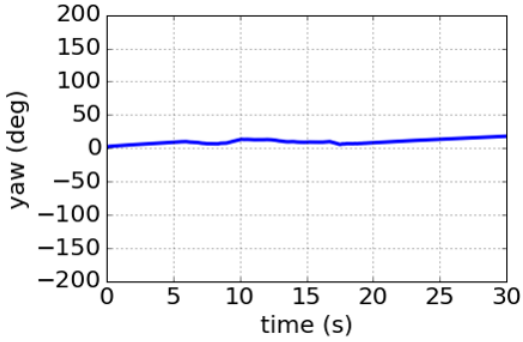

(c) Yaw angle.

Figure 6.26 Tait-Bryan angles as a function of time obtained through the EKF.

Motor No.2 test ($\theta = 0°$, $\phi = 180°$)

The test results are reported considering the OS initial position (pin location) to be θ=0°, ϕ=180°. Testbed operations are reported in Fig.6.27. Tait-Bryan angles as a function of time obtained through the EKF are depicted in Fig.6.28.

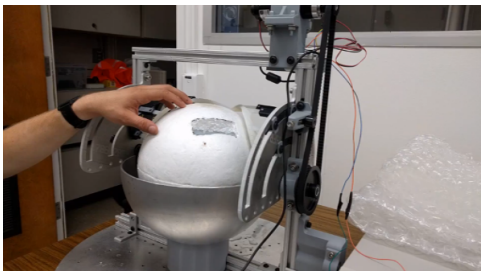

(a) Wiper starts its motion.

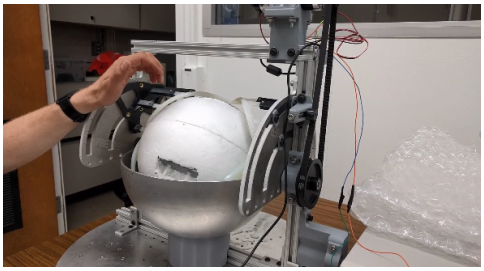

(b) Wiper interacts with the OS.

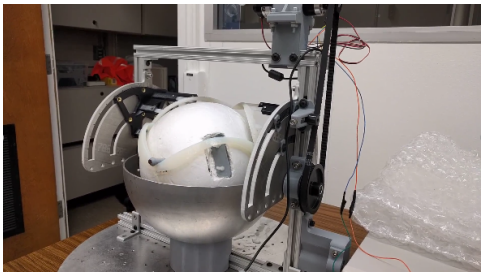

(c) Wiper engages with the pin and rotates the OS forward.

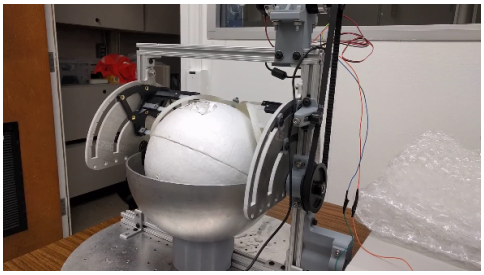

(d) Wiper brings the pin to its home location.

Figure 6.27 Example test to illustrate the testbed operations. In this case the pin was located at a position of (θ=0°, ϕ=180°).

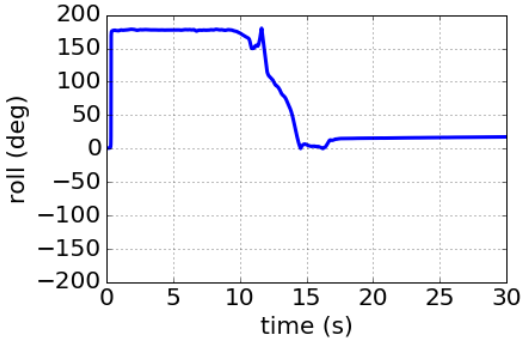

(a) Roll angle.

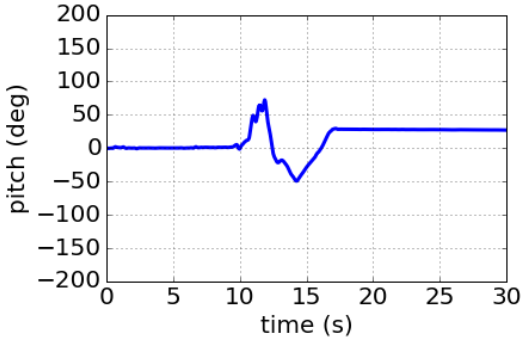

(b) Pitch angle.

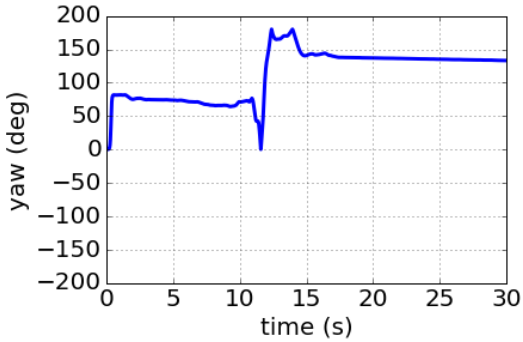

(c) Yaw angle.

Figure 6.28 Tait-Bryan angles as a function of time obtained through the EKF.

Motor No.2 test ($\theta = 60°$, $\phi = 120°$)

The test results are reported considering the OS initial position (pin location) to be θ=60°, ϕ=120°. Testbed operations are reported in Fig.6.29. Tait-Bryan angles as a function of time obtained through the EKF are depicted in Fig.6.30.

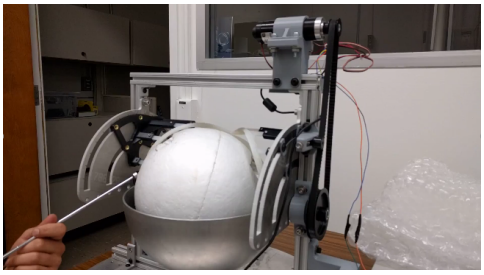

(a) Wiper starts its motion.

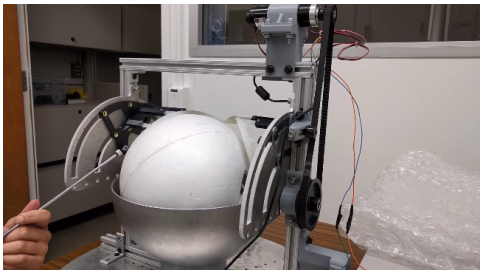

(b) Wiper interacts with the OS.

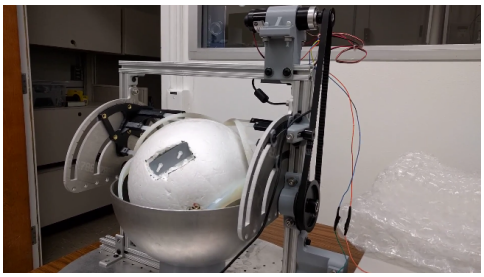

(c) Wiper engages with the pin and rotates the OS forward.

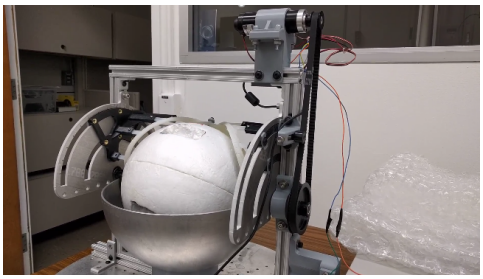

(d) Wiper brings the pin to its home location.

Figure 6.29 Example test to illustrate the testbed operations. In this case the pin was located at a position of (θ=60°, ϕ=120°).

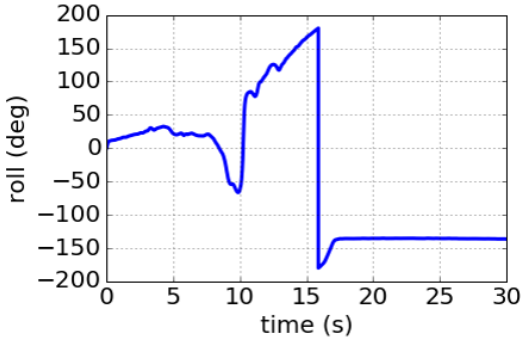

(a) Roll angle. At about 15s a huge spikes appears at the angle becomes negative. This was caused by the fact that during the reorientation the roll angle crosses the 180° region and the IMU measures the overturning.

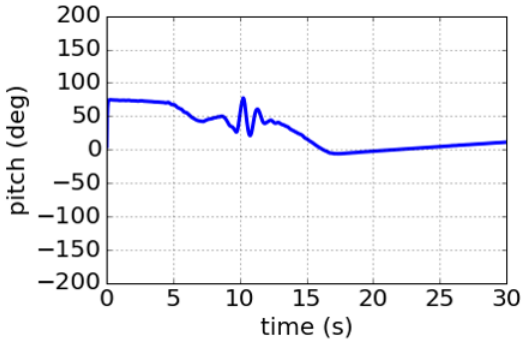

(b) Pitch angle.

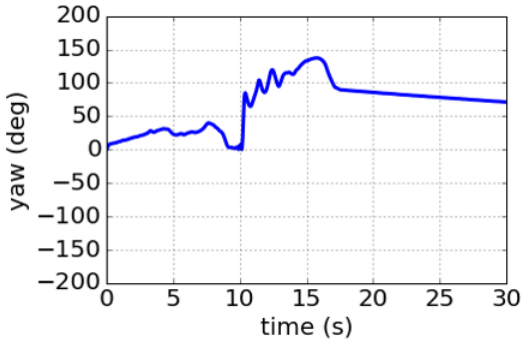

(c) Yaw angle.

Figure 6.30 Tait-Bryan angles as a function of time obtained through the EKF.

Current Sensing and Power Considerations

The current drained (10-bit resolution) was also measured by the motor during the Wiper rotation and the OS reorientation. For Motor No.2 the motor constant was expressed in Eq.6.26

$$k_m = \frac{M_S}{I_S}, \tag{6.26}$$

where M_S is the stall torque and I_S the stall current. From the data sheet k_m=1.91 $\frac{Nm}{A}$. In this way, measuring the current during the motor operation, knowing the motor constant, and knowing the motor gear ratio, it was possible to obtain the torque needed by the motor for the reorientation. The goal here is to achieve some considerations related to the power requested to reorient the real OS in space. All the following plots and measurements refer to the example depicted in Figg.6.25 and 6.26. The OS load torque from current measurements is reported in Fig.6.31(a). The maximum value obtained is 0.87Nm with a mean of 0.84Nm. Considering that the OS is a uniform styrofoam sphere, knowing its size and mass, it was possible to have an estimate of its inertia. Here the biased OS inertia was not considered. The following results were obtained without the biased inertia. Knowing the inertia and obtaining the angular acceleration from IMU data (interpolating gyro data and deriving them) it was possible to attain some values related to the torque felt by the OS during reorientation. They are reported in Fig.6.31(b). The maximum value obtained is 1.6Nm with a mean of 0.29Nm. The efficiency is reported in Fig.6.31(c) obtained as the ratio between the torque coming from the current sensing of the whole system without the OS due to friction, Wiper loading, and water interaction, and the torque coming from the current sensing of the system with the OS. The efficiency was high, due to the fact the the OS was light and sustained by water. The motor presented a too high stall torque to be able to be affected by the OS inertia. Instead Fig.6.31(b) shows that the OS itself feels the presence of the Wiper and it was perturbed by it. This happens because once the Wiper interacts with the OS, the OS moves and it generates IMU data variation. In conclusion, this system was characterized by a IMU slightly too sensitive and a motor lightly too powerful. Moreover, the OS interaction load was small compared to the Wiper load and gearbox friction to draw some conclusions in

regards to the whole system efficiency. This efficiency was considered only as an upper-limit efficiency for this mechanism given this testbed implementation.

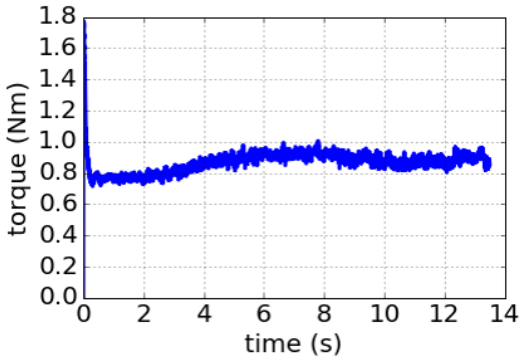

(a) OS load torque (from current sensing).

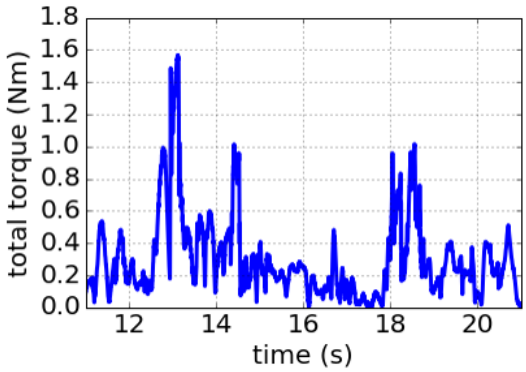

(b) OS load torque detail (from IMU data).

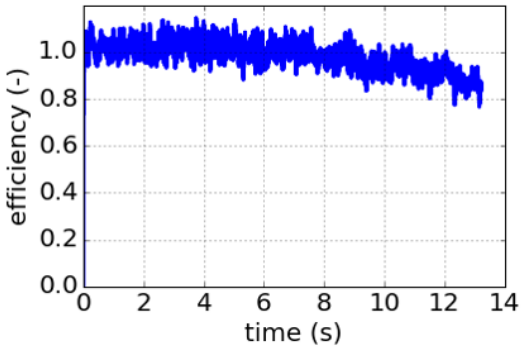

(c) Efficiency (from current sensing).

Figure 6.31 Torque measuring data.

However, this was not a problem to produce some considerations related to the power estimate. From a current sensing point of view the system required

about 3.24W. The testbed system power is given by

$$P_T = T \times \omega, \tag{6.27}$$

where T is the torque and ω is the Wiper angular velocity. The torque is equal to $T = I\alpha$, where $I = \frac{2MR^2}{5}$ is the OS inertia and α the OS angular acceleration. If P_S indicates the future flight system required power, the ratio between P_S and P_T is reported in Eq.6.28

$$\frac{P_S}{P_T} = \frac{\frac{2M_S R^2 \alpha\omega}{5}}{\frac{2M_T R^2 \alpha\omega}{5}} = \frac{M_S}{M_T}, \tag{6.28}$$

where R, α and ω are the same. Considering the mass ratio expressed in Eq.6.29

$$\frac{M_S}{M_T} \approx 25, \tag{6.29}$$

this bring to the result in Eq.6.30

$$P_S \approx 25 P_T = 80W + 25\% = 100W, \tag{6.30}$$

where 25% is the considered margin. This gives a reasonable order of magnitude for the needed motor power to reorient a potential OS.

Critical Pin Location ($\theta = 90°$, $\phi = 90°$) Results

Some tests are reported related to the most critical pin location (θ=90°, ϕ=90°), where the pin locates between the Wiper and the positive feature as close possible to the Wiper rotation axis. If this happens, the pin has to move towards the home location exploiting the whole Wiper profile thanks to the interaction with the positive feature. Moreover, also the pin diameter was varied accordingly to the theoretical results shown in Ch.4.

5mm Pin Diameter

(a) Wiper starts its motion.

(b) Wiper interacts with the OS.

(c) Pin moves on the Wiper profile.

(d) Wiper brings the pin to its home location.

Figure 6.32 Critical pin location test. In this case the pin diameter was 5mm and it was located at (θ=90°, ϕ=90°).

The critical pin location test, with the pin diameter of 5mm, is depicted Fig.6.32.

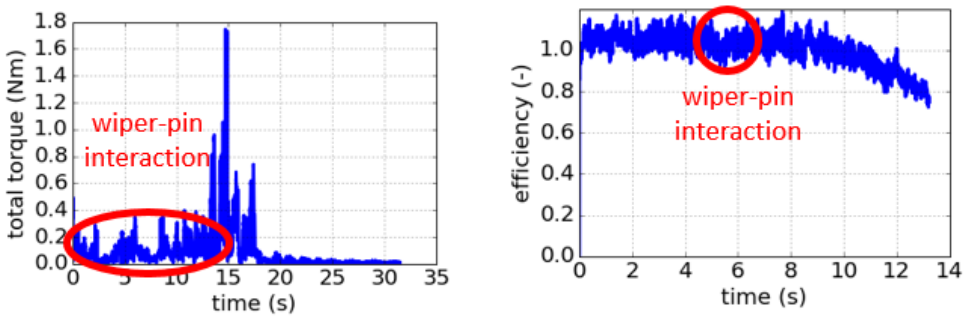

(a) OS load torque (from IMU data).

(b) OS efficency torque (from current sensing).

Figure 6.33 Torque end efficiency results for 5mm pin.

The OS load torque from IMU data is described by Fig.6.33(a), while Fig.6.33(b) represents the efficiency of the mechanism obtained through the current sensing measurements.

10mm Pin Diameter

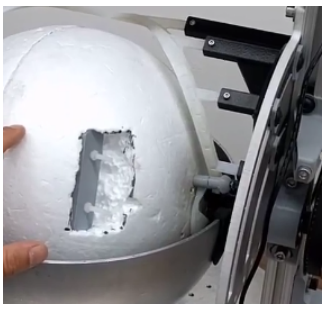

(a) Wiper starts its motion.

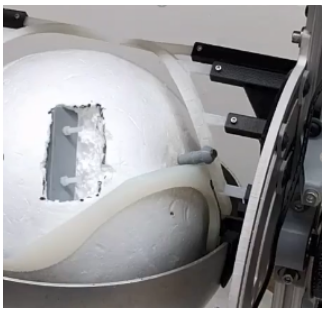

(b) Wiper interacts with the OS.

(c) Pin moves on the Wiper profile.

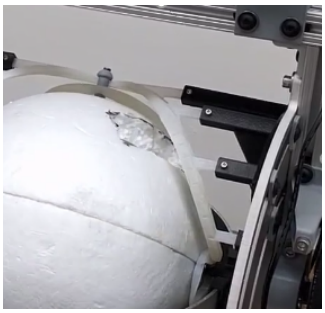

(d) Wiper brings the pin to its home location.

Figure 6.34 Critical pin location test. In this case the pin diameter was 10mm and it was located at (θ=90°, ϕ=90°).

The critical pin location test, with the pin diameter of 10mm, is depicted in Fig.6.34.

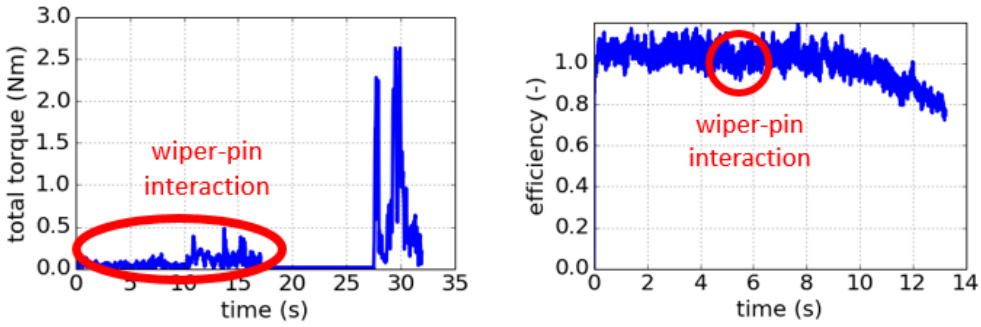

(a) OS load torque (from IMU data).

(b) OS efficency torque (from current sensing).

Figure 6.35 Torque end efficiency results for 10mm pin.

The OS load torque from IMU data is described by Fig.6.35(a), while Fig.6.35(b) represents the efficiency of the mechanism obtained through the current sensing measurements.

15mm Pin Diameter

(a) Wiper starts its motion.

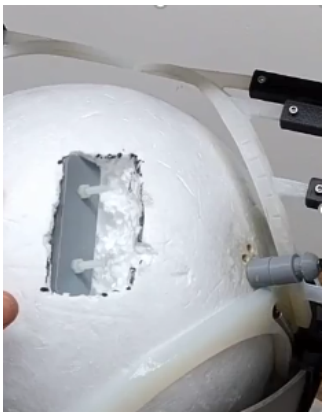

(b) Wiper interacts with the OS.

(c) Pin moves on the Wiper profile.

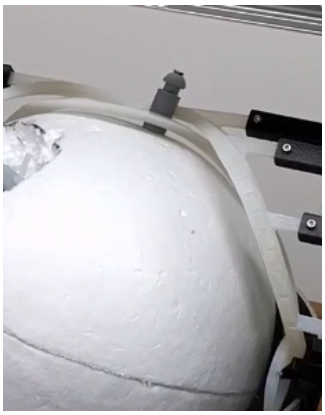

(d) Wiper brings the pin to its home location.

Figure 6.36 Critical pin location test. In this case the pin diameter was 15mm and it was located at (θ=90°, ϕ=90°).

The critical pin location test, with the pin diameter of 15mm, is depicted in Fig.6.36.

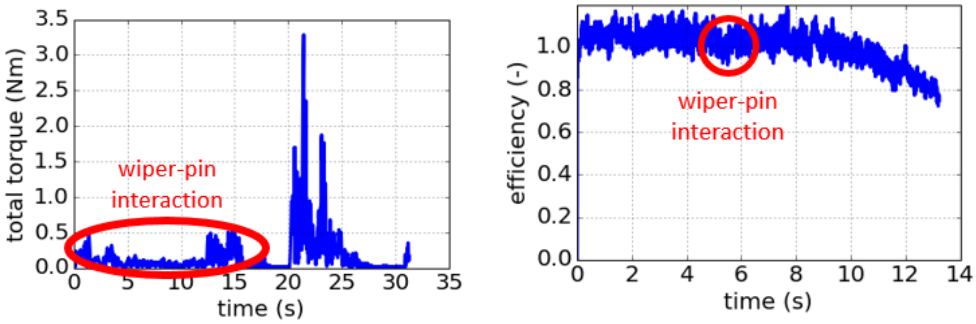

(a) OS load torque (from IMU data).

(b) OS efficency torque (from current sensing).

Figure 6.37 Torque end efficiency results for 15mm pin.

The OS load torque from IMU data is described by Fig.6.37(a), while Fig.6.37(b) represents the efficiency of the mechanism obtained through the current sensing measurements.

Non-Spherical OS

Some tests were also run using the same testbed but with a different OS: the non-spherical OS. It was composed by two hemispheres with different diameters, where the inner radius is 10mm smaller than outer radius, see Fig.6.38.

(a) Non-spherical OS top view.

(b) Non-spherical OS side view.

Figure 6.38 Non-spherical OS, the inner radius was 10mm smaller than outer radius [124].

Pin location: ($\theta = 90°$, $\phi = 0°$)

The critical pin location test for the non-spherical OS is reported in Fig.6.39. In this case the pin diameter was 10mm and it was located at (θ=90°, ϕ=0°).

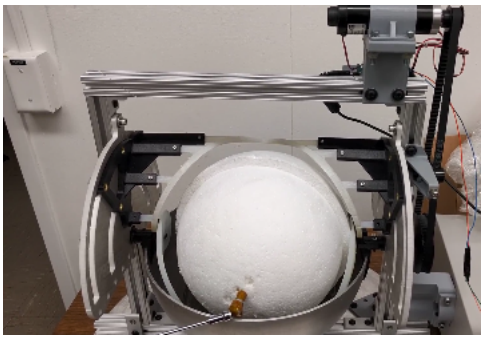

(a) Wiper starts its motion.

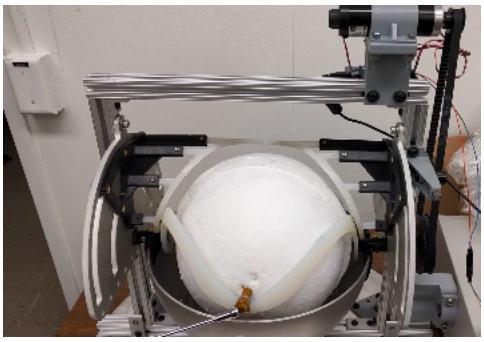

(b) Wiper interacts with the OS throught he pin.

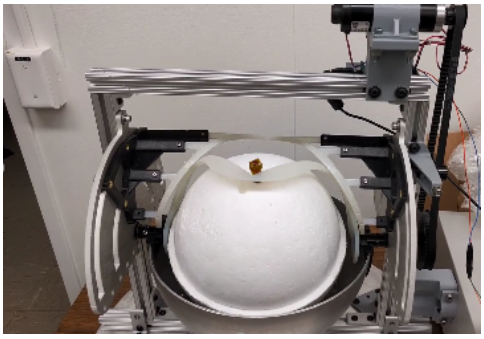

(c) Wiper interacts with the pin making the OS rotating.

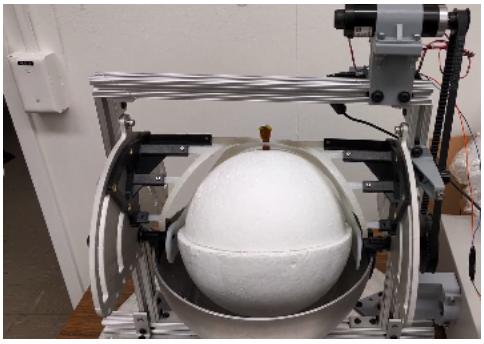

(d) Wiper brings the pin to its home location.

Figure 6.39 Critical pin location test for a non-spherical OS. In this case the pin diameter was 10mm and it was located at (θ=90°, ϕ=0°).

Pin location: ($\theta = 90°$, $\phi = 90°$)

The critical pin location test for the non-spherical OS is reported in Fig.6.40. In this case the pin diameter was 10mm and it was located at (θ=90°, ϕ=90°).

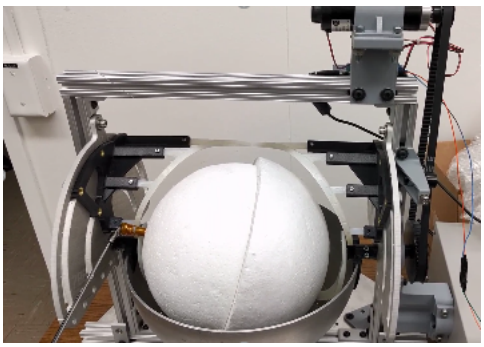

(a) Wiper starts its motion.

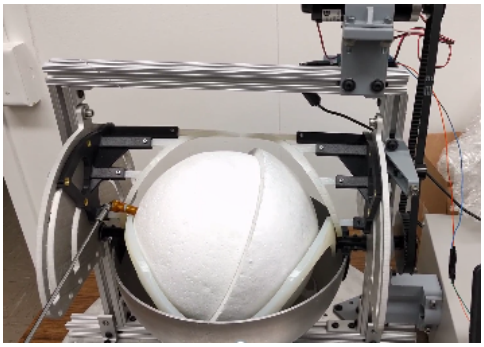

(b) Wiper interacts with the OS through the pin.

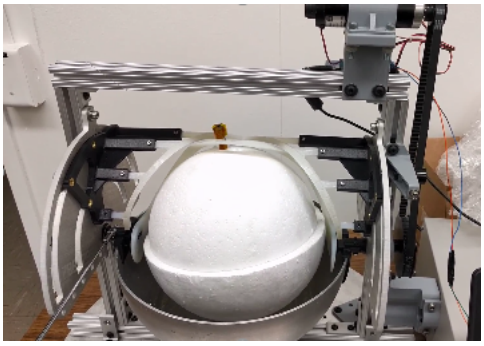

(c) Wiper interacts with the pin making the OS rotating.

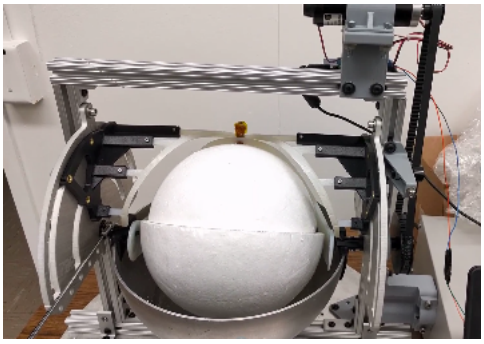

(d) Wiper brings the pin to its home location.

Figure 6.40 Critical pin location test for the non-spherical OS. In this case the pin diameter was 10mm and it was located at (θ=90°, ϕ=90°).

Pin location: ($\boldsymbol{\theta = 180°}$, $\boldsymbol{\phi = 0°}$)

The critical pin location test for the non-spherical OS is reported in Fig.6.41. In this case the pin diameter was 10mm and it was located at (θ=180°, ϕ=0°).

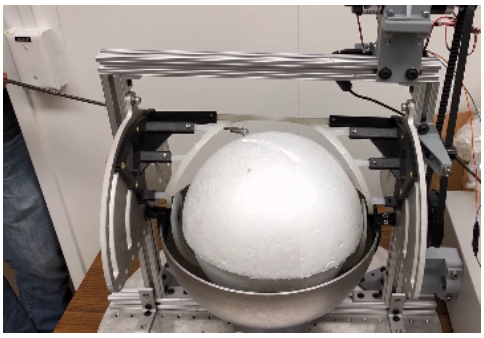

(a) Wiper starts its motion.

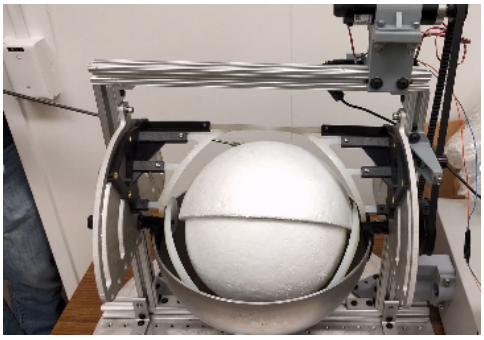

(b) Wiper interacts with the OS through the pin.

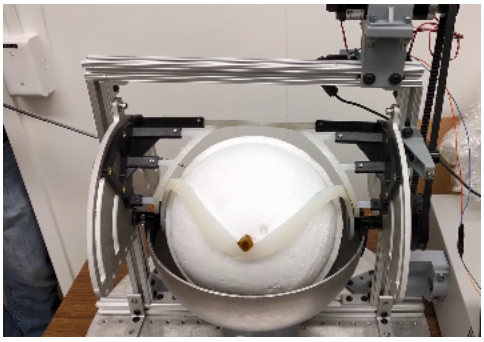

(c) Wiper interacts with the pin making the OS rotating.

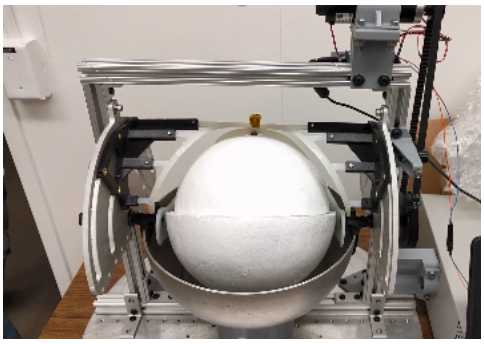

(d) Wiper brings the pin to its home location.

Figure 6.41 Critical pin location test for the non-spherical OS. In this case the pin diameter was 10mm and it was located at (θ=180°, ϕ=0°).

6.4.3 Results

With all the performed tests it was possible to realize that:

- All Wiper-pin mechanism possible jamming conditions were successfully solved.
- The optimized Wiper profile was successfully tested to show its ability to move the pin from the critical locations towards the final home location following the Wiper profile.
- Increasing the pin diameter resulted in a less motor torque from IMU data required to solve the possible jamming conditions.

- The current sensing motor torque efficiency was able to differentiate between the pin critical location (jamming conditions) and the pin non-critical locations.
- The current sensing motor torque efficiency did not seem to be affected by the increase in pin diameter. However, this may be due to the fact that the OS was light, the water helped to support it, and the motor torque was high.
- A reasonable first estimate of the required maximum power of 100W was obtained to reorient a potential OS.
- A non-spherical OS was successfully tested.

As shown in Fig.6.42 all the tests performed were able to lead the pin to the final home location ($\theta = 0°$, $\phi = 43°$).

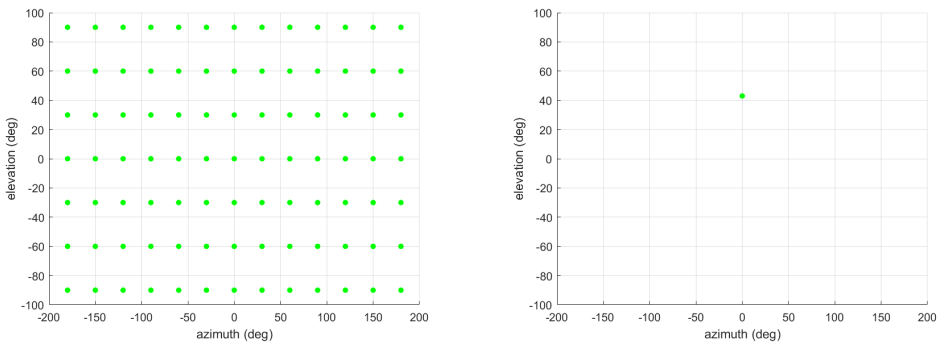

(a) Initial OS Pin directions. (b) Final OS Pin directions.

Figure 6.42 Testbed tests performed at different initial OS pin direction.

6.5 Conclusion

This thesis work addressed to a process to evaluate and produce a testbed for OS orientation, as a part of a notional MSR OS manipulation phases. Specifically, this mechanism consists of a Wiper sweeping the OS surface until it engages with a pin on the OS, ultimately orienting the OS via the pin. The Wiper profile was analytically optimized with respect to the MA of the Wiper

on the pin, and a closed-form solution was shown. This yields a deterministic approach during the orientation of the OS, which is a fundamental feature to be tested and validated to assess the maturity of this concept. The main results were as follows:

1. Qualitative figures of merit analysis to show the suitability of the Wiper mechanism from a systems engineering perspective.
2. Analytical model to describe the Wiper profile and its interaction with the positive feature and the pin. This analytical model was optimized to reach the final Wiper profile.
3. Experimental setup including hardware integration, sensors configuration and Extended Kalman Filter implementation in Python for IMU sensor fusion. This allows the obtainment of scientific data that were analyzed to show the proper working of this reorientation mechanism concept.
4. Successful testbed implementations.

6.5.1 Future Perspectives

The research conducted by MOSTT would potentially flow into ROCS flight project, that is the flight project program that would be in charge to accommodate all the manipulation mechanisms on board of the SRO spacecraft for a future MSR mission concept.

6.6 Acknowledgements

A special thank goes to J. Parrish for his support and his really valuable availability and mentorship. It was a great pleasure being exposed to ROCS under guide. I would like to thank also C. Whetsel for involving me with ROCS in the very first place. I would like to thank R. Mattingly, all the ROCS team members and the NASA JPL - Caltech Mars Exploration Directorate for their advices and material concerning this thesis.
I would like to thank all the MOSTT team members, in particular Dr. R. Mukherjee for his support. It was a pleasure working with him and learning

from him the proper professional attitude towards the work. He has been a great leader and a teacher too. I want to thank also J. Mayo for his support and patience in working together.
I really desire thanking Dr. L. Alkalai and Dr. A. Stoica to having hosted me during the period of my research at NASA JPL - Caltech, together with all the members of section 347.
I really desire to thank A. Margaryan for his continuous support through the JVSRP educational office at NASA JPL - Caltech.
It has been a great adventure and I am incredibly grateful to have the opportunity to spend so much time in a great place like NASA JPL - Caltech with amazing people, as the ones mentioned above. I do not take it for granted. Thank you very much again to everybody! I hope I did not forget anyone.

Dare mighty things!

This research was carried out at the Jet Propulsion Laboratory, California Institute of Technology, under a contract with the National Aeronautics and Space Administration. Copyright 2018 California Institute of Technology. Government sponsorship acknowledged. All rights reserved.

Conclusions

General Conclusion

This whole work was devoted to the design and implementations of impactive orbital manipulation mechanisms, enriched by two precious experiences in relevant locations. The first part of the PhD period was dedicated to the design of an on orbit robotic gripper mechanical system in collaboration with Thales Alenia Space in Turin, Italy. The second part of PhD period took place at NASA Jet Propulsion Laboratory - California Institute of Technology USA, supporting the design of an electro-mechanical system to reorient a spherical orbital sample for a potential Mars Sample Return mission concept.

The first main result of this work was identified in the conception of a close loop that reflects a path to support the creation and verification of innovative gripper concepts, see Fig.1. This itinerary brought to the creation of two different innovative orbital manipulation mechanisms. A deeper description of the obtained results are described in the next SubSections.

Thales Alenia Space Torino Project

In this work a robotic manipulator system and in particular a gripper able to grasp a payload in LEO was described. This action takes place in a semi-cooperative rendezvous scenario without docking. To obtain the desired goals, the following results were reached:

- The designed gripper respects the project guidelines and guarantees payload grasping and holding: Mass 2.5kg (<3kg), with a 25% mar-

gin; Volume 10l (<16l), with a 25% margin; Power = 15W actuator + electronics, with a 25% margin.

- The grasping tool system requirements identification were developed in terms of gripper requirements identification and handle requirements identification.
- Various prehension methods were studied. The gripper results is an impactive-ingressive robotic hand with a handle. Requirements for both these components are given through trade-off studies considering various criteria. Only a single actuator was adopted to govern two degrees of freedom per finger. Underactuation strategy was selected and a new gripper phalanx actuation approach was performed.
- A gripper development baseline configuration was executed in terms of geometric models, materials, software functional model, single finger kinematic and dynamic analysis functional models, structural analysis, together with a test report.
- Configuration designs were shown and the adopted choices were discussed.

NASA JPL - Caltech Project

In this work a potential Mars Sample Return architecture was described together with the NASA JPL - Caltech RTD MOSTT to evaluate and produce an end-to-end testbed to test all manipulation phases of an orbiting Sample. Summaries were reported of the previous studies about MSR campaigns and trade-off studies were run to compare the different criteria and figures of merit to rank the different mechanism concepts.

In particular, the author supported a MOSTT reorientation mechanism where a Wiper swipes an OS surface until it engages with an OS positive feature (pin) and through that, the Wiper reorients the OS. The Wiper profile was studied. Its profile was described in an analytical way and optimized, showing to be able to obtain a Wiper profile close-form solution. This brings to a deterministic approach during OS orientation and this is a fundamental feature to be tested and validated and to assess the maturity of this concept within a

possible future flight system. The Wiper mechanism was tested supporting the creation of some testbeds in order to validate this concept.

The main results were:

- Trade-off studies to evaluate system requirements, criteria and figures of merit to rank all the mechanical concepts.
- Testbed support integration for what concerns both hardware (3D printing, assembling), electronic (wiring) and actuators and sensors configuration and control.
- Analytical model to describe the Wiper profile and its interaction with the positive feature and the pin. This analytical model was optimized to arrive at the final profile, adopting as cost function parameters both the scissor angle and the mechanical advantage.
- Design of experiment considering hardware integration, sensors configuration and Extended Kalman Filter implementation in Python for IMU sensor fusion. This allows to obtain scientific data that were analyzed to show the proper working of this reorientation mechanism.

Bibliography

[1] B. Siciliano, O. Khatib, Handbook of Robotics, Springer (Malestrom), 2008.

[2] G. Genta, Introduction to the Mechanics of Space Robots, Springer (Space Technology Library), 2012.

[3] T. Matsueda, K. Kuraoka, K. Goma, T. Sumi, R. Okamura, JEMRMS system design and development status, CH30 10-619 11039, IEEE, 1991.

[4] G. Carbone, Grasping in Robotics, Springer, 2013.

[5] G. J. Monkman, S. Hesse, R. Steinmann, H. Schunk, Robot Grippers, Wiley-VCH, 2007.

[6] I. Yamano, T. Maeno, Five-fingered Robot Hand using Ultrasonic Motors and Elastic Elements, Proceedings of the 2005 IEEE International Conference on Robotics and Automation Barcelona, 2005.

[7] M. T. Mason, Mechanics of Robotic Manipulation, The MIT Press, 2001.

[8] R. M. Murray, Z. Li, S. Shankar Sastry, S. Shankara Sastry, A Mathematical Introduction to Robotic Manipulation, CRC Press, 1994.

[9] ESA Space Rider fact sheet.

[10] G. Tumino, Y. Gerard, IXV: Intermediate eXperimental Vehicle, ESA Fact Sheet, 2015.

[11] Vision and Voyages for Planetary Science in the Decade 2013-2022, The National Academies Press Washington, D.C. www.nap.edu, 2011.

[12] L. David, Mars Sample Return: Scientists Debate How to Bring Red Planet Rocks to Earth, Space Insider (www.space.com/37815-nasa-mars-sample-return-plans.html), 16 August 2017.

[13] G. Genta, J.-M. Salotti, A. Dupas, IAA Study Group 3.16: Cosmic Study on Global Human Mars System Missions Exploration, October 2015.

[14] P.R. Christensen, N.S. Gorelick, G.L. Mehall, and K.C. Murray, THEMIS Public Data Releases, Planetary Data System node, Arizona State University, http://themis-data.asu.edu.

[15] R.E. Arvidson, C.C. Allen, D.J. Des Marais, J. Grotzinger, N. Hinners, B. Jakosky, J.F. Mustard, R. Phillips, and C.R. Webster. Science Analysis of the November 3, 2005 Version of the Draft Mars Exploration Program Plan. January. Available at http://mepag.jpl.nasa.gov/reports/index.html. White papers received by decadal survey: John F. Mustard, Seeking Signs of Life on a Terrestrial Planet: An Integrated Strategy for the Next Decade of Mars Exploration; Douglas Stetson, Mars Exploration 2016-2032: Rationale and Principles for a Strategic Program, 2006.

[16] Mars Scientific Goals, Objectives, Investigations, and Priorities: 2015. V. Hamilton, ed., 74 p. white paper posted June, 2015 by the Mars Exploration Program Analysis Group (MEPAG) at http://mepag.nasa.gov/reports.cfm, 2015.

[17] R. Mattingly, L. May, Mars Sample Return as a Campaign, NASA, IEEE Proceedings, 2011.

[18] R. McGregor and L. Oshinowo, Flight 6A: Deployment and Checkout of the Space Station Remote Manipulator System (SSRMS), Proceeding of the 6th International Symposium on Artificial Intelligence and Robotics & Automation in Space: i-SAIRAS 2001, Canadian Space Agency, St-Hubert, Quebec, Canada, June 18-22, 2001.

[19] G. Hirzinger, K. Landzettel, J. Heindl, and J. Dietrich, ROTEX - The First Robot in Space, SAE Technical Paper 941444, doi:10.4271/941444, 1994.

[20] A. Albu-Schaeffer et al, ROKVISS Robotics Component Verification on ISS, Current Experimental Results on Parameter Identification, Orlando, Florida, May 15 to May 19, 2006.

[21] A. Albu-Schaeffer et al, ROKVISS Robotics Component Verification on ISS, Preliminary Results for Telepresence, Beijing, China, October 9 to 15, 2006.

[22] J. Walker, Orbital Express, Defense Advanced Research Projects Agency, March 2007.

[23] M. Caron, On-orbit Operations Support from the Canadian Space Agency Flight Control, Proceedings of the SpaceOps 2008 Conference. Virginia: AIAA, 2008.

[24] M. Hiltz, C. Rice, K. Boyle, et al., Canadarm: 20 Years of Mission Success through Adaptation, Proceedings of the 6th International Symposium on Artificial Intelligence and Robotics & Automation in Space. Quebec: CSA, 2001.

[25] K. Phung, K. Nguyen, M. Hiltz. RMS Operation Support: From the Space Shuttle to the Space Station, Proceeding of the 6th International Symposium on Artificial Intelligence and Robotics & Automation in Space i-SAIRAS 2001. Quebec, Canada, 2001.

[26] R. Stott, P. Schoonejans, F. Didot, et al., Current Status of the European Robotic Arm (ERA), its Launch on the Russian Multi-purpose Laboratory Module (MLM) and its Operation on the ISS, Proceedings of the 9th ESA Workshop on Advanced Space Technologies for Robotics and Automation ASTRA 2006. Noordwijk, The Netherlands, 2006.

[27] ESA, European Robotic Arm Factsheet, ESA-HSO-COU-007 document number, 2.0 review, International Space Station project, ERASMUS Centre - Directorate of Human Spaceflight and Operations, 2012.

[28] F. P. Meiboom, ERA's Development Programme. On Station, 2000.

[29] C. J. M. Heemskerk, M. Visser, D. Vrancken, et al., Extending ERA's Capabilities to Capture and Transfer Large Payloads, Proceedings of the 9th ESA Workshop on Advanced Space Technology for Robotics and Automation ASTRA 2006. Noordwijk: ESA, 2006.

[30] B. Rubinger, P. Fulford, L. Gregoris, et al., Self-Adapting Robotic Auxiliary Hand (SARAH) for SPDM Operations on the International Space Station, Proceedings of the 6th International Symposium on Artificial Intelligence and Robotics & Automation in Space i-SAIRAS 2001. Quebec, Canada, 2006.

[31] C. S. Lovchik, M. A. Diftler, The Robonaut Hand: A Dexterous Robot Hand For Space, Proceedings of the 1999 IEEE International Conference on Robotics & Automation Detroit, Michigan, May 1999.

[32] L. B. Bridgwater, et al., The Robonaut 2 hand - designed to do work with tools, Robotics and Automation (ICRA), 2012 IEEE International Conference on, NASA/JSC, Houston, TX, 14-18 May 2012.

[33] A.M. Dollar, R. Howe, Towards grasping in unstructured environments: grasper compliance and configuration optimization. Advanced Robotics, 19(5), 523-543, 2005.

[34] A.M. Dollar, R. Howe, The Highly Adaptive SDM Hand: Design and Performance Evaluation. International Journal of Robotics Research, 29(5), 585-597, 2010.

[35] C. Melchiorri, G. Vassura, Design of a three- finger gripper for intra-vehicular robotic manipulation. First IFAC Workshop on Space Robotics, SPRO98, Montreal, CA, October 19-22, 1998.

[36] G. Vassura, C. Melchiorri, Three-finger grasping for intra-vehicular space experiments. WAC, Maui, Hawaii, June 11-16, 2000.

[37] L. Biagiotti, C. Melchiorri, G. Vassura, Experimental activity on grasping objects in freefloating conditions. ASTRA, ESTEC, Noordwijk, Netherlands, December 5-7 2000.

[38] L. Biagiotti, C. Melchiorri, G. Vassura, Control of a robotic gripper for grasping objects in no- gravity conditions. ICRA, IEEE Int. Conf. on Robotics and Automation, Seoul, Korea, May 21-26 2001.

[39] L. Biagiotti, C. Melchiorri, G. Vassura, Position/ force control of an arm/gripper system for space manipulation. AIM, IEEE/ASME Int. Conf. on Advances in Mechatronics, Como, Italy, July 8-11 2001.

[40] M. Gabiccini, A. Bicchi, D. Prattichizzo, M. Malvezzi, On the Role of Hand Synergies in the Optimal Choice of Grasping Forces, Autonomoous Robots Volume 31, Issue 2-3, pp 235-252, 2011.

[41] G. Genta, **M. Dolci**, Robotic gripper for payload capture in low Earth orbit; accepted to the second edition of Journal of Chinese Society of Astronautics, July 2017.

[42] VEGA User's Manual, Arianespace, March 2006.

[43] G. Genta, **M. Dolci**, Robotic gripper for payload capture in low Earth orbit; ASME 2016 International Mechanical Engineering Congress & Exposition, IMECE 2016-65429, Phoenix (AZ USA), 11-17 November 2016.

[44] A. Dutta, P. Tsiotras, Hohmann-Hohmann and Hohmann-phasing Cooperative Rendezvous Maneuvers, The Journal of the Astronautical Sciences, Vol. 57, Nos. 1 & 2, pp. 393-417, 01/06 2009.

[45] **M. Dolci**, G. Genta, S. Ferraris, Robotic gripper technology for cargo transfer in low Earth orbit; 67th International Astronautical Congress, IAC-16,D2,3,3,x32043, Guadalajara, Mexico 26-30 September 2016.

[46] D. Richiardi, Preliminary Design of a Space Manipulator, Master's Degree Thesis at Politecnico di Torino and Thales Alenia Space Italia, Supervisor Prof. B Bona, October 2015.

[47] G. Genta, **M. Dolci**, Gripper for capturing a payload in Low Earth Orbit; Memorie Accademia delle Scienze di Torino, serie V - Classe di Scienze Fisiche ISSN 1120-1630, presented on January, 13th 2016.

[48] John C. Mankins, Technology Readiness levels, A White Paper, Advanced Concepts Office, Office of Space Access and Technology NASA, April 6 1995.

[49] Open Source Computer Vision, opencv.org.

[50] **M. Dolci**, S. Ferraris, G. Genta, P. Pellegrino, D. Richiardi, G. Scalise, Robotic system study for a LEO orbiting vehicle payload capturing; 23rd Conference of the Italian Association of Aeronautics and Astronautics", Politecnico di Torino (Italy), 17-19 November 2015.

[51] S. Garrido-Jurado, R. Munoz-Salinas, F.J Madrid-Cuevas, M.J. Mar'n-Jimenez, Automatic generation and detection of highly reliable fiducial markers under occlusion, Pattern Recognition, vo. 47, 6, 2280 - 2292, 0031-3203, 2014.

[52] L. Birglen, T. Laliberté, C. Gosselin, Underactuated Robotic Hands, Springer Tracts in Advanced Robotics, ISSN 1610-7438 Library of Congress Control, Number: 2007941942, Springer-Verlag Berlin Heidelberg, 2008.

[53] Y. Tlegenov, K. Telegenov, A. Shintemirov, An Open-Source 3D Printed Underactuated Robotic Gripper, IEEE, 2014.

[54] A. Bicchi, Hands for Dexterous Manipulation and Robust Grasping: A Difficult Road Toward Simplicity, IEEE Transactions on robotics and automation, vol. 16, no. 6, 2000.

[55] Torlon resins Engineering Data, Solvay Advanced Polymers.

[56] Maxon motor 2015 / 2016 high precision actuators and controls program.

[57] NSK Ltd. Precision Machinery & Parts e-Project team.

[58] V. Lumelsky, Whole-Body Robot Sensing Is Prerequisite for Human-Robot Interaction and Teams". Invited presentation, Workshop on Tactile Sensing in Humanoids - Tactile Sensors and Beyond, 9th IEEE-RAS International Conf. on Humanoid Robots (Humanoids'2009), Paris, France, Oct. 2009.

[59] R. S. Dahiya, P. Mittendorfer, M. Valle, G. Cheng, V. Lumelsky, Directions towards Effective Utilization of Tactile Skin, IEEE Sensors Journal, Vol. 13 (11), pp 4121, 4138, 2013.

[60] Matlab, Brushless DC Motor

[61] S. Dubowsky, E. Papadopoulos, The Kinematics, Dynamics and Control of Free-Flying and Free-Floating Space Robot Systems, IEEE Transactions on Robotics and Automation, vol. 9, No. 5, October 1993.

[62] G. Scalise, Study on Target Tracking Control for a Free-Floating Space Robot, Università degli studi di Roma La Sapienza, Prof. F. Curti, Master's Degree Thesis, 2012.

[63] S. Dubowsky, E. Papadopoulos The Kinematics, Dynamics and Control of Free-Flying and Free-Floating Space Robot Systems, IEEE Transactions on Robotics and Automation, vol. 9, No. 5, October, 1993.

[64] Y. Xu, T. Kanade, Space robotics: dynamics and control; Carnegie Mellon University Springer Science + Business Media, LLC, 1993.

[65] J. R. Wertz and W. J. Larson, Space Mission Analysis and Design; Space Technology Library, Space technology Series, third edition, 1999.

[66] S. Murchie, A. McEwen, P. Christensen, J. Mustard, and J.-P. Bibring, Discovery of Diverse Martian Aqueous Deposits from Orbital Remote Sensing, presentation from the Curation and Analysis Planning Team for Extraterrestrial Materials Workshop on Ground Truth from Mars, Science Payoff from a Sample Return Mission, Albuquerque, New Mexico, available at http://www.lpi.usra.edu/captem/msr2008/presentations/, April 21-23, 2008.

[67] iMARS. Preliminary Planning for an International Mars Sample Return Mission: Report of the International Mars Architecture for the Return of Samples (iMARS) Working Group, International Mars Architecture for the Return of Samples Working Group, 2008.

[68] An Astrobiology Strategy for the Exploration of Mars, The National Academies Press, Washington DC, 2007.

[69] M.J. Drake, W.V. Boynton, and D.P. Blanchard, The Case for Planetary Sample Return Missions: 1. Origin of the Solar System, Eos 68:105, 111-113, 1987.

[70] E. Klein et al., The Mobile MAV Concept for Mars Sample Return, IEEE Aerospace Conference, Montana, USA, 1-8 March 2014.

[71] R. Lock, Z. Bailey, T. Kowalkowski, Mars Sample Return Orbiter Concepts Using Solar Electric Propulsion for the Post-Mars2020 Decade, IEEE Aerospace Conference, Montana, USA, 1-8 March 2014.

[72] J.L. Gooding, M.H. Carr, and C.P. McKay, The Case for Planetary Sample Return Missions: 2. History of Mars, Eos 70:745, 754-755, 1989.

[73] G. Ryder, P.D. Spudis, and G.J. Taylor, The Case for Planetary Sample Return Missions: 3. The Origin and Evolution of the Moon and Its Environment, Eos 70:1495, 1505-1509, 1989.

[74] T.D. Swindle, J.S. Lewis, and L.A. McFadden, The Case for Planetary Sample Return Missions: 4. Near-Earth Asteroids and the History of Planetary Formation, Eos 72:473, 479-480, 1991.

[75] National Research Council, Assessment of Mars Science and Mission Priorities, The National Academies Press, Washington, D.C., pp. 83-88, 2001.

[76] National Research Council, Strategy for the Exploration of the Inner Planets: 1977-1987, National Academy of Sciences, Washington, D.C., 1978.

[77] National Research Council, Update to Strategy for Exploration of the Inner Planets, National Academy Press, Washington, D.C., 1990.

[78] National Research Council, International Cooperation for Mars Exploration and Sample Return, National Academy Press, Washington, D.C., 1990, pp. 1, 3, and 25. National Research Council, An Integrated Strategy for the Planetary Sciences: 1995-2010, National Academy Press, Washington, D.C., 1994.

[79] National Research Council, Review of NASA's Planned Mars Program, National Academy Press, Washington, D.C., pp. 3, 26, and 29, 1996.

[80] National Research Council, Assessment of Mars Science and Mission Priorities, The National Academies Press, Washington, D.C., 2001, pp. 3, 83-88, and 99-102, 2001.

[81] National Research Council, New Frontiers in the Solar System: An Integrated Exploration Strategy, The National Academies Press, Washington, D.C., pp. 85-87, 2003.

[82] National Research Council, An Astrobiology Strategy for the Exploration of Mars, The National Academies Press, Washington, D.C., pp.8-9 and 105-107, 2007.

[83] L.M. Pratt, C. Allen, A.C. Allwood, A. Anbar, S.K. Atreya, D.W. Beaty, M.H. Carr, A. Crisp, D.J.D. Marais, J.A. Grant, D.P. Glavin, et al.; Mars Astrobiology Explorer-Cacher (MAX-C): A Potential Rover Mission for 2018. Final report from the Mid-Range Rover Science Analysis Group (MRR-SAG). Posted by the Mars Exploration Program Analysis Group (MEPAG). November 10. Available at http://mepag.jpl.nasa.gov/reports/, 2009.

[84] L.E. Borg, D.J.D. Marais, D.W. Beaty, O. Aharonson, S.A. Benner, D.D. Bogard, J.C. Bridges, C.J. Budney, W.M. Calvin, B.C. Clark, J.L. Eigenbrode, et al.; Science priorities for Mars sample return. Astrobiology 8:489-535, 2008.

[85] National Aeronautics and Space Administration; Mission Concept Study: Planetary Science Decadal Survey Mars 2018 MAX-C Caching Rover, March 2010.

[86] S. Hayati, Strategic Technology Development for Future Mars Missions, white paper received by decadal survey.

[87] A. Ogilvie et al., Autonomous Satellite Servicing Using the Orbital Express Demonstration Manipulator System, International Symposium on Artificial Intelligence, Robotics and Automation in Space, Hollywood, USA, February 26 - 29, 2008.

[88] R. Kornfeld, J. Parrish, and S. Sell May, Mars Sample Return: Testing the Last Meter of Rendezvous and Sample Capture, Journal of Spacecraft and Rockets 44(3), June 2007.

[89] J. Parrish, To Mars and Back: Technologies for a Potential NASA Mars Sample Return, Mountain View, USA, 14 June 2017.

[90] J. Parrish, Returned Mars Sample Workshop, 80th Annual Meeting of the Meteoritical Society, Santa Fe USA, 24 July 2017.

[91] Planetary Science Decadal Survey MSR Orbiter Mission (Including Mars Returned Sample Handling); NASA HQ POC: Lisa May, March 2010.

[92] R. Oberto, Mars Sample Return, a Concept Point Design by Team-X (JPL's Advanced Project Design Team), 2002 IEEE Aerospace Conference Proceedings, Vol. 2, IEEE Publications, Piscataway, NJ, pp. 559-573, 2002.

[93] A. Kenneth Farley, H. Kenneth Williford, Scientific Rationale for Depot Caching on Mars 2020, California Institute of Technology. Government sponsorship acknowledged, 2015.

[94] K. McManamon, R. Lancaster, and N. Silva, ExoMars Rover Vehicle Perception System Arch. & Test Results. ASTRA Conference, 2013.

[95] P. Meacham, R. Lancaster, and N. Silva, The Development of the LPM for the ExoMars Rover Vehicle, ASTRA Conference, 2013.

[96] NASA/JPL-Caltech, available at https://www.nasa.gov/press-release/nasas-next-mars-rover-progresses-toward-2020-launch.

[97] S. Perino et al., The Evolution of an Orbiting Sample Container for Potential Mars Sample Return, IEEE Proceedings Aerospace Conference, 2017.

[98] National Aeronautics and Space Administration. Mission Concept Study: Planetary Science Decadal Survey MSR Lander Mission. In review.

[99] R. Friend, Orbital Express Program Summary and Mission Overview, Proc. SPIE 6958, 695803, 15 April 2008.

[100] National Research Council. 2009. Assessment of Planetary Protection Requirements for Mars Sample Return Missions.

[101] J.D. Rummel et al., A Draft Test Protocol for Detecting Possible Biohazards in Martian Samples Returned to Earth, NASA/CP-2002-211842, National Aeronautics and Space Administration, Washington, DC, 2002.

[102] Planetary Protection Provisions for Robotic Extraterrestrial Missions Responsible Office: Science Mission Directorate NASA Procedural Requirements, April 20, 2011.

[103] R.R. Wessen, C. Borden, J. Ziemer, J. Kwok, AIAA SPACE 2013 Conference and Exposition September 10-12, 2013, San Diego, CA AIAA 2013-5454, 2013.

[104] J. K. Ziemer, J. Ervin, and J. Lang, AIAA SPACE 2013 Conference and Exposition September 10-12, 2013, San Diego, CA AIAA 2013-5431, 2013.

[105] B. S. Bloom, M. D. Engelhart, E. J. Furst, W. H. Hill, D. R. Krathwohl, Taxonomy of educational objectives: The classification of educational goals. Handbook I: Cognitive domain. New York: David McKay Company, 1956.

[106] P. Younse, **M. Dolci**, K. Lalla, P. Ohta, E. Olds, L. Strahle, Systems Architecting using Bloom's Taxonomy to Promote Creative Engineering Synthesis, accepted to the 2018 IEEE Aerospace Conference, Montana, USA, 03-10 March 2018.

[107] M. T. Mason, J. K. Salisbury Jr., Robot hands and the Mechanics of Manipulation, MIT Press, 1985.

[108] M. R. Cutkosky, Robotic Grasping and Fine Manipulation, Kluwer Academic Publishers, 1985.

[109] A. Bicchi, A. Marigo, Dexterous Grippers: Putting Nonholonomy to Work for Fine Manipulation, International Journal of Robotics Research, 2001.

[110] R. R. Ma and A. M. Dollar, On Dexterity and Dexterous Manipulation, The 15th International Conference on Advanced Robotics Tallinn University of Technology Tallinn, Estonia, June 20-23, 2011.

[111] B. Sherwood, D. Pearson, D. B. Smith, R. Greeley, W. Whittaker, G. Woodcock, G. Barton, and W. Siegfried, Mars Sample Return: Architecture and Mission Design, 2002 IEEE Aerospace Conference Proceedings, Vol. 2, IEEE Publications, Piscataway, NJ, pp. 536-542, 2002.

[112] F. Mailland, K. Geleen, P. Coste, M. Zaccariotto, S. Debei, C. Bettanini, S. Cocuzza, E. Piersanti and E. Monchieri, "Sample Canister Capture Mechanism for Mars Sample Return: Design and Testing of an Elegant Breadboard Model" in 63rd International Astronautical Congress, Naples, Italy, 2012.

[113] R. Carta, D. Filippetto, M. Lavagna, F. Mailland, P. Falkner and J. Larranaga, Sample Canister Capture Mechanism for Mars Sample Return: Functional and Environmental Test of the Elegant Breadboard Model in 65th International Astronautical Congress, Toronto, Canada, 2014.

[114] R. Mukherjee, N. Abcouwer, J. Kim, R. Mccormick, P. Godart, P. Bailey, Technologies for mars on-orbit robotic sample capture and transfer concept, 2017 IEEE Aerospace Conference, Montana USA, 4-11 March 2017.

[115] J. Hopkins, OSCAR: Crew-Assisted Lunar Sample Return with Orion. Lockheed Martin. NASA Community Workshop on the Global Exploration Roadmap, April 2014.

[116] NASA Systems Engineering Handbook NASA/SP-2007-6105 Rev1.

[117] R. Mukherjee, B. Chamberlain-Simon, N. Abcouwer, R. Mc Cormick, R. Smith, T. Frederick, **M. Dolci**, Concepts for Mars On-Orbit Robotic Sample Capture and Transfer, submitted to 2017 IEEE Aerospace Conference, Montana, USA, 04-11 March 2017.

[118] Z. Pavi, V. Novoselac, Notes on TOPSIS Method, International Journal of Research in Engineering and Science (IJRES) ISSN (Online): 2320-9364, ISSN (Print): 2320-9356 www.ijres.org Volume 1 Issue 2, June. 2013.

[119] C.L. Hwang, and K. Yoon, Multiple attribute decision making: Methods and applications. Heidelberg: Springer. http://dx.doi.org/10.1007/978-3-642-48318-9, 1981.

[120] A. Zadeh Sarraf, A. Mohaghar, H. Bazargani, Developing TOPSIS method using statistical normalization for selecting knowledge management strategies. Journal of Industrial Engineering and Management, [S.l.], p. 860-875, ISSN 2013-0953, sep. 2013.

[121] P. Younse, **M. Dolci**, K. Lalla, P. Ohta, E. Olds, L. Strahle, An Orbiting Sample Capture System Architecture for Proposed Mars Sample Return, accepted to the 2018 IEEE Aerospace Conference, Montana, USA, 03-10 March 2018.

[122] N. C. Dafle et al, Extrinsic Dexterity: In-Hand Manipulation with External Forces, National Science Foundation [NSF-IIS- 0916557], Army Research Laboratory [W911NF-10-2-0016] and ABB, 2014.

[123] F. Zhu, L. Jones-Wilson, M. Peck, Capturing and Docking Spacecraft with Flux Pinned Interfaces, 67th International Astronautical Congress paper ID 32785, 2016.

[124] **M. Dolci**, J. Mayo, B. Chamberlain-Simon, R. Smith, J. Kim, W. Ubellacker, P. Ohta, R. Mukherjee, Electro-Mechanical System to Reorient a Spherical Orbital Sample for a Potential Mars Sample Return Mission Concept, submitted to Acta Astronautica, August 2017.

[125] J. J. Uicker, G. R. Pennock, and J. E. Shigley, Theory of Machines and Mechanisms, Oxford University Press, New York, 2003.

[126] A. Gray, Viviani's Curve. §8.6 in Modern Differential Geometry of Curves and Surfaces with Mathematica, 2nd ed. Boca Raton, FL: CRC Press, pp. 201-202, 1997.

[127] E. Kenison and H. C. Bradley, Descriptive Geometry. New York: Macmillan, p. 284, 1935.

[128] D. J. Struik, Lectures on Classical Differential Geometry. New York: Dover, 1988.

[129] M. Cavazzuti, Optimization Methods: From Theory to Design, DOI: 10.1007/978-3-642-31187-1-2, Springer-Verlag Berlin Heidelberg, 2013.

[130] F. G. Teixeira, Traité des courbes spéciales remarquables plane et gauches, Vol. 2. Coimbra, Portugal, 1908-1915. Reprinted New York: Chelsea, and Paris: Gabay, 1971.

[131] D. Von Seggern, CRC Standard Curves and Surfaces. Boca Raton, FL: CRC Press, p. 270, 1993.

[132] E. W. Weisstein, "Viviani's Curve." From MathWorld–A Wolfram Web Resource. http://mathworld.wolfram.com/VivianisCurve.html.

[133] A. Gray, "Tangent and Normal Lines to Plane Curves." §5.5 in Modern Differential Geometry of Curves and Surfaces with Mathematica, 2nd ed. Boca Raton, FL: CRC Press, pp. 108-111, 1997.

[134] E. Oberg, Machinery's Handbook 28th Edition, Industrial Press, 2008.

[135] www.protolabs.com.

[136] http://www.stratasys.com/3d-printers/design-series/objet260-connex3.

[137] www.mcmaster.com.

[138] www.cadsoft.io.

[139] store.arduino.cc.

[140] www.polulu.com.

[141] 80 / 20 Inc. The Industrial Erector Set, www.8020.net.

[142] www.phidgets.com.

[143] www.robotshop.com.

[144] R. E. Kalman and R. S. Bucy. New results in linear filtering and prediction theory. Journal of basic Engineering, 83(3):95-108, 1961.

[145] R. E. Kalman et al., A new approach to linear filtering and prediction problems. Journal of basic Engineering, 82(1):35-45, 1960.

[146] G. Wetzstein, Advanced IMU Sensor Fusion with Kalman Filtering, Stanford University, EE 267 Virtual Reality, Lecture 11, stanford.edu/class/ee267/, May 2, 2016.

[147] B. Eisenberg and R. Sullivan, Why is the Sum of Independent Normal Random Variables Normal, Math. Magazine, Vol. 81, p 362-366, 2008.

[148] S.-J. Chung, U. Ahsun, and J.-J. E. Slotine, Application of Synchronization to Formation Flying Spacecraft: Lagrangian Approach, Journal of Guidance, Control, and Dynamics, Vol. 32, No. 2, pp. 512-426. doi:10.2514/1.37261, March-April 2009.

[149] L. Ascorti, An Application of the Extended Kalman Filter to the Attitude Control of a Quadrotor, Politecnico di Milano, Master Thesis, 2013.

[150] X. Yun and E. R. Bachmann, Design, implementation, and experimental results of a quaternion-based kalman filter for human body motion tracking, Robotics, IEEE Transactions on, vol. 22, no. 6, pp. 1216-1227, 2006.

[151] A. Sabatini, Quaternion-Based Extended Kalman Filter for Determining Orientation by Inertial and Magnetic Sensing, IEEE Transactions on Biomedical Engineering, Vol. 53, No. 7, July 2006.

[152] O.H. Sebastian et al., Estimation of IMU and MARG orientation using a gradient descent algorithm, 2011 IEEE International Conference on Rehabilitation Robotics Rehab Week Zurich, ETH Zurich Science City, Switzerland, June 29 - July 1, 2011.

[153] H.J. Luinge et al., Estimation of Orientation with Gyroscope and Accelerometers, Proceedings of The First Joint BMES/EMBS Conference Serving Humanity, Advancing Technology, Oct 13-16, Atlanta GA, USA, 1999.

[154] J.E. Bortz, A New Mathematical Formulation for Strapdown Inertial Navigation, IEEE Transactions on Aerospace and Electronic Systems, Vol. AES-7, No. I, January 1971.

[155] M. Leccadito, A Kalman Filter Based Attitude Heading Reference System Using a Low Cost Inertial Measurement Unit, Theses and Dissertations Graduate School, Virginia Commonwealth University, 2013.

[156] C. Bjelbole, An Attitude Determination and Control System for CubeSTAR, University of Oslo, Master Thesis, 2013.

[157] V. Gavrilets, Autonomous Aerobatic Maneuvering of Miniature Helicopters, PhD Thesis, Massachusetts Institute of Technology, May 2003.

[158] J.L. Marins, An Extended Kalman Filter for Quaternion-Based Orientation Estimation Using MARG Sensors, Proceedings of the 2001 IEEE/RSJ International Conference on Intelligent Robots and Systems Maui, Hawaii, USA, Oct. 29 - Nov. 03, 2001.

[159] R.G. Brown, P. Y. C. Hwang, Introduction to Random Signals and Applied Kalman Filtering, Fourth Edition, John Wiley & Sons, Inc., 2012.

[160] Y. Chou, Statistical Analysis, Holt International, ISBN 0-03-089422-0, 1975.